

EPA-600/2-76-039

February 1976

Environmental Protection Technology Series

CHEMISTRY OF FUEL NITROGEN CONVERSION TO NITROGEN OXIDES IN COMBUSTION



Industrial Environmental Research Laboratory
Office of Research and Development
U.S. Environmental Protection Agency
Research Triangle Park, North Carolina 27711

RESEARCH REPORTING SERIES

Research reports of the Office of Research and Development, U.S. Environmental Protection Agency, have been grouped into five series. These five broad categories were established to facilitate further development and application of environmental technology. Elimination of traditional grouping was consciously planned to foster technology transfer and a maximum interface in related fields. The five series are:

1. Environmental Health Effects Research
2. Environmental Protection Technology
3. Ecological Research
4. Environmental Monitoring
5. Socioeconomic Environmental Studies

This report has been assigned to the ENVIRONMENTAL PROTECTION TECHNOLOGY series. This series describes research performed to develop and demonstrate instrumentation, equipment, and methodology to repair or prevent environmental degradation from point and non-point sources of pollution. This work provides the new or improved technology required for the control and treatment of pollution sources to meet environmental quality standards.

EPA REVIEW NOTICE

This report has been reviewed by the U.S. Environmental Protection Agency, and approved for publication. Approval does not signify that the contents necessarily reflect the views and policy of the Agency, nor does mention of trade names or commercial products constitute endorsement or recommendation for use.

This document is available to the public through the National Technical Information Service, Springfield, Virginia 22161.

EPA-600/2-76-039
February 1976

CHEMISTRY OF FUEL NITROGEN CONVERSION
TO NITROGEN OXIDES IN COMBUSTION

by

A. E. Axworthy, G. R. Schneider,
M. D. Shuman, and V. H. Dayan

Rocketdyne Division
Rockwell International
6633 Canoga Avenue
Canoga Park, California 91304

Contract No. 68-02-0635
ROAPs No. 21ADG-08/21BCC-12
Program Element No. 1AB014

EPA Project Officer: G. Blair Martin

Industrial Environmental Research Laboratory
Office of Energy, Minerals, and Industry
Research Triangle Park, NC 27711

Prepared for

U.S. ENVIRONMENTAL PROTECTION AGENCY
Office of Research and Development
Washington, DC 20460

ABSTRACT

The report gives results of an experimental and analytical investigation of chemical mechanisms involved in the conversion of fuel nitrogen to NO_x in combustion. The pyrolysis of fossil fuels and model fuel nitrogen compounds was investigated, droplet and particle combustion models were developed, and premixed flat-flame burner experiments were conducted to study the conversion of HCN and NH_3 to NO_x in low-pressure CH_4 - O_2 -Ar flames. Decomposition rates and products were measured in helium from 850 to 1100 C for pyridine, benzonitrile, quinoxaline, and pyrrole; products were measured for six No. 6 fuel oils, one crude oil, and two coals. HCN was the major nitrogen-containing pyrolysis product: the amount formed increased with temperature. NH_3 was a minor product and little if any N_2 was formed. The burner experiments demonstrated that fuel NO forms relatively slowly above the luminous zone in the same region where CO is oxidized to CO_2 or later. Although HCN and NH_3 gave similar yields of NO, the NH_3 reacted very early in the flame front; most of the HCN survived the luminous zone and then reacted slowly. A mechanism was proposed in which fuel NO forms via the reaction: $\text{O} + \text{NCO} = \text{NO} + \text{CO}$.

CONTENTS

	<u>Page</u>
Summary	1
Phase IA - Theoretical Analysis	1
Phase IB - Fuel and Model Compound Decomposition Studies	3
Phase II - Burner Studies of Fuel NO _x Formation	7
Introduction	17
Phase IA - Theoretical Analysis	19
Chemical Structures of Fuel Nitrogen Compounds	20
General Discussion of Fuel NO _x Formation	25
Kinetics and Mechanisms of Pyrolysis of Organic Nitrogen Compounds	29
Analysis of N-Compound Combustion	34
Combustion Models	49
Phase IB - Fuel and Model Compound Decomposition Studies	95
Introduction	95
Phase IB: Experimental	98
Results and Discussion - Model Compound Pyrolysis	109
Results and Discussion - Inert Pyrolysis of Fuels	148
Phase II - Burner Studies of Fuel NO _x Formation	161
Phase II: Experimental	161
Results and Discussion - Screening Experiments	177
Conclusions - Screening Experiments	199
Results and Discussion - Detailed Probing Experiments	200
Analysis of Results of Flame-Probing Experiments	267
Conclusions From Combustion Experiments	283
<u>Appendix A</u>	
Chemical Analysis Techniques	285
<u>Appendix B</u>	
Coal and Residue Analysis	301
<u>Appendix C</u>	
Modified ASTM Method D2036-72, Hydrogen Cyanide in a Helium Stream Containing Hydrogen Sulfide	303

CONTENTS (Concluded)

	<u>Page</u>
<u>Appendix D</u>	
Phenate Method for NH_3 Measurement-Standard Methods for the Examination of Water and Wastewater	307
<u>Appendix E</u>	
Derivation of NO Oxidation Equation	311
<u>Appendix F</u>	
Thermocouple Radiation Correction	313
<u>Appendix G</u>	
Flame-Probing Data	315
<u>Appendix H</u>	
Derivation of One-Dimensional Flow Equation Including Diffusion and Chemical Reaction	335
<u>Appendix I</u>	
Application of Models to Predict Combustion Behavior	337
Nomenclature	345
References	349

ILLUSTRATIONS

<u>No.</u>		<u>Page</u>
1	Comparison of Model Compound Decomposition Rates in Helium	5
2	Comparison of NO Flux Yield Profiles at Various Conditions	10
3	Distribution of Nitrogen in Wilmington Crude Oil	21
4	Representative Types of Basic Nitrogen Compounds Found in Petroleum	23
5	Representative Types of Nonbasic Nitrogen Compounds Found in Petroleum	24
6	Potential Paths for NO Formation in Fossil Fuel Combustion	28
7	Arrhenius Plots of Pyrolysis Rates for Picolines and Pyridine Obtained by Hurd and Simon	31
8	Equilibrium Products as a Function of Equivalence Ratio for CH _{1.6} -Air Flame at 2100 K and 1 Atmosphere	43
9	Equilibrium Products as a Function of Equivalence Ratio for CH _{1.6} -Air Flame at 1600 K and 1 Atmosphere	44
10	Droplet Vaporization Model	52
11	Droplet Mass and Composition	59
12	Droplet Temperature	60
13	Schematic of Reactant Diffusion and Reaction in a Flame Zone Surrounding a Fuel Droplet	61
14	Droplet Temperature	69
15	Vaporization Rate, Flame-Front Model	70
16	Critical Pressure for Hydrocarbons	71
17	Normal Boiling Point for Hydrocarbons	72
18	Schematic of Particle Burning Process	76
19	Volatile Matter Content	83
20	Fixed Carbon Content	83
21	Variation of Composition of Solid Matter With Degree of Burnout	84
22	Kinetic/Diffusion Model	86
23	Preliminary Kinetic Diffusion Model Results With Flame-Front Model Input	92

ILLUSTRATIONS (Continued)

<u>No.</u>		<u>Page</u>
24	Schematic of Apparatus	99
25	Model Compound Apparatus	102
26	Model Compound Apparatus	103
27	Fuel Pyrolysis Reactor	107
28	Model Compound Reactor, Temperature Profile, and Residence Time	111
29	Rate Data for Pyridine Pyrolysis in Helium	115
30	Pyridine Pyrolysis in Helium, Comparison of Experimental Results With First-Order Rate Expressions	117
31	Pyridine Pyrolysis in Helium, Calculated Percent Decomposed as a Function of Distance and Temperature	119
32	Pyridine Pyrolysis in Helium, Arrhenius Plot of Calculated Decomposition Half-Life	120
33	Rate Data for Model Compound Pyrolysis in Helium, Liquid Sample Injection	123
34	Pyridine Pyrolysis Results Using Vapor Injector	127
35	Effect of Oxygen on Decomposition Rate of Pyridine	128
36	Effect of Oxygen on Decomposition Rate of Benzonitrile	129
37	Effect of Oxygen Concentration on Rate of Pyridine Decomposition	130
38	Effect of Oxygen Concentration on Rate of Benzonitrile Decomposition	131
39	Organic Products of Inert Pyrolysis of Pyridine	134
40	Organic Products of Inert Pyrolysis of Quinoline	135
41	Organic Products of Inert Pyrolysis of Benzonitrile	136
42	Organic Products of Inert Pyrolysis of Pyrrole	137
43	Low-Pressure Flat-Flame Burner Apparatus	162
44	Flat-Flame Burner	164
45	Schematic of Chemiluminescent Analyzer Calibration System	172
46	Typical Calibration Curves for Molybdenum Converter at 800 C	175
47	Conversion of NH_3 to NO_x as a Function of Equivalence Ratio, ϕ , and Flowrate in Screening Experiments at a Pressure of 76 torr	182
48	Effect of Argon Dilution on Temperature at Sampling Point	185

ILLUSTRATIONS (Continued)

<u>No.</u>		<u>Page</u>
49	Effect of Argon Dilution on NO _x Yield	186
50	Comparison of NO _x Yield from NH ₃ and Temperature for Argon Dilution Screening Experiments	187
51	Effect of Sampling Distance on NO _x Yield From NH ₃ at a Pressure of 76 torr	190
52	Effect of Pressure on the NO _x Yield From NH ₃	193
53	Conversion of Additive to NO _x as a Function of Equivalence Ratio, ϕ , in Screening Experiments	195
54	Effect of Pressure on NO _x Yield from HCN	198
55	Comparison of Mole Fraction and Flux Curves, Flame 1, NH ₃ Addition With $\phi = 0.8$	207
56	Flame Temperature vs Time, Flame 1, NH ₃ Addition With $\phi = 0.8$	211
57	Species Mole Fraction vs Time, Flame 1, NH ₃ Addition With $\phi =$ 0.8	212
58	Species Flux vs Time, Flame 1, NH ₃ Addition With $\phi = 0.8$	213
59	Species Reaction Rate vs Time, Flame 1, NH ₃ Addition With $\phi = 0.8$	215
60	Flame Temperature vs Time, Flame 2, HCN Addition With $\phi = 0.8$	219
61	Species Mole Fraction vs Time, Flame 2, HCN Addition With $\phi = 0.8$	220
62	Species Flux vs Time, Flame 2, HCN Addition With $\phi = 0.8$	221
63	Species Reaction Rate vs Time, Flame 2, HCN Addition With $\phi = 0.8$	222
64	Flame Temperature vs Time, Flame 3, HCN Addition With $\phi = 1.5$	225
65	Species Mole Fraction vs Time, Flame 3, HCN Addition With $\phi = 1.5$	226
66	Species Flux vs Time, Flame 3, HCN Addition With $\phi = 1.5$	227
67	Species Reaction Rate vs Time, Flame 3, HCN Addition With $\phi = 1.5$	228
68	Flame Temperature vs Time, Flame 4, NH ₃ Addition With $\phi = 1.5$	231
69	Species Mole Fraction vs Time, Flame 4, NH ₃ Addition With $\phi = 1.5$	232
70	Species Flux vs Time, Flame 4, NH ₃ Addition With $\phi = 1.5$	233
71	Species Flux vs Time, Flame 4, NH ₃ Addition With $\phi = 1.5$	234

ILLUSTRATIONS (Concluded)

<u>No.</u>		<u>Page</u>
72	Species Reaction Rate vs Time, Flame 4, NH ₃ Addition With $\phi = 1.5$	235
73	Flame Temperature vs Time, Flame 5, HCN and Argon Addition With $\phi = 0.8$	240
74	Species Mole Fraction vs Time, Flame 5, HCN and Argon Addition With $\phi = 0.8$	241
75	Species Flux vs Time, Flame 5, HCN and Argon Addition With $\phi = 0.8$	242
76	Species Reaction Rate vs Time, Flame 5, HCN and Argon Addition With $\phi = 0.8$	243
77	Flame Temperature vs Time, Flame 6, HCN and NO Addition With $\phi = 0.8$	246
78	Species Mole Fraction vs Time, Flame 6, HCN and NO Addition With $\phi = 0.8$	247
79	Species Flux vs Time, Flame 6, HCN and NO Addition With $\phi = 0.8$	248
80	Species Reaction Rate vs Time, Flame 6, HCN and NO Addition With $\phi = 0.8$	249
81	Flame Temperature vs Time, Flame 7, HCN and NO Addition With $\phi = 1.5$	252
82	Species Mole Fraction vs Time, Flame 7, HCN and NO Addition With $\phi = 1.5$	253
83	Species Flux vs Time, Flame 7, HCN and NO Addition With $\phi = 1.5$	254
84	Species Reaction Rate vs Time, Flame 7, HCN and NO Addition With $\phi = 1.5$	255
85	Flame Temperature vs Time, Flame 8, NO Addition With $\phi = 1.5$	257
86	Species Mole Fraction vs Time, Flame 8, NO Addition With $\phi = 1.5$	258
87	Species Flux vs Time, Flame 8, NO Addition With $\phi = 1.5$	259
88	Species Reaction Rate vs Time, Flame 8, NO Addition With $\phi = 1.5$	260
89	Comparison of NO Flux Profiles for the Fuel-Rich Flames 3 and 8	262
90	Comparison of Flame 7 NO Flux Profile With Sum of NO Fluxes From Flames 3 and 8	263
91	Species Mole Fractions in C ₂ H ₄ -O ₂ -Ar Flame at Atmospheric Pressure, NO Added Initially at 265 ppm, $\phi = 1.5$	265

TABLES

<u>No.</u>		<u>Page</u>
1	Comparison of Results of HCN and NH ₃ Addition	13
2	Types of Elementary Reactions That May Be Involved in Fuel NO _x Formation	47
3	Estimated Properties for Fuel Grade No. 2	74
4	Hydrocarbon and Thermal NO Reactions	91
5	Reactions for Fuel Nitrogen	93
6	Fuel Samples	98
7	Assigned Wall Temperature Profile for Model Compound Reactor	110
8	Experimental Data on Rate of Pyridine Decomposition in Helium	114
9	Experimental Data on Rate of Model Compound Decomposition in Helium	122
10	Kinetic Parameters for Pyrolysis of Model Compounds in Helium	124
11	Experimental Data on Rate of Pyridine Decomposition in Helium	124
12	HCN Formation in Inert Pyrolysis of Model Compounds	139
13	Nitrogen Balance in Inert Pyrolysis of Pyridine	143
14	Product Mass Balances From Inert Pyrolysis	144
15	Residue Calculations	145
16	Summary of Experimental Data on HCN Formation From Inert Pyrolysis of Oils	150
17	Comparison of HCN Formation From Various Oils Under Inert Pyrolysis Conditions	151
18	Results of Measurements of N ₂ and NH ₃ From Inert Pyrolysis of Oils	153
19	Summary of Percent Fuel-N Converted to NH ₃ + N ₂ in Oil Pyrolysis	155
20	Summary of Micrograms N ₂ per mg Oil From Oil Pyrolysis	155
21	Summary of NO _x Measurements in Screening Experiments With Ammonia Additive	180
22	Effect of Argon Dilution on Oxygen Concentration of Reactant Mixture and Combustion Products	188
23	Summary of Pressure Effect Screening Experiments With NH ₃ Additive	192

TABLES (Concluded)

<u>No.</u>		<u>Page</u>
24	Summary of NO _x Measurements in Screening Experiments With HCN Additive	194
25	Summary of Pressure Effect Screening Experiments, NO _x Yield With HCN Additive	197
26	Conditions for Probing Experiments	201
27	Temperature Profiles	209
28	Conditions at Point of Maximum NO Formation Rate in Post-Flame Gases	270
29	Reaction Scheme for Fuel NO Formation From Ammonia and Hydrogen Cyanide	277

SUMMARY

The study reported here was carried out to investigate further the chemical mechanisms involved in fuel NO_x formation to obtain information that might aid in the development of new approaches for mitigating this problem. The program was conducted under the following three tasks:

Phase IA - Theoretical Analyses

Phase IB - Fuel and Model Compound Decomposition Studies

Phase II - Burner Studies of Fuel NO_x Formation

PHASE IA - THEORETICAL ANALYSIS

A theoretical study of fuel NO_x formation was conducted under this task to complement and to guide the experimental program. The objective of this analysis was to identify potential areas for experimental studies and to aid in data interpretation and development. The literature on nitrogen compounds in fossil fuels was surveyed to determine the chemical structures of the most common fuel nitrogen compounds.

The general reaction paths and physical processes most likely to be involved in fuel NO_x formation were then considered. The remainder of the qualitative analysis of fuel NO_x formation was divided into two areas: (1) consideration of the pyrolysis (pre-flame) type reactions that the volatile fuel nitrogen compounds will undergo (near the surface of the droplet or particle) before approaching the flame front, and (2) consideration of the combustion reactions of fuel nitrogen compounds and their reaction products. These areas relate, respectively, to the Phase IB pyrolysis experiments and the Phase II burner experiments.

The major effort under this theoretical analysis task was the development of a mathematical kinetic-diffusion model for the combustion of oil droplets and coal particles. Such a model was required to establish the physical and chemical conditions that will control the formation of fuel NO_x formation. In addition, the model is prepared to accept chemical rate data, as they become available, for the various reactions of fuel nitrogen compounds and their products. Thus, the model will be useful in testing various possible fuel NO_x formation mechanisms under heterogeneous combustion conditions.

Heterogeneous Combustion Modeling

Models development under this program include a droplet vaporization model, a droplet flame front model, a coal combustion model, and an average film kinetic/diffusion model. Each of these models has essentially the same current status, i.e., computer subprograms have been written, debugged, and checked out to ensure their operability in the very simplest of flow situations, which is the insertion of a single particle with prescribed initial conditions into a gas stream whose conditions are known over the length of the flow. They are ready to be incorporated as subprograms in a decoupled computerized combustion model. The role of the subprograms is to calculate spatial production of gaseous species that are transferred from a size-distributed condensed phase to the gas flowfield.

The computer program to model the heating and vaporization of multicomponent fuel droplets surrounded by a specified gas flowfield does not include any reactions of the fuel vapor components with the surrounding gas. The model accounts for changes in droplet density, latent heat of vaporization, vapor pressure, and vapor thermal and transport properties that arise because of the more rapid gasification of the more volatile droplet components during the course of vaporization. The computer program produces descriptions of the droplet vaporization rate, the average film (boundary layer) surrounding the droplet, the droplet temperature, liquid composition, and droplet diameter from ignition to final burnout.

The droplet flame front model is for the heating and combustion of multicomponent fuel droplets surrounded by a flame front and gives predictions for the combustion rate, droplet heating rate, and the radial location and temperature of the flame front under convective conditions assuming infinite rate fuel kinetics. The computer program produces descriptions similar to the droplet vaporization model with particular attention given to the average film thickness, diffusion rates through the film, vapor residence times within the film, and film temperature and composition profiles.

The coal combustion model comprises a complementary set of computer programs for analyzing the reactions attending combustion of a single condensed fuel particle including particle devolatilization and heterogeneous combustion at the particle surface. Calculated results include: local transient changes in each particle's bulk weight, temperature, and composition; radial temperature and major reaction species concentrations through the film surrounding the particle; and production rates for combustion products.

The kinetic/diffusion model includes the kinetics and diffusion in the droplet film of all compounds and intermediate species. Specifically, it accounts for quasi-global finite rate combustion of mixtures of hydrocarbon compounds, some of which may contain fuel nitrogen, and includes the production rates of fuel NO_x , thermal NO_x , other pollutants, and combustion products. The model solves simultaneously the energy equation, species continuity, and species diffusion equations using boundary conditions of the droplet surface, and the temperature and molar concentrations in the bulk gas stream.

PHASE IB - FUEL AND MODEL COMPOUND DECOMPOSITION STUDIES

The objective of this task was to conduct thermal decomposition studies at elevated temperatures to investigate the fate of nitrogen bound in fossil fuels (fuel-N) under conditions relevant to those existing in the initial phases of the combustion process. Pyrolysis experiments were conducted with model fuel nitrogen compounds to measure the kinetic parameters that determine under what

conditions (i.e., at what point in the flame) typical fuel nitrogen structures will decompose, and to identify the nitrogen-containing species that are formed. Later in the program, fuel oils and coals were pyrolyzed under conditions similar to those employed with the model compounds.

As representative of compounds having the common fuel-N structures, the model compounds pyridine, quinoline, pyrrole, and benzonitrile were chosen for study. After the major features of model compound pyrolysis had been established, fuel oils and coals were pyrolyzed under similar inert pyrolysis conditions, and the nitrogen-containing inorganic products were measured and compared with those formed from the model compounds.

Model Compound Pyrolysis

The model compound study involved the measurement under inert pyrolysis conditions of the decomposition rates, the nitrogen-containing inorganic products, and the major organic products. The oxidative pyrolysis of pyridine and benzonitrile was also investigated. The pyrolysis reactions were studied over the temperature range of 850 to 1100 C in a quartz flow reactor with an ID of 2 mm, a volume of 1 cc, a nominal residence time of $\frac{1}{2}$ second, and a sample size of 0.2 μ l of liquid. Organic decomposition products were measured by temperature-programmed GC, and the inorganic products (NH_3 , N_2 and HCN) were measured (at the microgram level) by a combination of wet-chemical and GC techniques.

Pyridine and pyrrole gave similarly shaped inert decomposition curves on plots of percent undecomposed versus reactor temperature under conditions of constant mass flowrate, Fig. 1, with slopes that remained steep until beyond 95-percent decomposition. The pyrrole is less stable than pyridine, the 50-percent decomposition temperature being lower by about 60 degrees C. Quinoline gave a decomposition curve that was nearly linear with temperature. Quinoline is less stable than all of the other compounds below 910 C, but is more stable than pyrrole above that

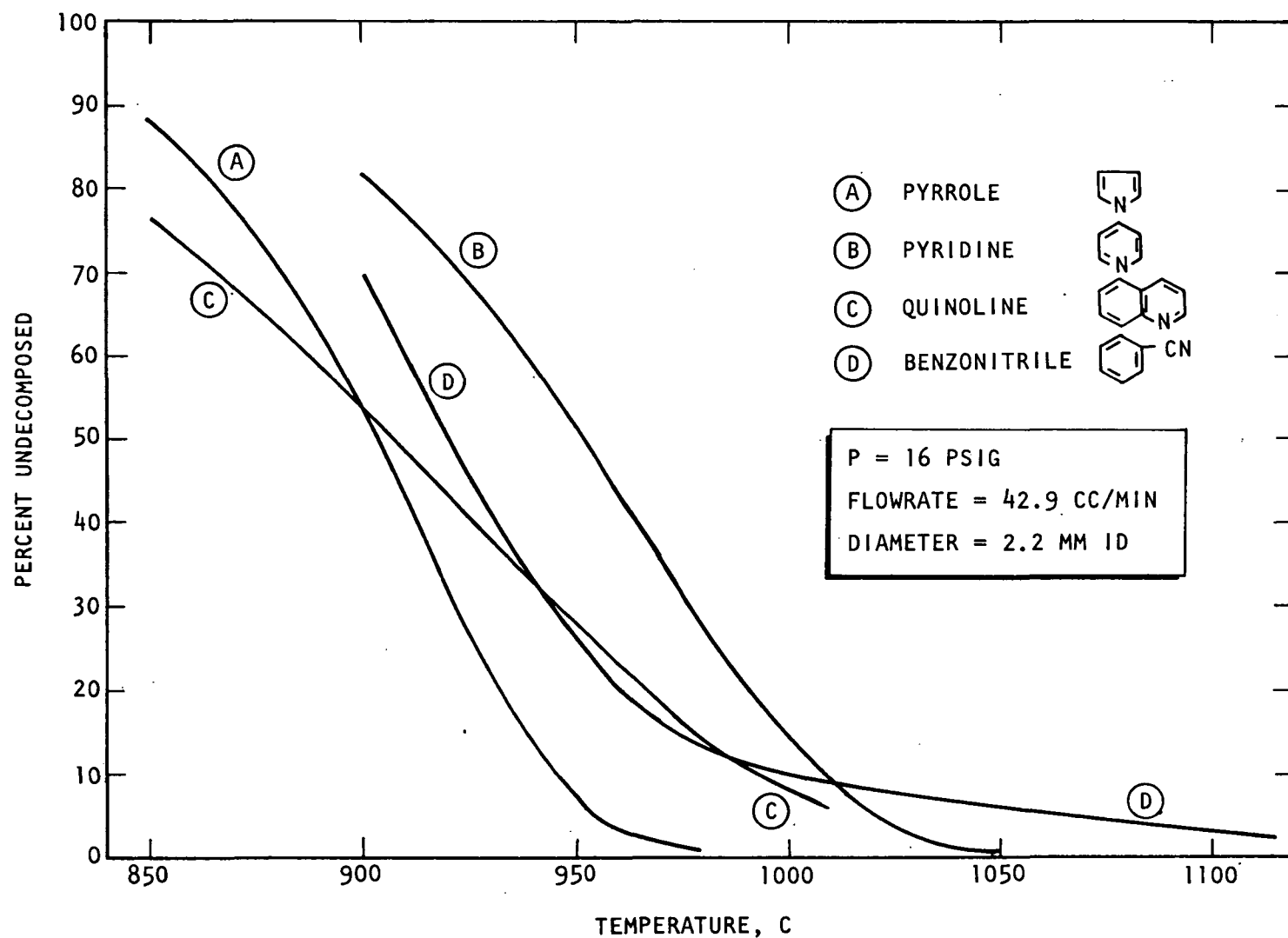


Figure 1. Comparison of Model Compound Decomposition Rates in Helium (constant pressure and mass flowrate)

temperature. Benzonitrile is unusual in that its decomposition curve remains steep up to about 960 C and then tails out at high temperatures. In fact, 3 percent remained undecomposed even at a temperature of 1100 C. Thus, below 1010 C, pyridine is more stable under these conditions than benzonitrile while, above 1010 C, the reverse is true.

The model compound decomposition rates were correlated with the following first-order rate expressions:

$$\text{Pyridine: } k = 3.8 \times 10^{12} \exp (-70,000/RT), \text{ sec}^{-1}$$

$$\text{Pyrrole: } k = 7.5 \times 10^{15} \exp (-85,000/RT), \text{ sec}^{-1}$$

$$\text{Quinoline: } k = 2.4 \times 10^8 \exp (-45,000/RT), \text{ sec}^{-1}$$

Benzonitrile did not fit any simple rate expression and the rate constant for pyridine was found to be a function of concentration. The extrapolated half-life for pyridine is 50 microseconds at 1800 K.

Much of the model compound nitrogen was found to form HCN under inert pyrolysis conditions and most of the remaining nitrogen appeared to be contained in the carbonaceous residue that formed in the reactor. The amount of HCN formed increased with temperatures as follows:

<u>Compound</u>	<u>Temperature, C</u>	<u>Percent N Converted to HCN</u>
Pyridine	960	40
	1105	102
Benzonitrile	955	50
	1105	81

The complete conversion of pyridine to HCN at 1105 C is a very significant result. These model compound results suggest that, at the higher temperatures involved in actual combustion, most of the volatile fuel nitrogen may form HCN

before reaching the flame front. It was found in Phase II of this study that HCN, once formed, is stable until well into the flame zone. Less than 10 percent of the model compound nitrogen is converted to NH_3 under inert pyrolysis conditions and no N_2 forms.

Fuel Pyrolysis

The pyrolysis of fuel oils under similar inert conditions in a flow reactor resulted in 14 to 25 percent conversion of fuel-N to HCN at 950 C and 23 to 42 percent conversion at about 1100 C. A Wilmington crude oil gave somewhat larger yields of HCN. Interestingly, the two coal samples that were studied gave yields of HCN similar to those obtained with fuel oils.

The amount of $\text{NH}_3 + \text{N}_2$ formed (per milligram of fuel) was nearly independent of temperature and fuel-N content. As with the model compounds, NH_3 was a minor product.

Because much of the nitrogen in coals and fuel oils remains in the residue, the volatile fuel nitrogen species may have inorganic product distributions similar to those of the model compounds. The fuel pyrolysis results definitely indicate that HCN is a likely important precursor to the formation of fuel NO_x in combustion.

PHASE II - BURNER STUDIES OF FUEL NO_x FORMATION

HCN and NH_3 were added to premixed $\text{CH}_4\text{-O}_2\text{-Ar}$ flames to investigate the combustion kinetics involved in the formation of NO from these combustion intermediates. NO was added initially in some experiments to determine its fate once formed. The burner was water-cooled and an uncooled quartz probe and an Al_2O_3 -coated thermocouple were used to measure species concentrations and temperature along the centerline of the burner. The burner was enclosed in a glass envelope so that a pressure of 0.1 atm could be maintained to spread the flame and permit more detailed probing. The mole fractions of the major stable species were measured by mass spectrometry.

A chemiluminescent analyzer (CA) measured NO directly and NO₂, HCN and NH₃ after conversion of these species to NO. A molybdenum catalyst converter was used at 400 C to convert NO₂ and at 800 C to partially convert HCN and NH₃. In most of the experiments, the NH₃ or HCN additive was initially at 2500 ppm molar, based on the total flowrate of all gases to the burner, and the Ar/O₂ ratio was the same as the N₂/O₂ ratio in air.

Screening Experiments

Before the detailed probing experiments were initiated, a series of screening experiments was conducted with the probes positioned well downstream (80 mm above the burner) to study the effects of various parameters on the overall NO yield, and to select the best conditions for detailed probing. The overall yields of NO were nearly the same from HCN and NH₃ when the conditions were identical. High NO yields on the order of 80 percent were obtained in fuel-lean flames but the yield dropped off continually when the flame was made more and more fuel rich.

Varying the pressure, burner feed rate or Ar/O₂ ratio usually affected the temperature apparently by changing the position of the flame front and thereby the rate of heat loss to the burner (argon dilution also decreased the adiabatic flame temperature and the effects were partially compensating because the lower temperature and reaction rates moved the flame further from the burner decreasing the heat loss). The observed NO yields appeared to correlate fairly directly with temperature, i.e., increasing somewhat with increasing temperature. Changing the reactant concentrations by varying the pressure or Ar/O₂ ratio had little effect on the final NO yield if the effect of the attendant temperature change was taken into account. This indicates that the reactions that form NO and N₂ are of the same order -- undoubtedly second. The rate of NO formation is presumably a strong function of species concentration even though the yield apparently is not.

Detailed Probing Experiments

Based on the results of the screening tests, detailed probing experiments were conducted at equivalence ratios, ϕ , of 0.8 (fuel-lean) and 1.5. A total of eight flame conditions were investigated. Flames 1 and 2 involved the addition of NH_3 and HCN, respectively, at $\phi = 0.8$. HCN and NH_3 were then added under fuel-rich conditions ($\phi = 1.5$) in flames 3 and 4. In flame 5, the Ar/O_2 ratio was increased 40 percent at $\phi = 0.8$. Both HCN and NO (675 ppm) were added to flames 6 ($\phi = 0.8$) and 7 ($\phi = 1.5$). In flame 8, NO was added alone (675 ppm) at $\phi = 1.5$.

The measured profiles of species mole fraction vs distance from the burner are affected by both the species reaction rate at various positions and the axial diffusion of the species. The probe data were analyzed by the procedure of Fristrom and Westenberg that corrects for diffusion permitting the species flux profiles to be calculated. The flux profiles establish directly the chemical reaction rates at various points in the flame. The importance of this diffusion correction in these low-pressure flames is demonstrated by the flame 1 results where the calculated NO flux is near zero at the top of the luminous zone even though the NO mole fraction has risen to 1300 ppm at that point. Within the accuracy of the rather large diffusion correction involved, these results establish that nearly all of the NO exiting the reactor forms above the luminous zone as does the NO present in the flame front. The flame-front NO results from upstream diffusion caused by a steep NO concentration gradient.

Before summarizing the results from each flame, the NO flux yields obtained for flames 1 through 4 are compared on a single plot in Fig. 2. The time scales were adjusted so that the tops of the luminous zones coincide in this figure. In the fuel-lean flames ($\phi = 0.8$), the NO forms rapidly and in high yield just above the luminous zone. With NH_3 additive, the NO forms more rapidly than with HCN (reaching its maximum rate of formation just before CO_2 formation reaches its maximum in the case of NH_3 and just after with HCN). In fuel-rich flames, the NO forms in low yield from either additive and most of the NO forms far above the luminous zone. There is an apparent surge of NO formation just above the top of the luminous zone.

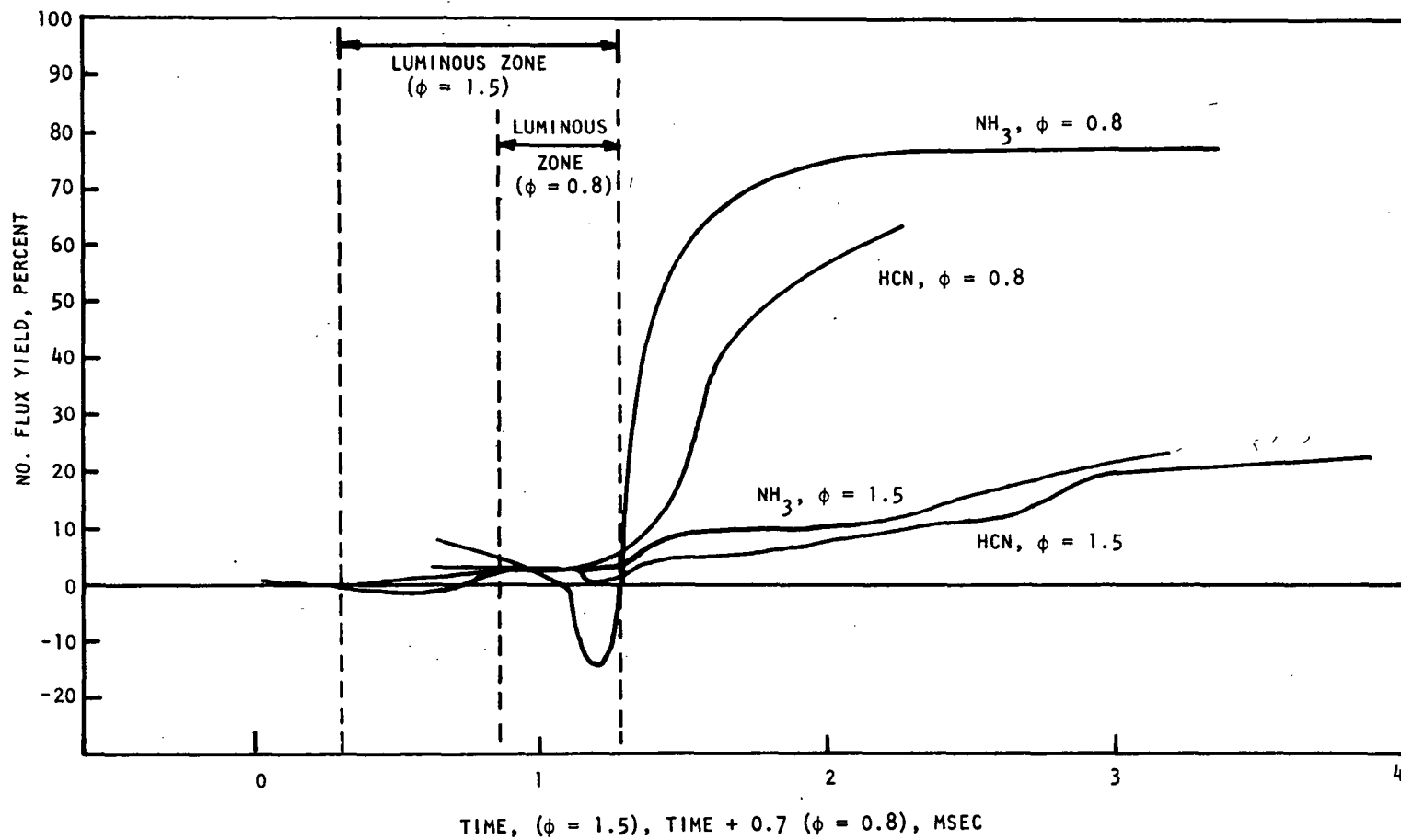


Figure 2. Comparison of NO Flux Yield Profiles at Various Conditions

Flame 1: NH_3 , $\phi = 0.8$. In the fuel-lean flame, all of the NH_3 reacts below the top of the luminous zone to form nitrogen species that are not measurable in the probe-converter-CA system. Less than 20 percent of the NH_3 is converted to N_2 because the final N_2 yield is 18 percent and N_2 is not expected to react in these moderate-temperature flames. The unidentified nitrogen intermediate (probably a free radical) forms NO rapidly and in high yield just above the luminous zone (Fig. 2).

Flame 2: HCN, $\phi = 0.8$. In contrast to NH_3 , most of the added HCN apparently survives the luminous zone in the fuel-lean flame. The "HCN"* reacts rapidly just above the luminous zone and NO forms in high yield reaching its maximum rate about 0.1 msec after the reaction of HCN reaches its maximum (the rate of CO_2 formation reaches a maximum between these two maxima). The relatively slow reaction of HCN appears to be the cause of the NO forming more slowly from HCN than from NH_3 (Fig. 2). It can be shown that in this flame much and possibly all of the NO is formed from an intermediate species that builds up above the luminous zone. In particular, the maximum rate of NO formation is more than twice the rate of HCN consumption at the point where the NO maximum rate occurs.

Flame 3: HCN, $\phi = 1.5$. In the fuel-rich flame, part of the HCN reacts in the luminous zone but most of the HCN again apparently survives the luminous zone. In this case, the HCN then reacts slowly forming NO in low yield far above the flame front (Fig. 2). Because of the low yield of NO in the rich flame, it is not possible to determine how directly the NO forms from HCN since the NO formation rate never exceeds the HCN consumption rate.

Flame 4: NH_3 , $\phi = 1.5$. In the fuel-rich flame, the NH_3 reacts in or below the luminous zone (as it does in the lean flame) forming about one-half HCN and one-half unmeasured nitrogen species. Above the luminous zone, "HCN" formed from NH_3

*Since the converter cannot distinguish between HCN and NH_3 directly, "HCN" denotes the NO formed in the converter (at 800 C) multiplied by the converter calibration factor for HCN.

reacts slowly at the same rate as does "HCN" when HCN is the additive. Thus, the mechanism of NO formation in the fuel-rich flame appears to be the same whether the additive is NH_3 or HCN and involves the formation of NO from HCN.

Comparison of Results. The conclusions drawn from the addition of NH_3 and HCN to lean and rich methane flames are compared in Table 1. NH_3 reacts much more rapidly than does HCN in both flames. The similarity of the overall NO yields from NH_3 and HCN in the rich flame (Fig. 2) apparently results from the fact that the NO forms from HCN with either additive. The reason for the similarity of the NO yields in the lean flame is not as apparent since a common stable intermediate is not formed. However, a common free radical intermediate could be involved.

Effect of Argon Dilution. An experiment, flame 5, was conducted with HCN addition at $\phi=0.8$ in which the Ar/O_2 ratio was increased by 40 percent and the total burner feed rate was reduced to increase the heat loss to the burner. Although these conditions reduced the maximum flame temperature by 150 degrees and the initial reactant concentrations by 23 percent, the maximum reaction rates for NO, HCN, CH_4 and CO_2 only decreased by 30, 8, 42 and 29 percent, respectively. An analysis of these results indicate that certain compensating effects control the maximum reaction rates and that the measured rates do have a normal dependency on temperature and species concentration.

Effect of NO Addition. When NO was added initially to the fuel-rich flame along with HCN (flame 7) or alone (flame 8), rapid consumption of NO occurred just below the top of luminous zone. NO then formed rapidly just above the luminous zone and decayed rapidly again further downstream. In the absence of added HCN, the consumed NO was partially converted (40 percent) to a measurable nitrogen species that was presumably HCN. When NO was added to the fuel-lean flame along with HCN (flame 6), a small consumption of NO occurred in the luminous zone before the formation of NO from HCN obscured any further reaction of the added NO.

TABLE 1. COMPARISON OF RESULTS OF HCN AND NH₃ ADDITION

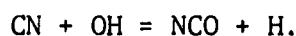
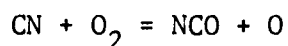
Additive	$\phi = 0.8$ (High NO Yields)	$\phi = 1.5$ (Low NO Yields)
HCN	<p>65% HCN survives LZ*</p> <p>HCN reacts rapidly above LZ</p> <p>All NO forms rapidly above LZ</p> <p>NO from intermediate</p>	<p>70% HCN survives LZ</p> <p>HCN reacts slowly above LZ</p> <p>All NO forms slowly above LZ</p> <p>NO from intermediate and/or HCN</p>
NH ₃	<p>All NH₃ reacts below top LZ</p> <p>NO forms rapidly above LZ</p> <p>All NO forms from intermediate</p>	<p>All NH₃ reacts below top LZ (one-half converted to HCN)</p> <p>"HCN" reacts slowly above LZ</p> <p>Most NO forms slowly above LZ</p> <p>NO from intermediate and/or HCN</p>

*LZ denotes luminous zone

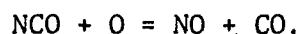
Reaction Mechanism

A possible reaction mechanism for the formation of NO and N_2 from NH_3 is presented. The experimental results indicate that a rather long-lived nitrogen intermediate forms in high concentration in the fuel-lean flame. A likely candidate that could have the required characteristics of (1) low reactivity in the luminous zone and (2) not forming NO in the probe-converter system is the NCO radical.*

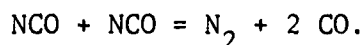
According to the proposed reaction scheme, CN radicals form in fuel-lean flames from NH_3 and (more slowly) from HCN and then react to form NCO



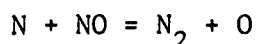
The NCO radical is postulated to be relatively stable and react rapidly with oxygen atoms above the luminous zone to form NO



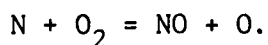
The most likely path for N_2 formation appears to be the reaction



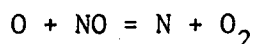
The amount of N_2 that can form via the reverse Zeldovich reaction



is limited by the competing reaction



The mechanism of NO formation in fuel-rich flames may also involve the NCO radical but there is little evidence relating to this point. The rapid consumption of NO in the fuel rich flame front must result from reaction with hydrocarbon radicals. It can be shown that the reverse Zeldovich reaction



is much too slow to cause the observed consumption of NO. Additional data and theoretical modeling are required to test this somewhat speculative overall mechanism for the formation of fuel NO.

*NCO could form N_2 in the probe via $2 NCO = N_2 + 2 CO$.

Measurements of NO_2 , made in the NH_3 addition experiments only, demonstrated that the maximum NO_2 mole fraction was only 8 ppm even though the NH_3 was added at 2500 ppm. The amount of NO_2 that can form may be limited by the formation rate of HO_2 radical, i.e., the HO_2 concentration may become depleted by reaction with NO to form NO_2 , preventing the formation of larger amounts of NO_2 .

INTRODUCTION

Nitrogen oxides (NO_x) are one of the major air pollutants emitted by stationary combustion sources.* Much of this NO_x is formed from the oxidation of N_2 at peak combustion temperatures ("thermal NO_x "), but a significant and probably increasing fraction of the emitted NO_x is being formed from the chemically bound nitrogen present in many fossil fuels ("fuel nitrogen") and is referred to as "fuel NO_x ." A number of studies have been made of the effects of combustion conditions on the extent of conversion of fuel nitrogen, and added nitrogen compounds, to NO_x . The theoretical and experimental study reported here was carried out to investigate further the chemical mechanisms involved in fuel NO_x formation and to obtain information that might aid in the development of new approaches for mitigating this problem. The major portion of the program was devoted to the experimental studies.

Petroleum crudes produced in this country contain from 0.01 to 0.94 percent nitrogen, with California crudes being noted for their high nitrogen contents. Because fuel nitrogen compounds are thermally stable and of rather low volatility, they are concentrated in the heavy oil and asphalt fractions during the refining of petroleum. Therefore, natural gas, LPG, gasolines, and distillates (including diesel and No. 2 fuel oils) generally contain little fuel nitrogen. Residual oils, such as No. 6 fuel oils, however, contain typically from 0.2 to 1.4 percent nitrogen depending on the source of the crude. Coals have higher nitrogen contents (on the average) than petroleum, with American coals ranging from 1.1 to 1.8 percent nitrogen. European soft coals appear to contain even more nitrogen.

Flagan (Ref. 1) has estimated recently that in 1968 about one-fourth of all the oxides of nitrogen emitted into the atmosphere of the United States, as the result of human activities, was from the oxidation of fuel nitrogen during combustion. The numbers used in his estimate indicate that nearly one-half of the total NO_x was from electric utility and industrial combustion sources, and a little more than one-half of this stationary source NO_x was fuel NO_x . Flagan's estimates are

*The NO formed in most combustion processes accounts for about 95-percent of the NO and the remainder is mainly NO_2 .

based, in part, on the assumptions that fossil fuels have an average nitrogen content of 1 percent, and 20 percent of this is converted, on the average, to NO. It is likely that the importance of fuel NO_x has increased since 1968 because some of the combustion techniques that are effective in reducing thermal NO_x do not reduce fuel NO_x. Furthermore, low nitrogen content fossil fuels are in shorter supply.

Most of the information on fuel NO_x that was available at the start of this program is discussed in an excellent review by Sternling and Wendt (Ref. 2) and in Ref. 3 through 5. During the course of this program, four technical symposia were held that highlighted the subject of fuel NO_x (Ref. 6 through 9). Several papers were also presented at the 14th and 15th Combustion Symposia (International) relating to this subject.

The present program was conducted under the following tasks:

Phase IA - Theoretical Analysis

Phase IB - Fuel and Model Compound Decomposition Studies

Phase II - Burner Studies of Fuel NO_x Formation

The Phase IA theoretical study was conducted to complement the experimental tasks. The major effort under this task was the development of a mathematical kinetic-diffusion model for droplet and particle combustion that predicts the conditions that will be encountered by fuel nitrogen compounds during combustion. In Phase IB, fuel oils, coals, and model fuel nitrogen compounds were pyrolyzed to investigate the nature of the decomposition reactions which the nitrogen compounds undergo in the early stages of combustion. Finally, the combustion kinetics of the potential fuel NO_x intermediates, HCN and NH₃, were investigated in subatmospheric, premixed CH₄-O₂-Ar flames in the Phase II study. The reduced pressure (0.1 atm) was used to spread the reaction sufficiently to permit detailed probing of the flame.

PHASE IA - THEORETICAL ANALYSIS

A theoretical study of fuel NO_x formation was conducted under this task to complement and to guide the experimental program. The objective of this analysis was to identify potential areas for experimental studies and to aid in data interpretation and development.

The literature on nitrogen compounds in fossil fuels was surveyed to determine the chemical structures of the most common fuel nitrogen compounds. The general reaction paths and physical processes most likely to be involved in fuel NO_x formation were then considered. The remainder of the qualitative analysis of fuel NO_x formation was divided into two areas: (1) consideration of the pyrolysis (pre-flame) type reactions that the volatile fuel nitrogen compounds will undergo (near the surface of the droplet or particle) before approaching the flamefront, and (2) consideration of the combustion reactions of fuel nitrogen compounds and their reaction products. These areas relate, respectively, to the Phase IB pyrolysis experiments and the Phase II burner experiments.

The major effort under this theoretical analysis task was the development of a mathematical kinetic-diffusion model for the combustion of oil droplets and coal particles. Such a model was required to establish the physical and chemical conditions which will control the formation of fuel NO_x formation. The types of information the program can provide that are directly relevant to this project include: (1) the temperature-time history of the nitrogen species, (2) the concentration profiles of O_2 and oxygen-containing radicals, and (3) the integrated rates of the various reactions in the extended Zeldovich mechanism for the formation of thermal NO_x (which will also be important in the formation of fuel NO_x if it turns out that N atoms are a principal intermediate in this process). In addition, the model is prepared to accept chemical rate data, as they become available, for the various reactions of fuel nitrogen compounds and their products. Thus, the model will be useful in testing various possible fuel NO_x formation mechanisms under heterogeneous combustion conditions.

CHEMICAL STRUCTURES OF FUEL NITROGEN COMPOUNDS

Ball, et al. (Ref. 10) have demonstrated an apparent correlation between the nitrogen content of petroleum crudes, the carbon residue of the crude, and the geological period in which the petroleum was formed. For a given geological period, the nitrogen content of the crude is approximately proportional to the carbon residue with the ratio of nitrogen to carbon residue increasing in the order: Cretaceous period (80 to 150 million years ago), Carboniferous (250 to 300 million years), and Tertiary (50 to 80 million). Having been formed in the Tertiary geological period, and having high carbon residues, the California crudes contain the highest average amounts of nitrogen (up to 0.65 weight percent).

Although the total amount of chemically bound nitrogen that is present in fossil fuels is quite well established, the identity and distribution of the chemical types of nitrogen are not. This is particularly true for coals because many of the coal-nitrogen compounds cannot be extracted from the solid in an unreacted form for identification and analysis. Most of the information on the structure of coal nitrogen compounds has been deduced from the nitrogen compounds that are obtained by extraction and from distillation. It has been established, however, that much of the nitrogen in heavy oils is in the form of heterocyclic organic compounds and the indications are that the same is true for coal nitrogen.

No comprehensive review is available, at present, of the literature on the measurement and identification of fuel nitrogen compounds. Although not intended as a comprehensive literature survey, some 46 publications relating to this subject are referenced (Ref. 10 through 55) in this report. Many of these citations were supplied by W. E. Haines of the Bureau of Mines, Laramie Energy Research Center, Laramie, Wyoming, and J. E. Haebig, of the Physical Sciences Division, Gulf Research and Development Company, Pittsburgh, Pennsylvania.

In the early studies of the composition of petroleum, there was little interest in identification of fuel nitrogen compounds. Interest in these compounds began to increase about 20 years ago with the advent of catalytic processing of crude

oils (Ref. 13). Even in trace amounts, nitrogen compounds cause serious problems in processing and in the stability of petroleum products. They cause catalyst poisoning and are involved in the formation of gums, lacquers, and precipitates.

The nitrogen present in petroleum is usually divided into two broad types: basic nitrogen, defined as that which is titratable with perchloric acid in acetic acid solution, and nonbasic nitrogen, which is not titratable. The basic nitrogen compounds are classified further according to their degree of basicity (Ref. 25 and 44). On the order of one-third of the nitrogen in petroleum is basic and the remainder is nonbasic according to the above definition (Ref. 25 and 47). The nitrogen compounds are concentrated in the higher-boiling crude oil fractions, with the nonbasic nitrogen compounds becoming more abundant as the boiling point of the fraction increases. This is demonstrated for Wilmington crude oil in Fig. 3, which was reproduced from Ref. 25.

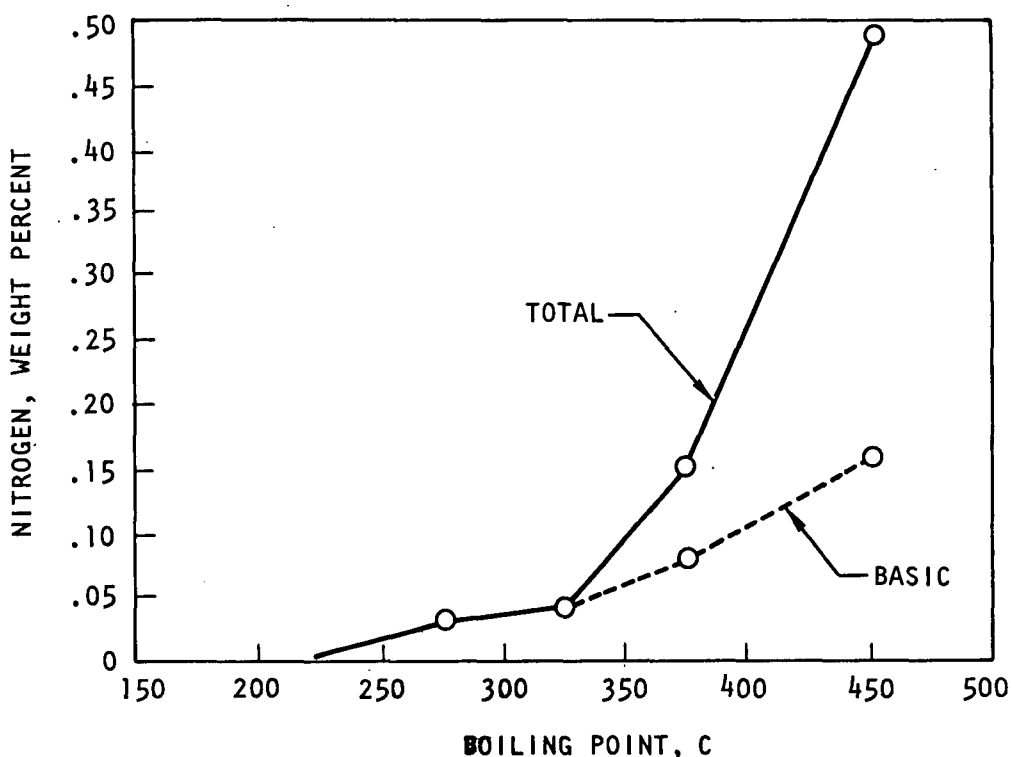


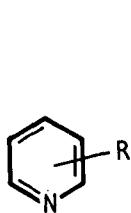
Figure 3. Distribution of Nitrogen in Wilmington Crude Oil

The basic fuel nitrogen compounds have been studied more extensively because they can be separated more easily from petroleum. The basic nitrogen compounds in petroleum are mainly pyridines, pyridans, quinolines, isoquinolines, acridines, phenanthridines, phenazines, pyrazines, and highly substituted pyrroles. The alkylanilines are important constituents of shale oil naptha (Ref. 16). The general structures for these basic nitrogen compounds are shown in Fig. 4. Also included in Fig. 4 are the structures of a pyridine and a pyridane that have been identified in Wilmington Crude (Ref. 15 and 25).

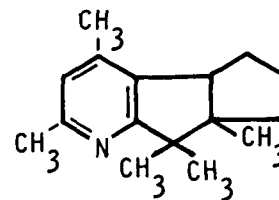
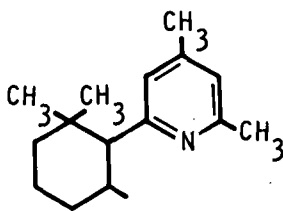
The nonbasic nitrogen compounds found in petroleum were reviewed by Latham et al. in 1965 (Ref. 36). As shown in Fig. 5, these include most pyrroles, the indoles, carbazoles, benzcarbazoles, amides such as quinolones, and benzonitriles. The amides are of interest because they contain nitrogen and oxygen in the same part of the molecule and, therefore, have some potential for forming NO directly during pyrolysis.

It can be seen from the structures in Fig. 4 and 5 that, in general, the six-membered ring heterocyclic nitrogen compounds containing a C=N double bond in the ring (so that there is no hydrogen atom attached to the nitrogen) are basic. In the five-membered heterocyclic rings, the nitrogen has a hydrogen atom attached and is nonbasic. Latham et al. (Ref. 36) consider the phenazines (Fig. 4) to be nonbasic, but Okuno et al. (Ref. 44) classify phenazines as strongly basic and point out that only one of the two-ring nitrogens is titrated quantitatively with perchloric acid. Nenner and Schulz have recently measured the electron affinities of the N-heterocyclics including phenazines (Ref. 56) but this property does not appear to relate to basicity.

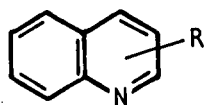
Although a great deal of experimental work has been done to determine the physical and chemical characteristics of coal and its byproducts, very little is known about the manner in which nitrogen is chemically bound in solid coal. From the structure of nitrogen-containing organic compounds found in the products of distillation of coal, there appears to be agreement that the major portion of



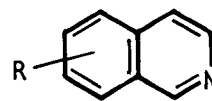
PYRIDINES



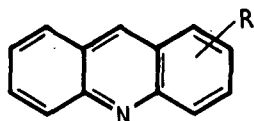
PYRIDANS



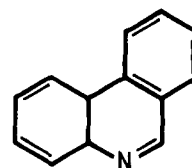
QUINOLINES



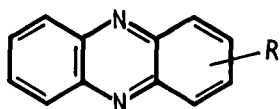
ISO-QUINOLINES



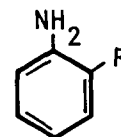
ACRIDINES



PHENANTHRIDINES

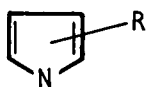


PHENAZINES

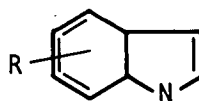


ANILINES

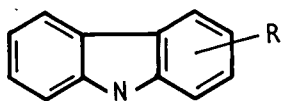
Figure 4. Representative Types of Basic Nitrogen Compounds Found in Petroleum



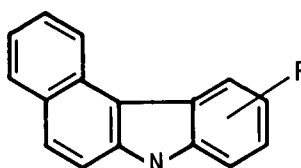
PYRROLES



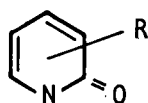
INDOLES



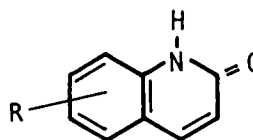
CARBAZOLES



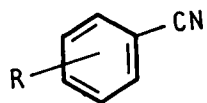
BENZCARBAZOLES



AMIDES



QUINOLONES



BENZONITRILES

Figure 5. Representative Types of Nonbasic Nitrogen Compounds Found in Petroleum

the nitrogen in coal is present as heterocyclic linkages in large molecules. The more abundant nitrogen compounds in low-temperature coal tars and light oil condensates include pyridines, picolines (methyl pyridines), lutidines (dimethyl pyridines), quinolines, acridines, and carbazoles (e.g., Ref. 57).

GENERAL DISCUSSION OF FUEL NO_x FORMATION

Before discussing in more detail the chemistry involved in the formation of fuel NO_x, the general features of the process will be outlined. Laboratory burner and combustor experiments have shown that in the case of fuel NO: (1) the NO forms very rapidly even at moderate temperatures, (2) the NO concentration increases continually early in the flame front until a concentration maximum is achieved, and (3) the fraction of fuel nitrogen converted to NO rather than N₂ is strongly dependent on the oxygen content of the mixture and decreases as the nitrogen content of the fuel increases.

Near quantitative conversion of nitrogen compounds to NO is observed in flat flame burner studies conducted under fuel-lean conditions. In combustor experiments, with fossil fuels, typical maximum extents of conversion of fuel nitrogen to NO (at equivalence ratios up to 1) are on the order of 50 percent for added model compounds, such as pyridine, and somewhat less for naturally occurring fuel nitrogen. All of the studies that have involved model fuel nitrogen compounds indicate that, for the additives tested, the extent of conversion to NO is relatively independent of the type of compound employed, but decreases as the additive concentration is increased. Data obtained in larger combustors and furnaces have demonstrated that fuel NO_x forms at much lower temperatures than does thermal NO_x and, therefore, control techniques based on temperature reduction that are effective in reducing thermal NO_x are not generally effective for fuel NO_x. However, Martin and Berkau (Ref. 58), Turner et al. (Ref. 4) and Heap et al. (Ref. 59 and 60) have shown that fuel NO_x formation can be reduced by staging and burner design.

Shaw and Thomas (Ref. 61) were apparently the first to demonstrate that NO can form from fuel nitrogen. In 1968, they studied the reactions of several nitrogen compounds, including pyridine, in low temperature CO flames and obtained up

to 50-percent conversion to NO. The next laboratory studies of fuel NO_x were those of Martin and Berkau (Ref. 3), Turner et al. (Ref. 4), and Bartok et al. (Ref. 5). Martin and Berkau added pyridine, piperidine, and quinoline to a low nitrogen distillate oil and measured conversion to NO in a high-pressure atomizing laboratory furnace. They found that the fraction of fuel nitrogen converted increases with the air-fuel stoichiometric ratio and decreases with fuel nitrogen concentration, but the total amount of NO formed increases with both SR and nitrogen content. The conversion of fuel nitrogen to NO was from 20 to 70 percent and relatively independent of the nitrogen compound type.

Turner, Andrews, and Siegmund added a variety of nitrogen compounds to a distillate oil and obtained results similar to those of Martin and Berkau. In a fire-tube-boiler domestic furnace, the extent of conversion to NO was independent of nitrogen compound type (for all additives with boiling points above about 75 C), being about 85 percent at the 0.25-percent N level and about 65 percent at 0.5-percent fuel N. They also studied residual oils containing various concentrations of (natural) fuel-N. About 60 percent of the fuel-N was converted to NO for fuels containing about 0.25-percent N and 40 percent was converted at 0.4- to 0.8-percent N.

Bartok, Engleman, Goldstein, and Del Valle added NO, NO₂, NH₃, C₂N₂, and CH₃NH₂ to a methane-air flame in a jet-stirred combustor and measured the NO concentrations in the combustion gas. The fraction of conversion to, or retention of, NO decreased as the mixture was made fuel rich. Under fuel-lean conditions, all of the added NO and NO₂ were recovered as NO and most of the NH₃, (CN)₂, and CH₃NH₂ were converted to NO, but the conversion was not complete.

A number of laboratory studies of fuel NO_x have since been reported. These include a shock tube study (Ref. 62), premixed flames (Ref. 63 through 73), diffusion flames (Ref. 68, 72, and 73), and a Rankine combustor (Ref. 74). Studies of fuel NO_x formation have been conducted in larger burners and furnaces with both neat fossil fuels and doped fuel oils (Ref. 1, 58 and 75 through 88). In addition to these experimental studies of fuel NO_x formation, publications dealing with the theoretical aspects have appeared (Ref. 2 and 89).

Pershing, Martin, and Berkau studied the influence of design variables on the production of thermal and fuel NO from residual oil and coal combustion (Ref. 79). They concluded that the conversion of fuel-bound nitrogen to NO during residual oil combustion is: (1) responsible for more than 50 percent of total NO emissions under all conditions with the fraction being greater with no air preheat, (2) relatively insensitive to flame zone temperature, (3) increased by increasing excess air at constant throat velocity, and (4) relatively unaffected by the addition of flue gas recirculation or by increased burner throat velocity. They also conclude that the conversion of fuel-N during coal combustion is: (1) responsible for 80 to 90 percent of the total NO emissions, (2) increased markedly by increasing excess air at constant velocity, and (3) unaffected by flue gas recirculation or changes in burner throat velocity. The effects on fuel NO formation of staged combustion, flue gas recycle and other design and operating variables have been investigated by Martin and Berkan (Ref. 58), Turner et al (Ref. 4), Heap et al (Ref. 59 and 60), and Armento (Ref. 90).

The types of physical and chemical processes that may be involved in the formation of NO_x in combustion are diagrammed in Fig. 6. The hydrocarbon species will burn with the air and can form thermal NO as shown at the top of the figure. Because nitrogen is present only at low concentrations, it may be assumed that most of the properties of the flame are independent of the reactions of the nitrogen species. These properties include temperature, flame speed, and the concentrations of most species that do not contain nitrogen.

The nitrogen compounds present in the fuel may: (1) form volatile nitrogen species by undergoing vaporization, pyrolysis, and/or oxidative pyrolysis, or (2) remain in the solid residue of the particle or droplet. The volatile nitrogen species can then react in the vapor phase to form low molecular weight single N-atom compounds or radicals, such as HCN, CN, or NH_x , or a nitrogen-containing soot particle. These intermediates can be oxidized to NO or form N_2 via reaction mechanisms that will be discussed later in the report. Part of the fuel NO may also form via heterogeneous reactions involving the combustion of the particle residue or any nitrogen-containing soot particles that form. Also shown at the bottom of Fig. 6 are some of the chemical reactions that produce N_2 . However, only those that involve NO appear likely to occur. These N_2 -forming reactions can also lead to interactions between the mechanisms for the formation of thermal and fuel NO.

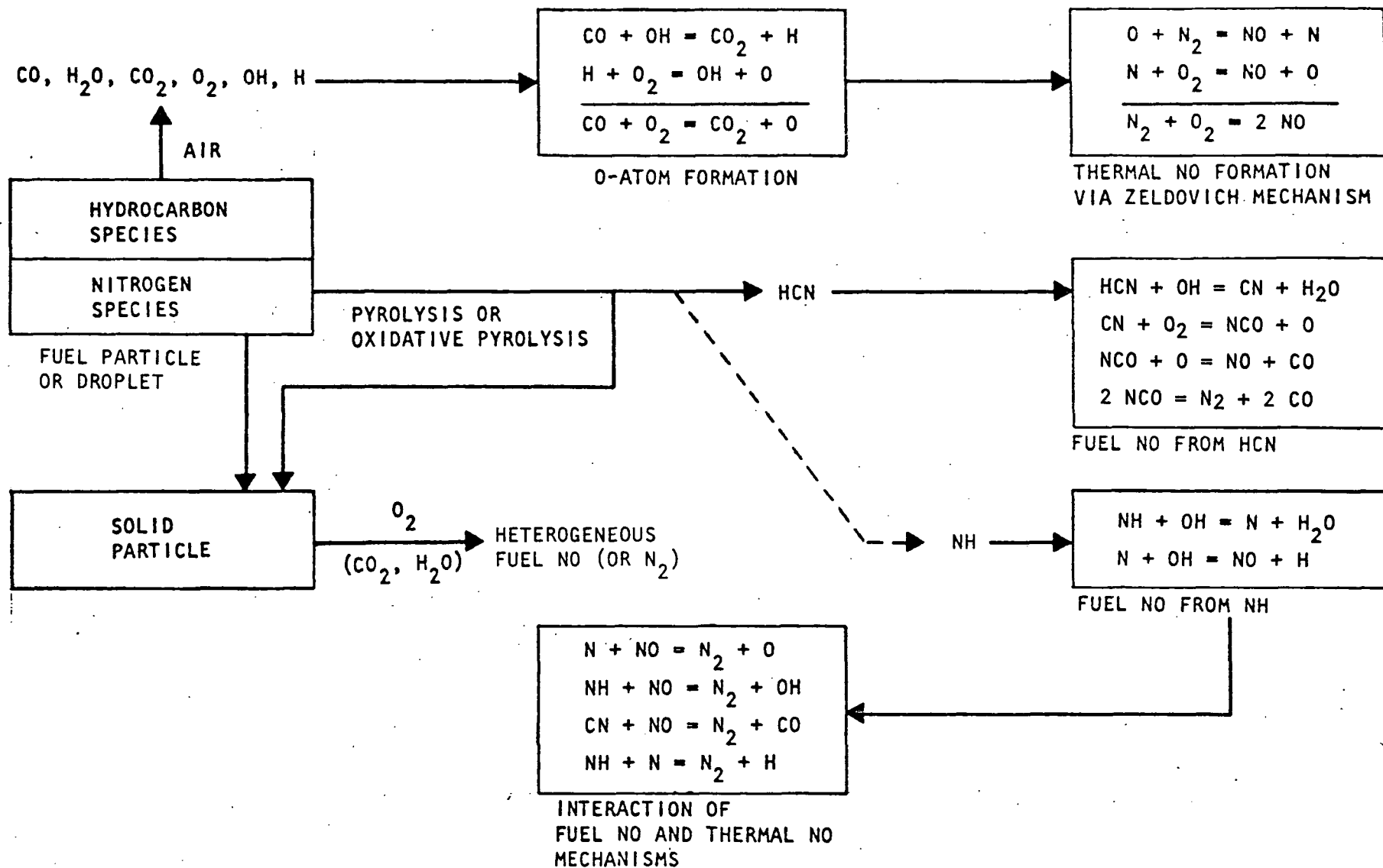


Figure 6 . Potential Paths for NO Formation in Fossil Fuel Combustion

KINETICS AND MECHANISMS OF PYROLYSIS OF ORGANIC NITROGEN COMPOUNDS

Only a limited number of studies have been conducted of the reactions of organic nitrogen compounds that may occur under "preflame" conditions. The investigation in 1962 by C. D. Hurd and coworkers of the pyrolysis mechanisms of pyridine and the picolines (Ref. 91 and 92) is the most relevant to this program. Johns et al. (Ref. 93) have compared the thermal stabilities, under a variety of conditions, of many organic compounds including some N-heterocyclics. Most of these data were obtained at only moderate temperatures and rather long heating times. Hirsch and Lilyquist (Ref. 94) compared the thermal stabilities of organic compounds using a pyrolysis-gas chromatography technique similar to that employed in the model compound pyrolysis studies of this program (Phase IB). Their measurements were made at lower temperatures than in the present study; 750 C for the less stable compounds and 870 C for the more stable. Both of these papers indicate that the heterocyclic nitrogen compounds are among the most stable of the organic compounds. Hirsch and Lilyquist found that, whereas diphenylamine decomposed 54 percent at 870 C and naphthalene decomposed 29 percent, pyridine decomposed only 6 percent and quinoline underwent less than 1 percent decomposition at this temperature. Benzene, however, was found to have about the same stability as pyridine (5-percent decomposed) in agreement with benzene being considered as a very stable organic molecule.

Hurd and coworkers pyrolyzed pyridine and the three picolines in a flow reactor at 700 to 850 C under inert conditions to study the mechanism of the pyrolytic formation of arenes such as benzene. They claim to have shown that the picolines, which are methyl substituted pyridines, are much less thermally stable than is pyridine (Ref. 91 and 92). This situation is relevant to the mechanism of fuel NO_x formation because most heterocyclic fuel nitrogen compounds are substituted.

However, the following kinetic calculations on the data of Hurd and Simon (Ref. 92), made under this program, demonstrate that this conclusion is not valid at the highest temperature of their study.

The values listed in Hurd and Simon's Table 1 for contact time and percent picoline recovered were converted to first-order rate constants and plotted in the Arrhenius form (Fig. 7). Although there is considerable scatter in the data, the rate expressions listed on the figure were fitted to each of the picolines. Hurd and Simon give only two decomposition rates for pyridine in their apparatus: 57-percent undecomposed after 5 seconds at 850 C* and 64-percent undecomposed** after 9 seconds at 825 C. The rate constants calculated for these points (0.112 and 0.050 sec^{-1} , respectively), and plotted in Fig. 7, give an activation energy for pyridine pyrolysis on the order of 80 kcal/mole. Although rate expressions obtained over a 25-degree temperature range cannot be accurate, the two pyridine rates reported by Hurd and Simon give the rate expression $k = 10^{14.67} \exp(-80200/RT)$, sec^{-1} , which is plotted in Fig. 7. Also plotted is the pyridine pyrolysis rate constant obtained in Phase IB of this program, $k = 10^{12.58} \exp(-70000/RT)$. The rates obtained from these two expressions agree within 25 percent at these two temperatures. This is excellent agreement considering the differences in the experimental techniques employed. The sample size used by Hurd and Simon was larger by at least a factor of 10^4 , and they allowed the residue to build up in their reactor (a problem that is discussed under Phase IB).

It can be seen from Fig. 7 that the picolines may be less stable than pyridine at the lower temperature studied by Hurd and Simon, but at 850 C pyridine and the picolines decompose at essentially the same rate. The differences are less than 10 percent, which is well within the expected experimental error. At the lower temperatures, the picolines probably decompose (as does toluene) by loss of hydrogen from a methyl group followed by decomposition of the pyridyl radical. If the trends in

*The pyridine data point at 850 C is not shown in Fig. 7 because it coincides with the 2-methylpyridine point.

**There is an apparent error on p. 4520 of Ref. 92 that is corrected on p. 4521. It was stated that "at 825 C and 9 seconds contact time, one-third of the pyridine was recovered but on the next page, "64% was recovered under these conditions."

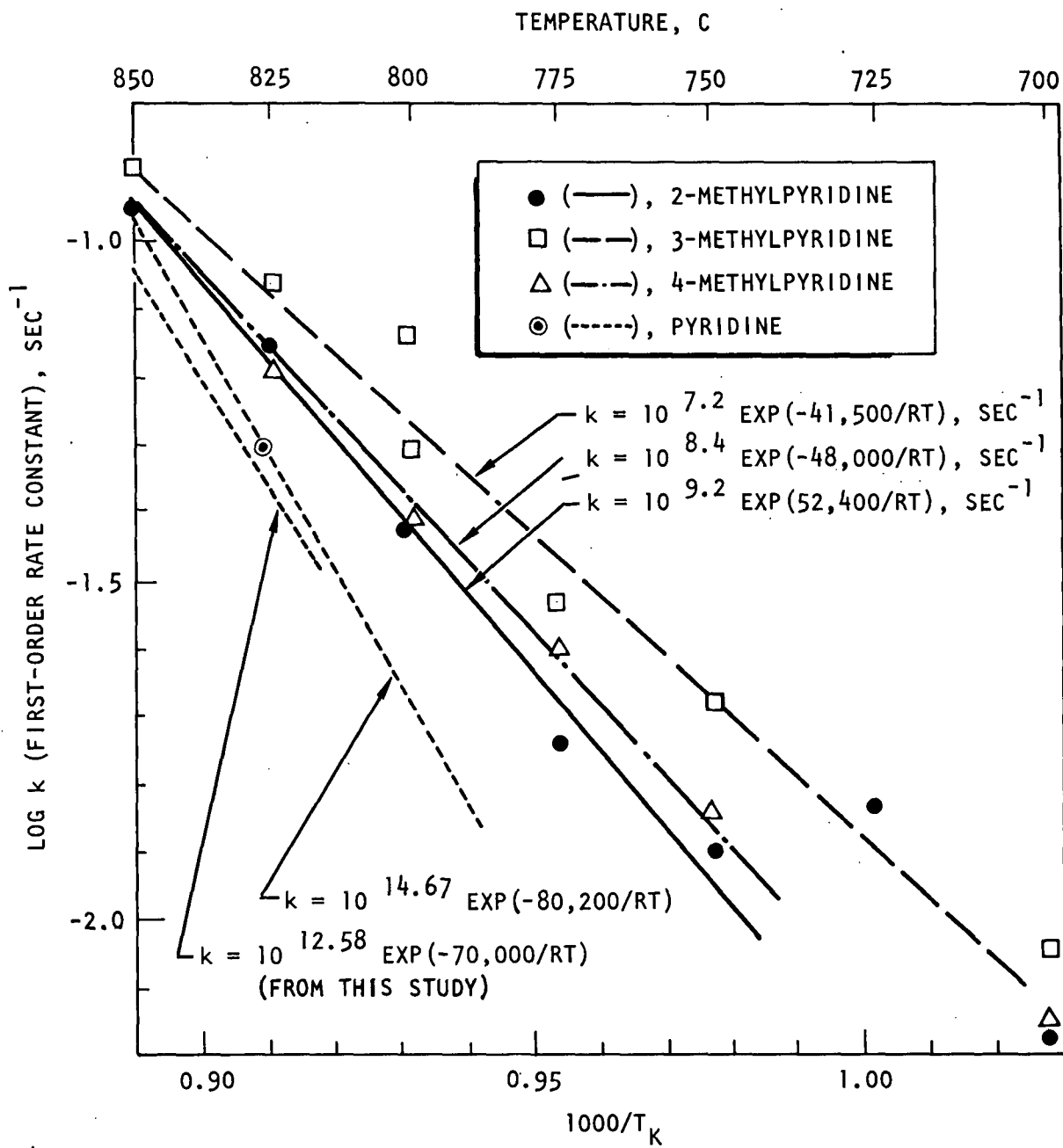


Figure 7. Arrhenius Plots of Pyrolysis Rates for Picolines and Pyridine Obtained by Hurd and Simon (Ref. 92)

Fig. 7 were to continue at higher temperatures, the picolines would become more stable than pyridine.* Since the rates become equal at 850 C, however, it is more likely that they will remain equal above 850 C. That is, the mechanism for the decomposition of the picolines may become the same as for pyridine involving either direct ring rupture or loss of a ring hydrogen followed by scission of the pyridyl ring. If this is the case, the rate of decomposition of heterocyclic nitrogen compounds will be nearly independent of the substituted groups at combustion temperature. This forms part of the rationale for studying low molecular weight model compounds in some of the Phase IB pyrolysis experiments, and for using the kinetic parameters for the decomposition of these model compounds to represent fuel N-compounds in the kinetic-diffusion mathematical combustion model.

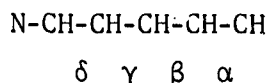
Hurd and Simon report the following products from the pyrolysis of pyridine and 2-picoline at 825 C:

Product	Mole Percent	
	Pyridine	2-Picoline
Benzene	0.18	0.39
Acetonitrile	0.2	1.3
Acrylonitrile	0.4	0.5
Benzonitrile	1.1	1.1
Quinoline	1.3	0.3
Pyridine	--	25
3-Picoline	--	1.2
4-Picoline	--	0.7
Residue (weight percent)	*	47

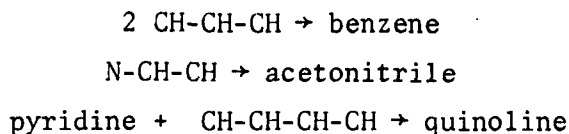
*A considerable but unmeasured amount.

*This is one of the subtleties of high-temperature chemistry. Not only do endothermic reactions become more favored thermodynamically as the temperature increases, but the rates of reactions having large activation energies increase faster than those of reactions having smaller activation energies. This point will come up again in the Phase IB discussion where it is suggested that thermal decomposition of fuel nitrogen compounds may be faster at combustion temperatures than their oxidative decomposition.

They explain the formation of the various products by cleavage of the pyridine ring at a C-N bond to give the radical:



which can cleave at the α , β , γ , or δ positions with the last two being favored by resonance. According to their proposed mechanisms, some of the observed products form as follows:



Sternling and Wendt have pointed out that rupture at the δ position leads to the formation of HCN. It will be seen that in the present study, the amount of HCN formed from pyridine increases as the temperature is increased from 950 to 1100 C. The quantitative conversion of pyridine to HCN occurs at 1100 C. In terms of the above mechanism, this would suggest increased scission of the δ bond at the higher temperatures. However, similar trends were observed in the amount of HCN formed from the model compound benzonitrile (the maximum conversion to HCN being about 80 percent at 1100 C). Thus, it may be necessary to consider other paths for HCN formation. Of course, the direct formation of a CN radical is likely in the case of benzonitrile.

A few other studies have been carried out that relate to the pyrolysis of nitrogen compounds of the type that may be present in fossil fuels (Ref. 95 through 99). However, these do not appear to contribute information of importance to the high-temperature chemistry of interest in fuel NO_x formation. However, a current study of the mechanism of the pyrolysis of ethylamine (Ref. 100) is of interest with respect to the later stages of combustion.

ANALYSIS OF N-COMPOUND COMBUSTION

More data are available relating to the fate of small nitrogen molecules, such as HCN and NH_3 , in the combustion process, and the results observed in Phase II of this program have added significantly to this body of data. Such data have given some indication of how the fuel nitrogen intermediates that form in the preflame reactions are finally converted to NO_x or N_2 in the flamefront, but the detailed mechanisms involved are not yet firmly established. The background and theoretical aspects of N-compound combustion will be discussed here.* This subject will be discussed further in the Phase II section of this report after the Phase II results, obtained with a premixed flat-flame burner, have been presented.

Burner Studies of NO_x Formation From N-Compounds

Fenimore (Ref. 66) added pyridine, methacrylonitrile, methylamine, and NH_3 to premixed ethylene- O_2 - N_2 and ethylene- O_2 -inert gas flames at atmospheric pressure and measured the yield of NO. He worked under conditions where the formation of thermal NO_x was not significant. Johnson (Ref. 71) measured NO formation from premixed, laminar CH_4 -air- NH_3 flames at a pressure slightly greater than atmospheric. Slater (Ref. 72) measured the recovery of added NO and the conversions of NH_3 , CH_3NH_2 , and pyridine to NO in both laminar premixed and diffusion CH_4 -air flames at atmospheric pressure. In all three of these studies, the NO was measured sufficiently far downstream that the NO had reached its final (exhaust) value. Bartok et al. (Ref. 5) used a premixed jet-stirred combustor to study the effects of adding NO, NO_2 , NH_3 , cyanogen, and CH_3NH_2 to a methane-air flame.

Using premixed ethylene- O_2 -Ar flames at atmospheric pressure and cooled probes to sample within the flame, De Soete investigated the conversion to NO of added NH_3 , ethanediamine, dibutylamine, and triethylamine (Ref. 63); cyanogen (Ref. 64); and the recovery of added NO (Ref. 65). In De Soete's experiments, as was also observed by Fenimore and in this study, nearly quantitative conversion to NO occurred

*Sternling and Wendt (Ref. 2) reviewed the information on N-compound combustion available in 1972.

in fuel-lean mixtures, but the yield fell off rapidly as the equivalence ratio was increased beyond stoichiometric. Interestingly, all of the amine additives as well as added NO formed substantial amounts of HCN early in the flame under fuel-rich conditions (Ref. 63 and 65). With cyanogen as the additive (Ref. 64), some of the NO formed from an HCN intermediate, but De Soete concluded that the oxidation of $(\text{CN})_2$ is the major path for NO formation. With cyanogen as the additive, HCN builds up as an intermediate reaching its maximum considerably before NO reaches its maximum. Analysis of the lower temperature experiments (Fig. 1 of Ref. 64) indicates that either another nitrogen-containing intermediate is formed or nearly all of the conversion to N_2 occurs before about 20 percent of the NO has been formed.* This can be seen from the following table (cyanogen was initially added to a concentration of 265 ppm which is equivalent to 530 ppm N):

Milliseconds	ppm N as:				
	Cyanogen	HCN	NO	Total	Unrecovered
0.12	210	18	50	278	252
0.35	75	81	150	306	224
0.55	32	105	210	347	183
1.4	0	12	297	309	221

If no other species are involved, nearly 50 percent of the N was converted to N_2 during the first 0.12 millisecond, after which nearly quantitative conversion of HCN and $(\text{CN})_2$ to NO occurred.** Another more likely explanation would be that early in the flame the unrecovered nitrogen was in the form of a radical, such as NCO, that somehow converts to N_2 in the probe. Later in the flame, the unrecovered nitrogen would exist as N_2 . When the additive was NO (Ref. 65), all of it was recovered under fuel-lean conditions, but the fraction of NO recovered fell off in fuel-rich mixtures. In fuel-lean ethylene flames, about one-fourth of the NO is apparently consumed early in the flame and then reforms. No such effect

*This analysis ignores diffusional effects. The flame was slightly fuel-rich ($\phi=1.07$).

**De Soete did not measure NH_3 or N_2 in his experiments. Therefore, NH_3 could have formed and then been converted to N_2 but this does not seem likely in light of the results reported in Phase II of this report.

was noted in H₂-O₂ flames with added NO. When De Soete added 265 ppm NO to a fuel-rich ethylene-O₂-Ar flame, the NO decreased to its final concentration of 65 ppm in about 0.16 msec, at which time the HCN reached its maximum measured concentration of 180 ppm (Fig. 5 of Ref. 65). The HCN then decayed rapidly, being completely consumed at 0.4 msec, while the NO concentration remained relatively constant. The formation of HCN in the flame front was so rapid that its maximum could have occurred between the measurement points and, therefore, have been greater than 180 ppm.

In addition to the flame-probing studies reported in Phase II of this report, which were conducted at a pressure of 0.1 atmosphere to spread out the flame zone, Merryman and Levy (Ref. 101) have probed methane-air flames (most at 1 atm) containing methylamine, pyridine, and piperidine. They observe that both in the presence and absence of added fuel nitrogen, significant amounts of NO₂ form in the flame zone. The NO₂ peaks just beyond the end of the visible flame and the maximum amount of NO₂ is equivalent to one-half or more of the NO concentration in the exhaust gases. The formation and decay of NO₂ is attributed to the reactions:



Merryman and Levy added small amounts of NO to methane-air flames and found that 80 percent of the NO is removed in the preflame region and the remainder is removed in the visible flame. Most of the NO is converted to NO₂ in this region and some "organic" nitrogen is formed that could be either NH₃ or HCN. In the post-flame gases, most of the NO₂ is converted to NO under fuel-lean conditions, and all is converted under fuel-rich conditions.

Mechanism of Thermal NO Formation

Except under very fuel-rich conditions, the amounts of thermal NO generated in homogeneous combustion can be predicted approximately (Ref. 62) by integrating the rates of the following three reactions (the first two of which were proposed by Zeldovich in 1946, Ref. 102 and 103, to explain the results of his classic experimental investigation of the formation of NO in combustion and explosions).

	<u>ΔH (298 K) kcal/mole</u>	
$O + N_2 = NO + N$	+75.0	(3)
$N + O_2 = NO + O$	-31.7	(4)
$N + OH = NO + H$	+18.6	(5)

Reaction 3 is rate-determining when NO is well below its equilibrium concentration and the rate of NO formation from N_2 depends mainly on the oxygen atom concentration in the flame and the local temperature. The rate of conversion of N_2 to NO has a very large temperature dependence because: (1) reaction 3 being endothermic by 75 kcal/mole has an activation energy of 75 kcal/mole, and (2) the concentration of O atoms in the flame is strongly temperature dependent. The global activation energy for the formation of thermal NO is about 135 kcal/mole* (Ref.104). For this reason, thermal NO forms near the maximum-temperature zone of the flame and some methods of reducing thermal NO involve the reduction of peak flame temperature, e.g., by exhaust gas recycle.

Mechanisms of Fuel NO Formation

The only detailed mechanisms for fuel NO formation that have been proposed are ones in which it is assumed that the original fuel nitrogen compounds decompose quantitatively, by an unspecified mechanism, to a simple nitrogen intermediate. Sternling and Wendt used a flame-sheet model to predict the extent to which fuel-N would be converted to NO in the combustion of H_2 -air mixtures (Ref. 2). They concluded that the fraction converted should increase with increasing temperature and decreasing fuel nitrogen concentration. Sternling and Wendt also concluded that among the gaseous products of pyrolysis, HCN is expected to be the most important. However, they assume in their calculations that the HCN is completely converted to N atoms (via a reaction such as $CN + O = CO + N$) which then react according to the Zeldovich mechanism--reactions 3 and 4.

*75 kcal/mole, from reaction 3 , plus one-half the bond dissociation energy of O_2 .

Fenimore (Ref. 66) found that the amount of NO he measured, $[\text{NO}]$, was related to the maximum possible NO, $[\text{NO}]_{\text{max}}$, which would form if all the additive were converted to NO, by the following expression:

$$\frac{[\text{NO}]}{x} = 1 - \exp \left[- \frac{[\text{NO}]_{\text{max}} + [\text{NO}]}{2x} \right] \quad (6)$$

where x is a parameter characteristic of the flame conditions (mixture ratio and temperature) but independent of the amount of additive.

Fenimore was able to derive Eq. 6 theoretically by assuming that every additive molecule forms the same intermediate, I, which reacts via the two competing paths:



thus,

$$- \frac{d[\text{I}]}{d[\text{NO}]} = \frac{x + [\text{NO}]}{x - [\text{NO}]} \quad (9)$$

where

$$x = k_7(\text{R})/k_8$$

Equation 6 is obtained by integrating Eq. 9 to complete reaction of the additive.

Species R in Eq. 7 is an oxygen-containing radical. Fenimore showed that the measured values of x are in agreement with $\text{R} = \text{OH}$ and $k_7/k_8 = 2$ to 3. The nature of the species I cannot be definitely established, but Fenimore concludes that I is most likely either NH_2 or an N atom. Fenimore's strongest argument against CN intermediates in fuel NO_x formation was that his general equation (Eq. 6) fits data on NO formation in $\text{NH}_3\text{-O}_2$ flames where CN species cannot form.

De Soete analyzed his results in terms of competing global reactions. In Ref. 63, he concluded that NO is formed at a rate proportional to the concentrations of O_2 and of the nitrogen intermediates, N^* , and is destroyed at a rate proportional to the concentrations of NO and N^* . This is similar to Fenimore's mechanism with $R = O_2$. The mechanism proposed by De Soete in Ref. 64 is also similar except that the rate of NO formation is proportional to $(O_2)^{1/2}$, suggesting that $R = O$ atom. De Soete proposed a similar overall mechanism in Ref. 65 and concluded that CN and HCN may be important intermediates in hydrocarbon flames, but NH_x species are not. He predicted that further treatment of his data will demonstrate that CN and HCN form N atoms as a key intermediate in the formation of fuel NO.

Constrained Equilibrium Models. Bowman has proposed (Ref. 62) that a constrained equilibrium model* will qualitatively predict the effects of mixture ratio and temperature on the yields of fuel NO. Flagan et al. (Ref. 1 and 89) have made quantitative calculations with two rate-constrained equilibrium models and compared the results with experimental data. These models will be described briefly.

Summary of Single-Constraint Equilibrium Model. This model assumes that early in the flame, the single-N species reach a constrained equilibrium with each other and all C-H-O species, the constraint being that N_2 is not allowed to form at this point in the flame. At equivalence ratios up to about 1.6, this assumption results in nearly all the fuel-N being converted to NO very early in the flame (i.e., at the constrained equilibrium condition). Some of the NO is then converted to N_2 ; the only two important reactions being $N + NO = N_2 + O$ and $NH + NO = N_2O + H$. This single-constraint model predicts that NO reaches its maximum very early in the flame and then decreases gradually to its final value with a characteristic decay time on the order of 1 to 100 milliseconds (see Fig. 2 and 3 of Ref. 89 in which T was taken as 2 to 14 milliseconds).

*The partial equilibrium approximations that have been proposed for modeling thermal NO_x formation have been reviewed by Leonard and Mellor (Ref. 105).

Summary of Three-Constraint Equilibrium Model. This model assumes that early in the flame, the single-N species reach a constrained equilibrium, the constraints being: (1) N_2 is not formed, (2) N-atoms are not formed, and (3) oxidized N-species (NO , HNO , NO_2 , etc.) are not formed. Starting with the constrained equilibrium composition, N and NO are allowed to form at the kinetic rates determined by the equations:



As in the single-constraint model, the N_2 forms via the reactions:



with the $N + NO$ reaction being of primary importance. (Note that this reaction scheme is equivalent to that proposed by Fenimore.) Integration of this mechanism predicts that the oxidation of fuel nitrogen occurs with a half-time on the order of 10 microseconds and that significant amounts of NO are reduced to N_2 via reaction with N and NH.

Comments on Constrained Equilibrium Models. These models predict generally the trends in NO yields observed by Fenimore (Ref. 66) and Johnson (Ref. 71). In both of these studies, the NO was measured at a fixed point some distance downstream from the flame front. The triple-constraint model is also in approximate agreement with most of the NO profiles reported from the flame-probing experiments

of De Soete (Ref. 63 and 64). That is, NO increases steadily with distance from the burner and the reactions are very fast with much of the NO forming in less than 0.1 millisecond. It is not apparent if this model can predict the results obtained by De Soete in his experiments with added NO (Ref. 65).

The single-constraint model, which is apparently the same as that proposed by Bowman, predicts that all of the fuel nitrogen is converted to NO and then, under fuel-rich conditions, part of the NO is converted to N_2 (by reaction with N or NH) to give the values measured downstream in experiments such as those of Fenimore. However, the detailed probing results of De Soete (and Phase II of this study) indicate that this model is not realistic because the NO concentration actually increases with distance from the burner.

The three-constraint equilibrium model appears to be more realistic but it is difficult to see its advantage over a direct integration of the kinetic system if sufficient forward (and reverse) reactions are included to permit the actual steady-state concentrations of each species to be estimated.

It can be seen that none of the proposed models for fuel NO formation give an indication of the actual chemical mechanisms involved because they are general enough to accept any principal intermediate that might form from the parent fuel nitrogen compound.

Thermochemical Considerations. Complete chemical equilibrium is not approached in hydrocarbon-air flames except for combustion systems that operate at unusually high pressures and/or temperatures.* In particular, thermal NO does not reach

*e.g., those that use O_2 enriched air, high preheat temperature, or initial adiabatic compression of the fuel-air mixture (as in the Otto cycle engine).

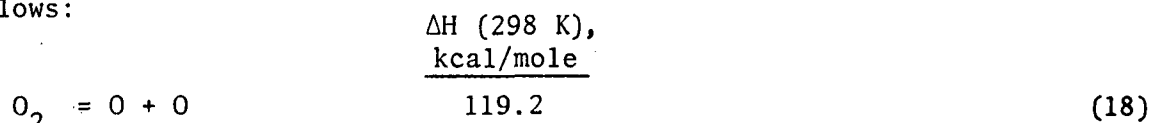
its equilibrium concentration (Ref. 106) until the gas begins to cool, and the equilibrium concentration decreases. The initial stages in hydrocarbon oxidation involve the formation of CO, rather than CO₂, and this can lead to CO concentrations much greater than the equilibrium values. The overshoot of CO can cause oxygen atom overshoot via the following two reactions:



It can be shown that if reactions 14 and 15 are at constrained equilibrium, $(\text{O})/(\text{O})_{\text{eq}} > (\text{CO})/(\text{CO})_{\text{eq}}$.

Although equilibrium is not attained, the consideration of the thermochemistry involved does give some indication of the relative concentrations at which species will be present in the flame under various conditions and, therefore, the likelihood of their involvement in NO formation. However, such information may be more directly applicable to thermal NO formation, which occurs mainly in the post-flame gases, than to fuel NO formation, which is believed to occur earlier in the flame and at lower temperatures. Shown in Fig. 8 and 9 are the mole fractions of the equilibrium combustion products as a function of fuel-air equivalence ratio for a hydrocarbon-air flame at 1 atmosphere and 2100 and 1600 K, respectively. The H/C molar ratio of the fuel was taken as 1.6 to approximate a heavy fuel oil. The H/C ratios in No. 6 fuel oils range from 1.4 to 1.8.

The species that contain oxygen that is available for NO formations are O₂, O, OH, CO₂, and H₂O. The energy required to obtain an O atom from each of these species is as follows:



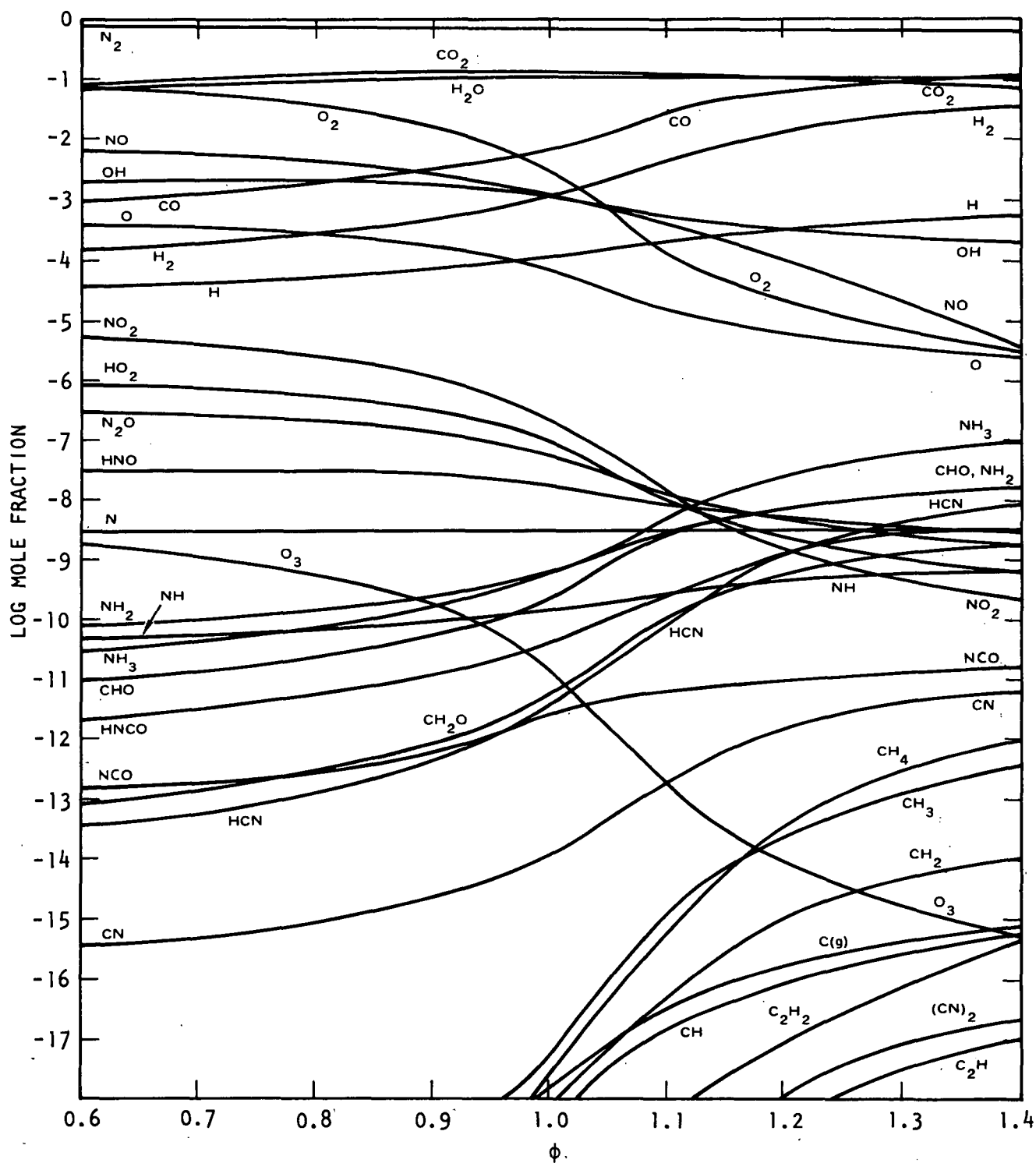


Figure 8. Equilibrium Products as a Function of Equivalence Ratio for $\text{CH}_{1.6}$ -Air Flame at 2100 K and 1 Atmosphere

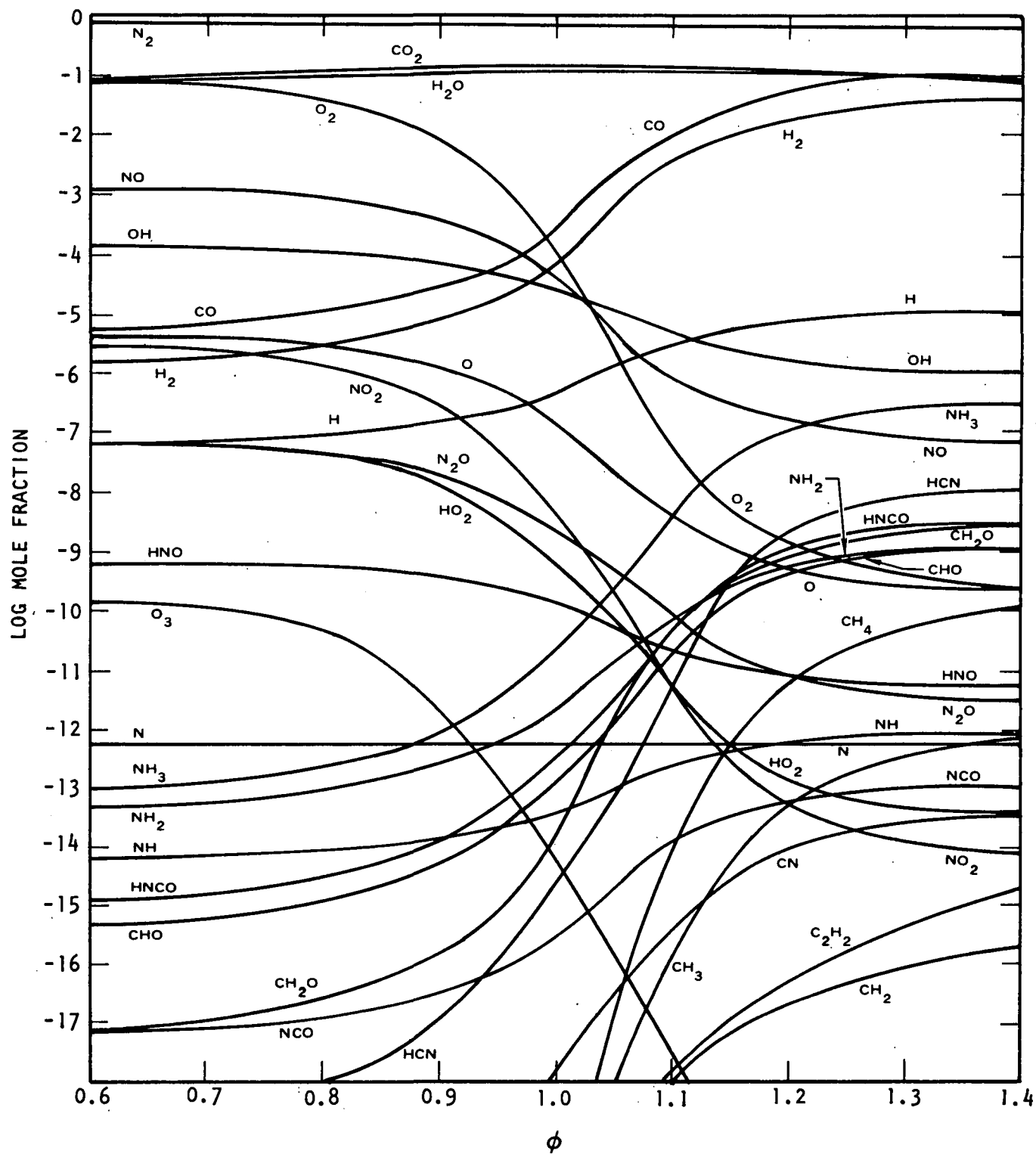


Figure 9. Equilibrium Products as a Function of Equivalence Ratio for $\text{CH}_{1.6}$ -Air Flame at 1600 K and 1 Atmosphere

Zeldovich chose reaction 4, $N + O_2 = NO + O$, as the second step in his thermal NO mechanism and reaction 5, $N + OH = NO + H$, has since been added to the extended Zeldovich mechanism. Because of the larger concentrations of CO_2 , the reaction $N + CO_2 = NO + CO$ will compete for N atoms unless its rate constant is much slower. It has been estimated (Ref. 107) this reaction has an activation energy of 25 kcal/mole, making its rate constant at 2000 K, more than 200 times smaller than those of reactions 4 and 5. If this estimate is correct, the $N + CO_2$ reaction will not be important. Even if this reaction turns out to be fast, its inclusion in the extended Zeldovich mechanism would not affect the calculated rate of thermal NO formation because reaction 3 is rate-determining.

The oxygen species that should be considered in the fuel NO mechanisms are O, O_2 , OH, and CO_2 . The extraction of an O atom from H_2O is not likely to be a fast process, and the reactions of N^* with CO_2 may also have sizable activation energies. It can be seen from Fig. 8 and 9 that the O-atom concentration is always less than that of OH by a factor of at least 10. Therefore, O-atom reactions will not be important in fuel NO formation unless (1) there is no equivalent reaction with OH, (2) the equivalent reaction with OH has a much lower rate constant, or (3) the O/OH ratio exceeds the equilibrium value.

Although the fuel- N^* species will be at much greater steady-state concentrations than the equilibrium concentrations shown in Fig. 8 and 9, these figures indicated which N^* species are favored thermodynamically. At 2100 K, nitrogen atom is the favored single-N species that does not contain oxygen up to about $\phi = 1.1$, above which NH_3 has the lowest free energy. The equilibrium concentration of NH_3 at 1600 K exceeds that of N atom above $\phi = 0.8$. Of the NH_x species, NH_3 predominates at all equivalence ratios at 1600 K and above $\phi = 1$ at 2100 K. Below $\phi = 1$ at 2100 K, $(NH_2) > (NH_3)$. The equilibrium concentrations in Fig. 8 indicate that NO is the favored single-N species up to very high mixture ratios. This is in agreement with the results obtained by Flagan et al. on the single-constraint constrained equilibrium model.

NH_3 is favored thermodynamically over HCN (and CN) at all temperatures and equivalence ratios. It should be noted that under these combustion conditions, solid carbon (soot) is not a favored combustion product. Therefore, HCN is favored over

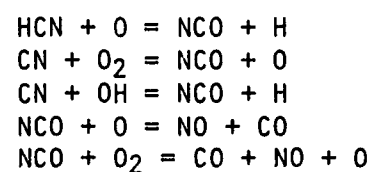
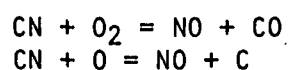
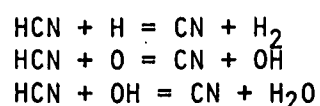
NH_3 in the presence of a solid carbon surface (see discussion under Phase IB), but NH_3 is favored in a homogeneous flame. The HCN that was observed to form from NH_3 in premixed flames (De Soete and Phase II of this study) must therefore have formed from: (1) the heterogeneous reaction of NH_3 with soot particles, or (2) the reaction of NH_3 with hydrocarbon species early in the flame before the fuel is consumed. The thermodynamic tendency for HCN to form NH_3 in the later stages of combustion (which can be shown to be independent of the concentration of HCN) leads to the very significant conclusion that HCN formed in fuel pyrolysis or in the early stages of combustion could either be oxidized to fuel NO or be converted to NH_3 which then forms fuel NO. NH_3 has not been observed to form in flames with added HCN, but De Soete's results (discussed earlier) are not incompatible with such a hypothesis.

Elementary Reactions in Fuel NO Formation. To eventually model in detail the formation of fuel NO, the important elementary reactions that nitrogen species undergo in combustion will have to be identified and their rate parameters established. Experimental pyrolysis data obtained under Phase IB of this program indicate that the nitrogen in heterocyclic fuel-N compounds may be converted mainly to HCN in the early stages of combustion. These data also provide preliminary rate parameters that permit estimates to be made of the rate of this conversion process as a function of temperature. It can be seen from this and the previous discussion that the elementary reactions that must be investigated are those involved in: (1) conversion of HCN and CN to NO, (2) conversion of HCN and CN to NH_x species and vice versa (3) oxidation of NH_x to NO, (4) conversion of NO and other N species to N_2 , and (5) conversion of NO to HCN. The burner studies conducted in Phase II were oriented toward the investigation of these types of processes and indicate that HCN, once formed, should survive deep into the flame front.

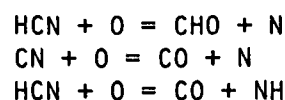
Many of the previous discussions of fuel NO formation mechanisms have been in terms of global or general mechanisms (e.g., the mechanisms of De Soete, Bowman, and Fenimore). However, Sternling and Wendt (Ref. 2), Flagan (Ref. 1), and Slater (Ref. 72) have discussed the types of elementary reactions that may be involved. The types of reactions they have considered are listed in Table 2.

TABLE 2. TYPES OF ELEMENTARY REACTIONS THAT MAY BE INVOLVED
IN FUEL NO_x FORMATION

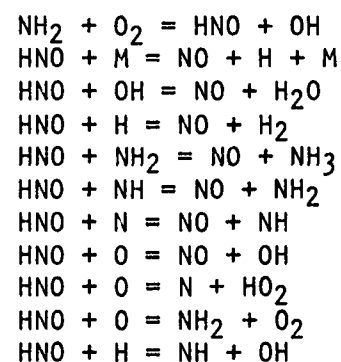
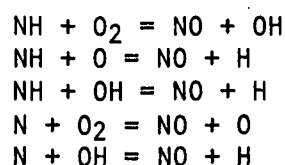
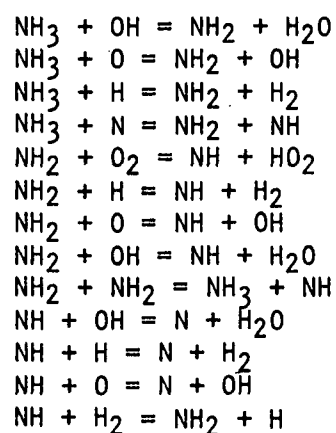
I. Conversion of HCN and CN to NO:



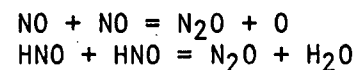
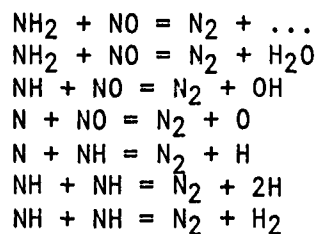
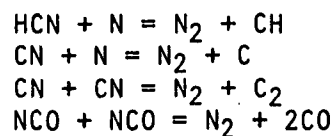
II. Conversion of HCN and CN to NH_x:



III: Oxidation of NH_x to NO:



IV. Formation of N₂:



Not all these processes are likely to occur, and a screening of the most probable processes is required before detailed reaction schemes can be postulated and tested. Some of this screening has been done by Sternling and Wendt (Ref. 2), Flagan (Ref. 1), Bartok and Engleman (Ref. 107) and, particularly, Slater (Ref. 72).

A few of the many possible elementary processes that may be involved in fuel NO_x formation have been incorporated in the combustion models that will be described in the next section to demonstrate that the models are capable of testing various detailed fuel NO_x mechanisms. As specific reaction rates become established as the most likely paths for fuel NO formation, these can be added to the mathematical model. A better mechanism for fuel NO_x formation is proposed near the end of this report based on the experimental burner results obtained under Phase II.

COMBUSTION MODELS

To understand or predict the resultant effect of fuel nitrogen, it is necessary to describe in detail the heterogeneous combustion of fuel oil sprays or coal particles. That is, determine droplet (particle) temperature and composition "life histories," as well as to delineate the temperature and gas composition profiles to which nitrogen-bearing compounds are exposed as they diffuse away from the droplet (particle) and into the flame zones of bulk combustion gas stream.

Until fairly recently, the spray combustion models, and the individual droplet models upon which they are based, assumed that when combustion reactions occur, they proceed abruptly to local thermodynamic equilibrium. As a result, they are adequate for analyzing gross combustion field behavior, but are inadequate for calculating the occurrence of species whose concentrations vary widely with departures from equilibrium. Combustion-generated pollutant species NO_x , smoke, and unburned hydrocarbons are prime examples of such species; their presence cannot be predicted with any confidence by the previous models.

Chemical kinetics of fuel vapor combustion within the drop-surface-to-flame boundary layer and the flame-to-free stream region have been employed only in single droplet models restricted to near-stagnant flow conditions (i.e., large flame/droplet radius ratios), quasi-steady gasification (i.e., constant droplet temperature), and single component droplets. Under such conditions, Fendell et al. (Ref. 108), using matched inner and outer expansions across the flame region, showed that earlier thin-flame and nonreacting vaporization models actually represent limiting cases of the more general treatment which includes finite-rate chemistry. Under the same restrictions, Bracco (Ref. 109) attacked the NO formation problem, but selected a simpler solution method. He solved the finite-rate hydrocarbon chemistry problem to get droplet-to-free-stream profiles of fuel, oxidant, and diluent species concentrations and temperature, and then used those data as input for a kinetic analysis of NO formation via the well known Zeldovich mechanism.

The principal objective of this task was to develop droplet/particle combustion models that could predict multicomponent droplet (particle) "life histories" and, also, the production rate of pollutants in the film surrounding the droplets (particles). One of the most important aspects of the pollutant formulation process was to describe the fate of fuel nitrogen compounds.

Four separate computer models were developed: (1) a droplet vaporization model, (2) a droplet flame front model, (3) a coal combustion model, and (4) a kinetic/diffusion model. These models were programmed so that they could be used as subprograms in a decoupled combustor flow program.

Inherent in all four models are the continuity, diffusion, and energy equations, but each differs in the assumptions and handling of the equations for its particular solution.

The two droplet models are used to calculate fuel droplet temperature and composition "life histories" and an approximation to the film temperature and composition profiles. The vaporization model neglects chemical reactions and the flame front model employs infinite rate kinetics for the reaction of the vaporizing species with oxygen and zero reaction rates for the other compounds present in the film surrounding the droplet.

The coal combustion model is used to calculate the coal particle temperature and composition "life history" including devolatilization and heterogeneous reactions at the particle surface. Chemical reactants in the film surrounding the particle are neglected.

The kinetic/diffusion model is used to calculate detailed kinetic and diffusion processes occurring in the film surrounding the fuel droplet or coal particle. This model is the main computer program for calculating pollutant generation rates including NO_x produced from fuel nitrogen compounds. Initial input profiles for the kinetic diffusion program are obtained from model calculations using the preceding fuel spray and coal combustion models. (See Appendix I for a description of the use of each model as well as criteria for the selection of the appropriate droplet program.)

Droplet Vaporization Model

Description of Model. The model for the heating and vaporization of multicomponent fuel droplets surrounded by a specified gas flowfield is depicted schematically in Fig. 10. It should be noted that the model does not include any reactions of the fuel vapor components with the surrounding gas.

The basic equations solved are the species diffusion equation:*

$$\dot{N}_j = -4\pi r^2 (c_j) \frac{dX_j}{dr} + X_j \sum_{m=1}^{n_t} \dot{N}_m \quad (22)$$

(molar flowrate
with respect to
fixed axes)
(molar flowrate
resulting from
diffusion)
(molar flowrate
resulting from
bulk flow)

species continuity equation:

$$\frac{d\dot{N}_j}{dr} = 4\pi r^2 R_j = 0, \quad (23)$$

(spatial variation
in molar flowrate)
(production of j by
homogeneous chemical
reaction)

and the energy equation

$$\frac{1}{4\pi r^2} \frac{d}{dr} \left\{ -4\pi r^2 k \frac{dT}{dr} + \sum_{m=1}^{n_t} \dot{N}_m H_m \right\} = 0 \quad (24)$$

(rate of energy output
by conduction)
(rate of energy output
by convection including
chemical energy)

*Symbols are defined in the Nomenclature List on page 345.

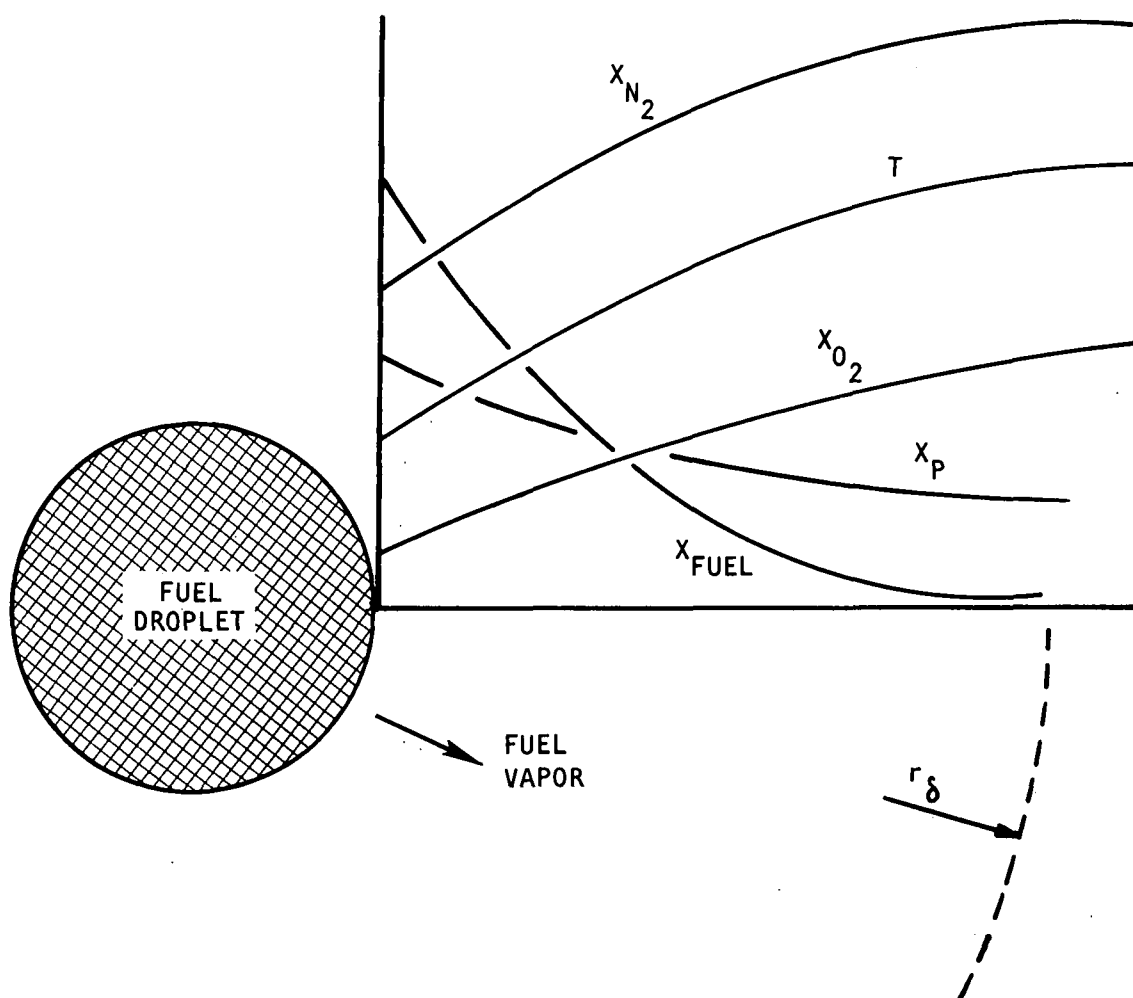


Figure 10. Droplet Vaporization Model

During the development and solution of the basic equations, the following assumptions are made:

1. The gas flow in the film surrounding the droplet is spherically symmetric and the film thickness is related empirically to the droplet Nusselt number or the ratio of convective to conductive heat transfer rate.
2. Fick's law is presumed valid throughout, implying equal binary diffusion coefficients which are evaluated at mean film conditions.
3. The thermal conductivity and gaseous specific heats are constant and evaluated at mean film conditions.
4. Temperature and concentration gradients within the droplet are ignored.
5. Fuel vapors are assumed to diffuse through the boundary layer (film) surrounding the droplet without undergoing pyrolysis or combustion reactions.
6. The fuel is specified as a multicomponent mixture of compounds having different properties, e.g., vapor pressure, molecular weight, etc.
7. Droplet temperature and composition varies with time.
8. The static pressure in the radial direction is constant.

Summing the diffusion equation over all vaporizing species yields:

$$\dot{N}_v + (4\pi r^2) \left(\frac{dX_v}{dr} \right) = \dot{N}_v X_v \quad (25)$$

where

$$\dot{N}_v \equiv \sum_{\substack{\text{vaporizing} \\ \text{species}}} \dot{N}_i \quad (\text{total vaporization rate}) \quad (26)$$

$$X_v \equiv \sum_{\substack{\text{vaporizing} \\ \text{species}}} X_i \quad (\text{total vaporizing mole fraction}) \quad (27)$$

Noting that the specie molar flowrates are constant (application of the species continuity equation), the preceding total vaporizing species diffusion equation is integrated between the droplet surface and the gas stream to yield the total vaporization rate:

$$\dot{N}_v = (4\pi r_d) (\overline{c\delta}) \left(\frac{Nu_m}{2} \right) \ln \left(\frac{1 - X_{vg}}{1 - X_{vd}} \right) \quad (28)$$

where the subscripts g and d represent the bulk gas and the gas at the droplet surface, and the outer boundary of the film is determined from the mass-transfer Nusselt number empirical relationship (Ref. 110):

$$r_{\delta_m} = \frac{r_d}{1 - \frac{2}{Nu_m}} \quad (29)$$

The mole fraction of the vaporizing species in the gas stream (X_{vg}) is determined by the gas stream composition. The mole fraction of the vaporizing species at the droplet surface (X_{vd}) is determined by:

$$X_{vd} = \frac{\text{vaporizing species}}{\sum_i Y_i} \frac{P_{vi}}{P} \quad (30)$$

where Y_i is the volume fraction of the i^{th} species inside the liquid droplet and P_{vi} is the vapor pressure, evaluated at droplet temperature, of that species.

Each droplet component vaporization rate is determined by integrating the component's diffusion equation between the droplet surface and the gas stream and is given by:

$$\frac{\dot{N}_i}{\dot{N}_v} (X_{vd} - X_{vg}) = X_{id} (1 - X_{vg}) - X_{ig} (1 - X_{vd}) \quad (31)$$

The liquid droplet radius is therefore determined by:

$$\frac{d}{dt} \left[\frac{4\pi}{3} r_d^3 \rho_d \right] = -\dot{N}_v \quad (32)$$

and its composition is determined by:

$$\frac{d}{dt} \left[\frac{4\pi}{3} r_d^3 Y_i \rho_{\ell_i} \right] = -\dot{N}_i \quad (33)$$

The droplet heating rate (heat delivered to the droplet surface) is determined by integrating the energy equation between the droplet surface and free stream. This is accomplished by integrating the energy equation between the droplet surface and a general radial location which yields:

$$-4\pi r^2 \bar{k} \frac{dT}{dr} + \dot{N}_v \bar{C}_{p_T} T = \dot{N}_v \bar{C}_{p_T} T_d + \dot{Q}_R - \dot{Q}_d - \dot{N}_v \Delta H_{vap_T} \quad (34)$$

where the average heat capacity of the gaseous mixture (\bar{C}_{p_T}) is:

$$\dot{N}_v \bar{C}_{p_T} \equiv \sum_i^{\text{vaporizing species}} \dot{N}_i \bar{C}_{p_i} \quad (35)$$

and the average heat of vaporization is:

$$\dot{N}_v \Delta H_{vap_T} = \sum_i^{\text{vaporizing species}} \dot{N}_i \Delta H_{vap_i} \quad (36)$$

and

$$\dot{Q}_R = \text{radiation heat transfer rate}$$

$$\dot{Q}_d = \frac{4\pi}{3} r_d^3 \rho_d C_{p_d} \frac{dT_d}{dt} - \text{droplet heating rate} \quad (37)$$

Integrating the preceding modified energy equation between the droplet surface and the gas stream yields the droplet heating rate:

$$\dot{Q}_d = \dot{Q}_R + (4\pi r_d) \bar{k} \left(\frac{Nu_H}{2} \right) \left[\frac{(T_g - T_d)}{(e^Z - 1)} - \frac{\Delta H_{vap,T}}{C_{p,T}} \right] Z \quad (38)$$

where the outer boundary of the thermal film is determined from the heat transfer Nusselt number by the empirical relationship (Ref. 110):

$$r_{\delta_H} = \frac{r_d}{1 - \frac{2}{Nu_H}} \quad (39)$$

and the "heat transfer blockage term" is:

$$Z \equiv \frac{\dot{N}_v \bar{C}_{p_r}}{(4\pi r_d) \bar{k}} \left(\frac{2}{Nu_H} \right) \quad (40)$$

Quasi-steady-state specie concentration profiles on the gas side of the droplet are determined from the integrated species diffusion equation and are given by:

$$\frac{X_i - \dot{N}_i/\dot{N}_v}{X_{i_d} - \dot{N}_i/\dot{N}_v} = \left[\frac{X_{i_g} - \dot{N}_i/\dot{N}_v}{X_{i_d} - \dot{N}_i/\dot{N}_v} \right] \frac{Nu_m}{2} \left(1 - \frac{r_d}{r} \right) \quad (41)$$

and the film gas temperature profile is determined from the integrated energy equation and is given by:

$$\frac{T - T_d}{T_g - T_d} = \frac{1}{(e^Z - 1)} \left\{ \exp \left[Z \left(\frac{Nu_H}{2} \right) \left(1 - \frac{r_d}{r} \right) \right] - 1 \right\} \quad (42)$$

The model described above accounts for changes in droplet density, latent heat of vaporization, vapor pressure, and average vapor thermal and transport properties that arise due to the more rapid gasification of the more volatile droplet components during the course of vaporization.

These equations are solved by a second-order explicit algorithm for the algebraic and differential equations describing the vaporization rate/droplet composition process and a second-order implicit algorithm for the equations that describe the heating process. As part of the computer program output, descriptions are given for the droplet vaporization rate, the average film (boundary layer) surrounding the droplet, the droplet temperature, liquid composition, and droplet diameter from ignition to final burnout. Particular attention has also been given to the calculation of the average film thickness, fuel vapor diffusion rates through the film, typical vapor residence times within the film, and film temperature and composition profiles.

The main limitations of the droplet vaporization model in predicting droplet vaporization and heating rates are: (1) spherical symmetry, i.e., the model equations were developed for nonconvective conditions, and convection is accounted for by employing empirical Nusselt numbers; (2) the exclusion of chemical reactions; and (3) the nonapplicability of the model at supercritical pressures. The model should be used in the analyses of burners with high convective loading, i.e., burners whose gas velocity is much greater than droplet velocities so that burning does not occur in a flamefront surrounding the droplet.

Model Calculations. Calculations using the droplet vaporization computer program were made with parametric variations in the initial fuel composition, initial droplet size, surrounding bulk gas temperature and composition, and degree of convection. In part, these calculations were made to check the operation of the model and to determine the effect of using average properties for determining droplet histories, rather than multicomponent properties. (Using average properties, if appropriate, would simplify the calculations.) An example of the effects of average versus variable droplet compositions is presented below. These calculations were run at the following conditions:

1. Relative gas to droplet velocity: 1 ft/sec
2. Initial droplet diameter: 40 microns

3. Gas temperature: 1000 R
4. Droplet composition:
 - a. Variable composition with two species which have different normal boiling points. Species selected were the upper and lower boiling point fractions for kerosene.
 - b. Fixed composition with an average normal boiling point based on the species used in 4a.

The droplet life histories calculated by assuming constant and variable droplet composition are presented in Fig. 11 (upper two curves). Note that both approaches (average and variable compositions) provide essentially the same results with respect to the overall burning rate. This is somewhat surprising since the actual composition of the droplet varies considerably, as shown by the lower two dashed curves. This result, however, is not expected to be generally true for all species since wider variations in properties can occur. Inspection of the lower curves, however, shows that the composition of the vapors leaving the droplet varies substantially with time. This illustrates the necessity of using a multi-component model to determine specie histories. Droplet temperature-time histories for the two cases are shown in Fig. 12. Note that the initial heatup rates are essentially equal for both cases; however, the maximum temperatures attained differ by as much as 75 R. This difference could be significant, depending on the sensitivity of the kinetics employed in the kinetic/diffusion model. (The kinetic/diffusion model requires the droplet surface temperature calculated by the droplet model for a boundary condition.)

Droplet Flame-Front Model

Description of Model. The model for the heating and combustion of multicomponent fuel droplet surrounded by a flame front is depicted schematically in Fig. 13.

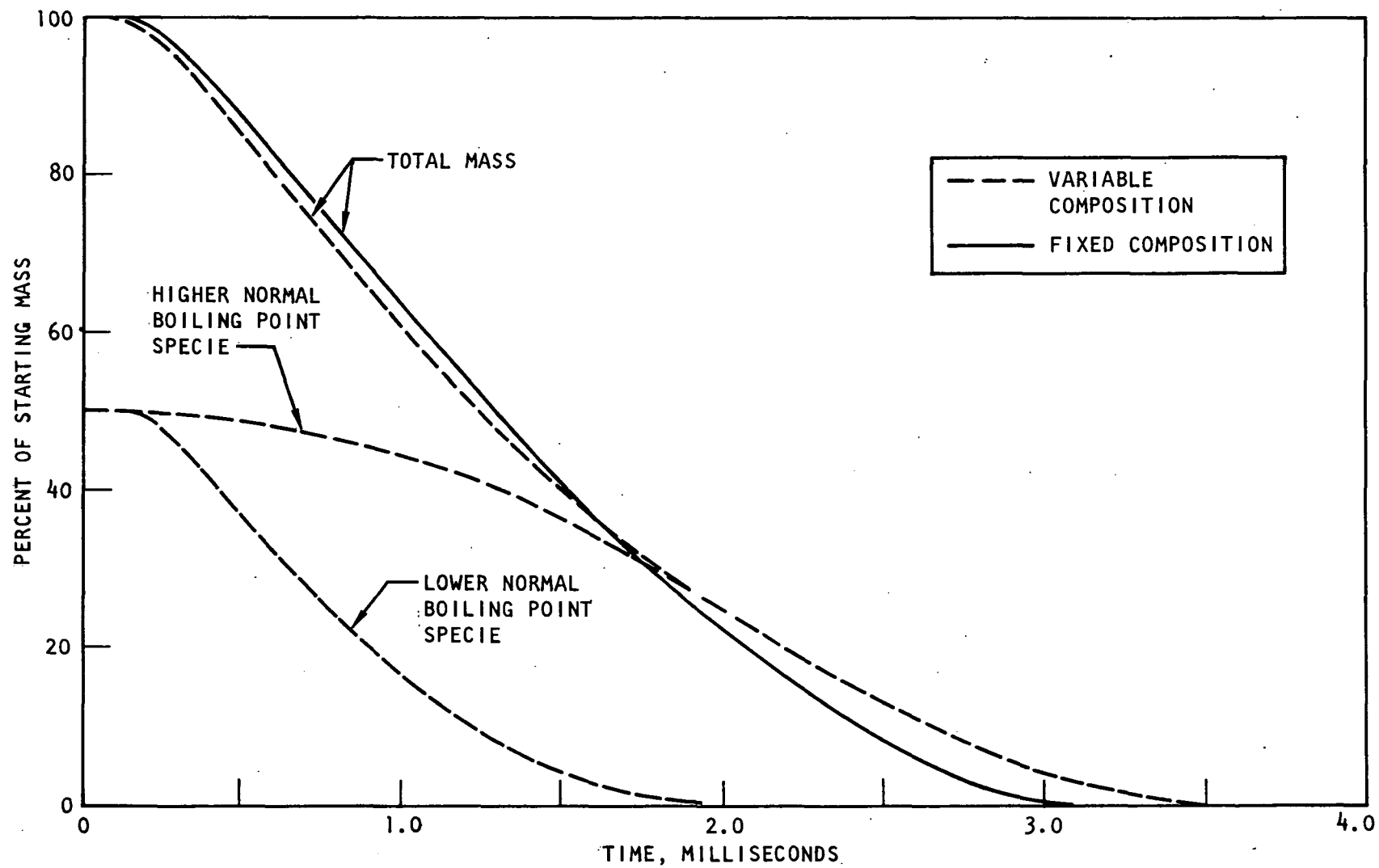


Figure 11. Droplet Mass and Composition

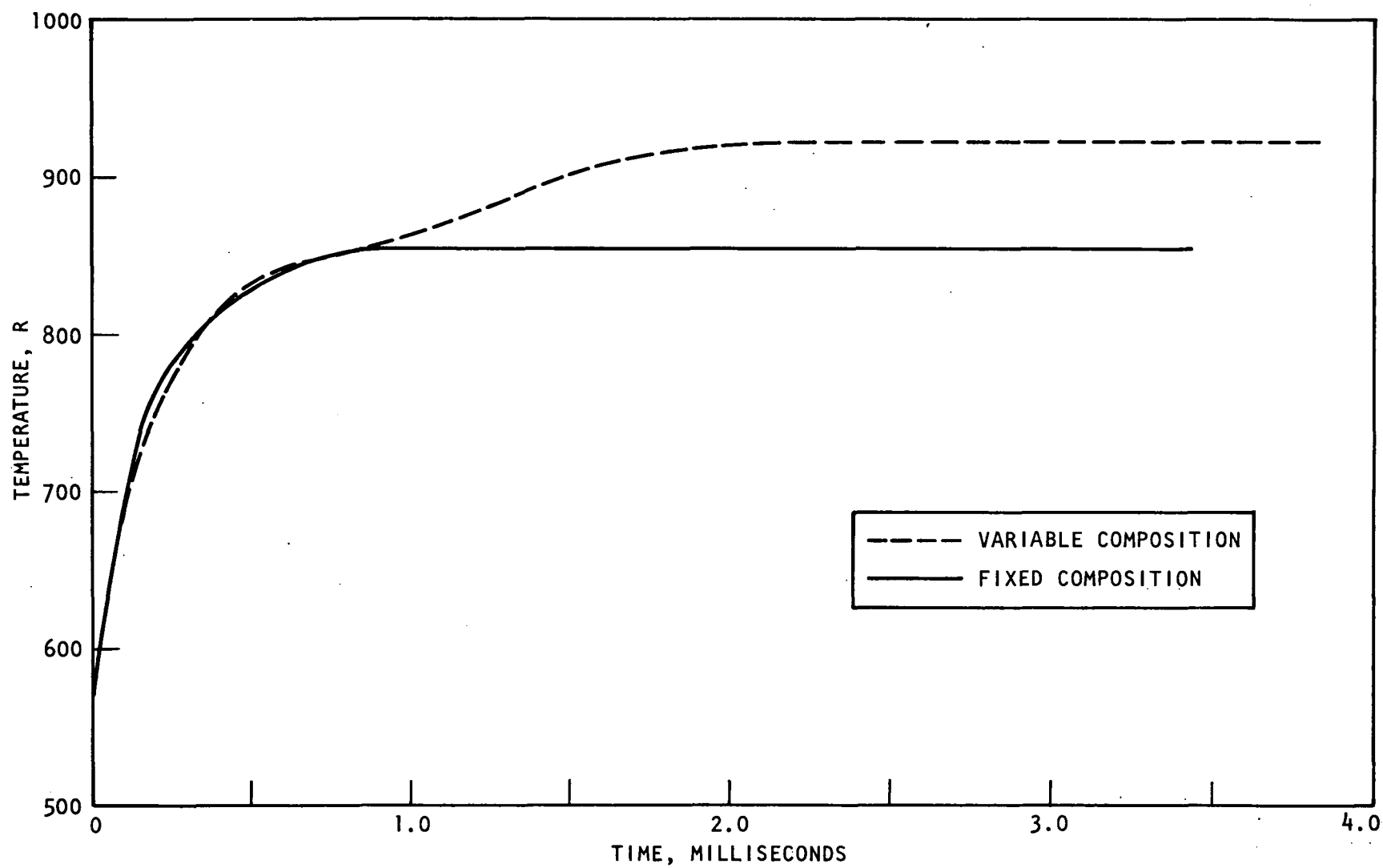


Figure 12. Droplet Temperature

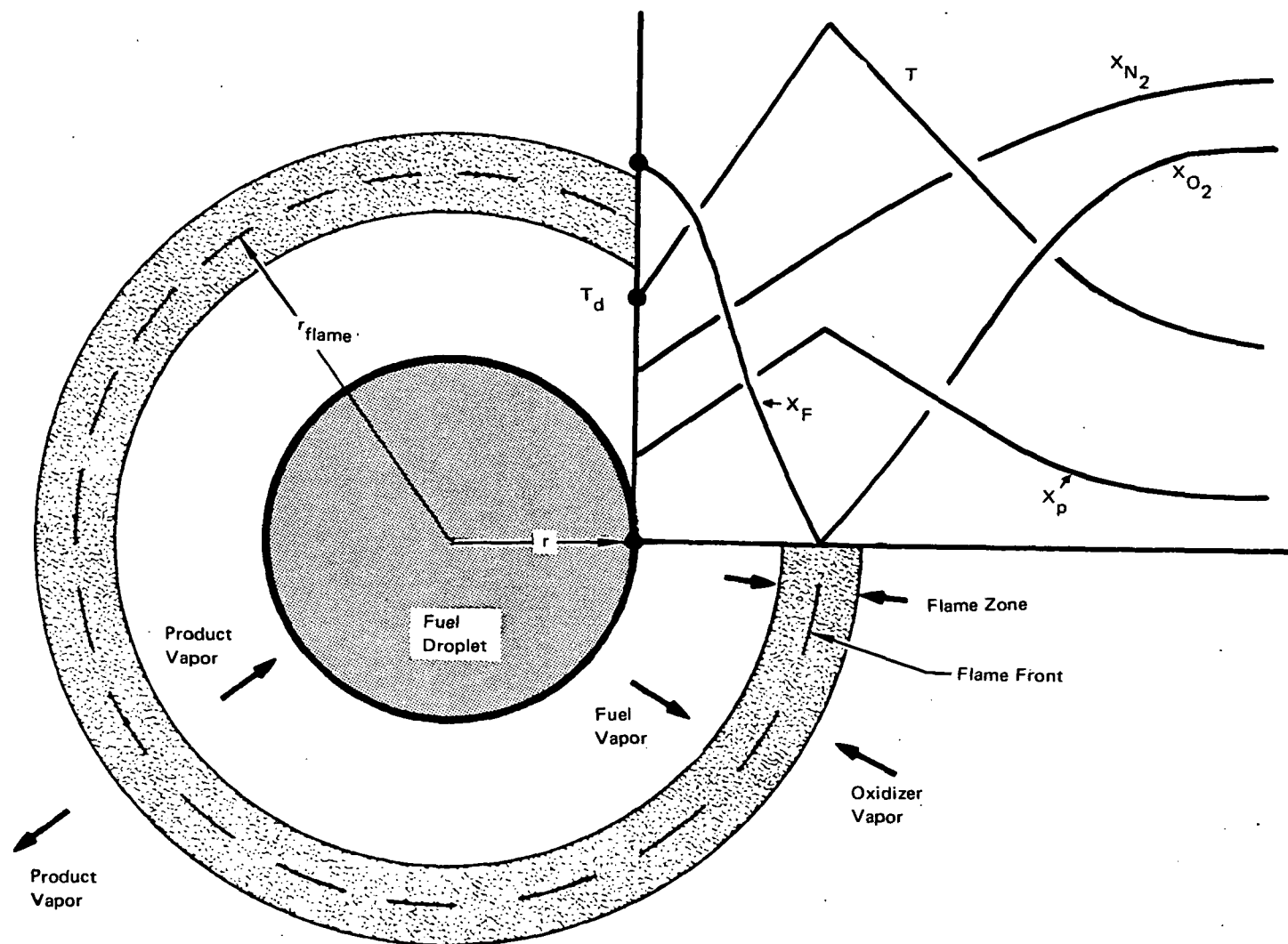


Figure 13. Schematic of Reactant Diffusion and Reaction in a Flame Zone Surrounding a Fuel Droplet

Included in the figure is a conceptual graph of the radial variations of the gas temperature and mole fractions of selected species through the vapor film, flame zone, and external mantle. Radial diffusion of the droplet vapors carries them into progressively higher temperatures until they reach the flame zone (flame front), where they are oxidized and burned.

Again, the basic equations solved are the species diffusion equation,

$$\dot{N}_j + (4\pi r^2) (c \mathcal{D}_j) \frac{dX_j}{dr} = X_j \sum_{m=1}^{n_t} \dot{N}_m \quad (43)$$

species continuity equation,

$$\frac{1}{4\pi r^2} \frac{d\dot{N}_j}{dr} = \eta R_j, \quad \eta = 0 \text{ if } r \neq r_f \quad (44)$$

and the energy equation,

$$\frac{1}{4\pi r^2} \frac{d}{dr} \left\{ -4\pi r^2 k \frac{dT}{dr} + \sum_{m=1}^{n_t} \dot{N}_m H_m \right\} = 0 \quad (45)$$

During the development and solution of the basic equations, the following assumptions were made:

1. The gas flow in the film surrounding the droplet is spherically symmetric and the film thickness is related empirically to the droplet Nusselt number.
2. Fick's law is presumed valid throughout, implying equal binary diffusion coefficients which are evaluated at mean film conditions.
3. The thermal conductivity and specific heats are constant and evaluated at mean film conditions.
4. Temperature and concentration gradients within the droplet are ignored.
5. Fuel combustion reactions are assumed to occur in an infinitely thin flame front at stoichiometric conditions with the products of combustion determined by equilibrium calculations at the stoichiometric conditions which include dissociation effects.

6. The fuel is specified as a multicomponent mixture of compounds having different properties, e.g., vapor pressure, molecular weight, etc.
7. Droplet temperature and composition varies with time.
8. The static pressure is constant.

The key equations solved by the computer program are summarized below without detailing their derivations. The derivations are similar to the vaporization model derivations presented in the preceding section except the integration has been performed in two steps. First the equations are integrated between the droplet surface and the flame front and then they are integrated between the flame front and the gas stream.

The total combustion rate, derived from the summation of the species diffusion equations, is given by:

$$\dot{N}_{T_I} = (4\pi r_d^2) \left(\frac{Nu_m}{2} \right) (\overline{c\mathcal{D}})_I \beta \ln \left[\frac{1 - X_{v_f}}{1 - X_{v_d}} \right] \quad (46)$$

where vaporizing species

$$X_v \equiv \sum_{i=1} X_i \quad (\text{total vaporizing mole fraction}) \quad (47)$$

$$\beta \equiv (2/Nu_m) / \left(1 - \frac{r_d}{r_f} \right) \quad (48)$$

r_f = radial location of the flame front, and the subscript I refers to conditions inside the flame front. (For most conditions, the mole fraction of the vaporizing species at the flame front (X_{v_f}) is zero.) The combustion rate of each of the droplet component species is determined from their diffusion equations and is given by:

$$\frac{\dot{N}_{i_I}}{\dot{N}_{T_I}} (X_{v_d} - X_{v_f}) = X_{i_d} (1 - X_{v_f}) - X_{i_f} (1 - X_{v_d}) \quad (49)$$

where the mole fractions of the vaporizing species (X_{i_f}) at the flame front are also normally zero. It should be noted that the molar flowrate inside the flame front of species other than vaporizing species is identically equal to zero, i.e., the boundary condition at the droplet surface for species other than vaporizing species is that their flowrates are zero and the species continuity requires that the flowrates remain zero inside the flame front.

The molar flowrate outside the flame front for each species is determined by the chemical reactions:

$$F_m - (v_{ox})_m O_2 \rightarrow \sum_j \text{products} (v_{prod,j})_m P_j \quad (50)$$

(Note: $v_{ox,m}$ is negative)

where F_m is the M^{th} vaporizing fuel species and P_j is the j^{th} product of combustion and is given by:

$$\dot{N}_{j\phi} = \sum_i v_{ji} \dot{N}_{iI} \quad (51)$$

The total molar flowrate outside the flame front is given by:

$$\dot{N}_{T\phi} = \bar{v}_T \dot{N}_{TI} \quad (52)$$

and the oxygen flowrate is:

$$\dot{N}_{ox\phi} = \bar{v}_{ox} \dot{N}_{TI} \quad (53)$$

where

$$\bar{v}_T \equiv \sum_i \sum_j v_{ji} \left(\frac{\dot{N}_{iI}}{\dot{N}_{TI}} \right) \quad (54)$$

$$\bar{v}_{ox} = \sum_i v_{ox,i} \left(\frac{\dot{N}_{iI}}{\dot{N}_{TI}} \right) \quad (55)$$

The radial location of the flame front is determined by employing the preceding expressions and film diffusion equations inside and outside the flame front and is given by:

$$(\beta - 1) \bar{v}_T \ln \left(\frac{1 - x_{vf}}{1 - x_{vd}} \right) = \frac{(\bar{c}_p)_\phi}{(\bar{c}_p)_I} \ln \left[\frac{x_{02g} - \bar{v}_{ox}/\bar{v}_T}{x_{02f} - \bar{v}_{ox}/\bar{v}_T} \right] \quad (56)$$

Where the mole fraction of oxygen at the flame front is assumed to be zero.

The droplet heating rate (heat delivered to the droplet surface) derived from the film energy equation inside the flame front is:

$$\dot{Q}_d = Q_R + (4\pi r_d) \bar{k}_I \left(\frac{Nu_H}{2} \right) Z_I \left[\frac{(T_f - T_d)}{\alpha_I - 1} - \frac{\Delta H_{vapT}}{\bar{c}_{p_{T_I}}} \right] \quad (57)$$

where

$$Z_I \equiv \frac{\dot{N}_{T_I} \bar{c}_{p_I}}{4\pi r_d \bar{k}_I} \left(\frac{2}{Nu_H} \right) \quad (58)$$

$$\alpha_I \equiv \frac{Z_I Nu_H}{\beta Nu_m} \quad (59)$$

$$\bar{c}_{p_{T_I}} \equiv \frac{1}{\dot{N}_{T_I}} \sum_i \dot{N}_{i_I} \bar{c}_{p_{i_I}} \quad (60)$$

$$\Delta H_{vapT} \equiv \frac{1}{\dot{N}_{T_I}} \sum_i \dot{N}_{i_I} \Delta H_{vap_i} \quad (61)$$

Similar expressions define the parameters α_ϕ and Z_ϕ outside the flame front.

The temperature of the flame front is determined by equating the heat of combustion to the change in the slope of the temperature (dT/dr) across the flame front, i.e.,

$$\begin{aligned} N_{T_I} q_c &= 4\pi r_f^2 \bar{k}_I \left(\frac{dT}{dr} \right)_{r_f^-} - 4\pi r_f^2 \bar{k}_\phi \left(\frac{dT}{dr} \right)_{r_f^+} \quad (62) \\ \text{(heat release rate due to combustion)} &\quad \text{(heat transfer rate away from the flame front due to conduction)} \end{aligned}$$

where

$$-q_c \equiv \frac{1}{\dot{N}_{T_I}} \sum_i \left(\dot{N}_{i_\phi} - N_{i_I} \right) H_{i_f} \quad (63)$$

$$H_{i_f} = \int_{298\text{ C}}^{T_f} C_{P_i} dT + \Delta H_{298_i}^0 \quad (64)$$

Employing these relationships and film energy equations inside and outside the flame front yields the flame temperature:

$$\begin{aligned} T_f &\left[\bar{C}_{P_{T_I}} \left(\frac{e^{\alpha_I}}{e^{\alpha_I} - 1} \right) + \frac{\dot{N}_{T_\phi}}{\dot{N}_{T_I}} \bar{C}_{P_{T_\phi}} \left(\frac{e^{\alpha_\phi}}{e^{\alpha_\phi} - 1} \right) \right] \\ &= q_c + \bar{C}_{P_{T_I}} T_d \left(\frac{e^{\alpha_I}}{e^{\alpha_I} - 1} \right) + \frac{\dot{N}_{T_\phi}}{\dot{N}_{T_I}} \bar{C}_{P_{T_\phi}} T_g \left(\frac{e^{\alpha_\phi}}{e^{\alpha_\phi} - 1} \right) \quad (65) \end{aligned}$$

Expression for liquid droplet radius and composition, and quasi-steady-state concentration and temperature profiles on the gas side of the droplet are defined and are similar to those given in the droplet vaporization model section.

The model described above accounts for changes in droplet density, latent heat of vaporization, vapor pressure, and average vapor thermal and transport properties that arise due to the more rapid gasification of the more volatile droplet

components during the course of combustion. Again, a second-order explicit algorithm is used to solve the algebraic and differential equations that describe the combustion rate/droplet composition process, and a second-order explicit algorithm is used to solve the equations that describe the heating process. As part of the computer program output, descriptions are given for the droplet combustion rate, the average film (boundary layer) surrounding the droplet, the droplet temperature, liquid composition, droplet diameter, and the radial location and temperature of the flame front from ignition to final burnout. Particular attention has also been given to the calculation of the average film thickness, diffusion rates through the film, typical vapor residence times within the film, and film temperature and composition profiles.

The main limitations of the droplet flame front model in predicting droplet combustion and heating rates are spherical symmetry, infinite fuel kinetics (flame front), exclusion of nonfuel reactions, and the nonapplicability of the model at supercritical pressures. The model should be used in the analysis of burners with low convective loading, i.e., burners whose gas and droplet velocities are approximately equal so that a flame can surround the droplet.

Model Calculations. Calculations using the droplet flame front model at the conditions listed below have been made with parametric variations in the fuel type, initial droplet size, surrounding bulk gas temperature and composition, and degree of convection. These calculations indicate that the maximum fuel droplet heating rate is approximately 10 to 80 R per microsecond for a 40-micron droplet. The higher heating rates are associated with high initial gas temperature and convective conditions. Radiation was found to have considerably less influence than these parameters. Under most flow conditions, the maximum heating rate is located at a position which corresponds to low droplet temperatures and low vaporization rates.

An example of droplet calculations using the flame front model are presented in Fig. 14 and 15. These calculations were run at the following conditions using fuel grade No. 2:

1. Relative gas to droplet velocity: 10 ft/sec
2. Initial droplet diameter: 40 microns
3. Gas temperature: 2000 R
4. Oxygen mass fraction: 0.15
5. Radiation heat transfer: zero

Since fuel oils are a distillate or residue of petroleum hydrocarbons, the fuel oils are actually composed of many different species which have widely different properties. Composition and physical properties of the species as functions of temperature are not, however, directly available and, therefore, properties required by the combustion model have been approximated. In any case, distillation curves and physical properties of hydrocarbons are available and the hydrocarbon properties are generally "smooth" functions of the number of carbon atoms in the compounds.

Known values (Ref. 111) of critical pressure and normal boiling temperature for hydrocarbons are plotted in Fig. 16 and 17 as functions of the number of carbon atoms (n) in the compounds. Boundaries were drawn through the data and extended up through $n = 40$ to estimate the required properties.

Employing known distillation curves (Ref. 112), fuel oil compositions and properties were determined using the following technique:

1. Fuel composition: the 0-, 10-, 50-, 90-, and 100-percent distillation temperatures were used to define the normal boiling points of five "species."
2. Species carbon content: determined using the normal boiling point and Fig. 17.

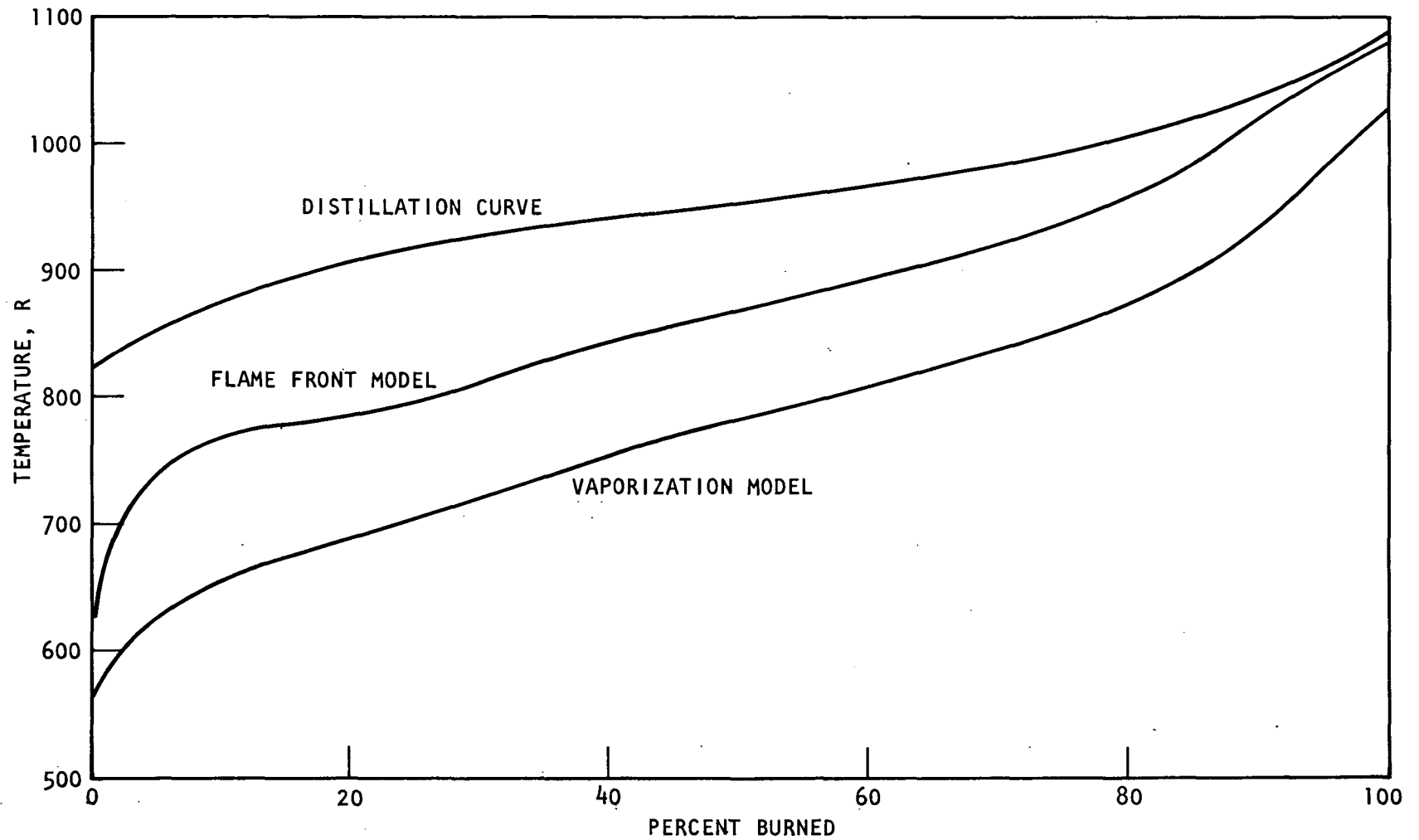


Figure 14. Droplet Temperature

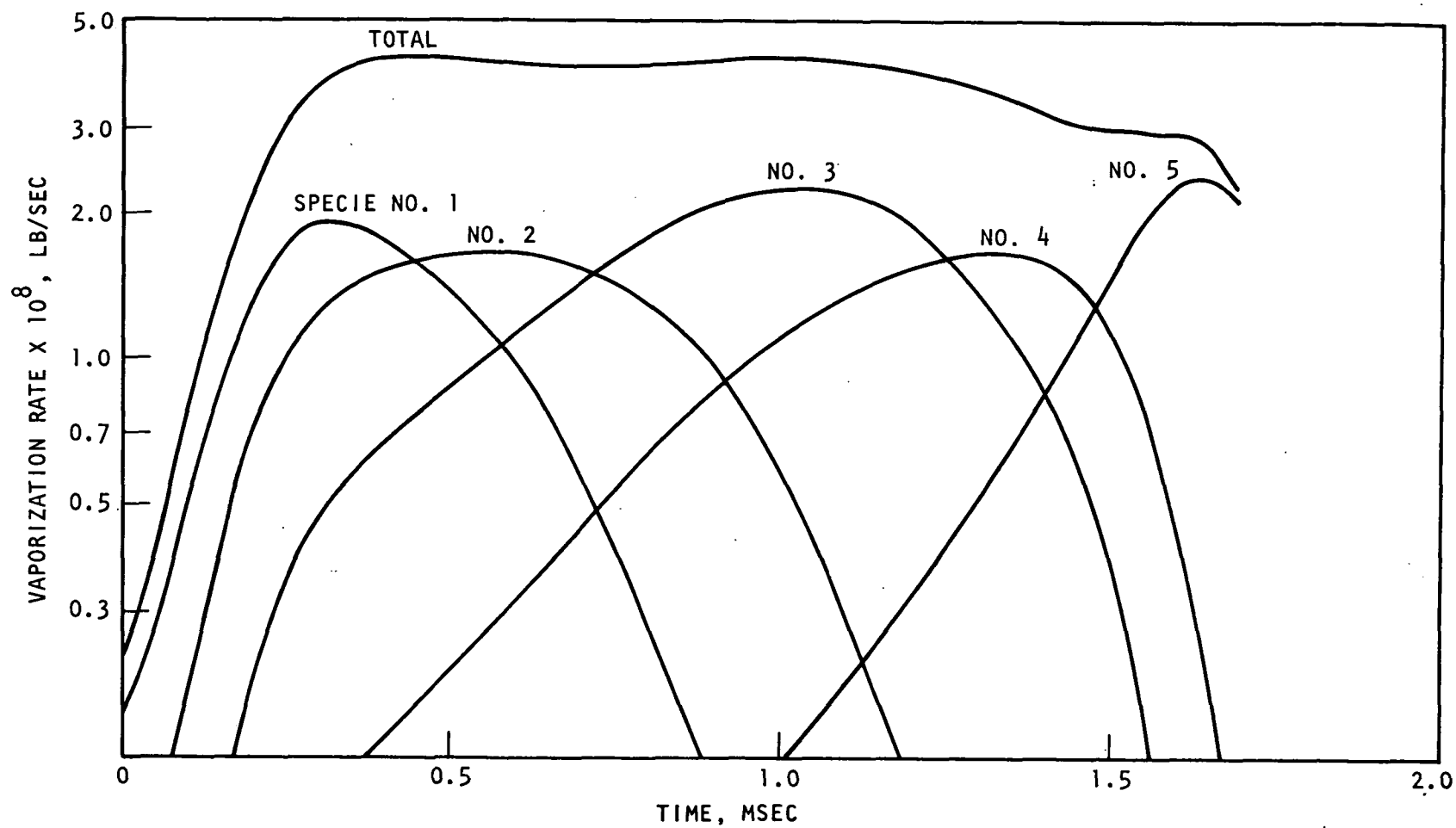


Figure 15, Vaporization Rate, Flame-Front Model

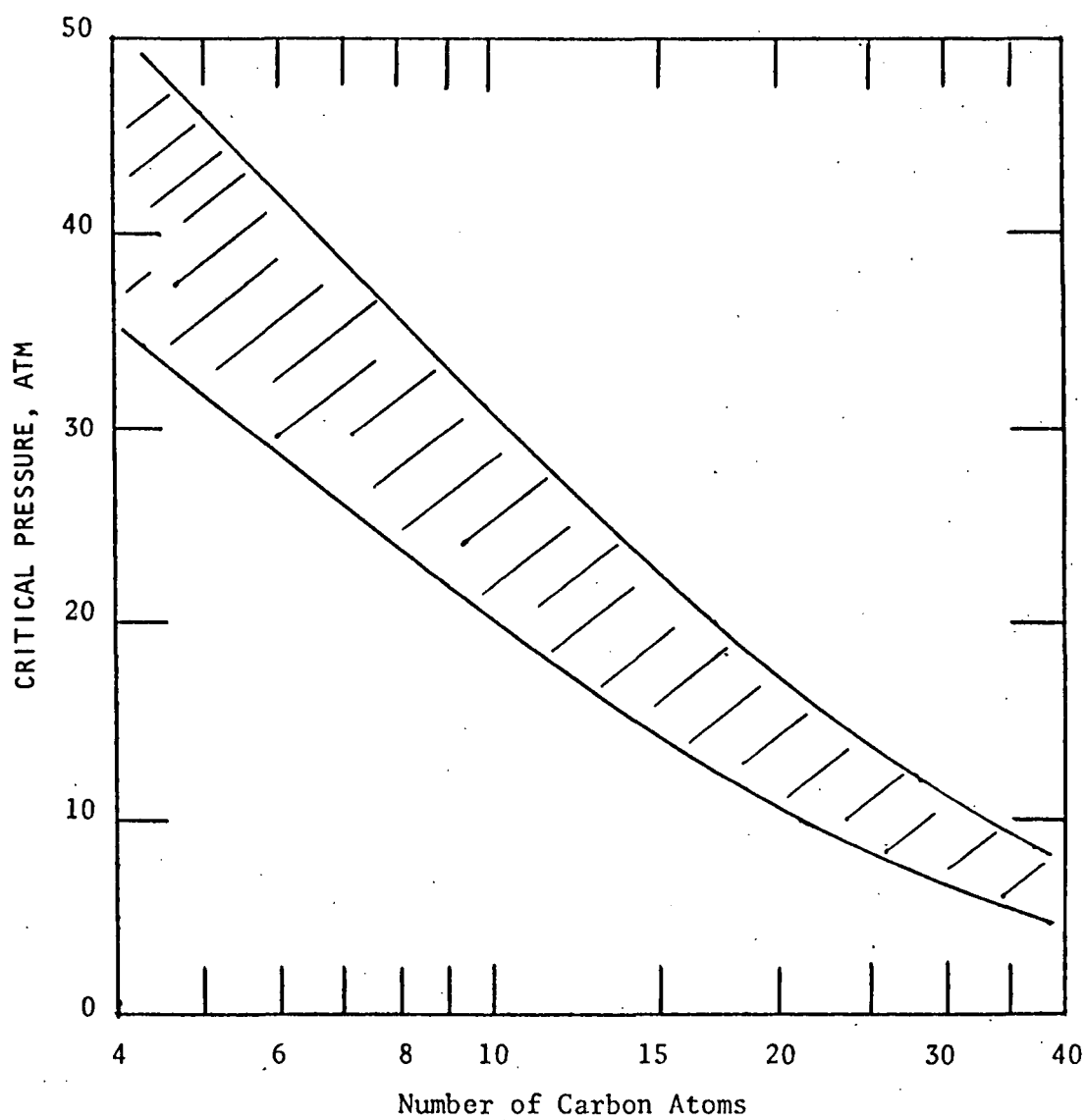


Figure 16. Critical Pressure for Hydrocarbons (Ref. 111)

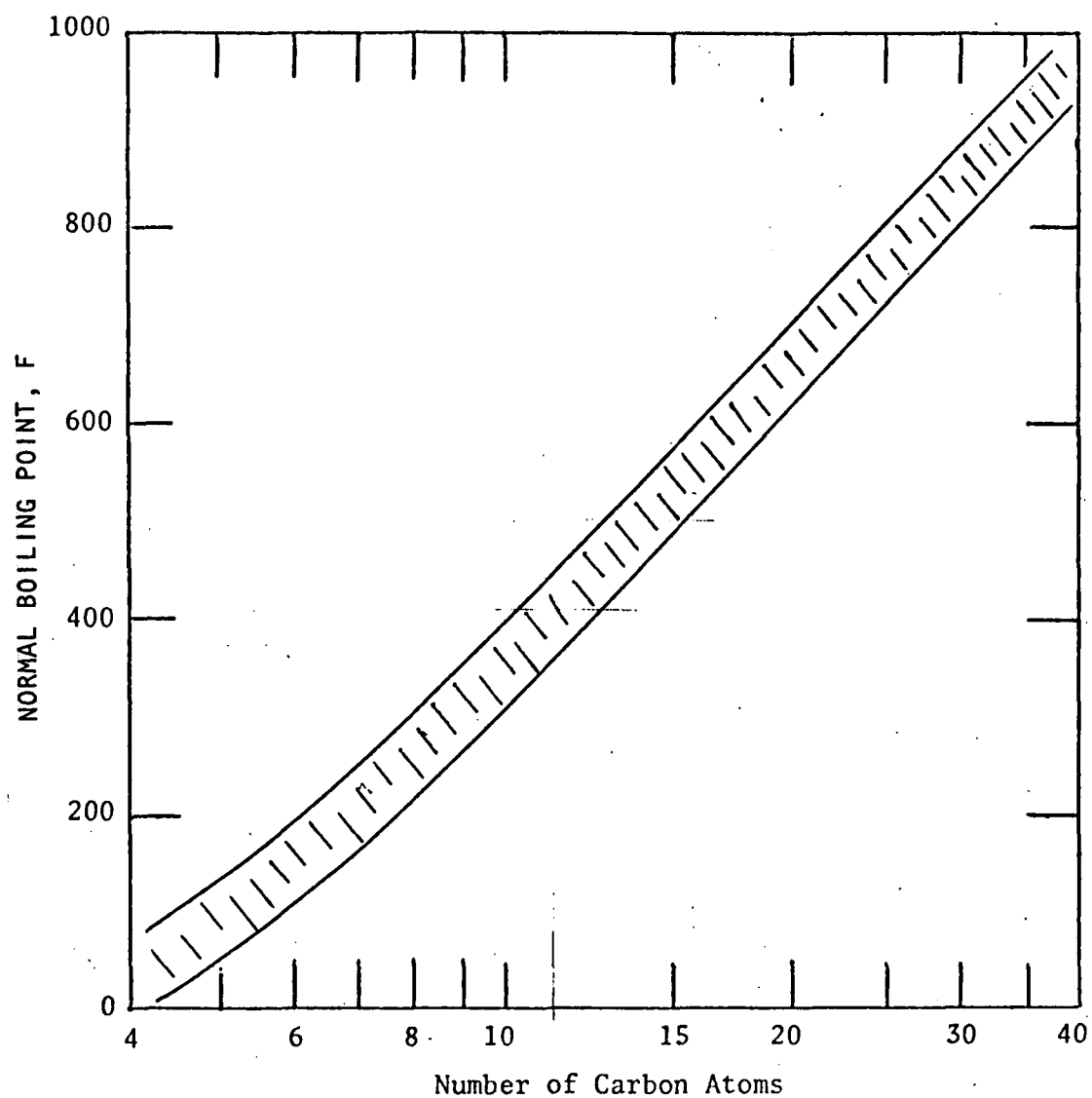


Figure 17. Normal Boiling Point for Hydrocarbons (Ref. 111)

3. Molecular weights defined by:

$$MW_i = (n_i)(MW_C) + (2n_i + 2) MW_H \quad (66)$$

4. Vapor pressures defined by the normal boiling point and the techniques outlined in Ref. 113, curve-fitted to:

$$\ln P_{V_i} = A + B/T \quad (67)$$

5. Critical pressures defined using the number of carbon atoms and Fig. 16.
6. Heat of vaporization, defined by the techniques outlined in Ref. 114, curve-fitted to:

$$\Delta H_V = \Delta H_{V_{NBP}} \left[\frac{C - T}{C - T_{NBP}} \right]^{0.38} \quad (68)$$

Shown in Table 3 is the final compositions and properties that have been selected to simulate fuel grade No. 2.

Examination of Fig. 14 and 15 shows that upon injection of the droplet into the gas stream, the combustion rate is very low and the heatup rate is very high. Also, the flame front is located close to the droplet surface and the "flame temperature" is initially very low due to the low incident rate of fuel vaporization. As the droplet temperature increases, the combustion rate of the lower normal boiling temperature species increases, the flame front moves away from the droplet surface and the flame temperature increases. This increase in flame temperature causes the heating rate to increase until the droplet temperature approaches the "wet bulb" temperature. Upon approaching the "wet bulb" temperature, the droplet heating rate decreases rapidly. As the combustion processes proceed from initial conditions to burnout, the droplet composition gradually changes to higher normal boiling point species and the droplet temperature continues to increase.

TABLE 3. ESTIMATED PROPERTIES FOR FUEL GRADE NO. 2

Specie	Mass Fraction	Molecular Weight	Critical Pressure, atm	Normal Boiling Point, F	A*	B*, R	ΔH_{VNB}^{**} , Btu/lb	C**, F
1	0.15	102	33	212	11.012	-7,400	132	525
2	0.20	123	28	292	11.503	-8,650	124	599
3	0.30	163	23	405	11.855	-10,255	112	716
4	0.20	194	20	478	12.401	-11,632	106	777
5	0.15	266	15	625	13.765	-14,935	91	891

$$*\ln P_v = A + B/T$$

$$**\Delta H_v = \Delta H_{vNB} \left[\frac{C - T}{C - T_{NB}} \right]^{0.38}$$

Coal Particle Model

Description of Model. The model for analyzing heterogenous combustion and devolatilization of coal particles is depicted schematically in Fig. 18. It should be noted that the model does not include reactions in the film surrounding the particle.

The basic equations solved are the species continuity equation in the film surrounding the particle:

$$\frac{1}{4\pi r^2} \frac{d\dot{N}_i}{dr} = R_i = 0, \quad (69)$$

species diffusion in the film;

$$\dot{N}_i + 4\pi r^2 (c\bar{D}) \frac{dX_i}{dr} = X_i \sum_{j=1}^{n_t} \dot{N}_j, \quad (70)$$

the energy equation in the film:

$$\frac{1}{4\pi r^2} \frac{d}{dr} \left\{ -4\pi r^2 \bar{k} \frac{dT}{dr} + \sum_{j=1}^{n_t} \dot{N}_j H_j \right\} = 0, \quad (71)$$

the particle continuity equation:

$$\frac{d}{dt} \left(\frac{4\pi}{3} r_s^3 \delta_c \right) = -\dot{R}_H (4\pi r_s^2) = -\dot{N}_c, \text{ and} \quad (72)$$

the devolatilization rate for the jth volatile component:

$$\frac{d}{dt} \left[\delta_{v_j} \frac{4\pi}{3} r_s^3 \right] = -R_{v_j} \left(\delta_{v_j} \frac{4\pi}{3} r_s^3 \right) - \dot{N}_c \left(\frac{\delta_{v_j}}{\delta_c} \right) = -\dot{N}_{v_j} \quad (73)$$

(Total rate change
of volatile mass)

(Volatile material
rate loss due to
devolatilization
reactions)

(Volatile ma-
terial rate
loss due to
heterogeneous
combustion)

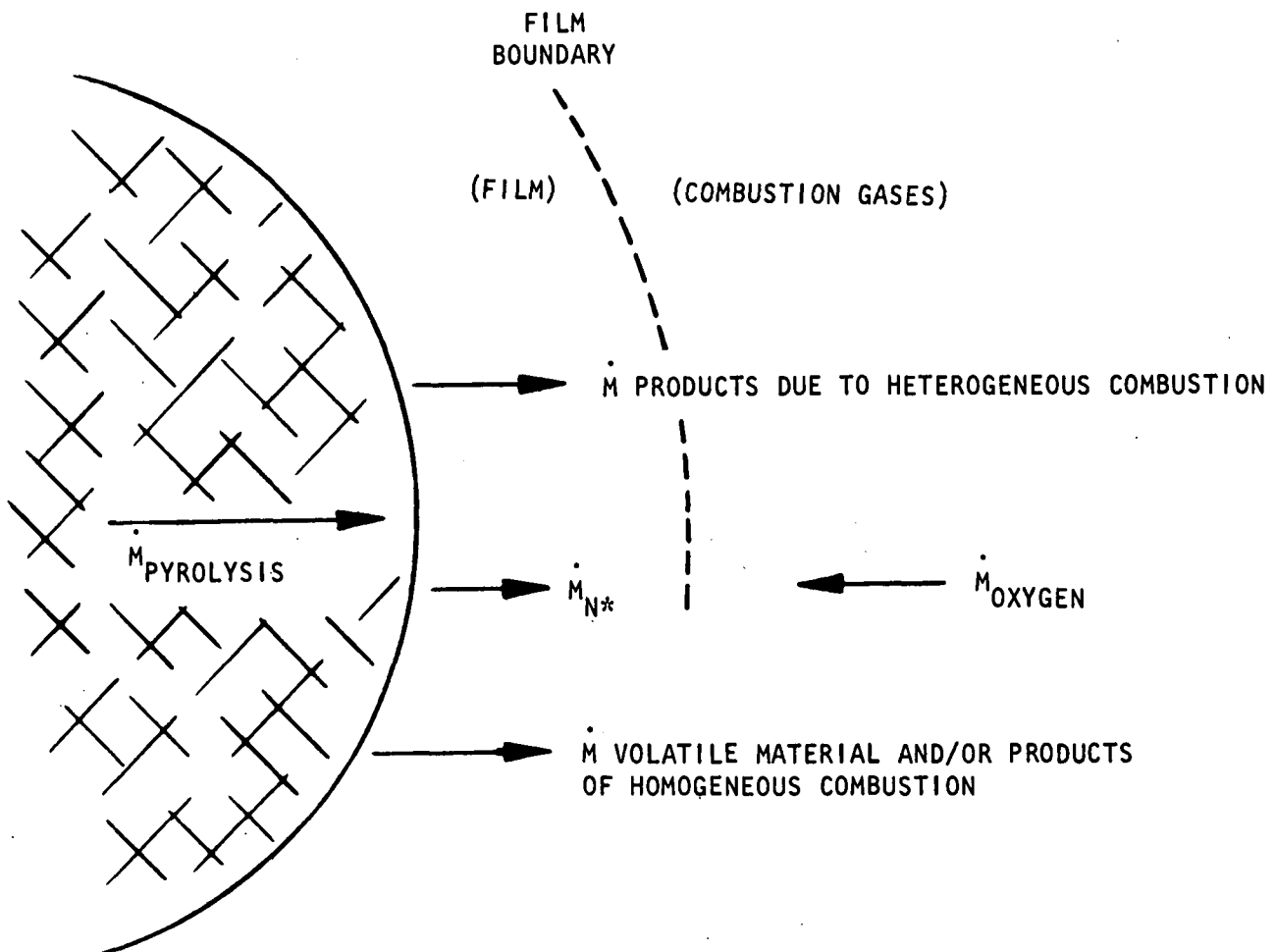


Figure 18. Schematic of Particle Burning Process

where δ_i is the density of the i th particle component based on total particle volume, and the particle energy equation:

$$\dot{Q}_s = \frac{4\pi}{3} r_s^3 \rho_p C_{p,p} \frac{dT_p}{dt} \quad (74)$$

(Heat transfer rate to the particle) (Rate change of particle temperature)

During the development and solution of the basic equations, the following assumptions were made:

1. The gas flow in the film surrounding the particle is spherically symmetric and the film thickness is related empirically to the particle Nusselt number.
2. Fick's law is presumed valid throughout, implying equal binary diffusion coefficients which are evaluated at mean film conditions.
3. The thermal conductivity and gaseous specific heats are constant and evaluated at mean film conditions.
4. Temperature and concentration gradients within the particle are ignored.
5. The gases are assumed to diffuse through the boundary layer (film) surrounding the particle without undergoing pyrolysis or combustion reactions.
6. The coal is specified as a mixture of coal and volatile material having different properties.
7. Particle temperature and composition varies with time.
8. The static pressure in the radial direction is constant.
9. Pore combustion is neglected but heterogeneous combustion of the coal at the particle surface is included. (This assumption has been modified under IR&D funding and the resulting coal model is presented in Appendix I.

Noting that the species molar flowrates are constant (application of the species continuity equation), the species diffusion equation is integrated between the particle surface and a general radial location to yield the mole fraction profile:

$$\ln \left[\frac{X_{i,t} \dot{N}_t - \dot{N}_i}{X_{i,s} \dot{N}_t - \dot{N}_i} \right] = \beta \left(\frac{Nu_m}{2} \right) \left(1 - \frac{r_s}{r} \right) \quad (75)$$

where

$$\beta \equiv \frac{\dot{N}_t}{4\pi r_s (c\bar{D})} \left(\frac{2}{Nu_m} \right) \quad (76)$$

and the molar flowrate of compound i is:

$$\dot{N}_i = \alpha'_{i,c} \dot{N}_c + \sum_{j=1}^{N_v} \alpha'_{i,j} \dot{N}_{v,j} \quad (77)$$

where $\alpha'_{i,c}$ is the stoichiometric coefficient of compound i for the heterogeneous reaction and $\alpha'_{i,j}$ is the stoichiometric coefficient of compound i for the products of combustion of the jth volatile material. The N_{vj} 's include all products of combustion and the volatile species. Therefore, the program has the option of reacting or not reacting the volatile material at the particle surface.

For a radius equal to the outer boundary of the film surrounding the particle, i.e.,

$$r = \frac{r_s}{1 - \frac{2}{Nu_m}} \quad (78)$$

the mole fraction of compound i at the particle surface is determined and is:

$$X_{i,s} = \frac{\dot{N}_i}{\dot{N}_t} + \left(X_{i,g} - \frac{\dot{N}_i}{\dot{N}_t} \right) e^{-\beta} \quad (79)$$

The particle heating rate is determined by integrating the film energy equation between the droplet surface and the free stream and is:

$$\dot{Q}_s = \dot{Q}_R + \dot{Q}_c + \sum_{i=1}^{n_t} \dot{Q}_{v_i} + \frac{\dot{N}_t C_{p_t} (T_g - T_s)}{(e^Z - 1)} \quad (80)$$

where

$$\begin{aligned} \dot{Q}_R &= \text{radiation heat transfer rate} \\ \dot{Q}_c &= \text{heat of combustion due to heterogeneous reactions} \\ \dot{Q}_{v_i} &= \text{heat of combustion due to volatile combustion} \\ \dot{N}_t C_{p_t} &= \sum_{i=1}^{n_t} C_{p_i} N_i \end{aligned} \quad (81)$$

$$Z = \frac{\dot{N}_t C_{p_t}}{2\pi r_s \bar{k} Nu_H} \quad (82)$$

and the outer boundary of the thermal film is determined by the empirical relationship:

$$r_{\delta_H} = \frac{r_s}{1 - \frac{2}{Nu_H}} \quad (83)$$

Quasi-steady-state film gas temperature profile is determined from the integrated energy equation and is given by:

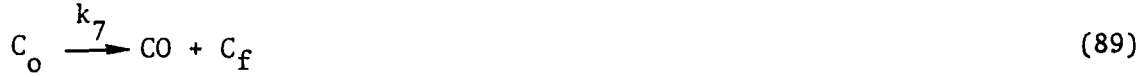
$$T = T_s + \frac{(T_g - T_s)}{(e^Z - 1)} \left\{ \exp \left[Z \left(\frac{Nu_H}{2} \right) \left(1 - \frac{r_s}{r} \right) \right] - 1 \right\} \quad (84)$$

To apply the preceding expressions in a computer model, the heterogenous surface reaction and devolatilization rates are required. The von Fredersdorff and Elliott (Ref. 115) approach to heterogeneous combustion at the particle surface is presently being used in the model. This involves a complex multistep

mechanism of gaseous adsorption, reaction, and desorption on the solid surface. In the process, different regions are assumed to exist simultaneously on the surface. Partial surface oxidation occurs at active sites (C_f) to form oxygen-occupied sites (C_o) according to the surface complex formation reactions:



a gasification reaction:



describes desorption of CO from the surface.

For steady state conditions:

$$\frac{d}{dt} (C_o) = \frac{d}{dt} (C_f) = 0 \quad (90)$$

and the reaction rate of carbon (n_c) is:

$$\begin{aligned} n_c & \left[\frac{k_1}{k_7} (O_2) + \frac{k_2}{k_7} (O) + \frac{k_3}{k_7} (CO_2) + \frac{k_4}{k_7} (CO) + \frac{k_5}{k_7} (H_2O) + \frac{k_6}{k_7} (H_2) + 1 \right] \\ & = (C_t) \left[k_1 (O_2) + k_2 (O) + k_3 (CO_2) + k_5 (H_2O) \right] \end{aligned} \quad (91)$$

where

$$(C_t) = (C_o) + (C_f) \quad (92)$$

Here, as in earlier models, the temperature-dependent surface reaction rates must be determined from experimental data. Equilibrium among oxidized carbon species and H_2 is assumed to take place in the gas phase, well away from the fuel surface.

The Howard and Essenhigh (Ref. 116) approach to devolatilization is employed in the combustion model. Pyrolysis rates for coal have been analyzed by several investigators (Ref. 116 and 117) and can be represented by:

$$\dot{N}_i = -\left(\frac{4\pi}{3} r_s^3\right) \frac{d\rho_i}{dt} = k_{o_i} \rho_i \left(\frac{4\pi}{3} r_s^3\right) \quad (93)$$

where

k_{o_i} = kinetic reaction rate of i th component

The k_{o_i} 's are temperature-dependent reaction rates which can be determined from experimental data.

The model described above accounts for heterogeneous combustion at the particle surface, devolatilization, particle temperature, and composition. A second-order implicit algorithm is used to solve the algebraic and differential equations that describe the heterogeneous reaction/devolatilization/particle composition process and the particle temperature. As part of the computer program output, descriptions are given for the heterogeneous reaction rate, devolatilization rates, the average film surrounding the particle, the particle temperature, composition, and radius from ignition to final burnout.

The main limitations of the model in predicting coal combustion are spherical symmetry, the exclusion of pore combustion, and the exclusion of chemical reactions in the film surrounding the particle.

Model Calculations

Life history calculations for burning coal particles have been made with this combustion model to compare its predictions with some available laboratory experimental data. Results of some of these calculations are presented in Fig. 19 through 21. Calculated particle composition histories are compared in these figures with experimental data from Ref. 116 (mass median particle radius for the experiments was 15 microns). Inspection of the initial time region of the volatile matter and fixed carbon content plots, (Fig. 19 and 20) suggest that during the first 0.05 second, volatile matter (Fig. 19) is evolved without heterogeneous combustion. This is suggested by the fact that no fixed carbon content is lost in the initial 0.05 second, while the volatile matter content drops about 5 percent during this time period. The heterogeneous combustion then begins and, thereafter, devolatilization proceeds simultaneously with surface combustion. Inspection of the slopes of the calculated curves in Fig. 21 suggests that volatile matter loss due to heterogeneous combustion contributes strongly to overall particle devolatilization. The increase in slope suggests that once the temperature of the particles becomes sufficiently high, both the principal devolatilization reactions and the heterogeneous combustion reactions are very fast and consequently, the loss of volatile matter by gaseous evolution is relatively faster than the fixed carbon loss due to heterogeneous combustion.

Inspection of Fig. 19 and 21 shows that after about 80 to 90 percent of the volatile matter is driven off (0.2 second), devolatilization becomes very slow and the remainder of the volatile material is simply burned off with fixed carbon by heterogeneous combustion. Examination of Fig. 20 reveals that, when compared with the data of Ref. 116, the reaction rate given by Ref. 118 appears to be too high and the reaction rate given by Ref. 119 is probably too low. However, since these calculations were performed using a monodisperse particle distribution, it is impossible at this time to determine from them the validity of: (1) the reaction rate, or (2) the fixed carbon model. The results do, however, lend confidence to the overall model approach in that they agree fairly well with the trends indicated by the coal particle combustion experiments.

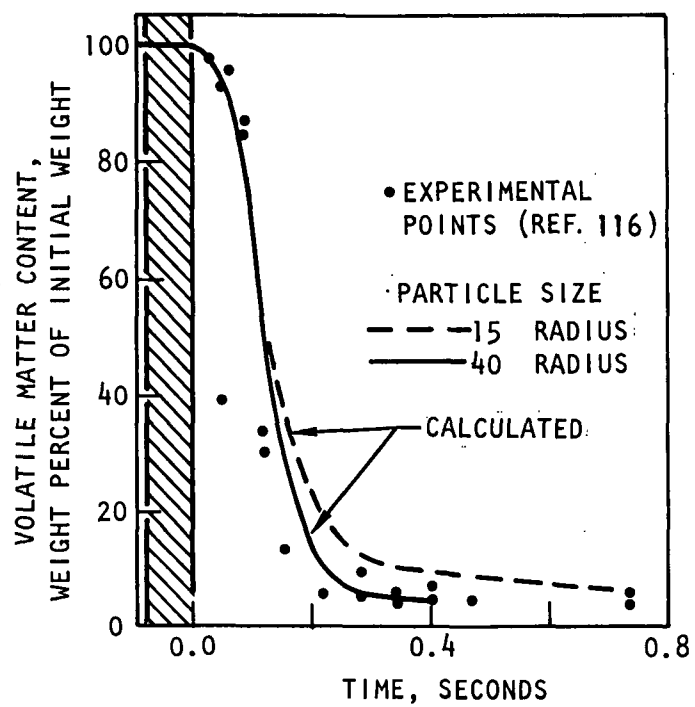


Figure 19. Volatile Matter Content

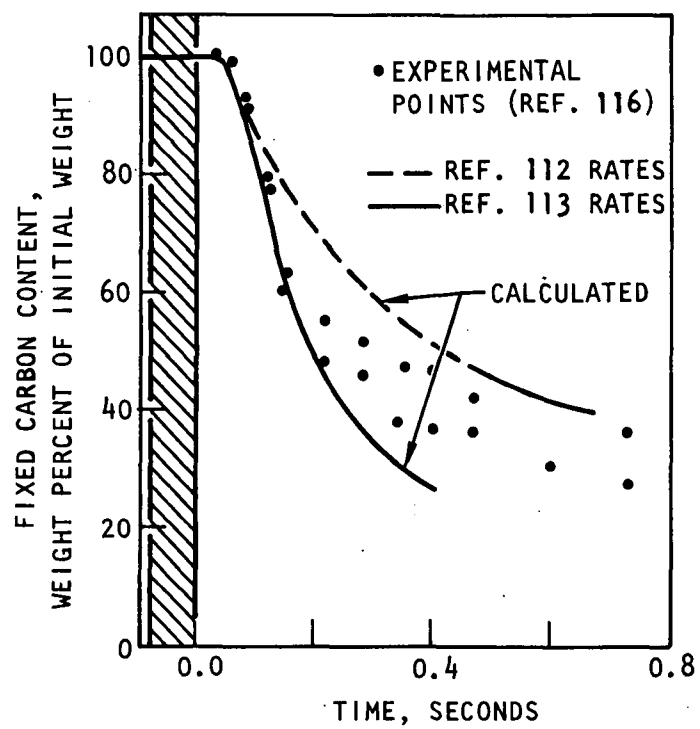


Figure 20. Fixed Carbon Content

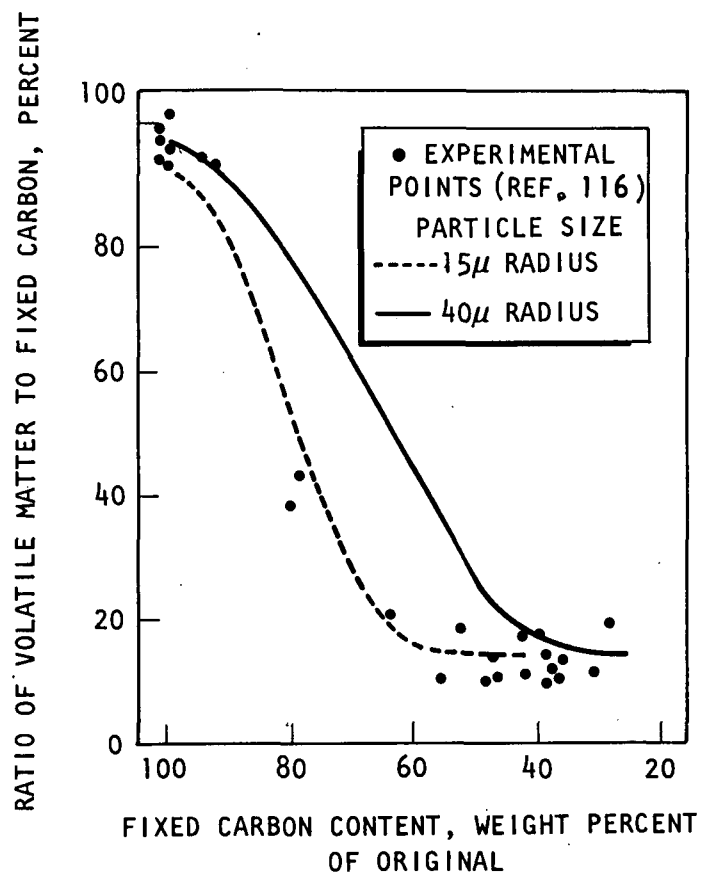


Figure 21. Variation of Composition of Solid Matter With Degree of Burnout

Kinetic/Diffusion Model

Description of Model. The model for the calculation of molar production rates and molar concentrations of all compounds in the film surrounding a droplet (particle) is depicted schematically in Fig. 22. Basic assumptions in the derivation of the model equations are: (1) spherical symmetry, and (2) the outer boundary of the film is determined by empirical Nusselt number correlation.

The basic equations solved are the species continuity equation:

$$\frac{1}{4\pi r^2} \frac{d\dot{N}_j}{dr} = \dot{R}_j \quad (94)$$

and the Stefan-Maxwell (diffusion) equation:

$$(4\pi r^2) (c\mathcal{D}_{j,m}) \frac{dX_j}{dr} = X_j \sum_{k=1}^{n_t} \dot{N}_k - \dot{N}_j \quad (95)$$

where

$$(c\mathcal{D}_{j,m}) \equiv \frac{\dot{N}_j - X_j \sum_k \dot{N}_k}{\sum_k \left(\frac{1}{c\mathcal{D}_{j,k}} \right) (X_k \dot{N}_j - X_j \dot{N}_k)} \quad (96)$$

This is similar to the diffusion equation used in the droplet vaporization and flame front models except nonequal binary diffusivities are employed.

The energy equation:

$$\frac{1}{4\pi r^2} \frac{d}{dr} \left[-4\pi r^2 k \frac{dT}{dr} + \sum_k \dot{N}_k H_k \right] = 0 \quad (97)$$

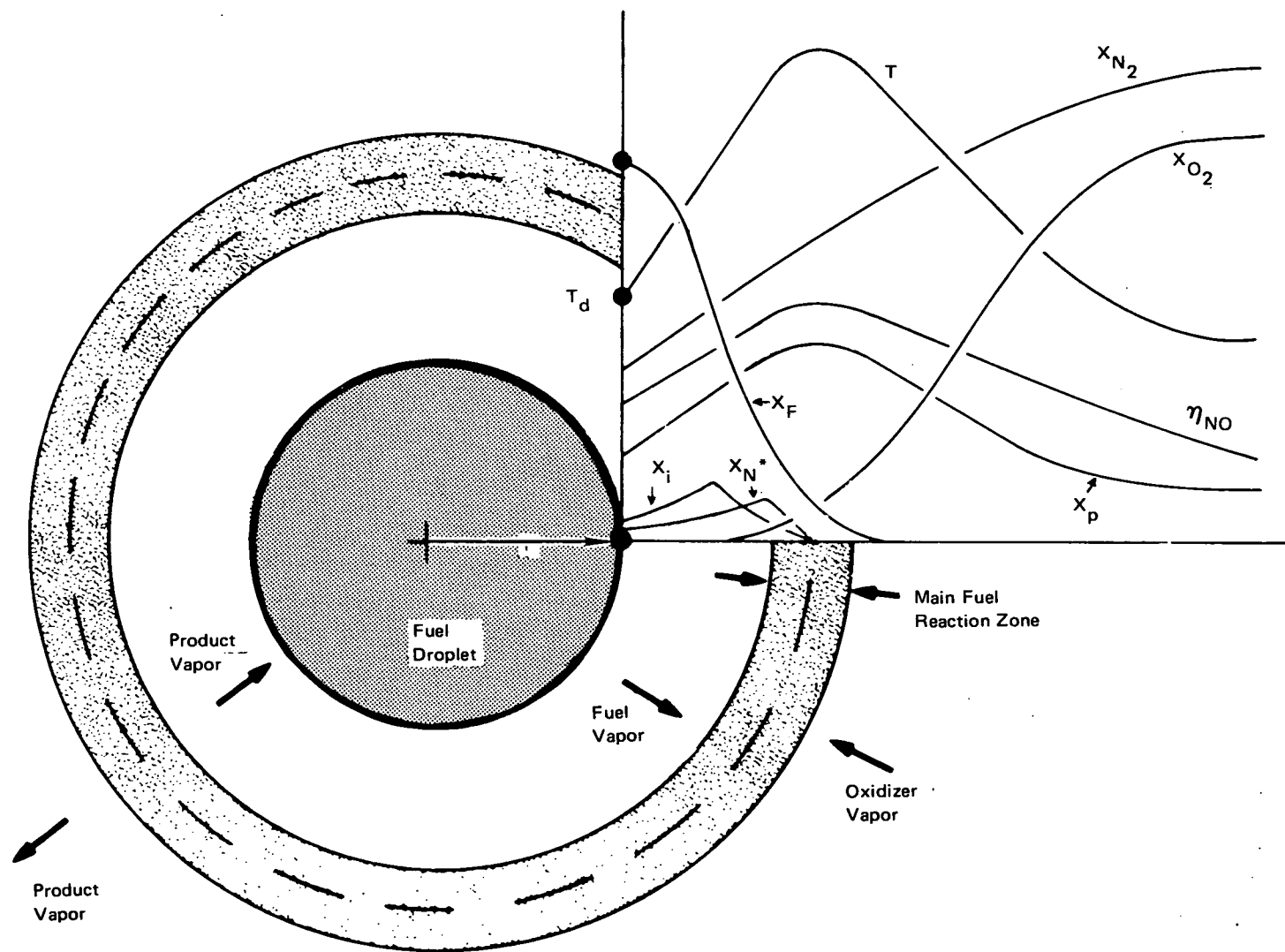


Figure 22. Kinetic/Diffusion Model

where

$$H_k = \int_{298^\circ K}^T C_{p_k} dT + \Delta H_{298_k}^O \quad (98)$$

For the general chemical reaction:



where $\check{v}_{j,i}$ and $\check{\check{v}}_{j,i}$ represent, respectively, the stoichiometric coefficients of the reactants and products for the i th reaction and the chemical species M_j , the forward reaction rate is:

$$k_{f_i} = B_i T^{\alpha_i} \exp \left[\frac{-\Delta E_i}{RT} \right] \quad (100)$$

and the reverse reaction rate is:

$$k_{b_i} = k_{f_i} / K_{c_i} \quad (101)$$

where B_i is the frequency factor, α_i is the temperature exponent, ΔE_i is the activation energy, and K_{c_i} is the equilibrium constant. The equilibrium constant is:

$$\ln K_{c_i} = -(\ln RT) \Delta n_i - \frac{\Delta H_i^O}{RT} + \frac{\Delta S_i^O}{R} \quad (102)$$

$$\Delta n_i \equiv \sum_{j=1}^{n_t} (\check{\check{v}}_{j,i} - \check{v}_{j,i}) \quad (103)$$

$$\Delta H_i^O \equiv \sum_{j=1}^{n_t} (\check{\check{v}}_{j,i} - \check{v}_{j,i}) H_{m_j}^O \quad (104)$$

$$\Delta S_i^0 \equiv \sum_{j=1}^{n_t} (v_{j,i}' - v_{j,i}) S_{m_j}^0 \quad (105)$$

where $H_{m_j}^0$ and $S_{m_j}^0$ are, respectively, the enthalpy and entropy of the chemical species m_j at 1 atmosphere.

Employing the preceding expressions, the total molar reaction rate for the j th species is given by:

$$\dot{R}_j = \sum_k^{n_R} (v_{j,k}' - v_{j,k}) \left[k_{f_k} (\bar{c})^{\bar{v}_k} \prod_{\ell} (cX_{\ell})^{v_{\ell,k}'} - k_{b_k} (\bar{c})^{\bar{v}_k} \prod_{\ell} (cX_{\ell})^{v_{\ell,k}} \right] \quad (106)$$

where \bar{v}_k is the third-body stoichiometric coefficient for the k th reaction.

At this time, it is convenient to express the preceding equations in a transformed coordinate system. This is done to aid in the numerical computational procedure. The transformed coordinate system is:

$$\xi \equiv \frac{Nu}{2} \left(1 - \frac{r_s}{r} \right) \quad (107)$$

since the outer boundary of the film is given by:

$$r_{\delta} = \frac{r_s}{1 - 2/Nu} \quad (108)$$

The transformed coordinate ξ varies from 0 to 1 for the domain of interest. Applying the preceding transformation to the basic equations yields the following set of transformed equations:

1. Species continuity equation:

$$\frac{d\dot{N}_j}{d\xi} = (4\pi r_s^3) \frac{2}{Nu} \frac{\dot{R}_j}{\left[1 - \left(\frac{2}{Nu} \right) \xi \right]^4} \quad (109)$$

2. Species diffusion equation:

$$(4\pi r_s) (c_{j,m}) \frac{dX_j}{d\xi} = X_j \sum_k \dot{N}_k - \dot{N}_j \quad (110)$$

3. Energy equation:

$$\begin{aligned} \left(\frac{dT}{d\xi} \right) \left[(4\pi r_s) k \left(\frac{Nu}{2} \right) \right] + \left(\frac{dT}{d\xi} \right) \left[(4\pi r_s) \left(\frac{Nu}{2} \right) \frac{dk}{d\xi} \right. \\ \left. - \sum_k \dot{N}_k C_{p_k} \right] - \sum_k H_k \frac{d\dot{N}_k}{d\xi} = 0 \end{aligned} \quad (111)$$

To numerically solve the preceding equations, the species continuity and diffusion equations are combined to yield the modified continuity equation:

$$\begin{aligned} \left(\frac{d^2 X_j}{d\xi^2} \right) \left[(4\pi r_s) (c_{j,m}) \left(\frac{Nu}{2} \right) \right] + \left(\frac{dX_j}{d\xi} \right) \left[(4\pi r_s) \left(\frac{Nu}{2} \right) \frac{d(c_{j,m})}{d\xi} - \sum_k \dot{N}_k \right] \\ - X_j \left[\frac{d}{d\xi} \left(\sum_k \dot{N}_k \right) \right] + (4\pi r_s^3) \left(\frac{2}{Nu} \right) \frac{\dot{R}_j}{\left[1 - \frac{2}{Nu} \xi \right]^4} = 0 \end{aligned} \quad (112)$$

The solution procedure presently employed by the kinetic/diffusion model to solve the preceding nonlinear equations consists of two second-order implicit algorithms. The first algorithm couples the modified continuity equations for the fuel compounds and the oxygen together with the energy equation to calculate the oxygen and fuel mole fraction profiles and the film temperature profile. For the other species, the second algorithm is used in a decoupled mode to calculate the mole fraction profiles employing the modified continuity equation. After all species mole fraction profiles have been updated, the program calculates molar flowrates based on the species continuity equation.

The kinetic/diffusion model includes the kinetics and diffusion of all compounds and intermediate species in the film surrounding a droplet or particle. Specifically, it accounts for finite-rate combustion of mixtures of hydrocarbon compounds, some of which may contain fuel nitrogen, and includes detailed kinetics and the production rates of fuel NO_x , thermal NO_x , and other pollutants and combustion products. The model input is structured such that quasi-global kinetics for hydrocarbons can be used if detailed rates are unavailable. The model solves simultaneously the energy equation, species continuity, and species diffusion equations using boundary conditions at the droplet (particle) surface, and the temperature and molar concentrations in the bulk gas stream.

Boundary conditions at the droplet (particle) surface can be obtained by executing the droplet vaporization, droplet flame front, or coal combustion models.

The main limitations of the kinetic/diffusion model is spherical symmetry and large computer execution times (i.e., $\sim 2\text{-}3$ min./calculation/number of axial locations). It is the main program for predicting pollutant formation rates in the film surrounding the droplet (particle).

Model Calculations. A limited number of preliminary calculations have been made using flame front model output data, selected fuel nitrogen compounds, and reaction rate data to input the kinetic/diffusion model. Using the reactions presented in Table 4, typical model calculations for a 40-micron droplet of No. 2 fuel oil indicated that the maximum production rate of thermal NO occurred on the oxygen-rich side close to the flame zone but that a substantial amount of NO was also produced on the fuel-rich side due to atomic oxygen and hydroxyl radical overshoot in addition to penetration of those species through the flame zone (Fig. 23). The calculated production rate of thermal NO under the conditions of Fig. 23 was only about 0.7 gram NO per kilogram fuel. This low value of thermal NO production rate was mainly controlled by the flame zone temperature which was 2080 K. The flame-zone temperature was lower than the equilibrium flame temperature due to conductive heat loss from the flame zone to the free stream. This heat loss was high because the flame zone is very close to the outer boundary of the gas film (boundary layer). It should be noted, again, that this model does not include continued production of thermal NO in the gas phase.

TABLE 4. HYDROCARBON AND THERMAL NO REACTIONS

1. $\text{CO} + \text{OH} = \text{CO}_2 + \text{H}$
2. $\text{O}_2 + \text{H}_2 = 2 \text{OH}$
3. $\text{OH} + \text{H}_2 = \text{H}_2\text{O} + \text{H}$
4. $\text{O}_2 + \text{H} = \text{OH} + \text{O}$
5. $\text{O} + \text{H}_2 = \text{OH} + \text{H}$
6. $\text{O} + \text{H}_2\text{O} = 2 \text{OH}$
7. $2 \text{H} + \text{M} = \text{H}_2 + \text{M}$
8. $2 \text{O} + \text{M} = \text{O}_2 + \text{M}$
9. $\text{O} + \text{H} + \text{M} = \text{OH} + \text{M}$
10. $\text{H} + \text{OH} + \text{M} = \text{H}_2\text{O} + \text{M}$
11. $\text{NO} + \text{M} = \text{N} + \text{O} + \text{M}$
12. $\text{N}_2 + \text{M} = 2\text{N} + \text{M}$
13. $\text{N}_2 + \text{O} = \text{NO} + \text{N}$
14. $\text{N} + \text{O}_2 = \text{NO} + \text{O}$
15. $\text{N} + \text{OH} = \text{NO} + \text{H}$
16. $\text{C}_n\text{H}_m + \left(\frac{n}{2} + \frac{m}{4}\right) \text{O}_2 \rightarrow n \text{CO} + \frac{m}{2} \text{H}_2\text{O}$

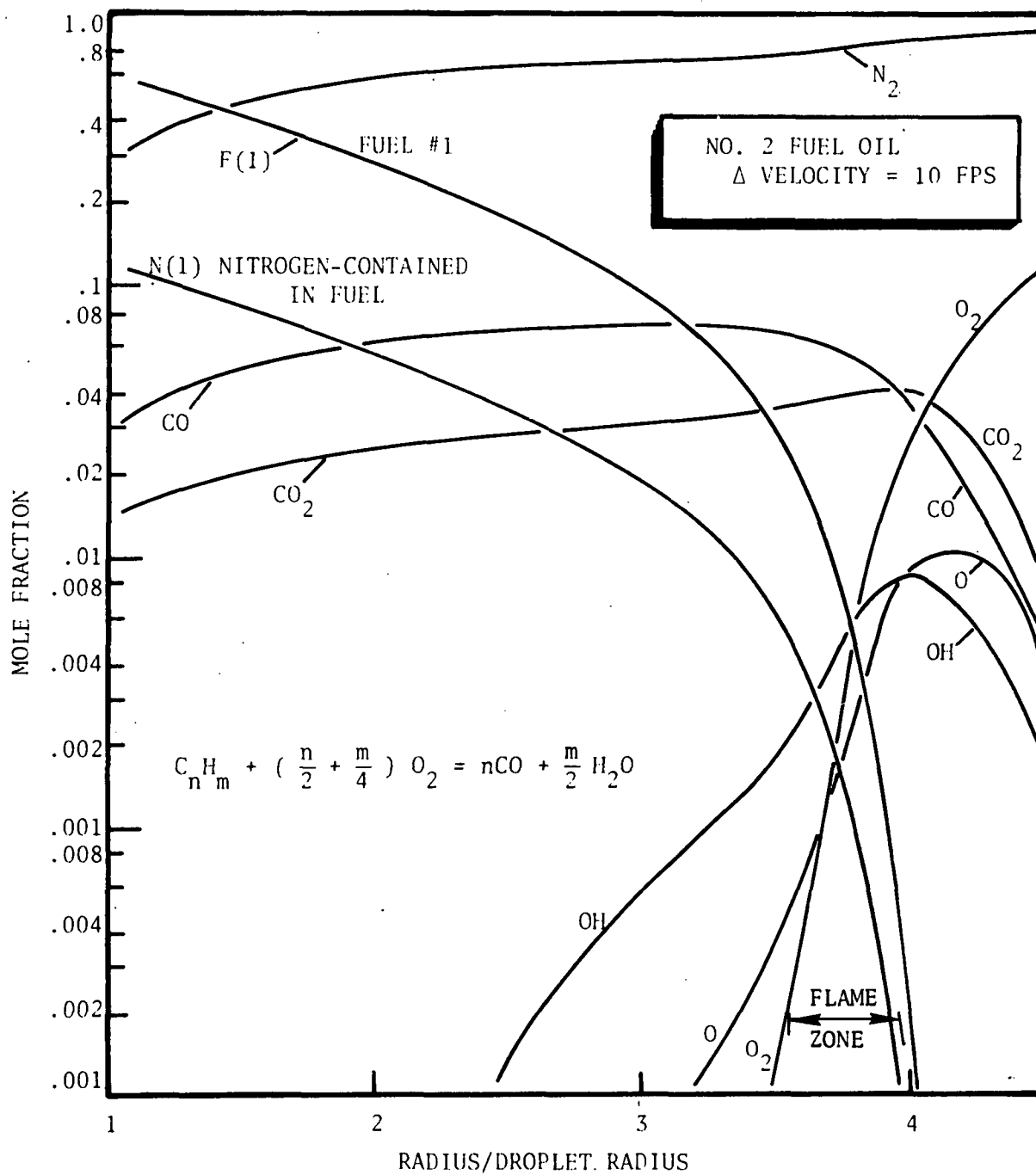


Figure 23. Preliminary Kinetic Diffusion Model Results
With Flame-Front Model Input

Fuel NO production rates were examined briefly by adding to the reactions in Table 4 the reactions listed in Table 5. The HCN path to fuel NO was included because nitrogen in some compounds can be converted almost completely to HCN during high-temperature, nonoxidative pyrolysis.

TABLE 5. REACTIONS FOR FUEL NITROGEN*

1.	$\text{HCN} + \text{M} = \text{CN} + \text{H} + \text{M}$
2.	$\text{HCN} + \text{O} = \text{OH} + \text{CN}$
3.	$\text{CN} + \text{O}_2 = \text{CO} + \text{NO}$
4.	$\text{CN} + \text{NO} = \text{CO} + \text{N}_2$
5.	$\text{CN} + \text{CN} = \text{C}_2 + \text{N}_2$
6.	$\text{HCN} + \text{H} = \text{H}_2 + \text{CN}$
7.	$\text{C}_{n'}\text{H}_{m'}\text{N}_{k'} = \text{C}_{(n'-k)}\text{H}_{(m'-k)} + k(\text{HCN})$
8.	$\text{C}_{n'}\text{H}_{m'}\text{N}_{k'} + \left(\frac{n'}{2} + \frac{m'}{4}\right) \text{O}_2 = n' \text{CO} + \frac{m'}{2} \text{H}_2\text{O} + \frac{k}{2} \text{N}_2$

With the Table 4 and 5 reactions and a vaporizing fuel mixture containing 1-percent (by mass) nitrogen, the calculated fuel NO production rate was approximately 7.4 grams NO per kilogram fuel. That corresponded to a fuel nitrogen to NO conversion efficiency of approximately 34 percent for the fuel grade No. 2 droplet.

These preliminary analysis results are indicative of the capabilities which the kinetic/diffusion model offers to a more complete pollutant production analysis.

*As discussed previously, these fuel-N reactions were used to test the operability of the model. Other reaction schemes will be included as they are shown to be important. A more plausible mechanism for fuel NO formation is proposed in the Phase II discussion of the burner results.

PHASE IB - FUEL AND MODEL COMPOUND DECOMPOSITION STUDIES

INTRODUCTION

Laboratory and field studies have been conducted to investigate conditions for the conversion of nitrogen compounds to NO_x during combustion. Prior to this contract, only a limited amount of effort had been expended, however, in investigating the pyrolysis of fossil fuels and nitrogen compounds under inert or oxidative conditions representative of the initial stages of combustion. The previous pyrolysis studies (e.g., Ref. 92) did not attempt to determine the major nitrogen-containing species that were formed.

The objective of this task was to conduct thermal decomposition studies at elevated temperatures to investigate the fate of nitrogen bound in fossil fuels (fuel-N) under conditions relevant to those existing in the initial phases of the combustion process. Pyrolysis experiments were conducted with model fuel-nitrogen compounds to measure the kinetic parameters that determine under what conditions (i.e., at what point in the flame) typical fuel nitrogen structures will decompose, and to identify the nitrogen-containing species that are formed. Later in the program, fuel oils and coals were pyrolyzed under conditions similar to those employed with the model compounds. The rationale for employing model compounds in part of the study was that the nitrogen exists in so many forms and molecular weight distributions in fossil fuels that the identification and direct study of actual fuel nitrogen compounds would not be feasible. However, it has been established that most fuel nitrogen exists in heterocyclic ring and nitrile structures.

As representative of compounds having these structures, the model compounds pyridine, quinoline, pyrrole, and benzonitrile were chosen for study. These lower

molecular weight analogs of the actual fuel nitrogen compounds have sufficient volatility to allow them to be pyrolyzed in the vapor phase. The side groups present in the natural fuel nitrogen compounds may decompose at much lower temperatures than the very thermally stable heterocyclic ring structures. However, it is this final step in the pyrolysis process (i.e., the scission of the heterocyclic ring) that should determine the fate of the fuel nitrogen as to whether the intermediate species that are formed will eventually result in the formation of CN, NH_x , or N_2 . The distribution of the fuel nitrogen among species of this type could determine the fraction of fuel nitrogen that is converted to NO_x in combustion. Burner studies (e.g., Phase IIA of this report) have indicated that HCN, $(\text{CN})_2$, and NH_3 all form NO readily in hydrocarbon combustion. Therefore, it was of particular interest whether conditions could be found that would promote the direct formation of N_2 in the initial pyrolysis process.

After the major features of model compound pyrolysis had been established, fuel oils and coals were pyrolyzed under similar inert pyrolysis conditions, and the nitrogen-containing inorganic products were measured and compared with those formed from the model compounds. In a fuel matrix consisting of mainly high boiling hydrocarbons, a nitrogen compound could undergo a different mode of pyrolysis because of chemical interactions and/or changes in its temperature-time profile. Also, whether the compound decomposes in the vapor or liquid phase will depend on its volatility and thermal stability.

Even though the N-heterocyclic compounds, in general, have good thermal stability, the thermal stability of individual compounds will vary over a wide range. Compounds which have long side chains will usually start to decompose at lower temperatures than unsubstituted heterocyclics. Depending on the point of bond cleavage, volatile or nonvolatile compounds may be formed which may or may not contain nitrogen. Thus, a study of the pyrolysis of fuel compounds can be quite complex.

Because of the host of possible volatile organic compounds that might be evolved from fuel pyrolysis, emphasis in the fuel experiments was placed on the measurement of

the inorganic nitrogen-containing decomposition products under conditions where most of the organic species would have decomposed. The organic pyrolysis products were determined, however, for the model compounds. The material which emerged as the principal volatile nitrogen-containing degradation product from model compounds, fuel oils, and coals was HCN.

Inert pyrolysis was emphasized in this initial pyrolysis study for two reasons: (1) in the case of heterogeneous droplet and particle combustion, the nitrogen species could undergo decomposition before they have approached close enough to the flame front for significant oxygen to be present; and (2) secondary processes may occur in the presence of oxygen that could mask the nature of the initial nitrogen-containing pyrolysis products that are formed.

PHASE IB: EXPERIMENTAL

A schematic diagram is shown in Fig. 24 of the experimental system used in the pyrolysis studies. Flow techniques were employed because this permitted the reaction times of volatile species to be kept quite small and facilitated the quenching and analysis of the pyrolysis products (e.g., by flowing through a bubbler to remove HCN or NH₃ or into a gas chromatograph to measure N₂ or various organic pyrolysis products). Therefore, the solid arrows in Fig. 24 represent the flow of helium carrier gas streams. During oxidative pyrolysis experiments (conducted with model compounds only) and reactor burn out, the carrier gas contained up to 20 percent oxygen. A description of the various test procedures and analytical methods follow.

Pyrolysis Samples

All of the model compounds were purchased from commercial sources, and were used as received. Petroleum samples were supplied to the program by the EPA, Gulf Research and Development Co., Bureau of Mines-Laramie Energy Research Center, CONOCO Oil Co., and Ultrasystems Inc. Coal and coke samples were supplied by the EPA, the International Flame Research Foundation, Bureau of Mines, Bruceton, Pa., and Babcock and Wilcox Co. The coal samples were ground before use. The fuel samples used are described in Table 6 and their reported analyses listed.

TABLE 6. FUEL SAMPLES

Fuel Type	Supplier	Crude Source	Analyses, percent	
			N	S
No. 6 Fuel Oil	Gulf	Venezuela	0.43	2.3
No. 6 Fuel Oil	Gulf	Various Crudes	0.44	0.73
No. 6 Fuel Oil	Gulf	Mainly California Crudes	1.41	1.63
No. 6 Fuel Oil	CONOCO	--	0.3	0.66
No. 6 Fuel Oil	EPA	--	0.22	0.9
No. 6 Fuel Oil	Ultrasystems	--	0.38	0.33
Wilmington Crude	Bureau of Mines, Laramie, Wyoming	--	0.63	1.59
Coal	EPA		1.17	3.0
Coal	IFRF		1.8	--

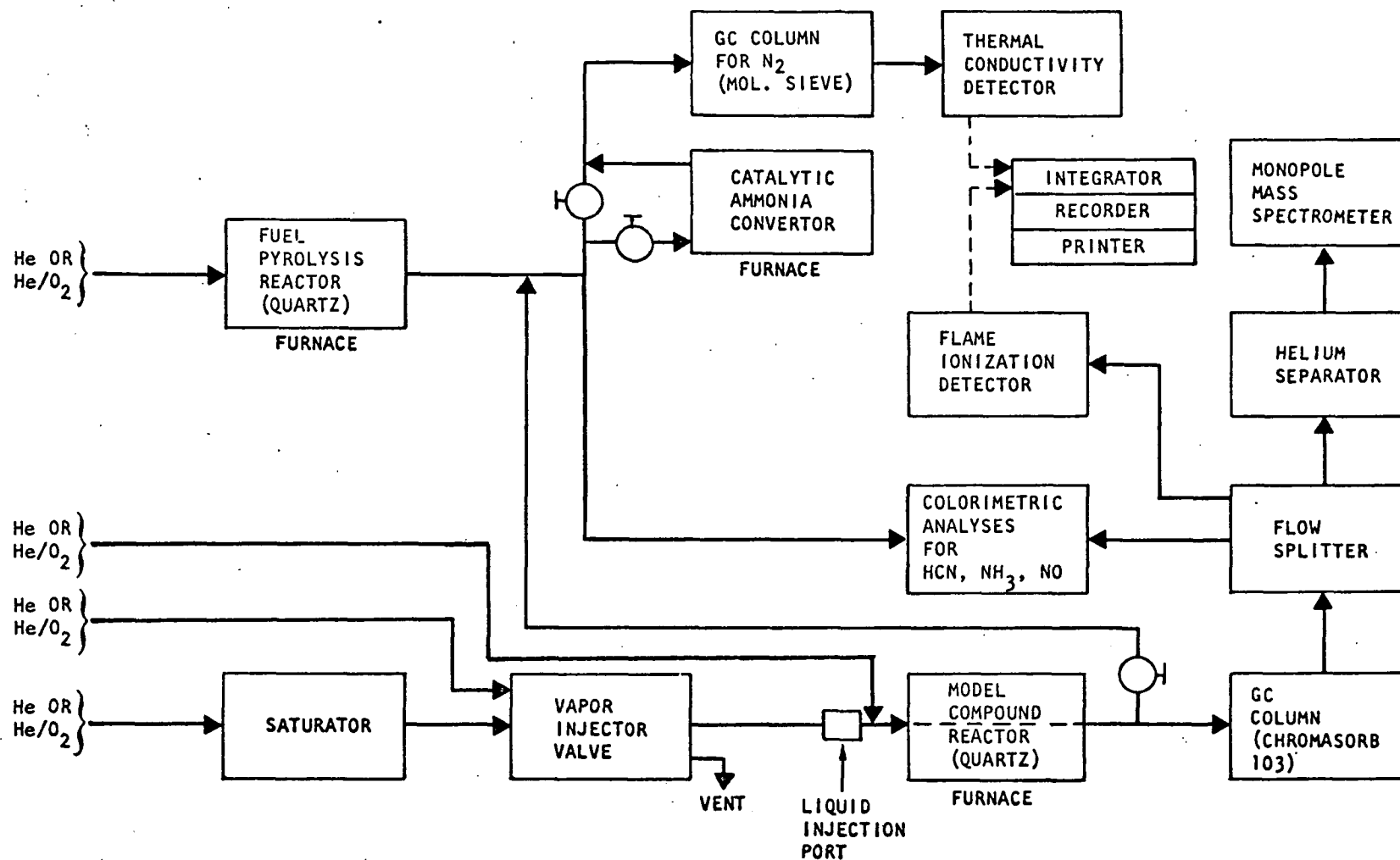


Figure 24. Schematic of Apparatus

Sample Measurement

The model compounds that were injected as liquids* were measured by means of 1-microliter Hamilton microsyringe (Model N7100). Calibration experiments established that 0.2- μ l samples (the size usually employed) were reproducible to better than ± 2 percent (usually ± 1 percent). The syringe (with tip up) was filled with sample contained in an inverted serum bottle. The plunger was pumped several times to expel any air and then drawn back to the 0.9- μ l mark. After removing the syringe from the serum bottle (still in a vertical position), the plunger was moved to the 0.2- μ l mark. The syringe was then inverted and the excess liquid removed from the exterior of the needle by wiping it against clean glass wool. There were indications that the use of a more absorbent material would draw some of the sample from the tip of the needle. The sample was immediately injected into the heated sample port. In a continuous series of experiments, the syringe was kept filled with sample between experiments and stored with the tip up and inserted through the septum of the inverted serum bottle. This prevented air bubbles from becoming trapped in the syringe.

The fuel oils, being more viscous than the model compounds, and the coal samples were weighed directly using a Mettler microbalance. The technique used for fuel oils was to dip a nichrome wire into the oil, weigh the wire and the drop of oil to the nearest μ g, and transfer the oil sample (1 to 2 mg) to the fuel reactor's sample holder (a quartz boat). The wire was reweighed and the sample's weight determined by difference. The EPA "in-house" No. 6 fuel oil was of such low viscosity that a larger diameter wire had to be used to hold a 1-mg drop.

In the case of the coal samples, an aluminum weighing pan that contained a V-shape piece of aluminum foil (holding several milligrams of the coal sample) and a nichrome wire was tared. The coal sample holder and wire were handled with forceps and a sample of the coal was transferred into the quartz boat with the boat positioned over the pan. This transfer was accomplished by scraping the coal into

*Measurement of samples introduced as vapor will be described later.

the boat with the nichrome wire. The quartz rod attached to the boat was gently vibrated by means of a file to remove any coal adhering to the outside of the boat. The pan, containing the foil, wire, and excess coal, was then reweighed and the amount of coal transferred was determined by the weight difference.

In general, coal samples ranging from 1.5 to 2 mg (weighed to the nearest μg) were used for the pyrolysis studies. To obtain a constant weight for the pan, it was necessary to wait about 15 minutes after transfer of the coal sample to the quartz boat. Since constant weight was immediately obtained when the aluminum pan and coal sample were initially weighed, the time required to obtain constant weight after transfer of the coal is attributed to static electricity and not, for example, to absorption of moisture from the atmosphere.

Apparatus and Procedures-Model Compound Pyrolysis

The model compound apparatus is shown schematically at the bottom of Fig. 24 and in two photographs (Fig. 25 and 26). The liquid model compound sample was vaporized in a helium carrier gas stream at an inlet system temperature of 160 C. The carrier gas then flowed through a 15-inch quartz reactor, with a nominal ID of 2 mm, that was heated at temperatures up to 1100 C in a temperature-controlled electric furnace. After passing through the pyrolysis reactor, the effluent gases were then analyzed for organic products by means of a gas chromatograph using a flame ionization detector. The analytical techniques used for analyses of the nitrogen-containing inorganic products are described in a subsequent section.

The furnace was 12 inches in length, with a quartz-to-metal graded seal attached at each end of the quartz reactor tube. Pt-Pt/Rh thermocouples were attached to the exterior of the reactor to measure the temperature and as sensors for the temperature controller.

The entire model compound flow system, from the sample injectors to the GC column, was constructed of 1/16-inch OD, stainless-steel tubing so that sharp GC peaks could be obtained. The number of T-connectors and valves was kept to a minimum

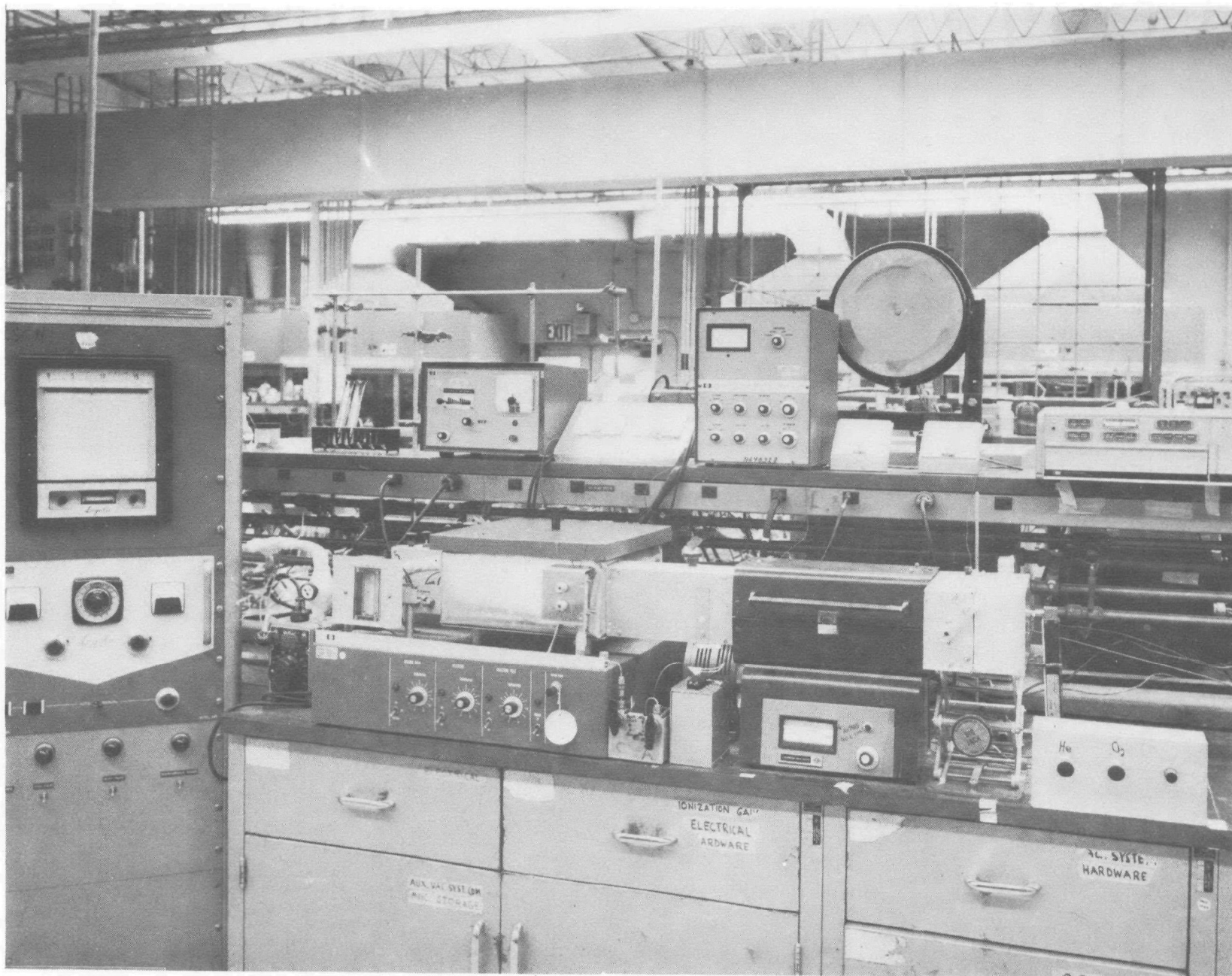
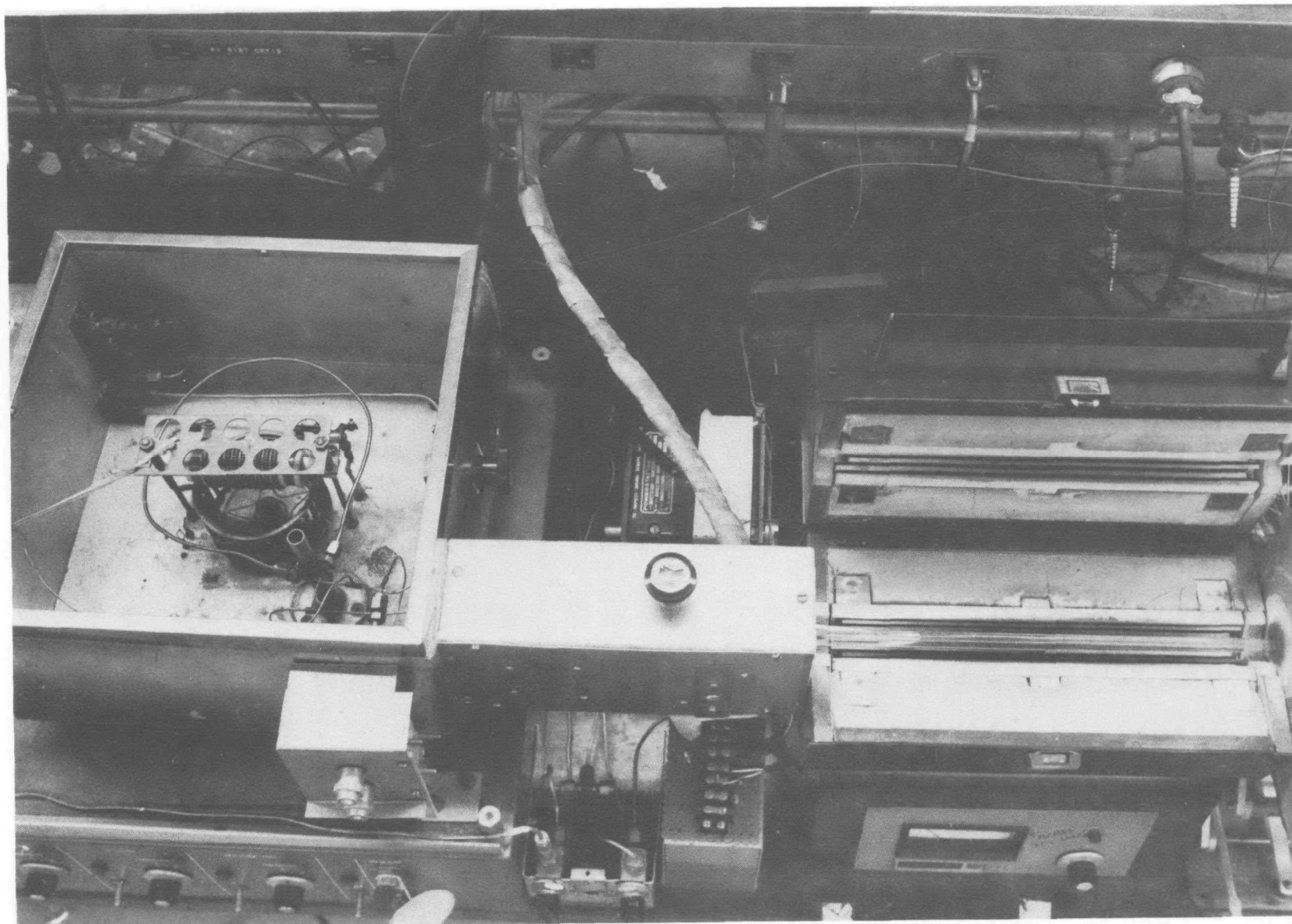


Figure 25. Model Compound Apparatus

5AA21-4/7/75-C1D



5AA21-4/7/75-C1A

Figure 26. Model Compound Apparatus (top view with furnace open and top removed from GC column oven)

for this same reason. The T's were made from drilled rods for minimum volume. The entire system was silver-soldered and small-volume bellows valves were used, giving a leak-free system. The system upstream of the reactor, including the sample injection devices, was contained in a small oven heated to 160 C. The downstream tubing and valves were heated to 180 C until the GC or chemical analysis train was reached.

Two-stage pressure regulators, set at 60 psig, were used to give constant carrier gas flowrates. The flowrates were held constant by the use of flow regulators, upstream of the sample injection ports, of the type that give flowrates independent of the downstream pressure. The pressure in the reactor, from 15 to 20 psig, was determined by the temperature of the GC column during sample injection (normally 60 C) and the carrier gas flowrate which was held at 43 cc/min, measured at room temperature and pressure, except in the first experimental series in which it was 50 cc/min. Calibrated gases containing 5- and 20-mole percent O₂ in helium were obtained from Matheson for use in the oxidative pyrolysis experiments and for reactor burnout between experiments.

Two methods were employed for vaporizing the model compound samples and introducing them into the carrier gas stream. The larger samples were introduced by the direct injection of a 0.2- μ l liquid sample into the heated carrier gas stream through a silicone rubber septum. This heated liquid sample injection port consisted of two concentric metal tubes with the inner tube ending about 1/8 inch from the septum. The septum seated against the outer tube which was threaded to hold the septum cap. The carrier gas flowed toward the septum in the outer tube and then down the center tube. During sample injection, the syringe needle was inserted about 2 inches into the center tube and the sample expelled. The center tube was packed with glass wool to wipe the sample drop from the needle and to ensure rapid vaporization of the sample. Sharp GC peaks were obtained even for the high-boiling liquid quinoline.

In some of the experimental series, pyridine was prevaporized and then introduced into the reactor carrier gas stream by use of a Caryle valve. In this "vapor

injection" technique, two loops of coiled stainless-steel tubing were attached to the Caryle valve, each having a nominal volume of 1 cc. Carrier gas (with or without oxygen) saturated with pyridine vapor at 0 C flowed through one loop (and was vented in a hood) and the reactor carrier gas stream flowed through the other. When the loops were suddenly interchanged by turning the Caryle valve, in which a spring-loaded teflon plate slides against a polished metal plate, a 1-cc slug of carrier gas containing pyridine was introduced into the reactor carrier gas stream.

In the model compound pyrolysis experiments, the carrier gas flowed continually either through the GC column, which was held at 60 C, or to the analysis train through a needle valve to give the normal backpressure in the reactor of 17 psig. In the experiments in which the GC was used, all or part of the carrier gas stream would flow to a H_2-O_2 flame ionization detector. A measured fraction of the stream could be directed to a monopole mass spectrometer for peak identification or to an analysis train (bubbler). One minute after sample injection, temperature programming of the GC column was initiated. The peaks were plotted on a recorder and the peak areas were measured and printed by use of an automatic integrator. The reactor was "burned out" after each experiment with an O_2 -helium mixture that was vented and the GC column was back flushed.

In the oxidative pyrolysis experiments, two helium carrier gas streams were used. With liquid sample injection, each stream flowed at 20 cc/min and they merged at a point between the sample introduction port and the inlet to the reactor. This was to ensure intimate mixing of O_2 with the sample. The stream introduced downstream of the port contained either 5- or 20-percent O_2 . Thus, the O_2 concentration at the reactor entrance was either 2.5- or 10-mole percent. In the vapor sample oxidative pyrolysis experiments, the stream saturated with the pyridine vapor and the carrier gas stream each contained 5-percent oxygen. In the oxidative pyrolysis experiments, the carrier gas was switched back to helium 15 seconds after sample injection so that the GC column would not be exposed to O_2 during temperature programming.

Apparatus and Procedures-Fuels Pyrolysis

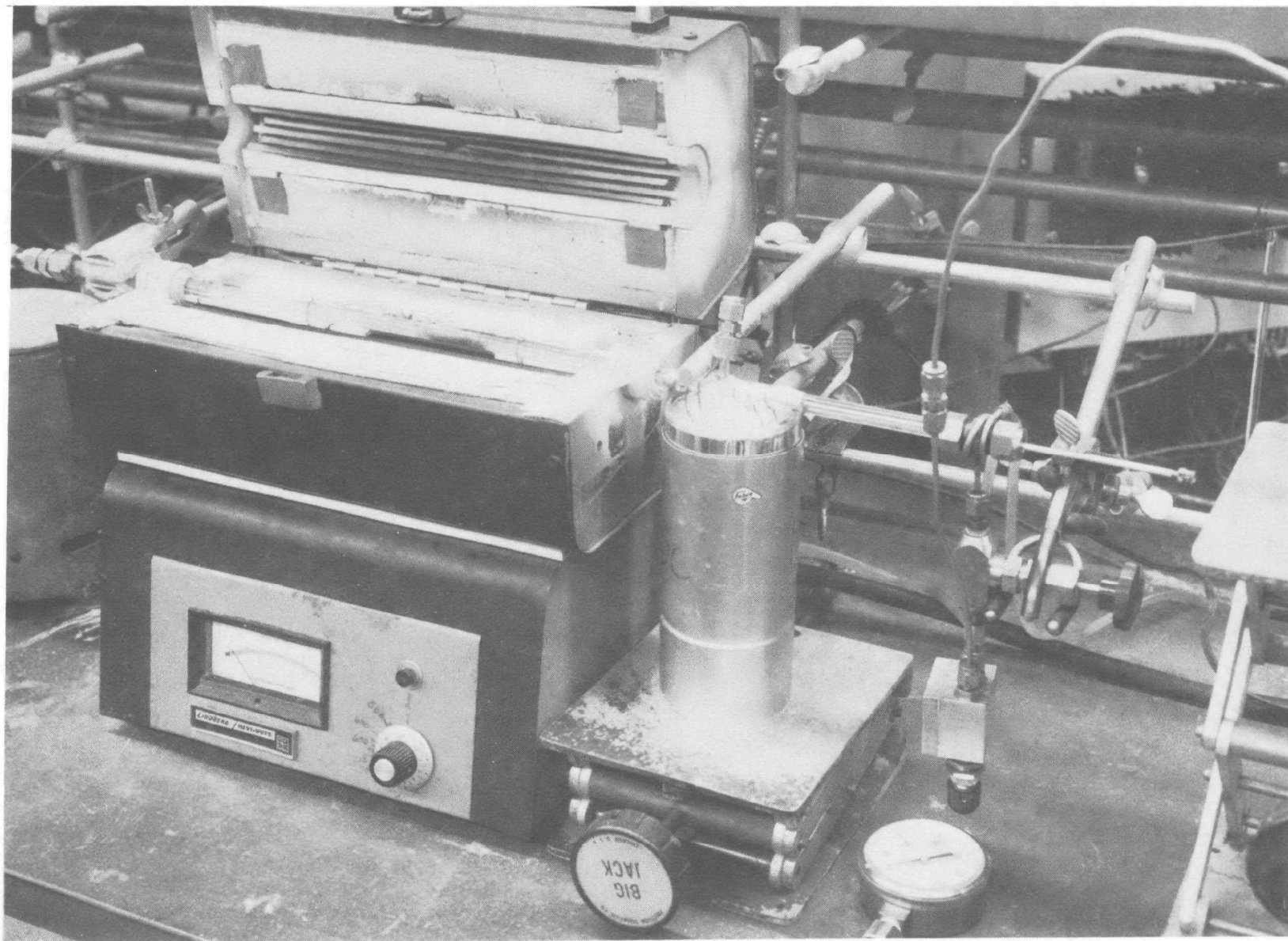
The main component of the fuel pyrolysis reactor (Fig. 27) consisted of a temperature controlled, electrically heated, capillary quartz tube reactor into which a sample of the fuel to be pyrolyzed was inserted. Pt-Pt/Rh thermocouples were used as a sensor for the controller and measurement of the temperature in the pyrolysis zone. The reported temperature was measured at the exterior of the tube at the position of the quartz boat during pyrolysis. As this is about 2 inches from the center of the furnace, the pyrolysis temperature is nearly the same as the maximum temperature at the center of the furnace (see Fig.28 for the temperature profile in this type of furnace). The sample insertion device consisted of a quartz boat attached to a quartz rod which, in turn, was attached, by means of a loop, to a stainless-steel rod. The overall length of the insertion device allowed the insertion of the boat into a 2-cc bulb blown into the quartz tube reactor.* The lightly greased metal rod of the insertion device ran through a rubber septum which was placed inside an AN fitting. This provided a gas-tight connection with the quartz tube reactor.

After a sample of the fuel had been weighed into the quartz boat, the insertion device was attached to the quartz tube reactor with helium flowing. The boat was only partially inserted into the quartz tube, outside the heated zone, and the exterior of the tube was cooled with liquid nitrogen to prevent any of the sample from being heated by radiation. The system was flushed with helium for about 10 minutes to purge any oxygen remaining in the system before pyrolysis of the sample was initiated.**

The fuel oil sample was then inserted very rapidly into the heated zone of the pyrolysis reactor to the stop position. The pyrolysis products were entrained in the helium stream and removed from the reactor. Analyses of the products from the pyrolyses are discussed in a subsequent section.

*This bulb can be seen as a dark zone in the photo in Fig. 27 because a coal residue had not yet been burned out.

**No oxidative pyrolysis experiments were conducted in the fuel reactor.



5AA21-4/7/75-C1B

Figure 27. Fuel Pyrolysis Reactor

The carrier gas flowrate in the fuel reactor was 20 cc/min and the pressure was ambient in the experiments that were designed to measure the amount of HCN formed.* In the experiments in which $N_2 + NH_3$ were measured, the GC required a backpressure of 12 psig. The flowrate was 40 cc/min in these experiments, giving similar residence times.

A glass wool plug was inserted in a metal fitting at the downstream end of the quartz reactor to trap any carbon particles that were present in the reactor product stream. After each fuel experiment, the reactor was burned out and the downstream tubing was rinsed with benzene to remove any tars that had condensed.** The quartz boat was cleaned in concentrated HCl and HNO_3 to remove traces of organic matter and metallic ash. In the coal experiments, the reactor and boat had to be lightly etched with HF solution after every few experiments to remove the residue and ash.

Temperature-programmed gas chromatography was used to identify and measure the major organic products from model compound pyrolysis. A number of special analytical methods were used to investigate the amounts of inorganic nitrogen products that were formed during the inert and oxidative pyrolysis of model compounds, fuel oils, and coal. These are described in Appendix A.

*It was demonstrated that the amount of HCN formed was not a strong function of flowrate.

**The first benzene passed through the tubing after each experiment came out slightly discolored.

RESULTS AND DISCUSSION - MODEL COMPOUND PYROLYSIS

The model compounds pyridine, quinoline, benzonitrile, and pyrrole were selected as representative of the types of nitrogen present in fuels. These nitrogen compounds were pyrolyzed in helium over the temperature range of 850 to 1100 C. The decomposition rates, the nitrogen-containing inorganic products, and the major organic products were measured. The oxidative pyrolysis of pyridine and benzonitrile was also investigated in mixtures of helium and oxygen.

The pyrolysis reactions were studied in a quartz reactor* with an ID of about 2 mm, a volume of 1 cc, and a nominal residence time of 1/2 second. The details of the apparatus and the experimental procedures are given in the Experimental section. The volatile pyrolysis products were removed from the reactor by a carrier gas which was helium. In the oxidative pyrolysis studies, a helium-oxygen mixture was used as the carrier gas. In most of the experiments, a liquid sample of the model compound (0.2 microliter) was injected into the carrier gas stream at 160 C, and vaporized before the gas entered the high-temperature zone of the reactor. These will be referred to as liquid samples, but it should be noted that the reactant is in the vapor state and well mixed with carrier gas before decomposition is initiated. A vapor injector was used in some of the pyridine experiments in which approximately 1 cc of carrier gas saturated with pyridine was suddenly introduced (by use of a Carle valve) into the carrier gas stream that flowed through the reactor. The only real experimental difference between the two sample injection techniques was that the liquid sample injection technique gave a greater model compound concentration (mole fraction of 0.03 versus ~ 0.003).

*A stainless-steel reactor was tested initially but it was found to decompose both HCN and NH_3 , preventing identification and measurement of these potential products.

The organic products from model compound pyrolysis were measured by temperature-programmed gas chromatography (GC) employing flame ionization detection. The pressure in the reactor, 16 to 20 psig, was controlled by the pressure drop in the GC column and the flowrate. The inorganic products NH_3 , N_2 , and HCN were measured by a combination of wet chemical and gas chromatographic techniques. Between experiments, the reactor was burned out to remove any carbonaceous residue that formed on the quartz wall and the GC column was backflushed to prevent high-molecular weight products from eluting during later experiments.

Decomposition Rates as a Function of Temperature

Pyrolysis experiments were conducted at temperature intervals of about 25 degrees and the GC peak areas were used to determine the fraction of the reactant that passed through the reactor undecomposed.

Measurements indicated that the reactor temperature was constant over the center 4 inches of the 12-inch furnace and then fell gradually to about 90 percent of the center temperature (expressed in degrees C) at a distance of 1 inch from each end of the furnace. Therefore, the assigned reactor wall temperature profile listed in Table 7 and plotted in Fig. 28 (for 1000 C) was used in calculating kinetic parameters from the model compound pyrolysis data.

TABLE 7. ASSIGNED WALL TEMPERATURE PROFILE FOR MODEL COMPOUND REACTOR
(Furnace Length = 12 Inches)

Distance From Center, inches	Percent of T_{max} , C
0 to 2	100.0
2.5	99.8
3.0	99.5
3.5	99.0
4.0	98.0
4.5	96.0
5.0	90.0
5 to 7	*

*At the ends of the furnace, the wall temperature was assumed to decrease linearly from 90 percent of T_{max} at a point 1 inch inside the furnace (5 inches from the center) to 160 C at a point 1 inch outside the furnace. Virtually no reaction occurs in this portion of the reactor.

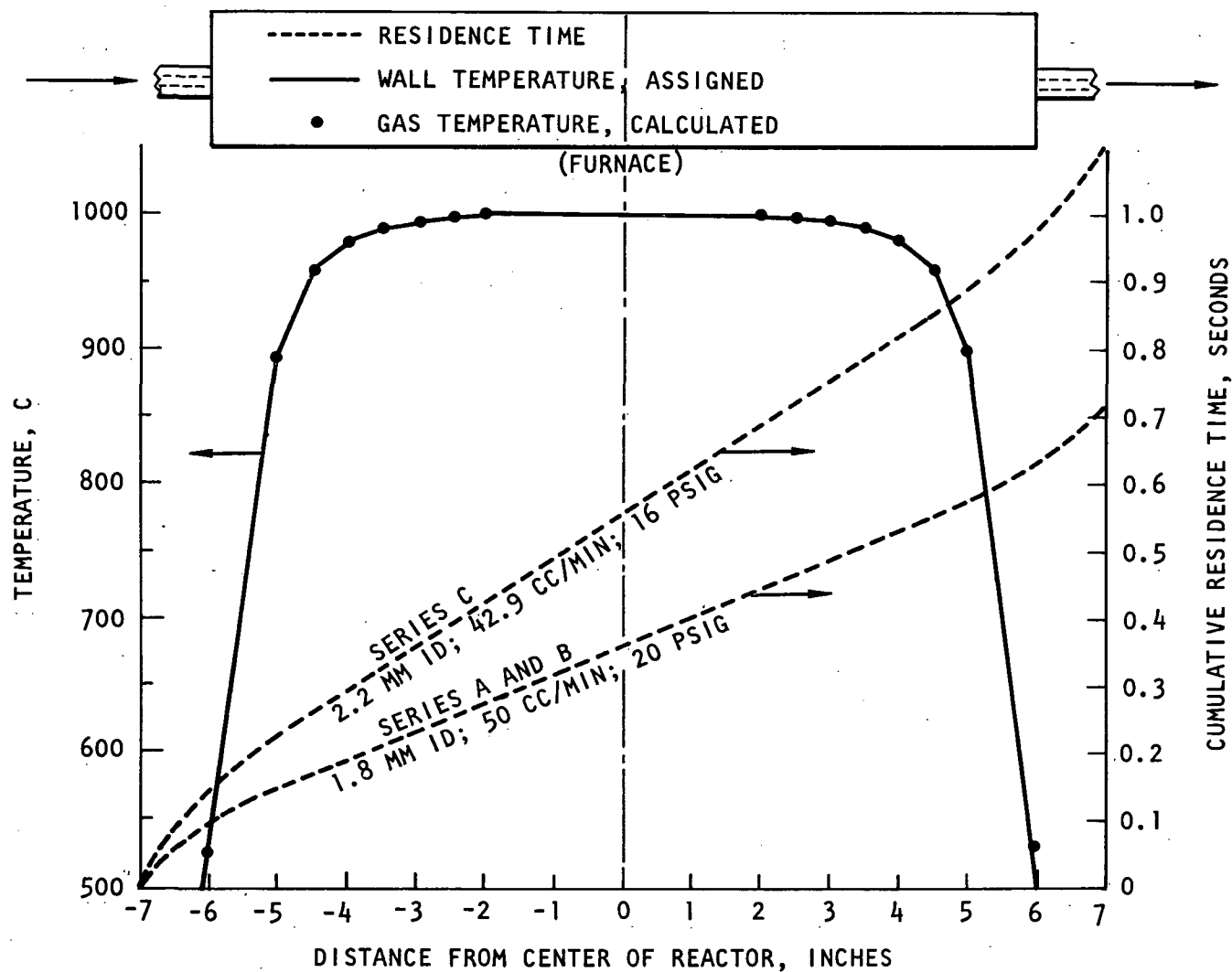


Figure 28. Model Compound Reactor, Temperature Profile, and Residence Time

The linear flow velocity (at 1000 C) was 23 inches/sec in the series A and B experiments and 15 inches/sec under the conditions in series C. At these flowrates, the flow is laminar, with $Nu = 4$, and the rate of change of the gas temperature is given by:

$$\frac{dT_G}{dx} = 9.8 \times 10^{-8} \times \frac{(MW)^{0.5} (T_G)^{0.6}}{F} \times (T_W - T_G) \quad (113)$$

where MW is the molecular weight (which was taken as 4 since the gas is nearly all helium), F is the mass flowrate in lb/sec, T_G is the gas temperature in degrees R, and T_W the wall temperature. Equation 113 was integrated, along with the reaction rate, with the computer program that was written to reduce the pyrolysis data. The calculated gas temperature follows the wall temperature within a fraction of a degree (as shown in Fig. 28), indicating that gas temperature lag is not a problem in the small-diameter reactors used in these experiments.

This can be shown directly from Eq. 113 as follows. The mass flowrate (in the series C experiments) is 3×10^{-7} lb/sec. At temperatures near 1000 C, Eq. 113 becomes:

$$\frac{dT_G}{dx} \cdot \frac{1}{(T_W - T_G)} = \frac{d\Delta T}{dx} \cdot \frac{1}{\Delta T} = 79 \text{ inch}^{-1} \quad (114)$$

Integration of Eq. 114 gives a characteristic distance, $D_{1/2}$, for the reduction of ΔT to one-half its initial value:

$$D_{1/2} = (\ln 2)/79 = 0.009 \text{ inch} \quad (115)$$

Also shown in Fig. 28 is the cumulative residence time (at 1000 C) calculated by integrating the gas flowrate through the reactor.

Liquid Sample Injection. The experimental decomposition curves obtained for the model compounds (in helium) are compared in Fig. 1 (presented in the report summary). Pyridine and pyrrole gave similarly shaped curves with slopes that remained steep until beyond 95-percent decomposition. The pyrrole is less stable than pyridine, the curves being separated by about 60 degrees. Quinoline gave a decomposition curve that was nearly linear with temperature. Quinoline is less stable than all of the other compounds below 910 C, but is more stable than pyrrole above that temperature. Benzonitrile is unusual in that its decomposition curve remains steep up to about 960 C and then tails out at high temperatures. In fact, 3 percent remained undecomposed even at a temperature of 1100 C. Thus, below 1010 C, pyridine is more stable under these conditions than benzonitrile while, above 1010 C, the reverse is true.

Calculation of Pyridine Kinetic Parameters. The experiments in which the extent of pyridine decomposition (in helium) was measured using liquid sample injection, are listed in Table 8 and these data are plotted in Fig. 29. In the series A and B liquid injection experiments, the helium flowrate was 50 cc/min (measured at room temperature and pressure), the reactor ID was 1.8 mm, and the pressure was 20 psig. In the series C liquid injection experiments, the residence time was longer because the reactor ID was 2.2 mm and the flowrate was 42.9 cc/min. The longer residence led to larger extents of decomposition in the series C experiments (Fig. 29), but it will be seen that the same rate expression is obtained. The pressure was 16 psig at this lower flowrate. As described in a footnote in Table 8, the decomposition rate would finally increase if sufficient carbonaceous residue were allowed to build up on the wall of the reactor.

TABLE 8. EXPERIMENTAL DATA ON RATE OF PYRIDINE DECOMPOSITION
IN HELIUM (LIQUID SAMPLE* INJECTION)

Series A (20 psig; 50 cc/min; 1.8 mm ID; $X_O \approx 0.030$):					
Experiment Number**	Temperature, C	Percent Undecomposed	Experiment Number	Temperature, C	Percent Undecomposed
9767-4-1	959	60	9767-4-7	1023	12
9767-4-2	966	54	9767-4-8	1024	11
9767-4-3	968	50	9767-4-9	1025	12
9767-4-4	998	28	9767-4-10	1046	3.7
9767-4-5	999	27	9767-4-11	1050	(2.1)***
9767-4-6	1009	21	9767-4-12	1050	(1.4)***
Series B (20 psig; 50 cc/min; 1.8 mm ID; $X_O \approx 0.030$):					
	Experiment Number	Temperature, C	Percent Undecomposed		
	9767-5-1	965	59		
	9767-5-2	963	56		
	9767-5-3	900	90		
	9767-5-4	904	87		
	9767-5-5	852	101		
Series C (16 psig; 43 cc/min; 2.2 mm ID; $X_O \approx 0.035$):					
Experiment Number	Temperature, C	Percent Undecomposed	Experiment Number	Temperature, C	Percent Undecomposed
9767-27-1	970	32	9768-11-1	1027	3.9
9767-27-2	974	30.2	9768-12-2	1024	3.7
9767-48-3	970	33.6	9768-15-3	1000	10.6
9767-48-4	1114	<0.01	9768-15-5	1001	7.8
9767-49-5	1124	<0.01	9768-20-6	975	44.7
9768-8-4	1053	0.87	9768-21-7	974	41.9
9768-10-4	1049	1.54	9768-21-8	950	(37.8)
9768-10-5	1053	1.10	9768-21-9	950	53.8
9768-10-6	1056	0.97	9768-23-2	950	50.8

*Liquid sample size: 0.2 microliters

**Experiments are numbered according to notebook, notebook page, and number in series.

***Residue was not burned out between experiments in Series A. This finally caused the Pyridine decomposition rate to increase markedly after 10 samples had been pyrolyzed. Starting with Series B, reactor was burned out after every experiment.

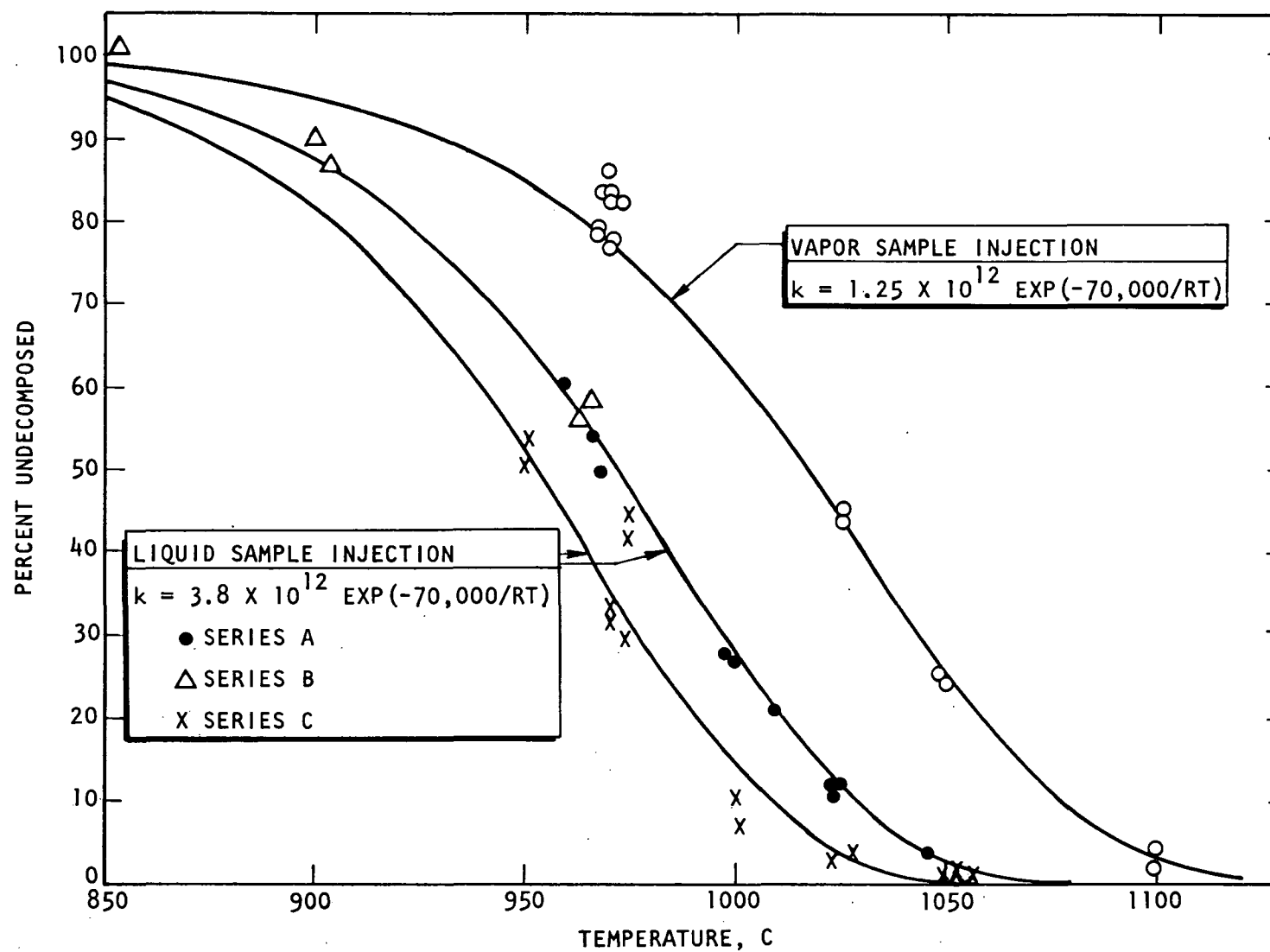


Figure 29. Rate Data for Pyridine Pyrolysis in Helium

A simple rate expression of the form,

$$-d(MC)/dt = A (MC)^N \exp (-E/RT) \quad (116)$$

where (MC) denotes the concentration of the model compound at any point in the reactor, was fitted to the model compound data where possible. Because a GC method was used to measure the reaction rate, the experimental error is large at small extents of decomposition (i.e., the rate is determined by the decrease in the area of the reactant peak and thus cannot be measured accurately with little reaction). Therefore, the kinetic parameters are determined mainly by the results obtained at large extents of reaction, and logarithmic plots such as that in Fig. 30 are useful in fitting the rate data.

Because the concentration, gas velocity, and reaction rate are temperature-dependent, it was necessary to integrate the rate expression¹¹⁶ through the reactor using the assigned temperature profile. The velocity (and residence time) also depends to some extent on the mole change that occurs during pyrolysis. The mole change, Δn , was assumed to be plus one for the model compounds* and it turned out that, because of the low mole fractions involved, varying Δn by a factor of 2 had no significant effect on the calculated residence times and rate parameters.

The pyridine data obtained using liquid sample injection was fitted to a first-order rate expression ($N = 1$). The theoretical curves[†] for $E = 65,000, 70,000,$ and $80,000$ kcal/mole are plotted in Fig. 30. The "A" factors for these curves were selected so that the percent undecomposed at 1000°C was equal to the experimental value of 28.2. It can be seen from Fig. 30 that the series A and B pyridine experiments fit quite well a first-order rate expression with the following constant:

$$k = 3.80 \times 10^{12} \exp(-70,000/RT), \text{ sec}^{-1} \quad (117)$$

However, the uncertainty in the activation energy is on the order of 5 kcal/mole, partly because the fraction reacted is changing quite rapidly with temperature

*For pyridine, e.g., the overall stoichiometry is approximately:

$\text{C}_5\text{H}_5\text{N} = \text{HCN} + 1/2 \text{CH}_4 + 7/2 \text{Cs} + \text{H}_2$, representing a Δn of 1.5.

[†]Obtained by integrating the rate expression through the reactor.

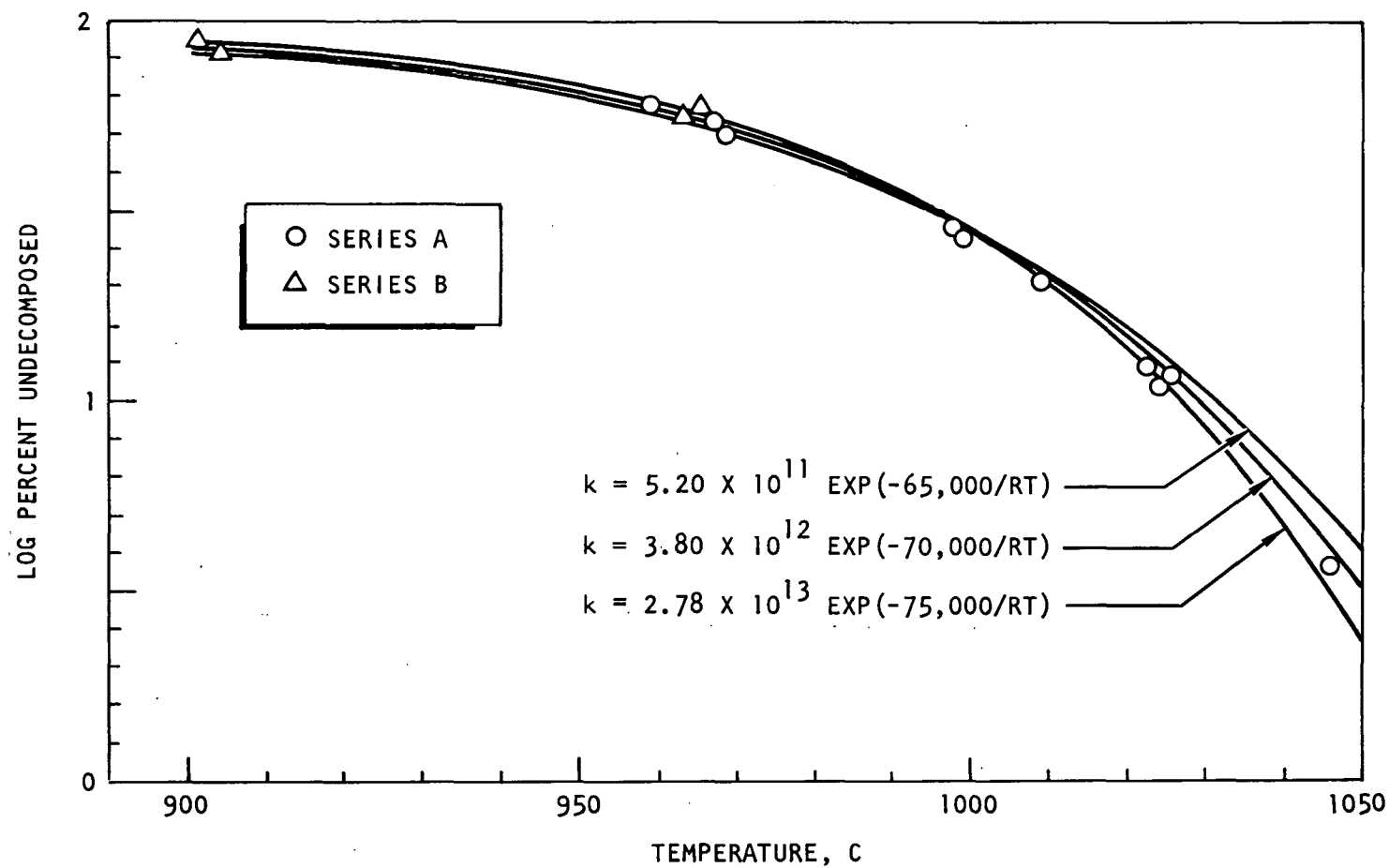


Figure 30. Pyridine Pyrolysis in Helium, Comparison of Experimental Results With First-Order Rate Expressions (log scale)

(on a log scale) at the larger extents of reaction. The A-factor in Eq. 117 is larger by a factor of 1.5 than was originally reported from these data (Ref. 120 and 121) because the exact integration of the reactor temperature profile resulted in an effectively shorter reactor.

It can be seen from Fig. 29 that this first-order rate expression for pyridine decomposition also fits the series C liquid injection experiments, although the fit is not quite as good (the vapor sample curve on the figure will be discussed later).

Discussion of Pyridine Decomposition Rate. The assignment of a rate expression for pyridine decomposition permits the reaction profiles through the reactor to be calculated using the computer program that was written to reduce the experimental data. These profiles are plotted in Fig. 31. At moderate temperatures from 960 to 1000 C, the reaction occurs gradually over the length of the reactor. At 1100 C, however, most of the reaction occurs in a zone about 2-1/2 inches in length. These calculations are in agreement with the positions of the carbonaceous deposits observed in those experiments where the furnace was opened before the residue was burned out.

The purpose of assigning kinetic parameters to the model compound pyrolysis data is to permit the decomposition rate to be extrapolated to the higher temperatures which the nitrogen-containing compound would encounter if it survived until quite close to the flame front in a combustion process. Shown in Fig. 32 is an Arrhenius plot of the half-life of pyridine as a function of temperature. The solid curve represents the rate constant in Eq. 117 and the dotted curve the other two rate expressions tested in Fig. 30. It can be seen that the (extrapolated) half-life for pyridine is about 0.05 millisecond at 1800 K, and will be in error by about 15 percent for each 1 kcal/mole that the activation energy is in error.

In their premixed burner studies with added pyridine, Merryman and Levy (Ref. 101 and 122) were able to predict the observed rate of pyridine disappearance by use of the inert pyrolysis rate expression previously reported from this program (Ref. 115 and 116). Why the presence of oxygen did not affect the decomposition rate of pyridine in their burner will be considered later (in the discussion of oxidative pyrolysis).

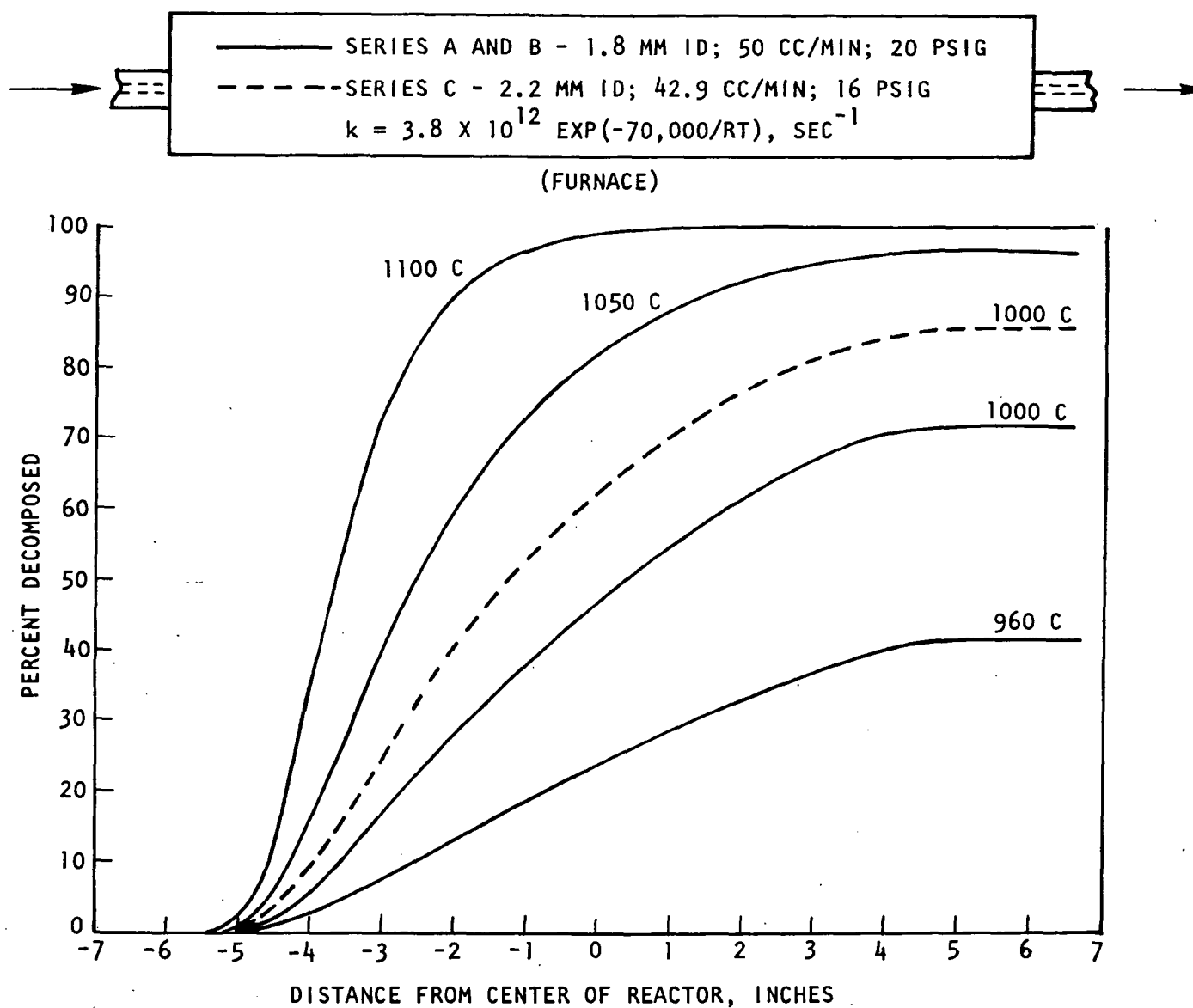


Figure 31. Pyridine Pyrolysis in Helium, Calculated Percent Decomposed as a Function of Distance and Temperature

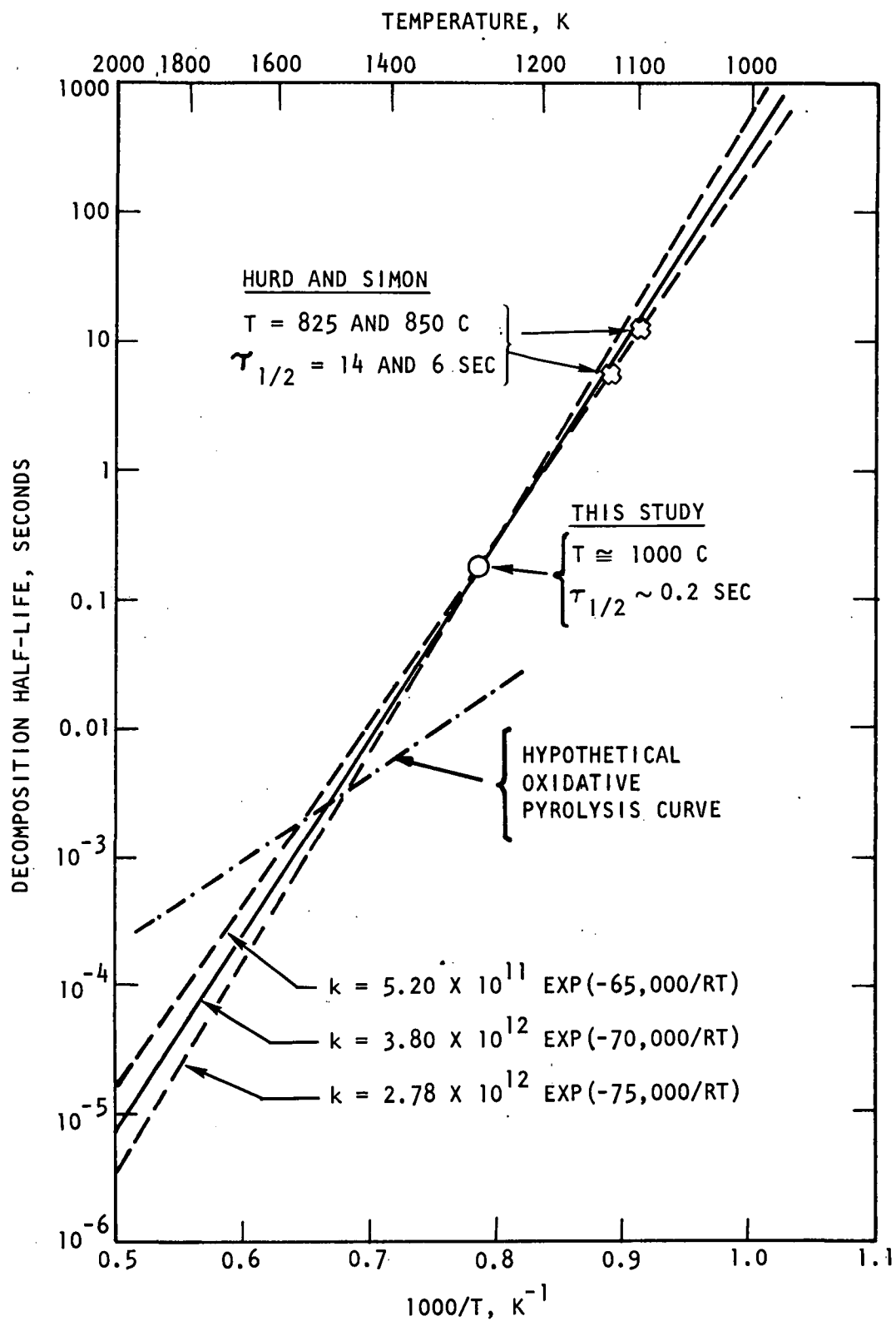


Figure 32. Pyridine Pyrolysis in Helium, Arrhenius Plot of Calculated Decomposition Half-Life

The only other major study of the inert pyrolysis of pyridine was that of Hurd and Simon (Ref. 92), which was discussed under Phase IA. The half-lives calculated at 825 and 850 C from the rate constants obtained from their data are 14 and 6 seconds, respectively (Fig. 32). The half-lives calculated from Eq. 117 are 15.6 and 7.6 seconds at these two temperatures, respectively, indicating good agreement between the decomposition rates obtained in the two studies (see Fig. 7).

Rate Parameters for Other Model Compounds. The pyrrole and quinoline decomposition rate data, listed in Table 9 and plotted in Fig. 33, were fitted to first-order rate expressions, using the detailed integration program, giving the kinetic parameters listed in Table 10 and the theoretical (solid) curves shown in Fig. 33 and 1. The rate parameters obtained for pyridine and pyrrole suggest that the rate-determining step is a unimolecular reaction. Such reactions typically have pre-exponential factors in the range of 10^{13} to 10^{16} sec^{-1} (Ref. 123). The surprising feature is that pyrrole, which is less aromatic than pyridine, has a higher activation energy for decomposition. The quinoline kinetic parameters suggest a heterogeneous reaction.

The rate data obtained with benzonitrile, Table 9 and Fig. 33 do not appear to fit any simple rate expression of the form of Eq. 116. The "tail" on the benzonitrile curve (i.e., 3-percent undecomposed at 1100 C) was further investigated because it was possible that a thermally stable product formed that had the same retention time as benzonitrile. This possibility was investigated using the mass spectrometer to analyze the eluted peak and there was no indication of the presence of any species other than benzonitrile.

Vapor Sample Injection. When the vapor sample injection system, described in the Experimental section, was used to introduce pyridine into the model compound reactor, the data listed in Table 11 and plotted in Fig. 29 were obtained. It is apparent that the half-life for pyridine decomposition is much less under these conditions. Interestingly, the vapor injector data fit fairly well a first-order rate expression again with a 70 kcal/mole activation energy. However, an A-factor of only 1.25×10^{12} must be used to give the fit shown in Fig. 29. This is smaller by a factor of 3 than the A-factor for the liquid injection data for pyridine.

TABLE 9. EXPERIMENTAL DATA* ON RATE OF MODEL COMPOUND
DECOMPOSITION IN HELIUM (LIQUID SAMPLE** INJECTION)

<u>Quinoline</u>					
Experiment Number	Temperature, C	Percent Undecomposed	Experiment Number	Temperature, C	Percent Undecomposed
9768-6-16	1116	0	13158-7-7	950	35.7
9768-47-4	852	74.7	13158-8-8	950	29.2
9768-47-5	852	77.2	13158-9-1	975	17.0
13158-6-3	900	47.6	13158-9-2	975	14.6
13158-7-4	900	49.5	13158-9-3	1000	9.6
13158-7-5	925	42.0	13158-10-4	1000	6.1
13158-7-6	925	40.9			
<u>Benzonitrile</u>					
9768-6-15	1115	2.4	9768-17-8	(975)	13.5
9768-7-2	1051	7.9	9768-20-4	975	14.6
9768-7-3	1051	6.1	9768-20-5	975	14.3
9768-12-3	1027	7.0	9768-42-12	940	32.5
9768-12-4	1027	6.9	9768-42-13	940	37.7
9768-16-6	998	10.2	9768-44-1	900	70.5
9768-16-7	996	9.6	9768-44-2	900	65.3
<u>Pyrrole</u>					
9768-19-3	975	≈1.2	13158-2-13	900	57.8
13158-1-8	852	79.9	13158-2-1	925	31.0
13158-1-9	852	79.9	13158-3-2	925	27.2
13158-1-10	875	77.3	13158-3-3	950	9.1
13158-1-11	875	86.5	13158-3-4	950	6.0
13158-1-12	900	67.2	13158-3-5	975	1.3

*Conditions were same as for Series C Pyridine experiments listed in Table

**Liquid sample size: 0.2 microliters

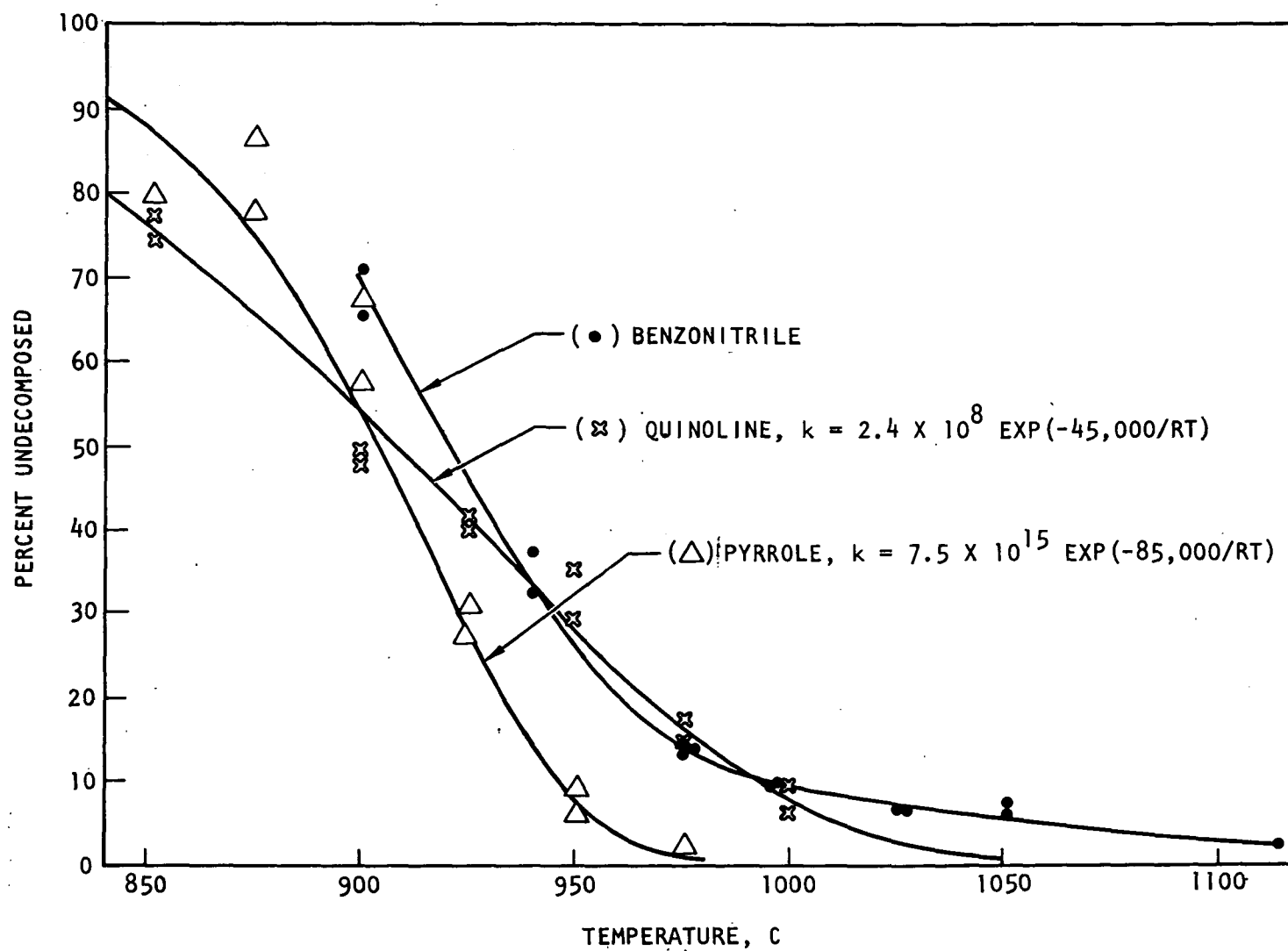


Figure 33. Rate Data for Model Compound Pyrolysis in Helium, Liquid Sample Injection
(See Fig. 29 for pyridine data)

TABLE 10. KINETIC PARAMETERS FOR PYROLYSIS OF MODEL
COMPOUNDS IN HELIUM (Liquid Sample Injection)

$$-dC/dt = k(C)^N = A \cdot (C)^N \cdot \exp(-E/RT)$$

	N	A, sec ⁻¹	E, kcal/mole
Pyridine	1	3.8 x 10 ¹²	70
Pyrrole	1	7.5 x 10 ¹⁵	85
Quinoline	1	2.4 x 10 ⁸	45

TABLE 11. EXPERIMENTAL DATA* ON RATE OF PYRIDINE DECOMPOSITION
IN HELIUM (Vapor Sample Injection)

Experiment Number	Temperature, C	Percent Undecomposed	Experiment Number	Temperature, C	Percent Undecomposed
9768-34-1	967	79.0	9768-37-12	1027	45.4
9768-35-3	970	76.3	9768-39-1	970	86.1
9768-35-4	970	83.1	9768-39-2	970	82.7
9768-36-5	968	78.1	9768-39-3	1050	24.4
9768-36-6	971	77.5	9768-39-4	1050	24.4
9768-36-7	973	81.7	9768-40-5	1100	1.9
9768-36-8	970	83.5	9768-40-6	1100	3.5
9768-37-11	1027	44.3			

*15 psig, 40.9 cc/min, 1.9 mm ID, X_O ≅ 0.003

The vapor injector experiments were conducted in a new quartz reactor with an ID of 1.9 mm at a pressure of 15 psig and a flowrate of 40.9 cc/min. The only major difference between the liquid and vapor sample injection experiments was the mole fraction of the pyridine vapor in the gas entering the reactor. To obtain an estimate of the pyridine mole fraction in the gas stream after injection of a liquid sample, the half-width of the methane peak (which is not held up on the GC column) was measured to determine how rapidly the pyridine vaporized in the injection system. The time required for the pyridine sample to vaporize is about 2 seconds. From this, it was calculated that the pyridine mole fraction was about 0.03 compared with 0.003 in the vapor injector experiments (calculated from the vapor pressure). This difference of a factor of 10 in pyridine concentration is the only apparent explanation for the longer half-life in the vapor injection experiments. That is, if the reaction order is greater than 1, the half-life would increase as the initial concentration decreases. Thus, the decomposition of pyridine fits a first-order rate expression when the initial concentration is held constant and the extent of decomposition is varied by increasing the temperature, but a reaction order of higher than 1 is indicated when the initial concentration is varied.

An attempt was made to fit the pyridine data to a higher-order simple rate expression, but no satisfactory fit was found. An order greater than 1.5 would be required to account for the concentration effect, but then a much greater activation energy is needed to give the proper temperature effect. Taking this approach, no simple rate expression was found that would fit all the pyridine data. The vapor injection results indicate that the inert pyrolysis of pyridine is not a simple unimolecular process.

Oxidative Pyrolysis. Oxidative pyrolysis experiments were conducted in the same manner as the inert pyrolysis experiments except that the carrier gas contained up to 10-percent oxygen. After sample injection, the flow was switched to helium carrier gas before temperature programming of the GC column was initiated to protect the column packing.

The vapor injector system was built specifically for the study of oxidative pyrolysis so that oxygen could be intimately mixed with the model compound vapor before it entered the reactor. When 5-percent oxygen was present in the carrier gas stream, the temperature for half decomposition was decreased from about 1020 to 780 C, as shown in Fig. 34.

To obtain larger amounts of products, the oxidative pyrolysis of model compounds was investigated further using liquid sample injection. To ensure good mixing with O_2 , one-half of the carrier gas stream (helium + oxygen) was brought in through the sample injection port and the remainder was mixed in, in a small-volume "T" (1/16-inch OD), after the sample had been vaporized but before the sample reached the reactor. The effect of oxygen at concentrations of 2.6 and 10.7 mole percent on the rate of decomposition of pyridine and benzonitrile, respectively, under these conditions, is shown in Fig. 35 and 36. These results are cross-plotted as a function of oxygen concentration in Fig. 37 and 38. With pyridine, the 50-percent decomposition temperature was reduced from about 950 to 925 C with 2.6-percent O_2 , and to 710 C with 10.7-percent O_2 . The benzonitrile 50-percent decomposition temperature was decreased from 925 C to 860 and 735 C with 2.6- and 10.7-percent O_2 , respectively. With 10.7-percent oxygen, the amount of the model compound reacted increases rapidly with temperature (Fig. 35 and 36) and then suddenly levels off. At 2.6-percent O_2 , the reaction rate levels off at lower extents of reaction with both compounds, and then increases again as the temperature region is reached in which appreciable decomposition occurs in the absence of O_2 .

The most likely explanation of these changes in rate with extent of decomposition is that the oxygen becomes depleted as the extent of reaction increases. The oxygen/pyridine molar ratio was about 3.5 in the liquid injection experiments with 10.7 percent O_2 . This is somewhat less than the stoichiometric ratio of 4.25 for conversion to CO, NO, and H_2O , and considerably less than the ratio of 6.75 required for conversion to CO_2 , NO, and H_2O . The oxygen/pyridine ratio in the vapor injection experiments (Fig. 34) was about 20. This could account for the continued rapid increase in extent of decomposition beyond 85-percent decomposition in Fig. 34 with only 5 percent O_2 , while the rate of pyridine decomposition slowed

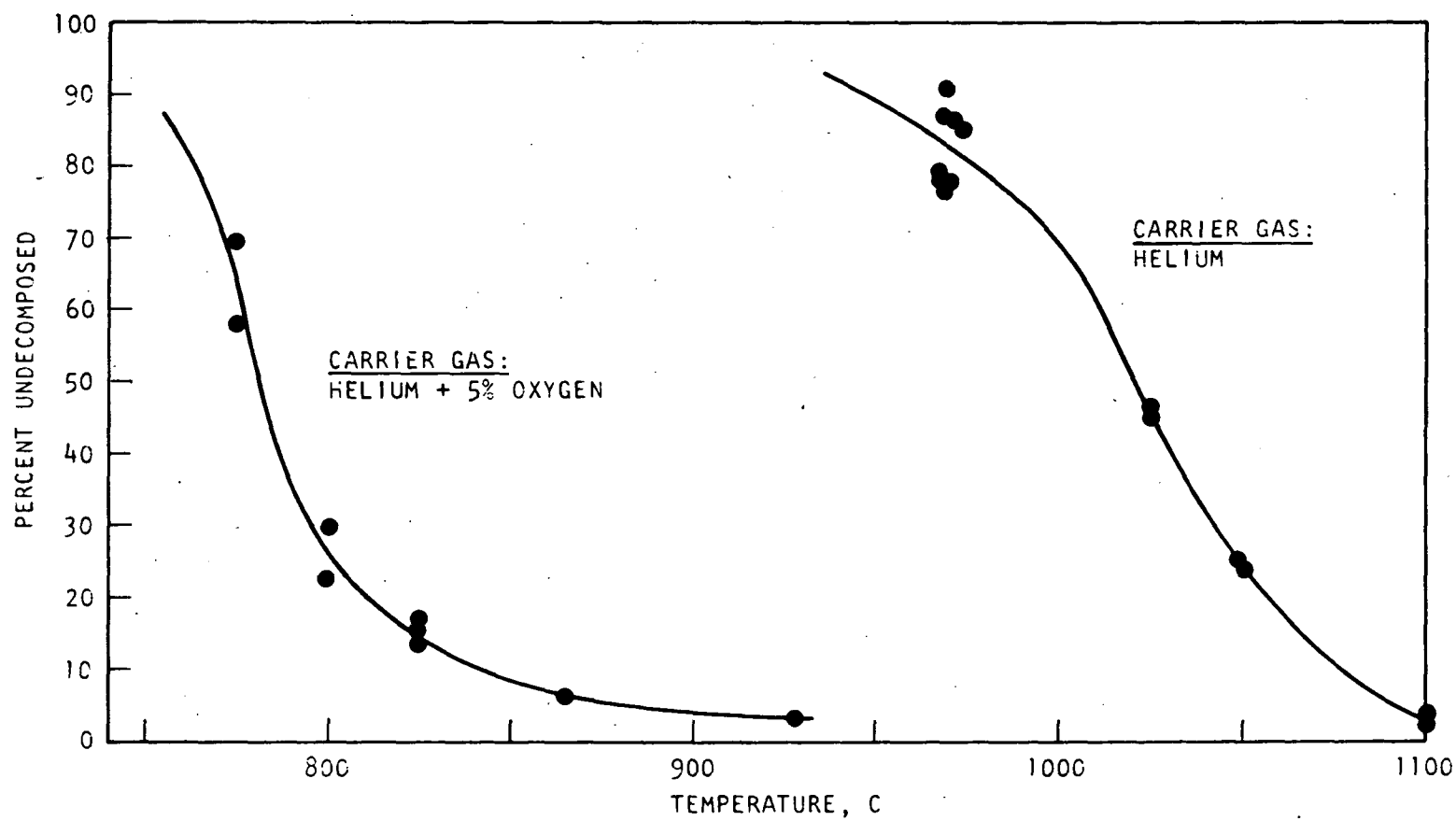


Figure 34. Pyridine Pyrolysis Results Using Vapor Injector

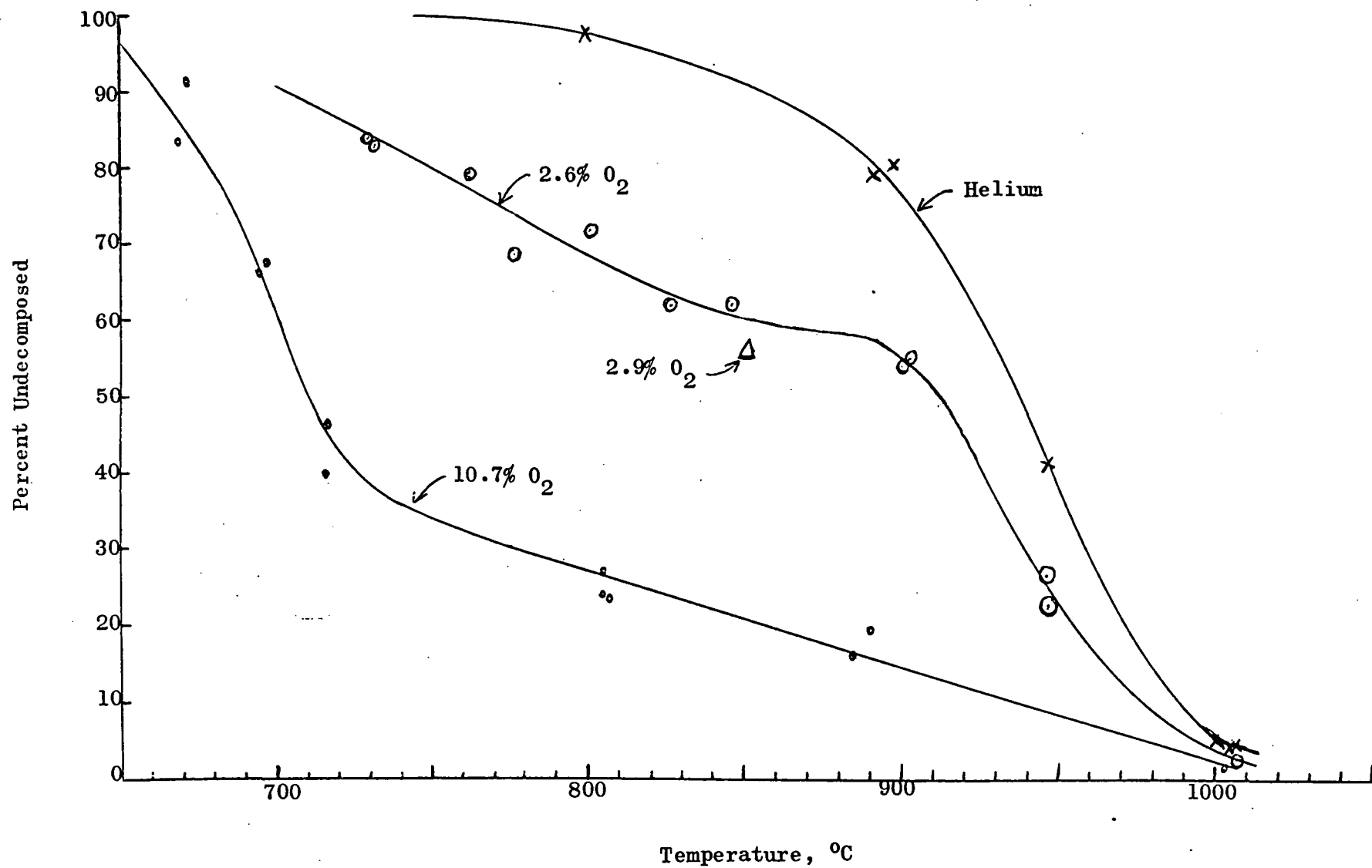


Figure 35. Effect of Oxygen on Decomposition Rate of Pyridine (Liquid Injection)

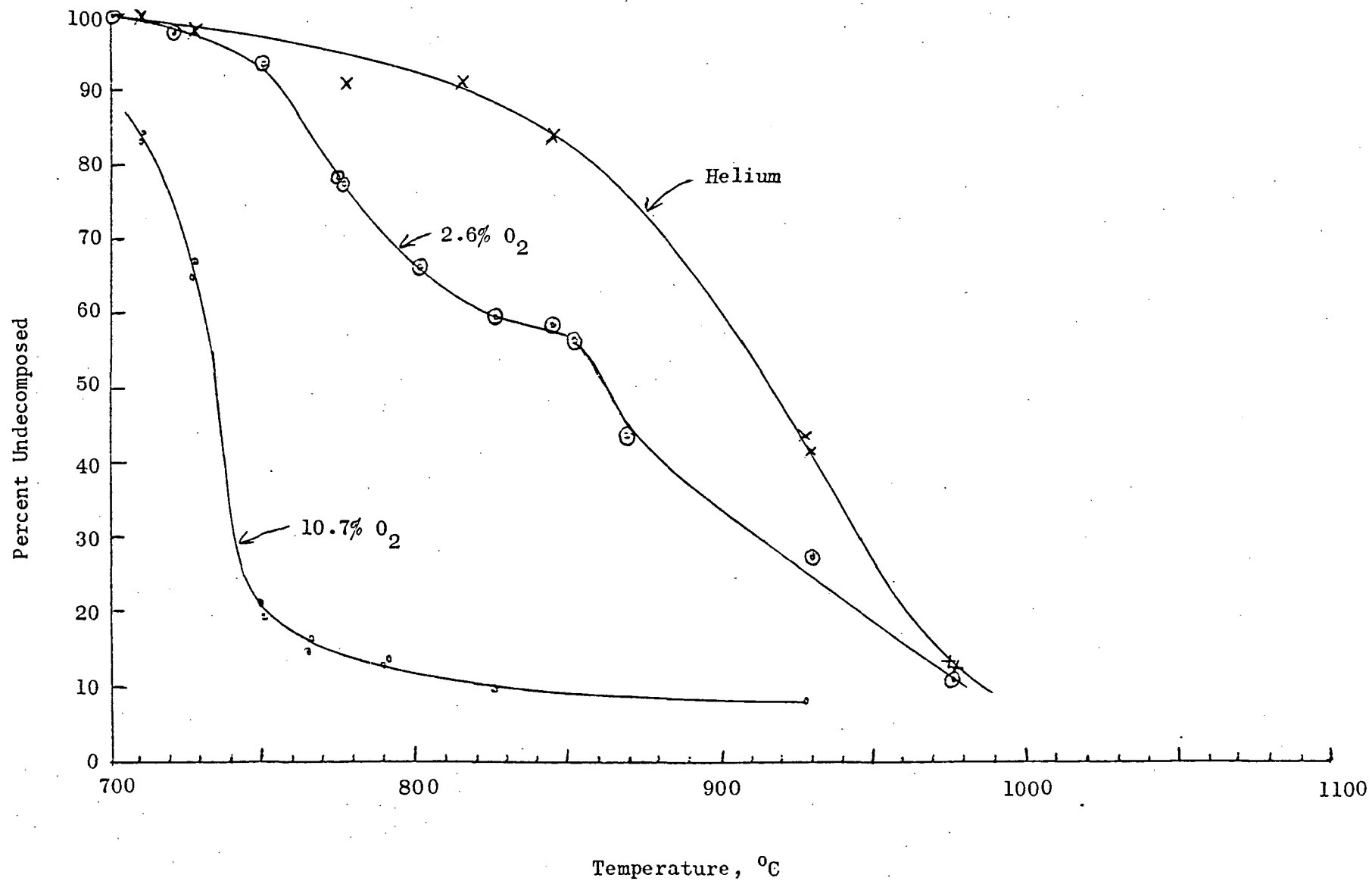


Figure 36. Effect of Oxygen on Decomposition Rate of Benzonitrile (Liquid Injection)

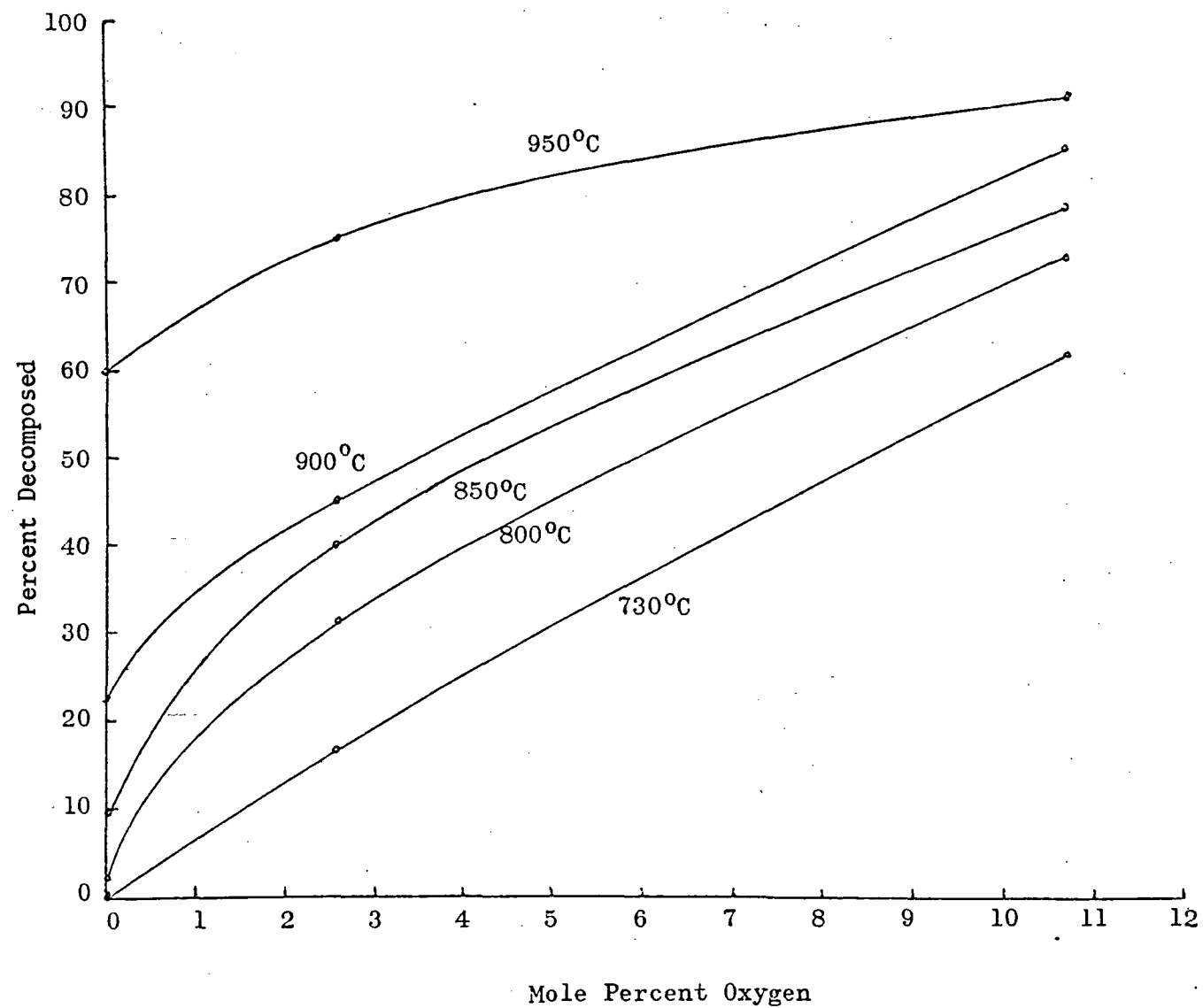


Figure 37. Effect of Oxygen Concentration on Rate of Pyridine Decomposition

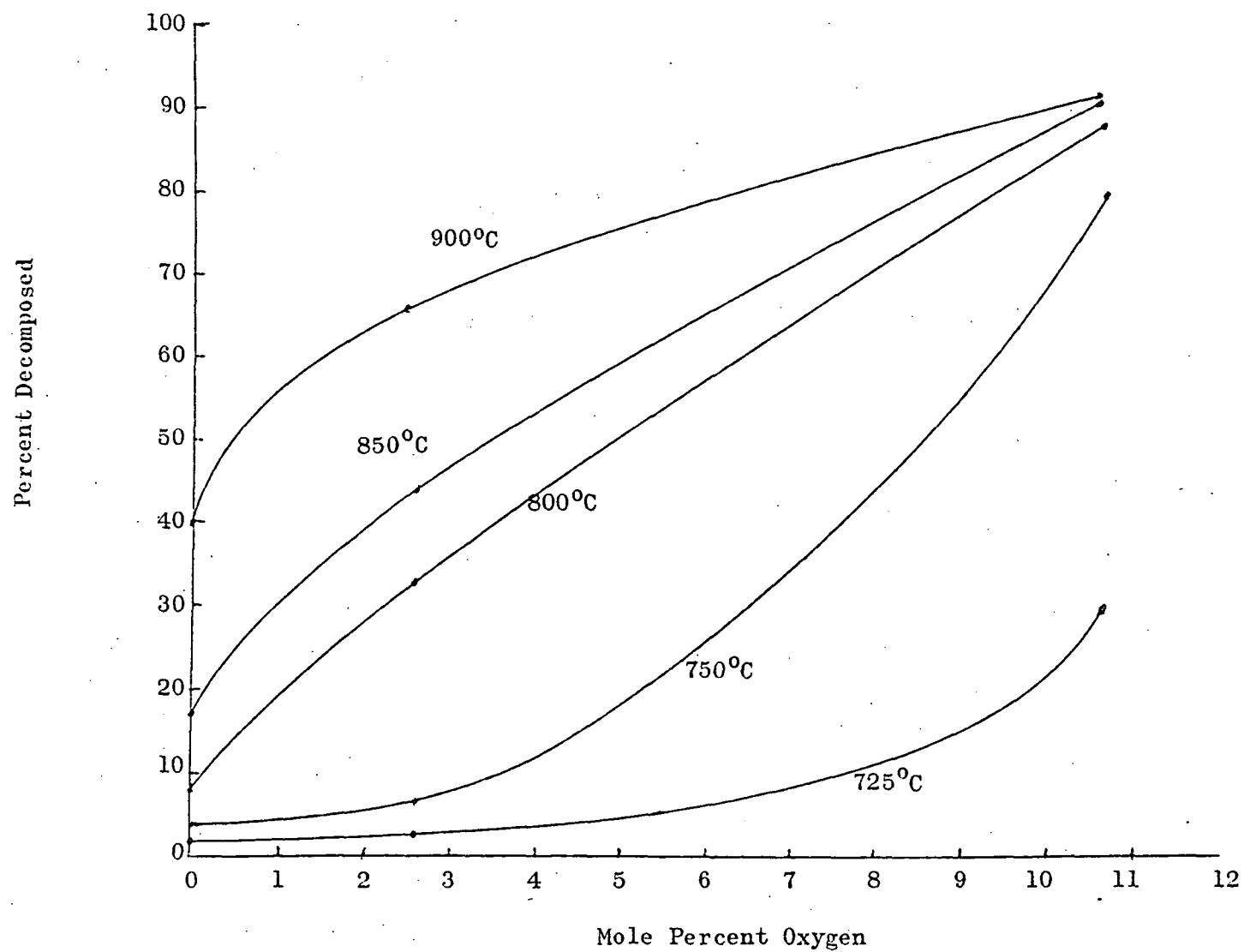


Figure 38. Effect of Oxygen Concentration on Rate of Benzonitrile Decomposition

at 65 percent reaction in the liquid sample experiments with 10.7 percent O_2 , Fig. 35 (because most of the oxygen may have been consumed). It can be seen from Fig. 36 that 2.6-percent oxygen has little effect on the decomposition of benzonitrile until a temperature of 750 C is reached at which about 80 percent decomposition occurs when 10.7-percent oxygen is present. This suggests that once the oxidative pyrolysis is initiated it tends to go rapidly to completion (perhaps via a chain reaction).

The rate of reaction of the model compounds increases greatly when O_2 is added to the carrier gas stream. To determine if this would be the case at the higher temperatures that would be encountered in or near a flame front, an exact rate expression for oxidative pyrolysis, with an accurate activation energy, is required. It is apparent that such a rate expression cannot be obtained from the present data, except possibly in the case of the vapor injection experiments, because the concentration of oxygen is decreasing in an unknown manner. Data obtained at small extents of reaction, where the O_2 concentration remains near its initial value, would permit an accurate rate expression to be derived. Because the technique employed in this study of oxidative pyrolysis involved measurement of the amount of unreacted compound, accurate decomposition rate data cannot be obtained at small extents of reaction.

It can be shown from an Arrhenius plot that if oxidative pyrolysis were faster by a factor of ten at 1000 C than inert pyrolysis, but the activation energy was only 30 kcal/mole for the oxidative pyrolysis, the half-life for oxidative pyrolysis would be longer by about an order of magnitude at 1800 K than that for inert pyrolysis (dotted line in Fig. 32). Therefore, inert pyrolysis could dominate at high temperatures even in the presence of oxygen if the heating rate were sufficiently fast. This could account for the fact that Merryman and Levy found pyridine to decay in their premixed burner studies at a rate predicted by our inert pyrolysis rate constant (Ref. 122). It is not presently possible, based on available data, to assess exactly the role of oxidative pyrolysis in the formation of fuel NO in combustion.

Decomposition Products

Using the techniques described in the Experimental section, the major organic and inorganic nitrogen-containing pyrolysis products were measured for the model compounds.

Organic Products of Inert Pyrolysis. The individual organic products (volatile below about 200 C) that were identified in the model compound decomposition products are shown in Fig. 39 through 42. Each curve denotes the weight percent that a given product represents of the amount of compound that has decomposed. Because the major interest was in the nitrogen-containing products, the amounts of these species that are formed are plotted as solid curves. The organic products obtained from pyridine at the lower temperatures (Fig. 39) are the same as those reported by Hurd and Simon, but are recovered at much higher concentrations. This probably resulted from the shorter residence time and the improved experimental procedure used during this study.* At higher temperatures, the less thermally stable products decrease in concentration and only the stable products are observed.[†] The major organic products from quinoline (Fig. 40) are similar to those from pyridine (benzene, benzonitrile, and methane). It will be shown that quinoline apparently forms mostly residue.

The major organic products from benzonitrile (Fig. 41) are benzene and biphenyl, indicating that the first step is a C-C bond rupture followed by hydrogen abstraction, to form benzene, and some association of phenyl radicals. This organic product distribution is that which could be expected (Ref. 124).

*Considerable residue built up in the reactor of Hurd and Simon. This may have catalyzed the formation of residue as was found during this study.

[†]Note that considerable benzonitrile is found in the products of pyridine decomposition even at 1100 C. This is in agreement with its high-temperature stability as shown in Fig. 1.

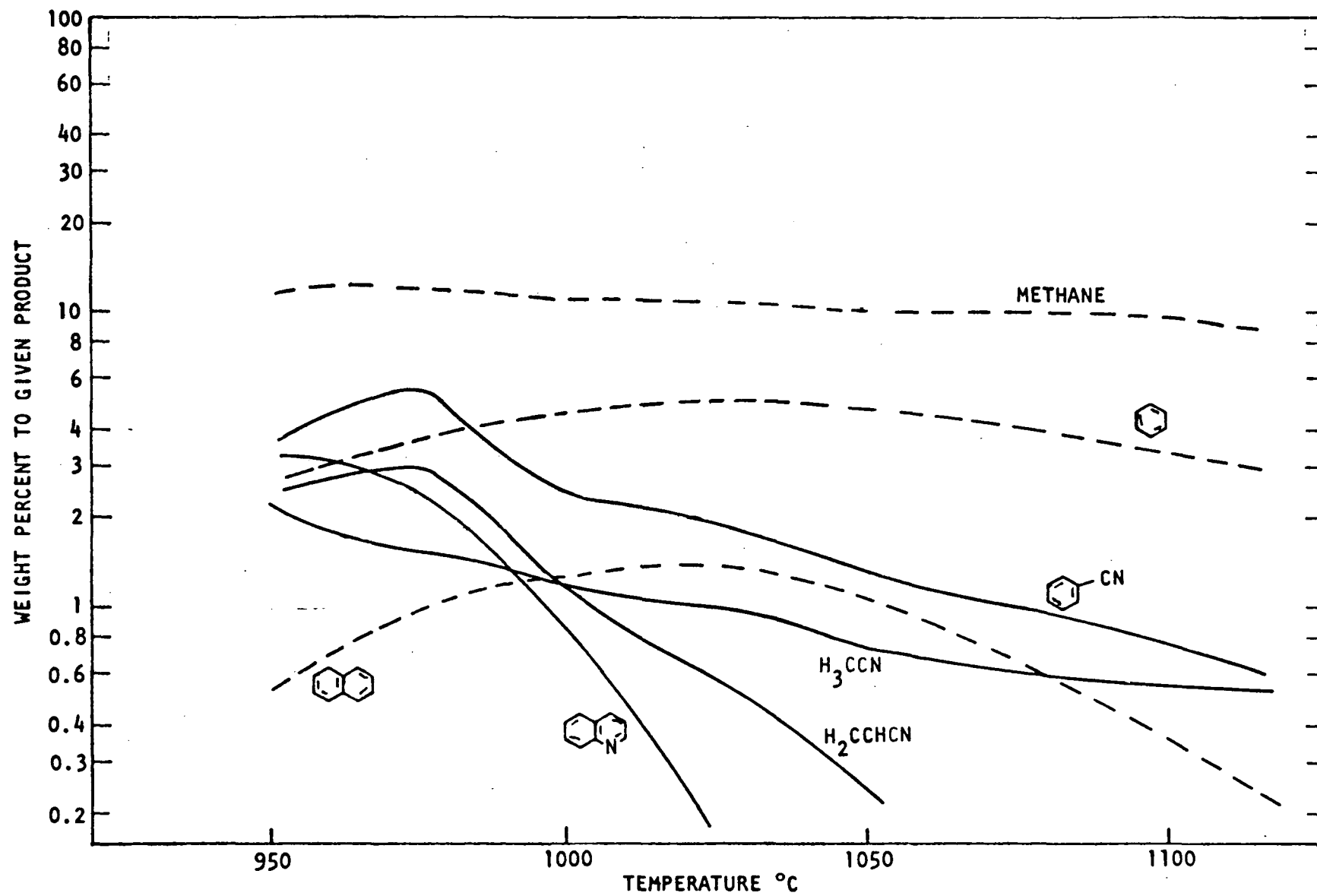


Figure 39. Organic Products of Inert Pyrolysis of Pyridine

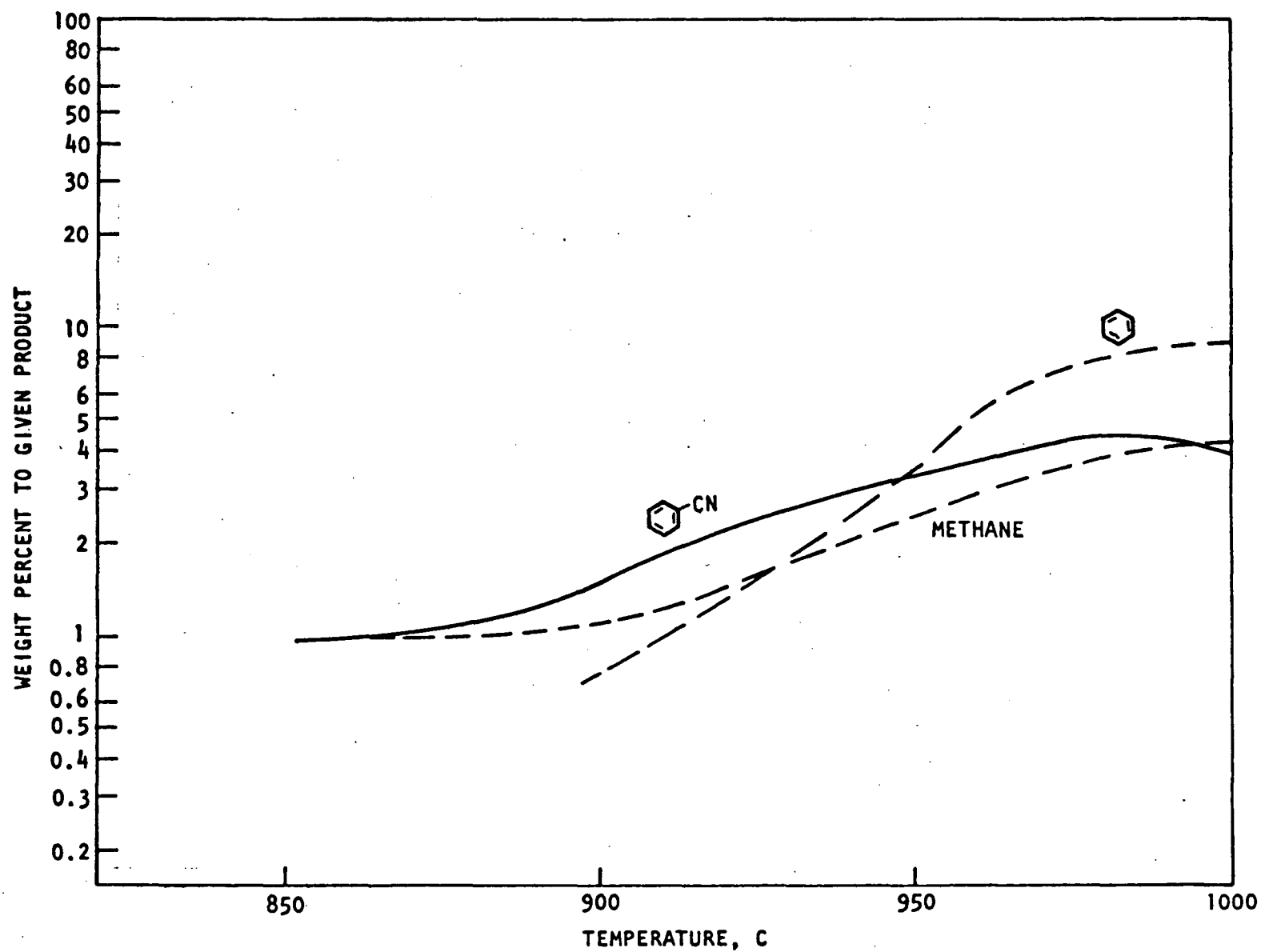


Figure 40. Organic Products of Inert Pyrolysis of Quinoline

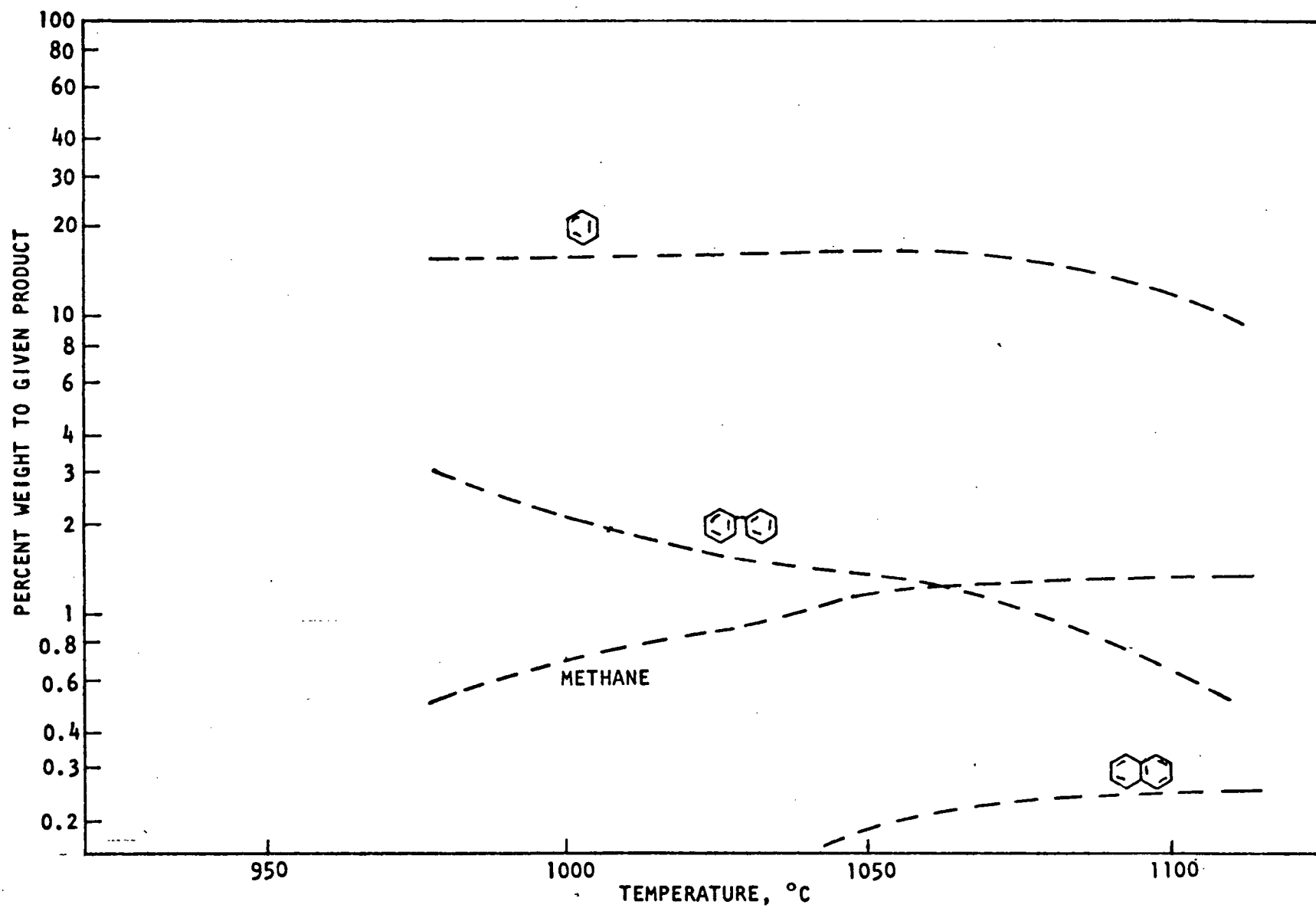


Figure 41. Organic Products of Inert Pyrolysis of Benzonitrile

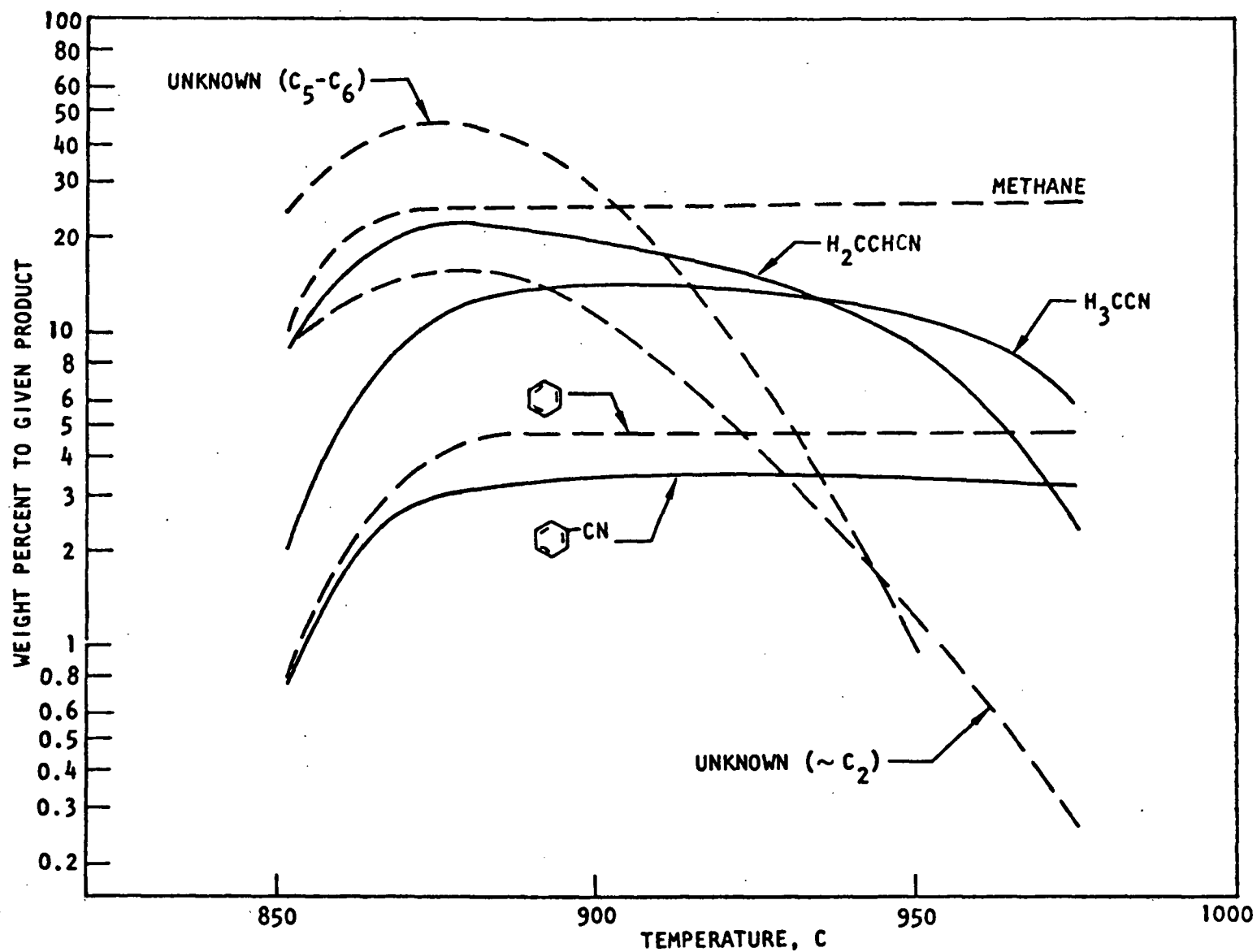


Figure 42. Organic Products of Inert Pyrolysis of Pyrrole

The experiments with pyrrole are interesting in that all of the carbon is recovered at low temperatures, i.e., little residue is formed. The unknown that accounts for 48 percent of the carbon at 875 C (Fig. 42) has a retention time on the GC column about the same as pyridine and the picolines, but the mass spectrometer was not in operation at the time these experiments were run. It would be quite unexpected if the first step in the pyrolysis of pyrrole turns out to be the formation of the aromatic pyridyl ring. If this product is pyridine, most of the pyrrole-N was recovered in the organic products at 875 C.

Inorganic Products of Inert PYrolysis. Since little of the model compound nitrogen was recovered in the organic pyrolysis products (except possibly in the case of pyrrole), the search for nitrogen in the inorganic products became of even more importance. It will be seen that only minor amounts of NH_3 and virtually no N_2 is formed in the pyrolysis of the model compounds. HCN, however, was found to be a major decomposition product, particularly at higher temperatures.

HCN From Model Compounds. As shown in Table 12, the amount of model compound nitrogen that is converted to HCN under inert pyrolysis conditions increases from 50 percent at 950 C to 80 percent at 1100 C for benzonitrile and from 40 at 950 C to 100 percent for pyridine at 1100 C. These high conversions to HCN from two structurally different fuel nitrogen compounds suggest that CN species may be the key intermediates in the formation of fuel NO in combustion where even higher temperatures and heating rates are involved. The common formation of HCN in pyrolysis would thus account for the observation that most nitrogen compounds are converted to NO to the same extent under a given combustion condition. No HCN measurements were made at elevated temperatures with pyrrole. HCN was found in some early experiments with quinoline at 1100 C (at about two-thirds the level found from benzonitrile), but the method for determining HCN used in those experiments was found not to be reliable (see Appendix A). These results suggest, however, that quinoline would have formed appreciable HCN at 1100 C if quantitative measurements had been made.

Hurd and Simon (Ref. 92) have reviewed the previous literature on the pyrolysis of pyridine. They note that HCN had been reported as a product, but no estimates

TABLE 12. HCN FORMATION IN INERT PYROLYSIS OF MODEL COMPOUNDS

	Temperature, C	Percent Decomposed	Percent N Converted to HCN*
Pyridine	956	(62)	35.6
	960	65	45.7
	959	65	36.8
Pyridine	1102	100	106
	1106	100	98
	1107	100	98
	1107	100	105
Benzonitrile	957	(71)	45
	955	69	53
Benzonitrile	1107	98.0	82
	1106	98.0	81

*Based on N content of decomposed portion of sample.

of the amount were given. Ruhemann (Ref. 125), for example, reported in 1929 that, on increasing the temperature of pyridine decomposition from 600 to 900 C, nuclear scission into HCN becomes important. Hurd and Simon do not mention if they observed HCN from pyridine, but state that with the picolines "HCN was formed in every run above 775 C, but no attempt was made to estimate it quantitatively."

After the quartz model compound reactor had been used in many experiments (probably several hundred hours at 950 to 1100 C), it became catalytic toward HCN decomposition, causing most of the HCN to be converted to N_2 at 1100 C, and lesser amounts at lower temperatures. The interior of the tube was frosted in appearance suggesting that it may have gradually reacted with the carbonaceous residues that were deposited and then burned off after each experiment. When the quartz tube had reached this condition, the decomposition rate of pyridine and benzonitrile did not change but, of course, much less HCN was recovered in the decomposition products. Installation of a new quartz reactor in the model compound apparatus restored the previous conditions. HCN gas was used to calibrate the HCN measurements before and after each series of experiments and to establish that heterogeneous decomposition of HCN was not occurring. Another direct indication of

the presence of large concentrations of HCN in the pyrolysis products was a baseline disruption of the gas chromatogram. The HCN came through effectively as a broad peak with a peak half-width as long as 10 minutes, depending on the amount of HCN present (with 7-1/2 degrees per minute temperature programming).

NH₃ From Model Compounds. Only small amounts of NH₃ were found in the model compound pyrolysis products, although considerable effort was expended on this measurement. Using both the NH₃ converter method (in which NH₃ is decomposed to N₂ and H₂ and the N₂ subsequently measured by GC) and the phenate method, the conversion of model compound nitrogen to NH₃ in pyrolysis at 960 C ranged from 0.8 to 4 percent for pyridine and 1.5 to 2.6 percent for benzonitrile. Calibration of the model compound reactor system with microgram quantities of NH₃ demonstrated that slightly more than one-half of the NH₃ that was passed through the system was recovered even with these small quantities (either as NH₃ in the phenate method or as N₂ by the converter method). The remainder of the NH₃ was probably adsorbed in the stainless-steel line between the reactor and the analysis train. These results do permit upper limits of 8 and 5 percent, respectively, to be placed on the amount of nitrogen that is converted to NH₃ in the pyrolysis of pyridine and benzonitrile.

The possibility was tested that NH₃ could react with the carbonaceous residue and form HCN and H₂. However, when known amounts of NH₃ were passed over the hot residue from the pyrolysis of pyridine at 1050 C, no detectable HCN was formed.

The equilibrium constant for the reaction:



is given by $K_p = P_{\text{H}_2} \cdot P_{\text{HCN}}/P_{\text{NH}_3}$. Therefore, if equilibrium is attained, P_{HCN} will equal P_{NH_3} when $P_{\text{H}_2} = K_p$. The values of K_p , obtained from the JANAF Thermochemical Tables, are 0.38 atm at 925 C and 5.7 atm at 1125 C. The partial pressure of H₂ should remain less than about 0.2 atm in the model compound experiments indicating that reaction 118 is favored thermodynamically. Therefore, the failure of HCN to form in the above experiment must be the result of kinetic limitations.

HCN has been produced from the reaction of NH_3 with coal (Ref. 126) at 1250 C. However, this is attributed to reactions of the type:



rather than to reaction 118. The conversion of NH_3 to HCN was observed by DeSoete (Ref. 63) in his premixed ethylene- O_2 flames. It appears that the possible role of NH_3 in the formation of HCN from nitrogen compounds during pyrolysis warrants further investigation.

N_2 From Model Compounds. It was demonstrated conclusively several times during the program that neither pyridine nor benzonitrile formed any detectable N_2 when pyrolyzed at temperatures between 950 and 1100 C. Calibrations with a dilute N_2 -helium gas mixture demonstrated that the molecular sieve GC used for the N_2 determination was capable of measuring a few tenths of a microgram of N_2 . Therefore, if any of the model compound nitrogen formed N_2 directly during pyrolysis it was much less than 1 percent.

The observation that N_2 does not form during model compound pyrolysis is not surprising considering the limited number of radical reactions that can lead to N_2 formation in the absence of oxygen (Ref. 2). The absence of N_2 formation is also in agreement with the observation that nitrogen compounds at low concentrations can undergo nearly complete conversion to NO under the proper (fuel-lean) conditions.

Although the model compounds do not form N_2 when pyrolyzed in a quartz reactor, a majority of the N_2 in pyridine (the only compound tested) is converted to N_2 in nickel or stainless-steel reactors at 1050 to 1100 C. This was observed in the nickel reactors used at the start of the program (63 percent N_2 from pyridine at 1000 C) and in the ammonia converter used near the end of the pyrolysis studies (90 percent N_2 from pyridine at 1050 C). Calibration experiments showed that in such metal reactors, NH_3 decomposes almost quantitatively to N_2 and more than one-half of HCN-N is converted to N_2 . Therefore, the formation of N_2 from pyridine in the metal reactors probably resulted from the decomposition on the metal surface of the HCN that forms from the pyridine, although the quantities of N_2 formed are somewhat larger than this hypothesis would predict. It will be seen

that this heterogeneous conversion of fuel-N to N_2 represents the only direct method that was found for promoting N_2 formation under pyrolysis conditions.* The heterogeneous decomposition of HCN (or NH_3) probably accounts for the low yields of HCN that were obtained from the reaction of coal and NH_3 when metal reactors were employed (Ref. 126).

Residue From Inert Pyrolysis. Hurd and Simon found that most of their pyridine was converted to residue under inert pyrolysis conditions. Black carbonaceous residues were observed to form on the reactor wall under inert pyrolysis conditions[†] from the model compounds employed in this study, but the amount of model compound carbon that was converted to residue was not determined directly. Of more concern for the purposes of this program was the amount of nitrogen that was contained in the residue.

After one inert pyrolysis experiment of pyridine at 960 C, the quartz reactor was removed from the apparatus without burnout. The tube was cut to a length that permitted it to be used directly as the combustion tube in an automatic Dumas nitrogen analyzer. The amount of nitrogen that was determined in the residue by this method represented 49 percent of the nitrogen present in the quantity of pyridine that had decomposed in this experiment. The accuracy of this result was limited by a rather high blank that was encountered in the Dumas measurement.

In another type of residue experiment, the residue from the pyrolysis of pyridine at 950 C was heated (slowly) to 1110 C. No detectable HCN was produced during this process. This suggests that the HCN formed during model compound pyrolysis at 1100 C does not form from pyrolysis of the residue after it has formed on the reactor wall. This possibility cannot be ruled out completely on the basis of this experiment, however, because the rate at which the furnace temperature could be increased was necessarily slow at these high temperatures.

*Robertus et al. (Ref. 127) attempted to prevaporize the fuel-N compounds in coal so that they could be converted to N_2 before reaching the flame (presumably by a process such as this) but were not successful.

[†]A residue could have formed in the oxidative pyrolysis experiments, but it would have burned off immediately.

Product Mass Balances-Inert Pyrolysis. A complete mass balance for the inert pyrolysis products cannot be made because the quantities and compositions of the residues were not determined. However, the mass balance for nitrogen can be calculated for pyridine because the amount of nitrogen in the residue was measured at 960 C and all of the pyridine nitrogen is recovered as HCN at 1100 C. The nitrogen balance for the inert pyrolysis of pyridine is summarized in Table 13.

TABLE 13. NITROGEN BALANCE IN INERT PYROLYSIS OF PYRIDINE

Product	Percent N in Product*	
	960 C	1100 C
Residue	49	NM [†]
HCN	40	102
Benzonitrile	5	0.5
Quinoline	3	<0.1
Acrylonitrile	3	<0.1
NH ₃	<8	NM
N ₂	<0.1	NM
	<hr/> ≈100	<hr/> 102

*Based on N in decomposed portion of sample
(65 percent at 960 C and 99.9 at 1100 C)

[†]NM = not measured

A summary of the carbon and nitrogen mass balances for the inert pyrolysis of the model compounds is shown in Table 14. Based on the assumption that the carbon and nitrogen not found in the measured products was contained in the residue, the following amounts of material were calculated as being in the residue (Table 15).

TABLE 14. PRODUCT MASS BALANCES FROM INERT PYROLYSIS

Reactant	Temperature, C	Carbon, Percent Found In:					Nitrogen, Percent Found In:			
		CH ₄	Other Organic Products	HCN	Unknown Peaks	Residue by Difference	Nitrogen, Percent Found In:			
							Organic Products	Residue	HCN	Total [†]
Pyridine	950	12	18	8	10	62	12	49	40	101
	1000	10	13	12*	2	63	6	NM	60*	66
	1050	10	8	16*	0	66	2	NM	80*	82
	1100	9	4	20	0	67	1	NM	101	102
Quinoline	900	1	2	3**	1	93	2	NM	25**	27
	950	2	6	4**	3	85	3	NM	35**	38
	1000	4	12	5**	2	77	4	NM	45**	49
	1100	4	7	6**	0	83	1	NM	55**	56
Benzonitrile	950	0.2	20	7	1	72	0	NM	48	48
	1000	0.7	19	9*	0	71	0	NM	59*	59
	1050	1.2	22	10*	0	67	0	NM	70*	70
	1100	1.4	12	12	0	75	0	NM	82	82
Pyrrole	900	26	34	NM	40	0	68 [†]	NM	NM	68
	950	27	26	NM	3	44	26	NM	NM	26
	975	26	18	NM	0	56	11	NM	NM	11

*Interpolated

**Estimated based on qualitative measurements

[†]The remainder of the nitrogen is believed to be in the residue

*Assume that unknown is Pyridine

NM = not measured

TABLE 15. RESIDUE CALCULATIONS

	Carbon, Percent in Residue						Nitrogen, Percent in Residue**					
	900	950	975	1000	1050	1100	900	950	975	1000	1050	1100
Pyridine		32		63	66	67		49		34	18	0
Quinoline	93	85		77		83	73	62		51		44
Benzonitrile		72		71	67	75		52		41	30	18
Pyrrole	0*	44	56	32*			32*	74	89			

*This suggests that NH_3 or HCN may have formed from pyrrole at 900 C; these measurements were not made.

**In residue or inorganic products for pyrrole.

Products of Oxidative Pyrolysis. The products of oxidative pyrolysis were not investigated in any detail. The organic products from pyridine and benzonitrile were quite similar in type and amounts to those obtained from inert pyrolysis. No significant new products were formed (i.e., no additional GC peaks appeared that would indicate the formation of partially oxidized species). These observations suggest that, as was the case in inert pyrolysis, once reaction of the molecule has been initiated, the reaction proceeds readily until mainly inorganic products are formed.

Two experiments were conducted to determine how much pyridine nitrogen is converted to NO in oxidative pyrolysis. Duplicate experiments were conducted on the oxidative pyrolysis of pyridine in 5-percent oxygen at 860 C (the total pressure was 15 psig as usual). The helium stream from the reactor was collected in an evacuated flask for 2 minutes after the sample was injected and the NO determined by the Saltzman method as described in the Experimental section. In a third experiment under these conditions, the extent of pyridine decomposition was measured. The pyridine decomposed to the extent of 52 percent in agreement with Fig. 37.

The first two experiments gave identical amounts of NO_x , 3.8 micrograms (calculated as NO). Correcting this for unreacted NO* gives 4.6 micrograms of NO. Since 0.2 microliter of pyridine contains 35 micrograms of nitrogen, the decomposed

*Correction calculations for the Saltzman method are discussed in Appendix A.

pyridine (52 percent) would yield 39 micrograms of NO if all nitrogen were converted to NO in the oxidative pyrolysis process. Thus, only 12 percent of the nitrogen from the decomposed pyridine was recovered as NO_x. Calibration tests were not run to ensure that no NO was lost by reaction or absorption in the line from the reactor to the sampling flask. The results obtained in these experiments suggest that at least pyridyl nitrogen is not readily converted to NO under these (fuel-rich) conditions of oxidative pyrolysis, but calibration runs are required to confirm this.

Conclusions From the Pyrolysis of Model Compounds

1. The heterocyclic nitrogen compounds and nitriles are quite thermally stable in an inert atmosphere with 50-percent decomposition temperatures in the range of 910 to 960 C (for a nominal residence time of 0.5 second in a quartz reactor).
2. Pyrrole is much less thermally stable than pyridine under these inert pyrolysis conditions. Quinoline and benzonitrile are less stable than pyridine below 1000 C, but benzonitrile is more stable above 1000 C.
3. From 30 to 90 percent of the carbon that was present in the pyrolyzed model compounds is apparently contained in the residue that forms on the wall of the reactor. Much of the model compound nitrogen remains in the residue at lower pyrolysis temperatures.
4. The major volatile organic products from the inert pyrolysis of pyridine are methane, benzene, and benzonitrile. Quinoline forms mainly benzonitrile and some methane and, at higher temperatures, benzene. Benzonitrile forms mainly benzene and biphenyl; pyrrole forms methane, acrylonitrile, acetonitrile, benzene and benzonitrile. In addition, pyrrole forms two organic products that were not identified, one of which is a C₅ or C₆ compound that has the same GC retention time as pyridine. This compound is the major product from the low-temperature pyrolysis of pyrrole.

5. The distribution of organic products from inert pyrolysis changes as the reactor temperature is increased with the more thermally stable products being favored at the higher temperatures. This suggests that the initial product distribution may be temperature independent, i.e., that a two-stage process is occurring at the higher temperatures. The possibility cannot be ruled out, however, that the primary product distribution is a function of temperature.
6. The presence of 2- to 10-percent oxygen in the carrier gas stream reduces the temperature required for a given extent of model compound decomposition by up to 250 C.
7. The major volatile nitrogen-containing product from the inert pyrolysis of the model compounds is HCN. The amount that forms increases with temperature and the quantitative conversion of pyridine-N to HCN occurs at 1100 C. This is probably the most important result that was obtained in the model compound experiments.
8. Only a few percent NH_3 and virtually no N_2 forms in the inert pyrolysis of pyridine or benzonitrile.
9. The pyrolysis results obtained with model fuel nitrogen compounds indicate that HCN and CN species are more likely precursors to fuel NO formation in combustion than are NH_3 and NH_x radicals.

RESULTS AND DISCUSSION--INERT PYROLYSIS OF FUELS

The pyrolysis of fuel samples (six No. 6 fuel oils, one crude oil, and two coals) was conducted under inert conditions in a small-volume quartz flow reactor similar to that used for the model compounds. The details of the reactor and the analysis procedures have been discussed. The sample sizes ranged from 1 to 2 milligrams and the residence time in the reactor was on the order of 2 seconds. The quartz reactor was 2 mm ID and 12 inches in length. The ID of the reactor increased to 6 mm for a distance of 2 cm at the point (about 4 inches into the furnace) at which the fuel samples were pyrolyzed. The purpose of this volume was to accommodate the larger volumes of gaseous products that form from the pyrolysis of the fuel samples which were 5 to 10 times larger than the model compound samples. Otherwise, the volatile species that are released from the fuel as it is heated would have a much shorter residence time in the reactor than did the model compound vapors. For example, 1 mg of No. 6 fuel oil would form about 5 cc of hydrogen (at 1100 C) if the pyrolysis products were simply carbon and H_2 (assuming a carbon/hydrogen mass ratio of 8).

The fuel sample was weighed into a small quartz boat and the boat was placed in the reactor tube in a cold zone external to the furnace. After any air had been purged from the system by the helium flow, the boat was rapidly moved into the furnace by means of a rod attached to the quartz boat that extended to the exterior of the apparatus through a rubber septum. The carrier helium flowing from the reactor was analyzed for HCN, N_2 , and NH_3 . The HCN was determined by a colorimetric technique after scrubbing it from the gas stream in a bubbler containing aqueous Na_2CO_3 with $CdCO_3$ suspended in the solution.

HCN From Fuel Oil Pyrolysis

The evidence obtained from the pyrolysis of the model compounds that HCN was a major decomposition product prompted an investigation of HCN formation in the decomposition of fuel oils. Initially, the pyrolysis gases were analyzed for HCN using an Orion cyanide electrode. It was found that the sulfide ion present

as H_2S in the pyrolysis gases could interfere in HCN analyses by this technique and, subsequently, an ASTM colorimetric method for HCN determination was modified and developed for this analysis. A detailed description of this analytical method is given in the Experimental section.

Two nominal pyrolysis temperatures, 950 and 1100 C, were used in these studies. Inert pyrolysis of six No. 6 fuel oils and one crude oil gave the results summarized in Tables 16 and 17. These results indicate that HCN is a major product of pyrolysis of fuel oils and that the amount of HCN produced at 1100 C is substantially greater than at 950 C. However, the extent of nitrogen conversion to HCN is less with fuel oils than from the inert pyrolysis of model compounds. The difference in the behavior of the model compounds and fuel oils may be due to a number of factors which could include: (1) part of the nitrogen present in fuel oils may be in chemical structures different from those of the model compounds, (2) the presence of the other components of the fuel oil may modify the pyrolysis reactions, (3) part of the fuel nitrogen may remain in the oil residue (Ref. 2), because of a higher boiling point or (4) the heating rate may be slower in the oil pyrolysis experiments. In any case, these results indicate HCN to be an important intermediate in fuel NO_x formation in combustion processes. At the higher heating rates and temperatures encountered in combustion, HCN could be the principal intermediate.

NH_3 and N_2 From Fuel Oil Pyrolysis

The presence of appreciable quantities of HCN in the pyrolysis products of fuel oils is very significant inasmuch as the oxidation of NH_3 and/or NH_x radicals has usually been considered as the principal path for fuel NO_x formation. To determine if NH_3 was also a major product of fuel oil pyrolysis, analyses of the pyrolysis gases were performed for this inorganic nitrogen species.

A number of analytical techniques were evaluated for determining the ammonia formed. Most of these methods lacked the sensitivity required to detect the small amounts of ammonia that could form from the pyrolysis of milligram samples of fuel oils, one of which contained only 0.22 percent N. Interference from H_2S

TABLE 16. SUMMARY OF EXPERIMENTAL DATA ON HCN FORMATION
FROM INERT PYROLYSIS OF OILS

Sample	Temperature, C	% Fuel-Nitrogen Converted to HCN	
		% HCN	Average
Gulf No. 6 Fuel Oil (Venezuelan Crude) 0.43% N, 2.3% S	1106 953	33.5, 32.3 19.7, 19.0	32.9 19.4
Gulf No. 6 Fuel Oil (Various Crudes) 0.44% N, 0.73% S	1103 950	38.0, 39.6 23.1, 23.3	38.8 23.2
Gulf No. 6 Fuel Oil (Mainly California Crudes) 1.41% N, 1.6% S	1108 950	23.3, 23.2 14.2, 14.7	23.2 14.4
Conoco No. 6 Fuel Oil 0.3% N, 0.7% S	1108 952	43.2, 40.9 19.8, 21.0	42.0 20.4
"EPA" No. 6 Fuel Oil (In-House) 0.22% N, 0.9% S	1103 953	36.8, 37.3 24.3, 24.8	37.0 24.6
No. 6 Fuel Oil (from Ultrasytems) 0.38% N, 0.3% S	1104 950	35.3, 35.0 18.5, 17.2	35.2 17.8
Wilmington Crude Oil 0.63% N, 1.6% S	1107 950	51.5, 48.1 29.4, 31.3	49.8 30.3

TABLE 17. COMPARISON OF HCN FORMATION FROM VARIOUS OILS UNDER
INERT PYROLYSIS CONDITIONS

Sample	% N to HCN		HCN (950 c)/HCN (1100 c)
	(1100 c)	(950 c)	
Gulf No. 6 Fuel Oil (Venezuelan Crude) 0.43% N, 2.3% S	32.9	19.4	0.59
Gulf No. 6 Fuel Oil (Various Crudes) 0.44% N, 0.73% S	38.8	23.2	0.60
Gulf No. 6 Fuel Oil (Mainly California Crudes) 1.41% N, 1.6% S	23.2	14.5	0.63
Conoco No. 6 Fuel Oil 0.3% N, 0.7% S	42.0	20.4	0.49
"EPA" No. 6 Fuel Oil (In-House) 0.22% N, 0.9% S	37.0	24.6	0.67
No. 6 Fuel Oil (from Ultrasystems) 0.38% N, 0.3% S	35.2	17.8	0.51
Wilmington Crude Oil 0.63% N, 1.6% S	49.8	30.3	0.61

and other sulfur species also had to be considered. Two analytical techniques were finally developed. The first involved the catalytic decomposition of ammonia to N_2 and measurement of the N_2 by gas chromatography. The second method utilized the sodium phenate colorimetric analysis. Both of these methods are discussed in detail in the experimental section.

Two major experimental difficulties were encountered during the examination of the pyrolysis gases for NH_3 content. First, continual use of the quartz reactor tube for fuel oil and coal pyrolysis results in changing what was initially an "inert" surface toward NH_3 decomposition to one that is catalytically active. Thus, it was found that 90 percent or more of any NH_3 passed through the used fuel reactor was converted to N_2 at temperatures of 950 C or above. It was postulated that this catalytic behavior of the tube walls was the consequence of deposits from trace quantities of metals present in the fuel oils and particularly from the ash in the coal samples. This problem was not encountered in the model compound reactor.

The second difficulty associated with the determination of NH_3 was the fact that a major part of any HCN formed was also catalytically decomposed to N_2 in the ammonia converter. Decomposition of HCN in the reactor was not a problem except in some of the coal experiments discussed in the next section. Once it had been established that most of any NH_3 formed was decomposed immediately in the quartz reactor, it was decided to decompose any remaining NH_3 to N_2 by an auxiliary catalytic converter. By this means, the sum of the elemental N_2 and NH_3 formed during pyrolysis was determined. To accomplish this, it was necessary to remove HCN from the pyrolysis gases to prevent its catalytic decomposition in the converter. Attempts to find converter conditions that were specific to NH_3 conversion were not successful. The removal of HCN from the pyrolysis gases was accomplished by means of an Ascarite (NaOH on asbestos) trap. The trap was heated to 150 C to avoid potential problems with moisture. Tests performed with HCN passed into the Ascarite trap demonstrated its quantitative removal.

The results listed in Table 18 gave the $N_2 + NH_3$ values found at pyrolysis temperatures of 950 and 1100 C for four of the oils that had been tested previously for

TABLE 18. RESULTS OF MEASUREMENTS OF N_2 AND NH_3 (AS N_2)
FROM INERT PYROLYSIS OF OILS

Run	Fuel Oil, % N	Reactor Temperature, C	Through Converter?	Weight of Oil, mg	$\mu\text{gm N per}$ mg of Oil (calculated)	$\mu\text{gm } N_2 \text{ per}$ mg of Oil (measured)	% -N as N_2
18*	EPA No. 6 (0.22)	954	Yes	1.457	2.20	0.55	25.0
19*	↓	953	Yes	1.360	2.20	0.52	23.6
20*	↓	954	Yes	1.341	2.20	(0.60)	(27.3)
31	↓	960	Yes	1.344	2.20	0.52	23.6
37	↓	954	Yes	1.328	2.20	0.51	23.2
						0.52 ± 0.01 (average)	23.8 ± 0.5 (average)
42	EPA No. 6 (0.22)	1102	Yes	1.453	2.20	0.60	27.3
43	↓	1102	Yes	1.319	2.20	0.64	29.1
						0.62 ± 0.02 (average)	28.2 ± 1.0 (average)
46	EPA No. 6 (0.22)	1105	No	1.323	2.20	0.54	24.6
47	↓	1106	No	1.399	2.20	0.43	19.6
21*	Wilmington Crude (0.63)	954	Yes	1.136	6.30	0.66	10.5
22*	↓	950	Yes	1.446	6.30	0.66	10.5
33	↓	959	Yes	1.281	6.30	0.76	12.1
34	↓	957	Yes	1.366	6.30	0.57	9.0
						0.66 ± 0.05 (average)	10.5 ± 0.8 (average)
38	Wilmington Crude (0.63)	1103	Yes	1.246	6.30	0.74	11.7
39	↓	1102	Yes	1.386	6.30	0.76	12.1
						0.75 ± 0.01 (average)	11.9 ± 0.2 (average)
48	Wilmington Crude (0.63)	1103	No	1.227	6.30	0.80	12.7
49	↓	1102	No	1.091	6.30	0.87	13.8
23	Gulf No. 6 (1.41)	953	Yes	1.478	14.1	0.94	6.7
25	↓	956	Yes	1.076	14.1	0.73	5.2
35	↓	957	Yes	1.193	14.1	0.73	5.2
36	↓	959	Yes	1.458	14.1	0.52	3.7
						0.73 ± 0.10 (average)	5.2 ± 0.8 (average)
40	Gulf No. 6 (1.41)	1102	Yes	1.389	14.1	0.78	5.5
41	↓	1101	Yes	1.193	14.1	0.89	6.3
						0.83 ± 0.05 (average)	5.9 ± 0.4 (average)
50**	Gulf No. 6 (1.41)	1107	No	1.377	14.1	0.72	5.1
52**	↓	1106	No	1.186	14.1	0.92	6.5
51**	Gulf No. 6 (1.41)	1104	Yes	1.213	14.1	3.48	24.7
44	Ultrasystems No. 6 (0.38)	1099	Yes	1.415	3.8	0.61	16.1
45	Ultrasystems No. 6 (0.38)	1099	No	1.462	3.8	0.50	13.2

*Runs 18 through 25 were with Ascarite trap at 25 C; in all others, the trap was at 150 C

**The Ascarite trap was removed from the system in runs 50, 51, and 52

HCN formation. These results indicate the small quantities of nitrogen that were measured as well as the precision of the analyses. The average results from Table 18 are summarized in Tables 19 and 20. The EPA No. 6 oil gave the highest percentage conversion to $N_2 + NH_3$ in inert pyrolysis and its nitrogen content is the lowest of the oils tested. The amount of N_2 measured as the consequence of pyrolysis of the EPA oil represented about one-fourth of the nitrogen contained in the sample.

Interestingly, the absolute amount of N_2 that is formed (representing $NH_3 + N_2$) was found to be only weakly dependent on the bound nitrogen content of the oil and the temperature of the reactor (Tables 18 and 20). It is conceivable that part of the N_2 present in the pyrolysis products was due to dissolved N_2 , but this hypothesis is weakened by the fact that the inert pyrolysis of model compounds in a quartz reactor yielded no detectable N_2 if the converter was bypassed (see above). However, the solubility of N_2 (at 1 atmosphere) is 0.14 mole percent in turbine oil (Ref. 128). If the molecular weight of the oil is 140, the solubility of N_2 is 0.3 microgram per milligram of oil, which is about one-half the value shown in Table 20.

The results given in Tables 19 and 20 indicate that the amount of N_2 formed changed only slightly when the converter was bypassed. This strongly suggests that nearly all of the N_2 was, therefore, formed in the quartz reactor. Thus, it is not possible to give an accurate value for NH_3 content in the pyrolysis gases. Since this converter was shown in calibration experiments to convert pyridine to N_2 (probably via HCN formation and decomposition), the limited effect of the converter also indicates that volatile fuel nitrogen compounds are not present in the reactor products and being converted to N_2 in the converter.

During studies on the catalytic decomposition of HCN, it was found that about 60-percent conversion to N_2 occurred at a temperature of 1050 C. In run 51 (Table 18) the Ascarite trap was removed and all of the gases, including any HCN, were passed through the converter. The increase in N_2 formed was 2.65 μgm per mg

TABLE 19. SUMMARY OF PERCENT FUEL-N CONVERTED
TO $\text{NH}_3 + \text{N}_2$ IN OIL PYROLYSIS
(Measured as N_2)

Oil Sample	% N	Reactor Products Through Ascarite Trap and Converter		Reactor Products Bypass Converter
		950 C	1100 C	1100 C
EPA No. 6	0.22	23.8 \pm 0.5	28.2 \pm 1.0	24.6, 19.6
Wilmington Crude	0.63	10.5 \pm 0.8	10.9 \pm 0.2	12.7, 13.8
Gulf No. 6	1.41	5.2 \pm 0.8	5.9 \pm 0.4	5.1, 6.5
Ultrasystem No. 6	0.38	--	16.1	13.1

TABLE 20. SUMMARY OF MICROGRAMS N_2 PER mg OIL
FROM OIL PYROLYSIS

Oil Sample	% N	Reactor Products Through Ascarite Trap and Converter		Reactor Products Bypass Converter
		950 C	1100 C	1100 C
EPA No. 6	0.22	0.52 \pm 0.01	0.62 \pm 0.02	0.54, 0.43
Wilmington Crude	0.63	0.66 \pm 0.05	0.75 \pm 0.01	0.80, 0.87
Gulf No. 6	1.41	0.73 \pm 0.10	0.83 \pm 0.05	0.72, 0.92
Ultrasystem No. 6	0.38	--	0.61	0.50

of oil (3.48-0.83). Since this oil had previously been found to form 23.2 percent HCN (defined as percent fuel-N converted to HCN) at 1100 C (Table 17), the increased amount of N_2 represented about 80-percent conversion of the HCN postulated to be present. Thus, this test served to demonstrate once again the effectiveness of the Ascarite trap for HCN removal. Calibration samples of HCN were passed through the quartz reactor periodically at 1100 C to ensure that no significant amount of HCN decomposition occurred in the reactor.

HCN From Coal Pyrolysis

Inert pyrolysis of a limited number of coal samples gave results similar to those obtained from the pyrolysis of fuel oils: considerable HCN and smaller amounts of $N_2 + NH_3$ with much of the fuel nitrogen apparently remaining in the nonvolatile residue.

A particular experimental problem associated with these tests was the decomposition of HCN in the presence of deposits from the coal pyrolysis runs. Simple burnout of the residues did not restore the inert property of the reactor walls. Chemical etching of the quartz reactor tube and boat, after removal from the ancillary equipment, with 30- to 60-percent HF solutions, was necessary after every two or three runs with coal. To ensure the validity of the reported HCN measurements, HCN calibrations were run before and after each coal pyrolysis experiment. The calibration experiments indicated that: (1) at most, only a couple percent of HCN decomposed in a freshly chemically etched reactor at 1100 C, and (2) after two or three coal samples had been pyrolyzed in an etched tube, the decomposition of HCN at 1100 C was 5 to 40 percent (i.e., the residue effect is not predictable and may be a function of coal type and pyrolysis temperature).

Samples of EPA and IFRF-N coals (1.5 to 2 milligrams) were pyrolyzed in helium and the HCN formed was measured by the barbituric acid colorimetric method. The results of the two coals were as follows:

Coal Sample	% N	% Fuel-N Converted to HCN	
		957 C	1106 C
EPA	1.17	20.3, 18.0	29.8, 30.2
IFRF-N	1.8	--	26.2, 22.7

NH₃ and N₂ From Coal Pyrolysis

Chemical etching of the quartz tube reactor after coal samples had been pyrolyzed in it restored its compatibility with HCN at elevated temperatures, but did not prevent catalytic decomposition of NH₃. Thus, it was necessary to measure total N₂ (N₂ + NH₃) by the GC method, as was done for the fuel oil pyrolysis studies. The total N₂ formed from inert pyrolysis of the EPA coal in two experiments at 954 C were 8.3 and 10.5 percent conversion of fuel-N, or 0.97 and 1.23 µg of N₂ per mg of coal, respectively. This quantity is somewhat higher than the 0.5 to 0.7 µg of N₂ per mg that was obtained from the fuel oils at this temperature. Some of the measured N₂ could have been produced by the catalytic decomposition of HCN in the quartz reactor.*

Discussion of Fuel Results

The inorganic nitrogen product distribution for coal is surprisingly similar to that obtained with the fuel oils. The fuel oils underwent from 23- to 42-percent conversion to HCN at 1100 C and the two coals studied gave 24- and 30-percent HCN, respectively, at this temperature. The oils formed 15- to 25-percent HCN at 950 C, and the EPA coal formed 19-percent HCN at this temperature and about 10-percent NH₃ + N₂. The ratio HCN (950 C)/HCN (1100 C) varied from 0.50 to 0.67 for the oils, while this ratio was 0.67 for the EPA coal. The conversion of fuel nitrogen in the oils to N₂ + NH₃ varied from 0.5 to 0.7 µgm (as N₂) per mg of oil at 950 C. The EPA coal produced nearly twice this amount of N₂ + NH₃, but these products still only accounted for about 10 percent of the nitrogen in the coal.

This similarity of product distributions suggests that the percolation of the pyrolysis products of coal through a hot solid matrix before entering the vapor phase has little effect. Under combustion conditions where the flame front has not collapsed onto the surface of the particle, the mechanisms for fuel NO formation may be similar, therefore, for coal and fuel oils. The results obtained under

*This was not a problem in the fuel oil experiments.

this program strongly suggest that this mechanism for homogeneous fuel NO formation involves CN species rather than NH_x species or NH_3 .

Although the maximum amount of fuel-N that was converted to HCN was from 25 to 35 percent, this could represent most of the "volatile-N" in the fuels, especially in the case of the coals. Sternling and Wendt (Ref. 2) estimated that 60 percent of the fuel-N would remain in the initial residue from the vaporization of a residual oil and 80 percent on the average, from the vaporization of coal. They point out that some additional nitrogen will become volatile during the pyrolysis of the char, but the amount is unknown. The reverse process must also be considered, i.e., the formation of residue during pyrolysis from initially volatile nitrogen compounds. In the fuel pyrolysis experiments, a carbonaceous residue formed on the reactor wall downstream of the sample boat. In any event, the quantities of HCN that were measured may well contain most of the volatile fuel nitrogen and, therefore, HCN may be the principal intermediate in the formation of "homogeneous" fuel NO.

Information on how fuel nitrogen compounds are distributed between the volatile fractions and the char is quite limited (Ref. 2). Data reviewed in Ref. 71 indicate that, for a number of types of coal, only about one-third of the fuel nitrogen is contained in the volatile fraction (even at pyrolysis temperatures up to 1300 K). cursory experiments were conducted to investigate the volatility of the nitrogen compounds in the coals used in this study. Unfortunately, the results obtained were clouded by the fact that analyses conducted 4 months apart by the same commercial laboratory gave quite different total nitrogen contents for these coals. These results are presented in Appendix B.

In most previous studies of the rapid pyrolysis of coals, the nitrogen-containing products such as HCN and NH_3 were not collected and measured. However, Ramachandran et al., in India (Ref. 120), rapidly pyrolyzed an "N-enriched" coal (coal fertilizer which contains about 20 percent nitrogen and is prepared by reacting coal with NH_3) and measured quantities of HCN that appear to be in good agreement with the amounts obtained in this study. Both slow and rapid heating were employed and substantial

yields of NH_3 and HCN were obtained. Increasing the pyrolysis temperature from 900 to 1200 C increases both N_2 and HCN. AT a heating rate of only 5 degrees/minute, the HCN yield was 60 pounds HCN per ton of coal. By thermal shock heating at high temperatures, the HCN yield was increased to 266 pounds HCN per ton. This represents 35 percent of the total N in the coal. The high yields of N_2 and NH_3 obtained indicate that the type of nitrogen compounds present in the enriched coal are quite different from natural fuel nitrogen compounds.

PHASE II - BURNER STUDIES OF FUEL NO_x FORMATION

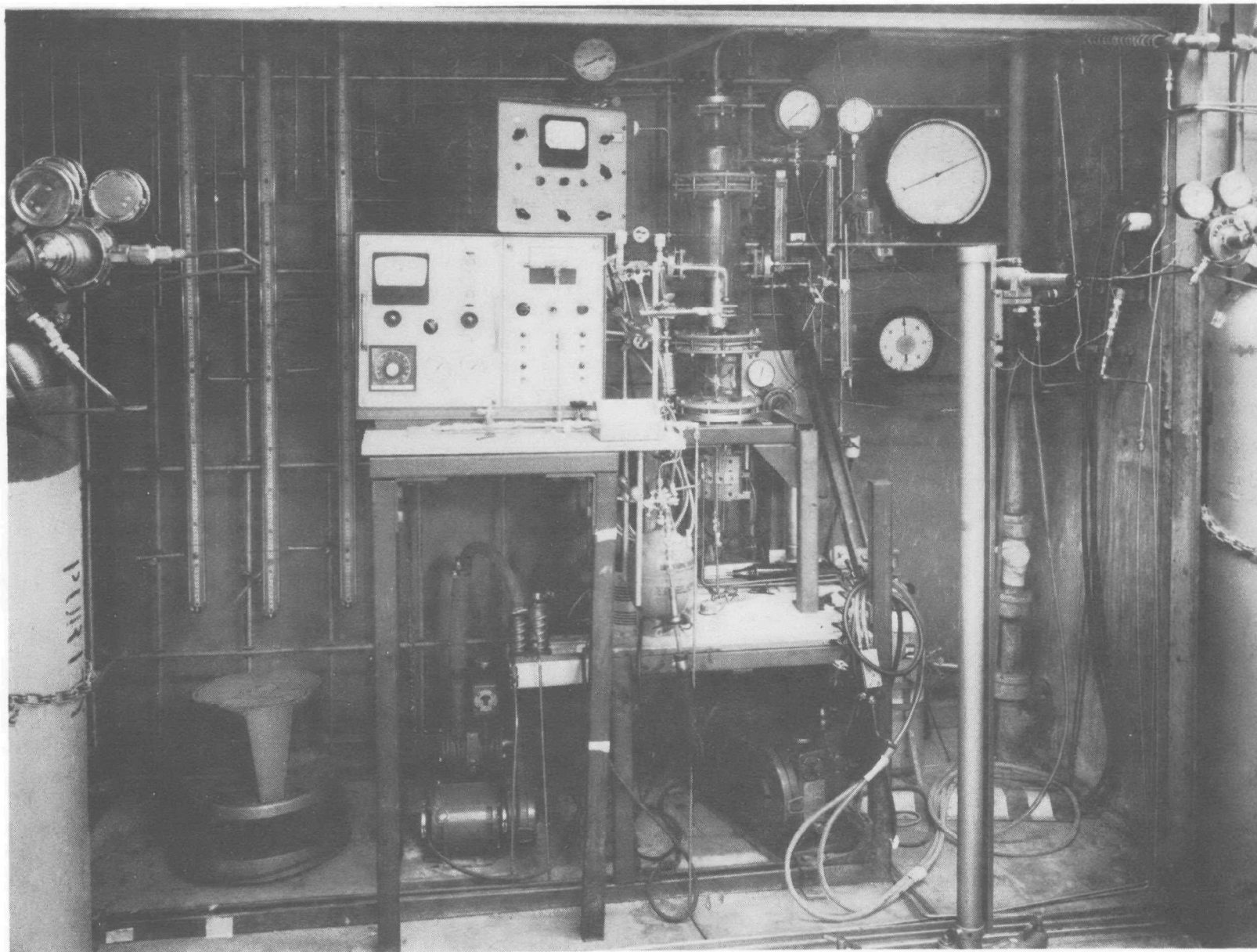
The phase I pyrolysis experiments, which investigated the chemical processes that occur in the preflame stages of combustion, demonstrated that HCN is probably the major initial nitrogen-containing species formed from fossil fuels. Some NH₃ may form as well. The objective of the Phase II burner study was to investigate in detail the kinetics and mechanisms of fuel NO_x formation in flames from the potential combustion intermediates HCN and NH₃.

HCN and NH₃ were added to premixed, flat CH₄-O₂-Ar flames and the temperature and species concentrations measured at various distances above the burner. NO was also employed as an additive in some experiments to determine its fate once formed. Argon was used as the diluent rather than N₂ to preclude the possible formation of thermal NO_x. The experiments were conducted at a pressure of 0.1 atm to spread the flame zone.

The measured species profiles, when corrected for downstream diffusion of reactants and upstream diffusion of products, establish where in the flame the added nitrogen compounds react and the NO forms and the rates at which these processes occur. Therefore, such measurements determine, in principle, the global rates of fuel NO_x formation as a function of distance (time), temperature and species concentration.

PHASE II: EXPERIMENTAL

A photograph of the low-pressure flat-flame burner system used in these experiments is shown in Fig. 43. The apparatus consists of a water-cooled burner port with a micrometer positioner, a low-pressure chamber with a large vacuum pump, a quartz microprobe for gas sampling, a thermocouple probe, a gas-sampling manifold with a small oil diffusion pump and fore pump, a chemiluminescent analyzer, and a gas metering system. The pressure in the chamber is normally held at 76 torr. The gases are metered by means of critical flow orifices for CH₄, O₂, and Ar feed to the burner and Brook's flowmeters for Ar purge gas and the N-compound additives. These items will be described at greater length in the following pages.



5AA21-4/7/75-C1C

Figure 43. Low-Pressure Flat-Flame Burner Apparatus

Burner

The flat-flame burner port was machined from 2-inch nominal schedule 40 stainless-steel pipe and screws into an aluminum base where an O-ring seal provides a pressure-tight fit. A drawing of the burner is shown in Fig. 44. Cemented in a recess at the burner exit is a 1/8-inch-thick sintered porous plate which furnishes a flat velocity profile across the ports. The porous plate was cut from a sheet of 1/8-inch-thick stock composed of sintered-steel (type 316L) particles and having a mean pore size of 65 microns (Pall Trinity Micro Corporation). An 8-mesh stainless steel screen was spot welded to the top of the burner port about 1/8 inch above the porous plate to act as a flame holder. Immediately below the porous plate, and in contact with it, is a 1/8-inch copper tubing coil for water cooling the burner; the copper tubing enters and exits the burner through flexible lead fittings located in the aluminum base. The burner interior, below the copper coil, is filled with Pyrex balls (Fig. 44) of various sizes to promote gas mixing and to negate chances of combustion occurring inside the burner. Gas is fed to the burner via a length of 3/8-inch stainless-steel tubing which also serves as a pedestal, or support, and is used to position the burner with respect to the fixed gas sampling and thermocouple probes.

The 3/8-inch stainless-steel tubing "pedestal" enters the low-pressure chamber enclosing the flat-flame burner via a rotary vacuum connector seal (CEC type No. SR-37) fitted to the steel base of the chamber. Outside the chamber, the pedestal is firmly clamped to a micrometer-driven translation stage which, in turn, is anchored to the base of the low-pressure chamber with a right-angle bracket. The micrometer-driven translation stage has a 50-mm movement and can easily be positioned with a precision of less than 0.01 mm and locked in place. Spring loading of the translation stage was inadequate to move the burner up when the micrometer was so adjusted. This required the translation stage to be manually moved up to the new micrometer position. Below the translation stage, the 3/8-inch-stainless steel tube is connected to 1/4-inch copper tubing containing a large single turn of tubing to facilitate the vertical movement of the burner. Moving the burner

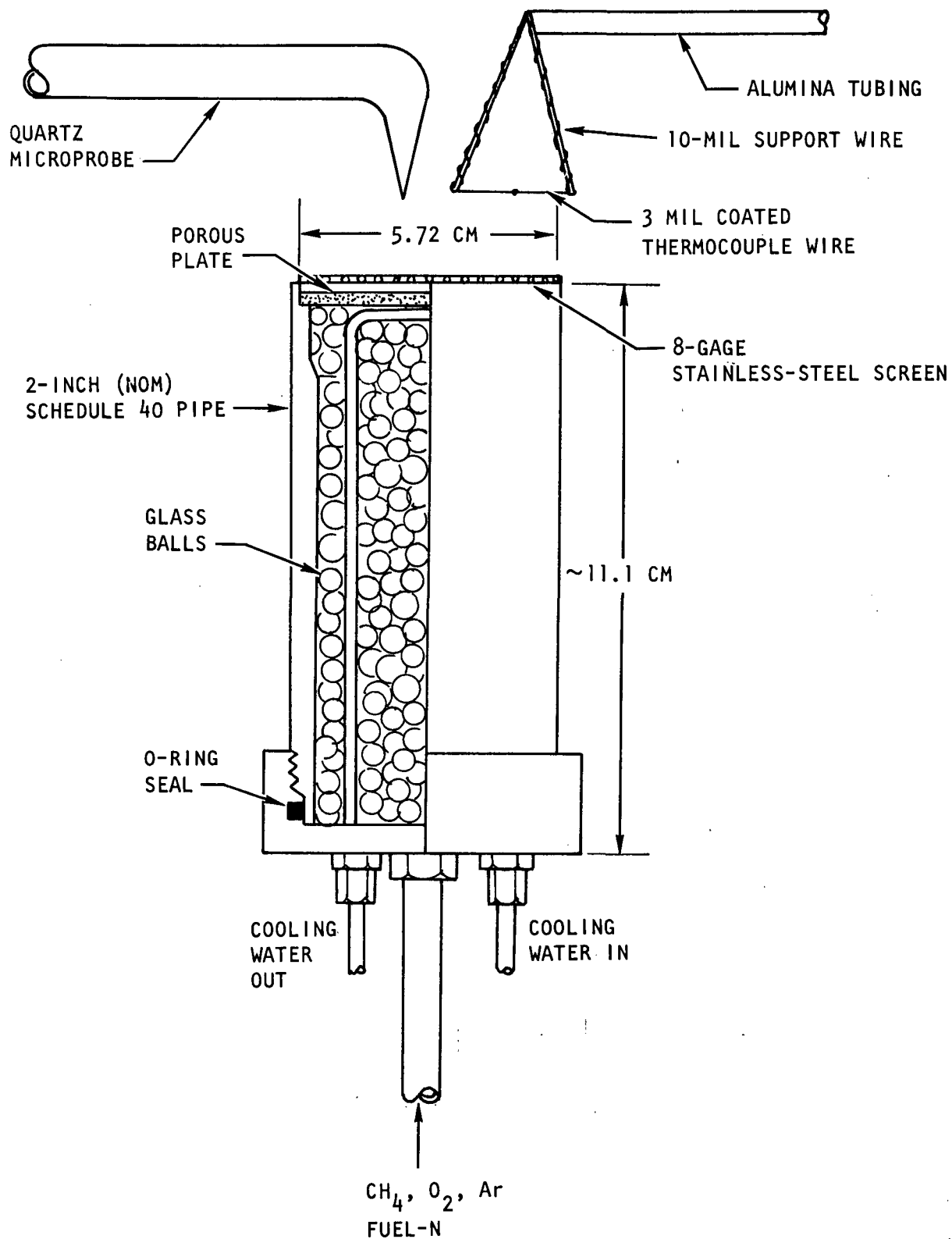


Figure 44. Flat-Flame Burner (Cut-Away View)

over a distance greater than 50 mm can be done by loosening the clamp holding the burner pedestal to the translation stage, manually positioning the burner, and then reclamping the pedestal. The distance moved by the burner in such a case must then be determined by using a cathetometer.

The flame was ignited with a high-voltage spark fed into the low-pressure chamber to the burner with an insulated igniter rod. The spark was generated by touching the igniter wire outside the chamber with a Tesla coil. Ignition was carried out at 130 to 150 torr, after which the pressure was reduced to the value desired. Fuel-rich mixtures were more difficult to ignite and, as a result, the flame would be ignited closer to stoichiometric condition and then the CH_4 feed would be increased to obtain the desired equivalence ratio.

Low-Pressure Chamber

The low-pressure chamber consists of three pieces of 4-inch ID Pyrex pipe connected with glass pipe joints and gaskets (Fig. 43): a lower section, a cross with 1-inch ID side arms, and a reducer section to go from 4-inch ID to 1-inch ID. The two side arms for the cross are capped with aluminum plates containing Swagelok fittings with Teflon inserts to hold the gas sampling microprobe and the Pt-Pt/10%Rh thermocouple probe. The reducer forms the top of the chamber and is connected to 3/4-inch stainless-steel tubing leading to a pressure control valve and a large vacuum pump. As long as the pump can maintain a pressure ratio greater than 2 across the valve, the pressure control valve is, in effect, a critical flow orifice with a variable area. With sonic flow at the valve, pressure fluctuation from the pump will not propagate back to the low-pressure chamber. The base of the low-pressure chamber is fabricated of 1/2-inch aluminum plate and contains fittings for the burner pedestal (burner gas supply), cooling water entrance and exit, pressure tap, an insulated igniter feedthrough, and an argon gas purge line. There are, in addition, four screw holes for mounting the bracket for the micrometer-positioned translation stage.

The chamber pressure was monitored with a Heise gage marked off in 1 torr divisions from 0 to 1000 torr. The gage was adjusted frequently for changes in barometric pressure.

Gas Flow Metering

Methane, oxygen, and argon for the burner were supplied from cylinders with pressure regulators to drop the pressure to about 50 psig. Each gas line is equipped with line filters (Matheson Gas Products) to keep large particles out of the flow metering system. The gases were metered with critical flow orifices consisting of accurately sized sapphire orifice jewels (Aurele Gatti, Inc.). The small jewels were mounted by force fitting them into Teflon holders which were then inserted by a force fit into Swagelok fittings. Upstream pressure on the orifices was accurately regulated by Brook's model 8601 line pressure regulators. Mercury manometers, approximately 2 meters long, were used to measure the upstream pressure at the orifices. As long as the pressure ratio is greater than the critical ratio,

$$\left(\frac{2}{1 + \gamma} \right)^{\gamma/\gamma-1} \quad (120)$$

the orifice flowrate will be independent of the downstream pressure. The flow system is quite similar to that reported by Andersen and Friedman (Ref. 130).

Flowrate calibration of the critical-flow orifices and flowmeters was obtained by measuring the rate of pressure rise in a known volume being filled with the metered gas. A Heise gage equipped with a potentiometer provided a means of recording P versus time in the known volume.

The methane used was 99.97 percent pure (ultrahigh purity-Matheson), the argon was 99.99 percent pure and contained a maximum of 15 ppm N₂ and 5 ppm O₂, while the oxygen was 99.96 percent pure and contained a maximum of 10 ppm N₂ and 3000 ppm Ar. The lecture bottle of anhydrous ammonia had a minimum purity of 99.99 percent and the commercial hydrogen cyanide had a specified minimum purity of 99.5 percent with 0.5 percent maximum water.

Gas-Sampling Microprobe

Gas samples were taken at various distances through the flat flame (along the center line) by a quartz microprobe. The probe was uncooled; the reacting gases were quenched aerodynamically by expanding them from the pressure in the reaction chamber (usually 76 torr) to about 1 torr. The probes were constructed from 9-mm quartz tubing which was pulled to taper down to a very small-diameter tip containing the sonic sampling orifice. About 25 mm from the tip, the sampling probe was bent 90 degrees so that the reacting gases in the flame could be sampled parallel to the gas flow when the microprobe was mounted in one of the 1-inch-diameter side arms of the low-pressure chamber. The necessary design considerations for microprobes that will result in a minimum flame disturbance have been described in the literature (Ref. 131). The diameter of the sonic orifice at the tip of the tapered probes was always between the recommended values of 10 and 100 microns to ensure that the flow disturbance occurring upstream of the probe as a result of the sampling rate would be minimized.

The flames examined in this experimental program were about at the upper temperature limit that could be handled with the uncooled quartz probes. Radiation cooling permits the probes to be used to sample gases at temperatures somewhat higher than the softening point of the quartz. After each detailed probing experiment, the microprobe sampling orifice was visually inspected for damage with a binocular microscope. It was then checked by sampling an N_2 -NO standard gas mixture at 76 torr using the chemiluminescent analyzer (CA) to (in effect) determine if changes had occurred in the sampling rate which would indicate changes in the orifice diameter. The gas sampling rate was important to this experimental program because the capillary flowmeters in the CA were bypassed (the reasons for this will be discussed later in this report).

Temperature Measurement

Temperature measurements in the flame were performed with Pt-Pt/10%Rh thermocouples. The thermocouple junction was formed from either 1- or 3-mil wire by flame welding the wires using a very small flame under a binocular microscope. (The use of 1-mil

wire was discontinued after the NH_3 screening tests; thereafter, 3-mil wire was used). As much as possible, excess metal at the thermocouple junction was trimmed away. The 3-mil thermocouple was then given a 2- to 3-micron-thick coating of Al_2O_3 using a sputtering technique available in one of our laboratories. Coating the platinum wire prevents the catalysis of reactions on its surface that would heat the wire and result in erroneous temperature measurements.

Thermocouple Coatings. Al_2O_3 coatings were employed because of a lack of success with the widely used SiO_2 coatings. Before using the Al_2O_3 -coated wires, the silica-coated thermocouples were used for NH_3 additive screening tests where they were made well above the flame front. When an attempt was made to determine a temperature profile completely through a flame at $\phi = 0.8$ or 1.5 for the detailed probing experiments, the noncatalytic SiO_2 coating would fail at gas temperatures of 1860 to 1900 K (corrected for radiation cooling of the thermocouple). The wire temperature at failure would be just below 1700 K. An examination of the wire surface revealed the SiO_2 had beaded up and exposed the metal surface.

The SiO_2 was deposited on the thermocouple wires by vaporizing dimethylpolysiloxane (Dow Corning 200 Fluid) into the gas fed to a Meker burner and passing the thermocouple wire through the flame gases (Ref. 131 and 132). When trouble was experienced with the SiO_2 coating, the thermocouple wires were carefully cleaned by immersion in acetone and then in concentrated nitric acid before they were coated. A recorder was connected to the thermocouple to be coated and the SiO_2 coatings were applied at 1800 K (Ref. 132). When the coatings continued to fail, the thermocouple wire diameter was increased from 1 to 3 mils to obtain more radiation cooling. The maximum temperature measured before SiO_2 coating failure in any of these series of tests was about 1910 K.

Several methods of applying Al_2O_3 coatings were examined after the use of SiO_2 was abandoned. An alumina base ceramic, used in the electronics industry as a dielectric material in thick-film circuitry, was applied to the wire and fired on at 1530 K. A check of the thermocouple after firing the ceramic indicated that it was no longer reliable. Perhaps some of the glassy binding materials

(silicates) in the ceramic attacked the thermocouple junction or, possibly, the spot-welded joints, where the thermocouple wire was attached to the 10-mil support wire, were loosened by the ceramic during the firing process.

A plasma-spray gun technique for applying an Al_2O_3 coating was tested briefly. A small length of 3-mil platinum wire was coated with Al_2O_3 particles. The coating did not adhere well to the metal, but formed a protective casing around the wire. With practice on the part of the spray gun operator, it might have been possible to lay down an even, thin coating of Al_2O_3 particles on the wire, but the initial attempt produced a thick coating. In addition to its thickness, the coating, composed of Al_2O_3 particles partially fused together, appeared to be porous. In a thinner coating, this porosity might result in less protection of the platinum surface.

The third approach to applying an Al_2O_3 coating, a high-vacuum sputtering technique, proved successful. The coating is glassy in appearance and very adherent. The coated wire was stiff and springy and when bent into a tight loop, would tend to kink or bend sharply at several points rather than bend smoothly. Experiments indicated the Al_2O_3 coatings applied were good up to a thermocouple wire temperature of about 1900 K which, for the 3-mil wire and flow conditions used in these experiments, would mean a gas temperature of about 2100 K because of radiation cooling. Al_2O_3 coating failure appears to result from differences in the thermal expansion of the metal and the aluminum oxide which leads to crazing of the oxide coating. To avoid problems of coating deterioration, the thermocouple was replaced after each detailed probing experiment.

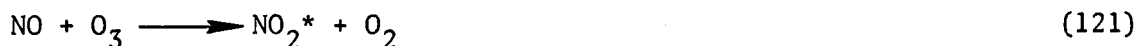
Thermocouple Probe. The thermocouple probe itself consisted of 10-mil thermocouple wire support arms of Pt and Pt/10%Rh strung through a two-hole alumina tube and cemented in place with Sauereisen cement (No. 29). The support arms extend out about 35 mm from the end of the cement-sealed two-hole alumina tube (Fig. 44). The alumina tube was, in turn, cemented into a short length of 1/4-inch stainless-steel tubing. A 1/4-inch Swagelok fitting, drilled through to pass the 1/4-inch tubing of the thermocouple probe and fitted with Teflon inserts,

severed as a feed-through for the thermocouple probe to enter the low-pressure chamber. The 3-mil thermocouple wire was strung through small eyelets formed at the ends of the 10-mil support wires, wound around the support wire, and then spot welded to it. Normally, an 18- to 20-mm length of 3-mil thermocouple wire was suspended between the support arms. The length of the suspended wire is dictated by the 1-inch diameter of the side arm in the low-pressure chamber through which the thermocouple must slide to be set in place over the burner. The support arms are bent 90 degrees from the probe so that the arms hang downward when the thermocouple probe is inserted over the burner. This is done to minimize sagging of the support arms that might result from long exposure to high temperature. Sagging of the 3-mil wire is lessened by the glassy, very adherent Al_2O_3 coating which makes the 3-mil wire stiffer and springy, and by reliance on the 10-mil support wire to keep the 3-mil wire under slight tension.

The thermocouple readings must be corrected for the effect of radiation cooling to ascertain the true gas temperature. The procedure used to obtain the temperature correction is described in Appendix F.

Chemiluminescent Analyzer

The gas sample withdrawn from the flame was analyzed for NO , NO_2 , NH_3 , and HCN with a chemiluminescent gas analyzer (CA). The CA used was a model 10A self-contained unit manufactured by the Thermo-Electron Corporation. This instrument utilizes the chemiluminescent reaction between NO and O_3 as a means of monitoring NO concentration, i.e.,



The ozone is produced from an O_2 supply by an ozonator in the instrument and mixed with the sample gas in a flow reactor. A photomultiplier and optical filter mounted at one end of the reactor monitors photons emitted by the electronically excited NO_2 . The number of photons detected per unit time is primarily a function

of both NO concentration and the sample flowrate through the reactor. The residence time of gas in the CA reactor is quite large compared to the reaction time so that the photon emission rate is directly proportional to the feed rate. Since the excited NO_2 can also lose energy via collisions with other species, the rate of photon emission can be a function of pressure, at sufficiently high pressures, and alter the direct relationship between the sample flowrate and the photon emission rate.

The CA contains a capillary flow metering system designed to operate with a reactor pressure between 3 and 10 torr and a gas sample pressure of 1 atmosphere. Since the gas samples from the flat-flame burner was to be quenched by expansion to about 1 torr and the gas was sampled through a sonic orifice with a diameter less than 100 microns, the flow metering system in the CA was superfluous and was removed. The pressure in the reaction chamber was adjusted by turning a control valve installed in the ozone feed line until the reactor pressure was 0.8 torr with no sample feed. With sample feed the pressure increased to about 0.9 torr and the use of the calibrated air leak (described later) increased this another 0.1 or 0.2 torr.

Calibration for NO. The CA was calibrated for use with the sonic sampling orifice of the quartz microprobe by inserting the microprobe in a small calibration chamber (Fig. 45) containing a standardized mixture of 92 ppm NO in N_2 at 76 torr (the pressure at which the detailed probing experiments were performed). A calibration adjustment knob on the CA was used to adjust the dial reading of the CA until it agreed with the NO concentration in the standard gas. The molar flowrate, \dot{N}_s , of the standard gas to the CA (as limited by the flow through the probe orifice) is given by:*

$$\dot{N}_s = CA_o P_s \sqrt{\frac{g\gamma_s}{M_s R T_s} \left(\frac{2}{\gamma_s + 1} \right)^{(\gamma_s + 1)/(\gamma_s - 1)}} \quad (123)$$

*The variables in the following equations are defined in the Nomenclature List on page 345.

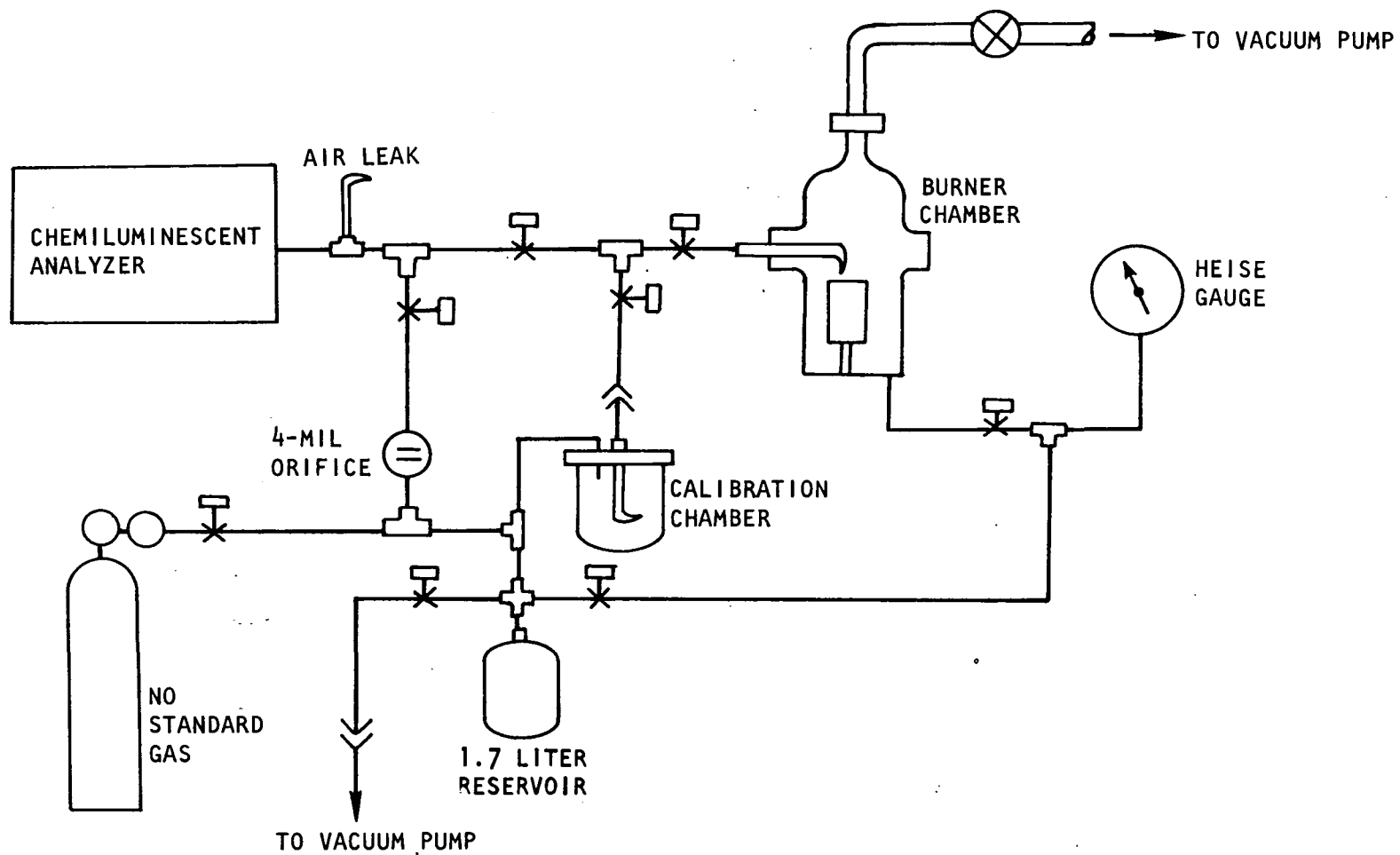


Figure 45. Schematic of Chemiluminescent Analyzer Calibration System

For a standardization mixture that is mainly N_2 :

$$\dot{N}_s = CA_o P_s \sqrt{\frac{g}{59.75 RT_s}} \quad (124)$$

Normally C , A_o , g , R , and P_s will be constant throughout a calibration of the instrument and its subsequent use to measure ppm NO in an unknown. When using the microprobe to measure NO concentration in an unknown (i.e., the flame) the ppm NO reading of the CA must be corrected for the change in the molar feed rate through the orifice between the measurement of the calibration standard and the unknown. The equation for this correction is:

$$\dot{N}_u = \dot{N}_s \sqrt{\frac{59.75}{M_u} \frac{T_s}{T_u} \gamma_u \left(\frac{2}{\gamma_u + 1} \right)^{(\gamma_u + 1)/(\gamma_u - 1)}} \quad (125)$$

T_s is the temperature of the standard gas at the critical flow orifice and T_u is the temperature of the "unknown" gas at the critical flow orifice. Since a lower unknown flowrate, \dot{N}_u , would produce a lower ppm NO reading on the CA, the correction to the ppm NO reading on the CA dial is given by:

$$\text{NO corrected} = \text{NO read} \times \frac{\dot{N}_s}{\dot{N}_u} \quad (126)$$

The linearity of the response of the CA to the sample flowrate was checked (because of the effect of collision rate on the probability of photon emission) by noting the CA reading of NO concentration in the standard gas as the pressure on the sonic sampling orifice (p_s in Eq. 123) was changed. For room-temperature calibrations with the orifice size and CA reaction chamber pressure used, the response did become nonlinear at sample pressures much above 76 torr. Therefore, Eq. 126 would not be accurate for higher pressure room-temperature calibrations. Because of the lower gas densities involved, the CA response was linear with respect to sample flowrate when probing flames at pressures as high as 0.4 atm.

Because the CA will drift slightly over a period of time, it is convenient to have a method for checking its calibration during an experiment without having to shut down, remove the microprobe from the low-pressure chamber, and install it in the

calibration chamber setup. A means of doing this was devised and plumbed into the CA sample feed line (Fig. 45). A 4-mil (approximately 100 microns) sapphire jewel, mounted similarly to the orifice jewels used for metering CH_4 , Ar, and O_2 to the burner, was setup to meter the NO standard gas at the desired upstream pressure (76 torr usually) in a parallel feed line to the CA. With the microprobe installed in the calibration setup, when the CA is properly adjusted for the microprobe flow, the response of the CA to the calibration gas fed through the 4-mil orifice at the same upstream pressure is noted. One can then use the NO reading obtained with the 4-mil orifice as a calibration standard for the CA-microprobe combination. The upstream pressure on the 4-mil orifice and the calibration chamber for the microprobe is measured with a Heise gage.

Conversion of N-Species to NO. Concentration measurements of nitrogen compounds other than NO are quite possible with a CA if they can be reliably converted to NO. Supplied with the Thermo-Electron Corporation CA is a heated (400 C) catalytic converter (and a temperature regulator) for converting NO_2 to NO. If operated at higher temperatures, this catalyst (molybdenum) can also be used to convert NH_3 and HCN to NO. Calibration curves were obtained for the percent conversion of both NH_3 and HCN to NO. In the absence of sufficient O_2 concentrations in the gas sample, the percent conversion of NH_3 and HCN to NO on the catalyst dropped appreciably. Thus, a controlled air leak was installed in the CA sample line (Fig. 45). The air leak is a small hole in a piece of quartz tubing set in a side arm to the sample line. Under these conditions, the conversion of NH_3 to NO in the molybdenum converter ranged from 45 to 60 percent, depending on the NH_3 concentration, and the range for HCN conversion was 60 to 87 percent.

Typical calibration curves are shown in Fig. 46 for HCN, with and without air added to the sample, and for NH_3 with added air (a complete calibration was not made for NH_3 without the air leak). With added air, the conversion of HCN to NO was nearly quantitative up to 750 ppm. The HCN curve then broke sharply with the additional HCN (above 750 ppm) being converted only to the extent of about 50 percent. The NH_3 calibration curve was nearly linear giving about 50 percent conversion at all concentrations. The calibrations were conducted by microprobe sampling of metered mixtures of the additive in unburned Ar, O_2 and CH_4 as the gas mixture

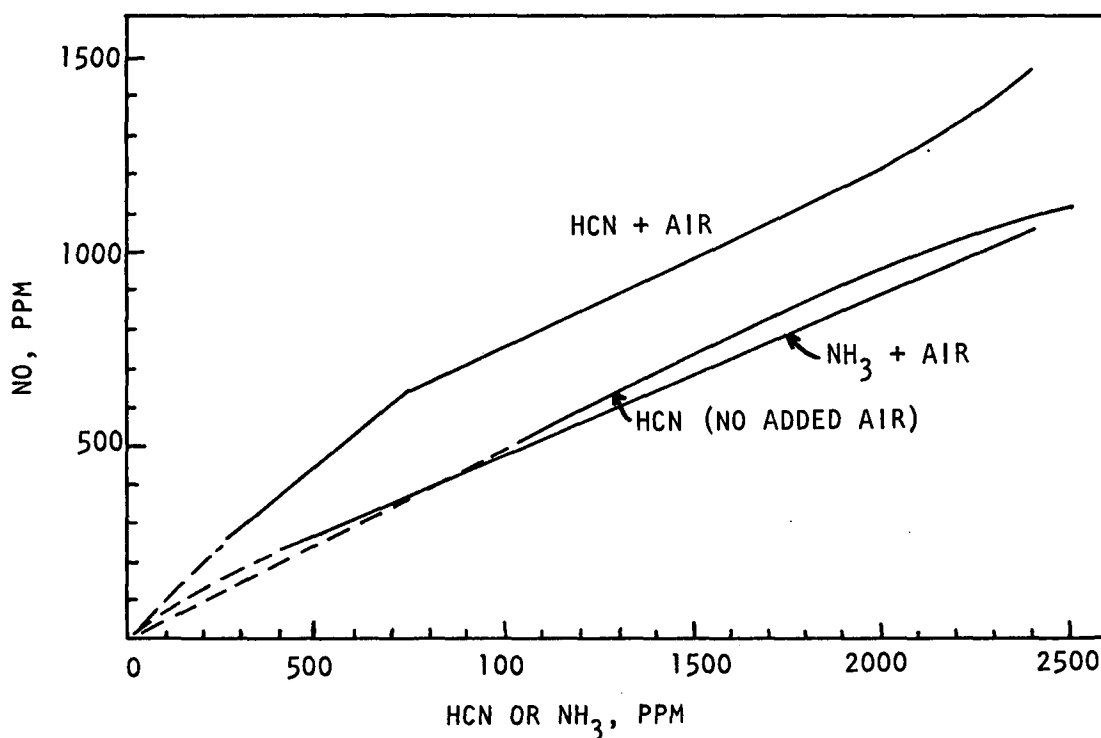


Figure 46. Typical Calibration Curves for Molybdenum Converter at 800 C (Solid Curves Denote Range of Measurements)

issued from the burner. When using the metered air leak, the conversion efficiency was shown to be independent of the O_2 content of the sample entering the probe (from 0 to 30 percent). No calibration curve was obtained for cyanogen but brief tests indicated that it also was converted to NO by the molybdenum catalyst at 800 C.

The percent conversion to NO was a function of the actual amount of NH_3 or HCN passing over the catalyst per unit time. Consequently, when using the catalytic converter, the CA meter reading of NO ppm was first converted to the equivalent amount of NH_3 or HCN via the calibration curve, then the correction to the ppm NH_3 or HCN was made for the change in the sampling rate at the sonic orifice of the microprobe according to Eq. 125 and 126.

The molybdenum catalyst that is supplied by the CA manufacturer for the conversion of NO_2 to NO is not a true catalyst but rather a regenerable reactant. The "catalyst" was not intended for use at temperatures over 500 C because an oxidation

process, which can apparently be reversed if it occurs below 500 C (by passing a stream of H_2 through the converter for several hours), becomes irreversible at higher temperatures. When used at 800 C, the catalyst may change in efficacy for conversion of NH_3 and HCN to NO as an oxide coating develops. As a result, the catalyst calibration curve must be checked often.

Gas Sample Analyses

Batch gas samples taken during an experiment were analyzed by an outside commercial laboratory using mass spectroscopy. The gas samples were taken and stored in 1-liter sample bottles until they were analyzed. The sample bottles had two feed lines, one with a break seal and the other open but with a slight constriction. After the sample bottle was mounted on the sample manifold, it was evacuated to several microtorr with an oil diffusion pump and heated. The bottle was then filled to a pressure of several torr with gas sampled from the flame, evacuated to several microtorr again, and heated with a torch (the glass around the feed line constriction was heated until a slight softening was perceived). After the second filling with sample gas to a pressure of 1 to 2 torr a torch was used to seal the inlet line at the constriction. The break seal in the remaining line was opened when the bottle was mounted on the inlet system of the mass spectrometer for analysis.

The analyses reported the mole fractions of H_2 , CH_4 , NH_3 , H_2O , C_2H_2 , CO, N_2 , O_2 , Ar, CO_2 , NO_x (including NO and NO_2), H_2CO , C_2H_6 , C_2H_4 , and HCN. During the course of experimentation, it soon became clear that the mole fractions reported for NH_3 , HCN, N_2 , and usually NO_x were quite inaccurate and that some H_2O was always missing from the analyses. Therefore, NH_3 , HCN, and NO analyses were obtained by the use of the CA operating "in line," i.e., in a continuous stream of freshly sampled gas. An alternative means of analysis for N_2 in the low-pressure gas samples was not developed.

The mass spectroscopy (MS) results were corrected for the missed H_2O as well as possible by use of a material balance for H and O. There are difficulties associated with using a material balance on a rapidly reacting gas mixture in which

diffusion plays a role. Strictly speaking, one should utilize all of the gas samples and obtain flux profiles through the flame for each of the species and from the flux data determine the deficient components. This, however, can be long and tedious process even when the diffusion coefficients for the species are available. The procedure used here to roughly determine the amount of missing H_2O consisted of using the argon analysis as a base since it does not change appreciably in mole fraction through the flame and, hence, requires no diffusion correction. The Ar was used to calculate the total H and O from the metered $CH_4/O_2/Ar$ feed rates; the amount of H and O missing were found by subtracting the H and O material balance obtained by the MS analysis from the total H and O calculated from the Ar. Usually, the ratio of missing H to missing O was about 2. In all circumstances, the value for the missing H was divided by 2 and used as the value for the missing H_2O . All the mole fractions were then normalized to a sum of 1.00.

RESULTS AND DISCUSSION - SCREENING EXPERIMENTS

A series of screening tests was conducted first to select the proper conditions for the detailed probing experiments. These tests involved the determination of the effects of a number of variables on the NO_x yields from NH_3 and HCN additives in premixed CH_4-O_2-Ar flames. The input concentration of NH_3 or HCN and the concentration of NO_x in the completely burned gas, measured about 80 mm above the burner in most experiments, were compared (the luminous zone of the flame was about 3 mm above the flame holder). The flame temperature was also measured at this sampling point. These screening experiments, which have been designated as input-output experiments, can be carried out quickly permitting the effects of a large number of variables to be screened.

The variables tested in the experiments reported here included: fuel-air equivalence ratio (ϕ), argon dilution, additive concentration and type, pressure, and burner feed rate. It will be seen that the general effects of changing these variables were studied but the input-output experiments could not be analyzed in as much detail as the flame probing experiments because the temperature-time profiles between the burner and the sampling point were not measured. The detailed

probing experiments, conducted later, showed that the temperature reaches a maximum about 8 mm above the flame holder and then decays gradually. At $\phi = 0.8$ and 1.5, the temperature was found to have dropped by about 250 K from its maximum value at a point 80 mm above the burner.

Typically, after the CH_4 , O_2 , and Ar feed rates were established and the burner had been lighted and achieved thermal equilibrium with the system, the axial temperature profile was determined with a coated Pt-Pt/10%Rh thermocouple around the point from which the quartz microprobe would withdraw gas samples. The thermocouple was then withdrawn from the flame and the microprobe inserted to obtain a measure of the NO_x concentration using the chemiluminescent analyzer (CA). Most of the screening experiments were run with the CA in the NO_x mode (molybdenum converter at 400 C) but runs without the converter (NO mode), gave the same results within about 1 percent. As discussed in the previous Experimental Section, the gas temperature at the sampling point must be known to correct the CA reading for changes in the sampling rate through the critical-flow sampling orifice. The molecular weight and γ of the sampled gas, which also are required to determine the sample gas flowrate through the orifice, were taken to be the values computed at thermodynamic equilibrium at the adiabatic flame temperature for the system. To obtain an axial position reference, the distance from the tip of the burner to the location of the thermocouple and microprobe (at one axial position point) was measured with a cathetometer. Thereafter, the micrometer on the translation stage used to position the burner was employed to measure burner location relative to that initial reference measurement.

A diluent ratio, denoted as DR, is defined as the molar ratio, Ar/O_2 , in the burner feed divided by the N_2/O_2 ratio in air. Therefore, DR was defined as 1 when $\text{Ar}/\text{O}_2 = 3.76$ because this is the $(\text{N}_2 + \text{Ar})/\text{O}_2$ ratio in air. Conducting experiments at a DR of 1 results in the mole fractions of reactants being the same as in CH_4 -air flames of the same equivalence ratio. However, the lower heat capacity of argon results in much higher adiabatic flame temperatures. Duplication of the heat capacity of air requires a DR of 1.6. The maximum flame temperatures measured at DR = 1 in the detailed probing experiments (reported in the next section) were only slightly higher than the adiabatic temperatures for CH_4 -air flames because of heat loss to the burner face.

Ammonia Addition

Input-output experiments were conducted with ammonia added to the premixed feed gas. In most experiments, the nominal ammonia concentration was 2500 ppm (molar) based on the total inlet gas flow, including argon and oxygen. At an equivalence ratio of 1 and a DR of 1 (argon/oxygen molar ratio of 3.76), an ammonia concentration of 2500 ppm defined in this manner is equivalent to the addition of 2.3 weight percent nitrogen to the methane. This high additive concentration was selected to permit the nitrogen species to be measured by mass spectrometry although this method of analysis for nitrogen species was later abandoned in favor of the CA.

Effect of Equivalence Ratio and Feed Rate on NO_x Yield. If the NO_x yield was to be determined from $\phi = 0.5$ to 1.5, without damaging the thermocouple or microprobe, it was imperative that the measurements be performed far enough downstream to ensure that temperatures less than 2000 to 2100 K would be encountered. After a number of tests, it was decided that a distance of 80 mm above the burner would be satisfactory for these experiments. The results of all ammonia addition screening experiments at 76 torr are summarized in Table 21. The initial measurements of NO_x yield were made with DR = 1 and a total burner feed rate (except for the NH_3 additive) of 6014 cc/min at $\phi = 0.5$, with an additional 60 cc/min of CH_4 for each 0.1 increase in ϕ . These experiments are listed as Series A at the top of Table 21 and are plotted on the lower curve in Fig. 47. In the second series of input-output experiments with added NH_3 (Series B of Table 21), the diluent ratio was held at 1.0 and the total feed rate to the burner was increased to 7520 cc/min (plus the NH_3 additive). It can be seen from Fig. 47 that increasing the feed rate increases the NO_x yield with the maximum effect being at about $\phi = 0.8$.

The temperatures listed in Table 21 for these two experimental series (A and B) indicate that increasing the feed rate increases the temperature by as much as 300 K with the maximum increase being obtained near stoichiometric. These observations suggest that the increase in NO_x yield with feed rate results from an increase in the flame temperature brought about by the flame front being moved farther away from the flame holder allowing less heat loss to the water-cooled burner. At $\phi = 1.4$ and 1.5, the feed rate of 7520 cc/min caused the flame to blow off.

TABLE 21. SUMMARY OF NO_x MEASUREMENTS IN SCREENING EXPERIMENTS
WITH AMMONIA ADDITIVE (p = 76 torr)

Experiment No.	ϕ	Diluent Ratio (DR)	Symbol Used in Figures	Distance From Burner, mm	T, K [*]	Feedrate, cc/min at STP	NO _x ,** ppm	NH ₃ ,*** ppm	Percent NH ₃ Converted
A-1	0.5	1.0	○	81.50	1446	6014	2011	2692	74.4
A-2	0.8	1.0	○	77.45	1488	6194	1846	2560	73.3
A-3	0.9	1.0	○	77.74	1512	6254	1777	2503	71.0
A-4	1.0	1.0	○	81.40	1542	6314	1623	2433	66.9
A-5	1.1	1.0	○	75.95	1661	6374	1424	2408	59.1
A-6	1.2	1.0	○	75.96	1618	6434	1185	2358	50.2
A-7	1.3	1.0	○	76.25	1599	6494	1258	2315	44.2
A-8	1.4	1.0	○	80.70	1622	6554	932	2314	40.3
B-1	0.5	1.0	×	81.30	1456	7520	1964	2564	76.6
B-2	0.7	1.0	×	81.30	1676	7520	2086	2547	81.9
B-3	0.8	1.0	×	80.70	1731	7520	2098	2563	81.9
B-4	1.0	1.0		80.70	1846	7520	1976	2519	78.4****
B-5	1.0	1.0	×	80.08	1856	7520	1823	2519	72.4
B-6	1.1	1.0	×	81.00	1816	7520	1571	2432	64.6
B-7	1.2	1.0	×	80.75	1772	7520	1339	2484	53.9
B-8	1.3	1.0	×	80.70	1735	7520	1179	2404	49.0
C-1	0.5	1.0	●	41.65	1570	6014	2354	2660	88.5
C-2	0.6	1.0	●	40.15	1656	6074	2246	2655	84.6
C-3	0.6	1.0	●	19.98	1776	6074	2365	2655	89.1
D-1	0.9	1.2		75.75	1756	7157	1773	2234	75.0
D-2	0.9	1.2	▲	75.75	1756	7157	1929	2468	76.2
D-3	0.9	1.4		75.75	1821	8060	1572	1994	78.8
D-4	0.9	1.4	■	75.75	1821	8060	1989	2476	80.4
D-5	0.9	1.6		77.77	1762	8963	1466	1783	82.2
D-6	0.9	1.6	◆	77.77	1765	8963	2012	2482	81.1
D-7	1.0	1.2		80.60	1664	7217	1607	2197	73.2

TABLE 21. (Concluded)

Experiment No.	ϕ	Diluent Ratio (DR)	Symbol Used in Figures	Distance From Burner, mm	T, K*	Feedrate, cc/min at STP	NO _x ,** ppm	NH ₃ ,*** ppm	Percent NH ₃ Converted
D-8	1.0	1.2	▲	80.60	1664	7217	1796	2399	74.9
D-9	1.0	1.4		80.60	1717	8120	1523	1967	77.4
D-10	1.0	1.4	■	80.60	1722	8120	1920	2473	77.6
D-11	1.0	1.6		80.50	1732	9023	1372	1775	77.3
D-12	1.0	1.6	◆	80.50	1736	9023	1921	2488	77.2
E-1	0.8	1.2	▲	80.40	1651	7520	1935	2487	77.8
E-2	0.8	1.4	■	79.50	1644	7520	1949	2523	77.2
E-3	0.8	1.6	◆	79.55	1527	7520	1957	2528	77.4
E-4	1.1	1.2	▲	81.00	1797	7520	1629	2488	65.5
E-5	1.1	1.4	■	81.35	1773	7520	1676	2476	67.7
E-6	1.1	1.6	◆	81.00	1764	7520	1694	2552	66.4
F-1	0.8	1.6		19.87	1734	7419	2015	2517	80.1
F-2	0.8	1.6		19.91	1729	7419	2640	3390	77.9
F-3	0.8	1.6		19.91	1729	7419	3436	4909	70.0
G-1	0.7	1.0	●	47.60	1935	8763	2158	2579	83.7
G-2	0.7	1.0	●	42.59	1962	8763	2236	2579	86.7
G-3	0.7	1.0	●	37.56	1968	8763	2286	2579	88.7
G-4	0.7	1.0	●	32.62	2016	8763	2308	2579	89.5
H-1	0.8	1.6	●	22.75	1732	7419	1995	2517	79.5
H-2	0.8	1.6	●	26.90	1726	7419	2001	2517	79.5
H-3	0.8	1.6	●	28.88	1723	7419	2125	2517	80.0
H-4	0.8	1.6	●	17.49	1732	7419	2014	2517	80.2
H-5	0.8	1.6	●	17.95	1723	7419	2008	2517	79.8
H-6	0.8	1.6		14.95	1723	7419	1766	2314	76.3****
I-1	1.5	1.0		49.35	1776	6247	757	2349	32.2

*Temperature has been corrected for radiation as described in Appendix F.

**ppm (molar) of NO_x in the gas sampled.

***ppm NH₃ that would be in gas if the NH₃ did not react and the other species reacted to chemical equilibrium at the adiabatic flame temperature (i.e., corrected for reaction mole change).

****Result not plotted in figures because apparently spurious.

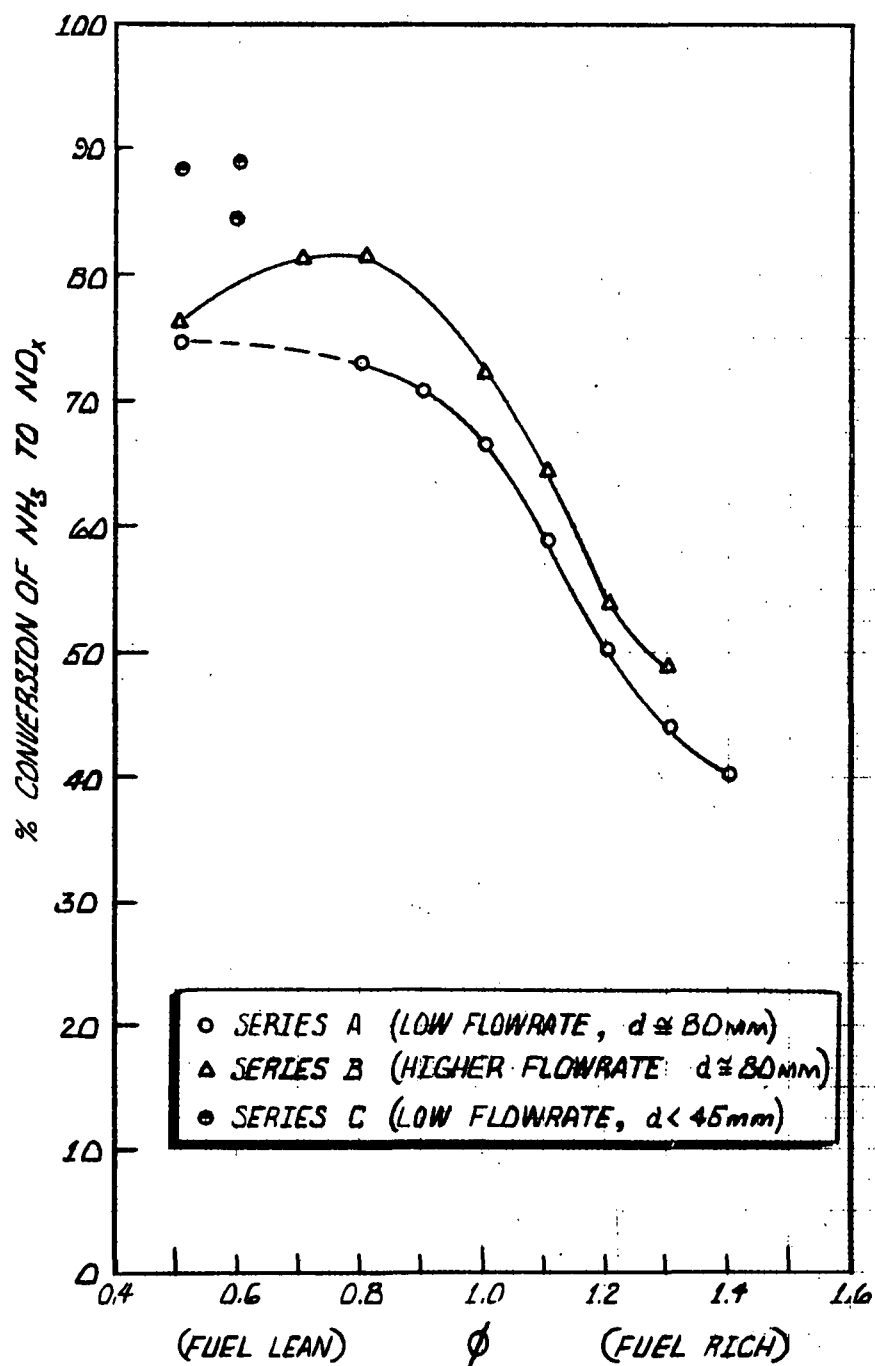


Figure 47. Conversion of NH_3 to NO_x as a Function of Equivalence Ratio, ϕ , and Flowrate in Screening Experiments at a Pressure of 76 torr

In sufficiently lean and rich mixtures, the lower flame velocity should result in a flame reaction zone far enough from the burner to reduce heat losses and the low and high feed rate correlation curves in Fig. 47 should approach one another at mixture ratios far removed from stoichiometric. As an illustration of this, at $\phi = 0.5$ (experiment B-1), the 7520 cc/min feed rate caused the flame to distort from its normally flat appearance and lift some distance above the burner. With a 20 percent lower feed rate (A-1), which would place the experiment in the lower feed rate category, the percent conversion of NH_3 to NO_x was essentially the same.

Regardless of the complications introduced by energy losses from the flame to the burner, it is readily apparent in Fig. 47 that for $\phi < 1.0$ (fuel-lean flames) the yield of NO_x is quite high while for $\phi > 1$ the yield decreases rapidly as ϕ is increased. Similar effects of mixture ratio on NO_x yield have been reported by other investigators (Ref. 66, 71 and 72). Based on the results of the other investigations even higher NO_x yields would be expected at lower NH_3 concentrations.

The data reported here at the higher flowrate show a decline in NO_x yield, measured at a fixed distance from the burner, as ϕ is decreased from 0.8 to 0.5. However, higher yields of NO_x were obtained when the measurements were made closer to the luminous zone of the flames at $\phi = 0.5$ and 0.6 (Series C in Table 21) as shown in Fig. 47, suggesting that some of the NO_x is decomposing before reaching the probe when the measurements are taken far above the flame front. The rate of a small shift toward equilibrium in the post-flame gases would be enhanced by the excess oxygen present under fuel-lean conditions.

Effect of Argon Dilution. Screening experiments were performed with diluent ratios of 1.2, 1.4, and 1.6 at $\phi = 0.8, 0.9, 1.0$, and 1.1. At $\phi = 0.9$ and 1.0 (Series D in Table 21), the conditions were the same as in the Series A low flowrate experiments and the argon feed rate to the burner was increased while leaving the CH_4 and O_2 feed rates unchanged. Instead of causing a decrease in temperature because of the added heat capacity, the additional argon produced a higher combustion gas temperature at the gas sampling point (Fig. 48) and a sizable increase in the NO_x yield (Fig. 49). The increased feed rate apparently served to lift the flame

reaction zone away from the water-cooled burner increasing the maximum flame temperatures. This change in reaction temperature tends to obscure the direct effects of argon dilution of NO_x yield.

At $\phi = 0.8$ and 1.1 (Series E in Table 21), the Ar/O_2 ratio was increased while the total feed rate to the burner was kept constant at 7520 cc/min plus NH_3 additive (as in the Series B experiments). Although the temperature at the sampling point did decrease with argon dilution (Fig. 48), the change was not as large as would be predicted from the effect of the added heat capacity on the adiabatic flame temperature (at $\phi = 0.8$, the adiabatic temperature decreases from 2300 to 2097 K as DR is increased from 1.0 to 1.4). Argon dilution again altered the proximity of the flame front to the burner and, hence, changed the rate of heat loss to the burner. At $\phi = 0.8$, the measured temperature decreased sharply with argon addition and was accompanied by a decline in conversion to NO_x . The temperature decreased only slightly at $\phi = 1.1$ and the addition of argon had little effect on the amount of NO_x formed.

The argon dilution data are replotted in Fig. 50 to demonstrate the approximate direct relationship between gas temperature and NO_x yield at $\phi = 0.8, 0.9$ and 1.0 . At $\phi = 1.1$, the addition of argon under these conditions had little effect on temperature or NO_x yield.

In contrast to the indications of a direct relationship between T and NO_x yield illustrated in Fig. 48 and 49, is the absence of an effect on NO_x yield of the lower reactant concentrations accompanying argon dilution. This is best illustrated by reference to Table 22 which lists calculated oxygen concentrations before and after combustion, assuming equilibrium combustion products at the adiabatic flame temperature. At $\phi = 1.1$, for instance, the O_2 concentration varies widely with argon dilution; however, Fig. 49 indicates only a very small change in NO_x yield. The interpretation of the argon addition results at $\phi = 0.9$ and 1.0 are again clouded by the increase in temperature that accompanied the increase in flowrate. Argon addition decreases all reactant concentrations by the same ratio (except NH_3) and hence, decreases the rates of all reactions of the same order by a constant factor. These results appear to indicate that as long as the

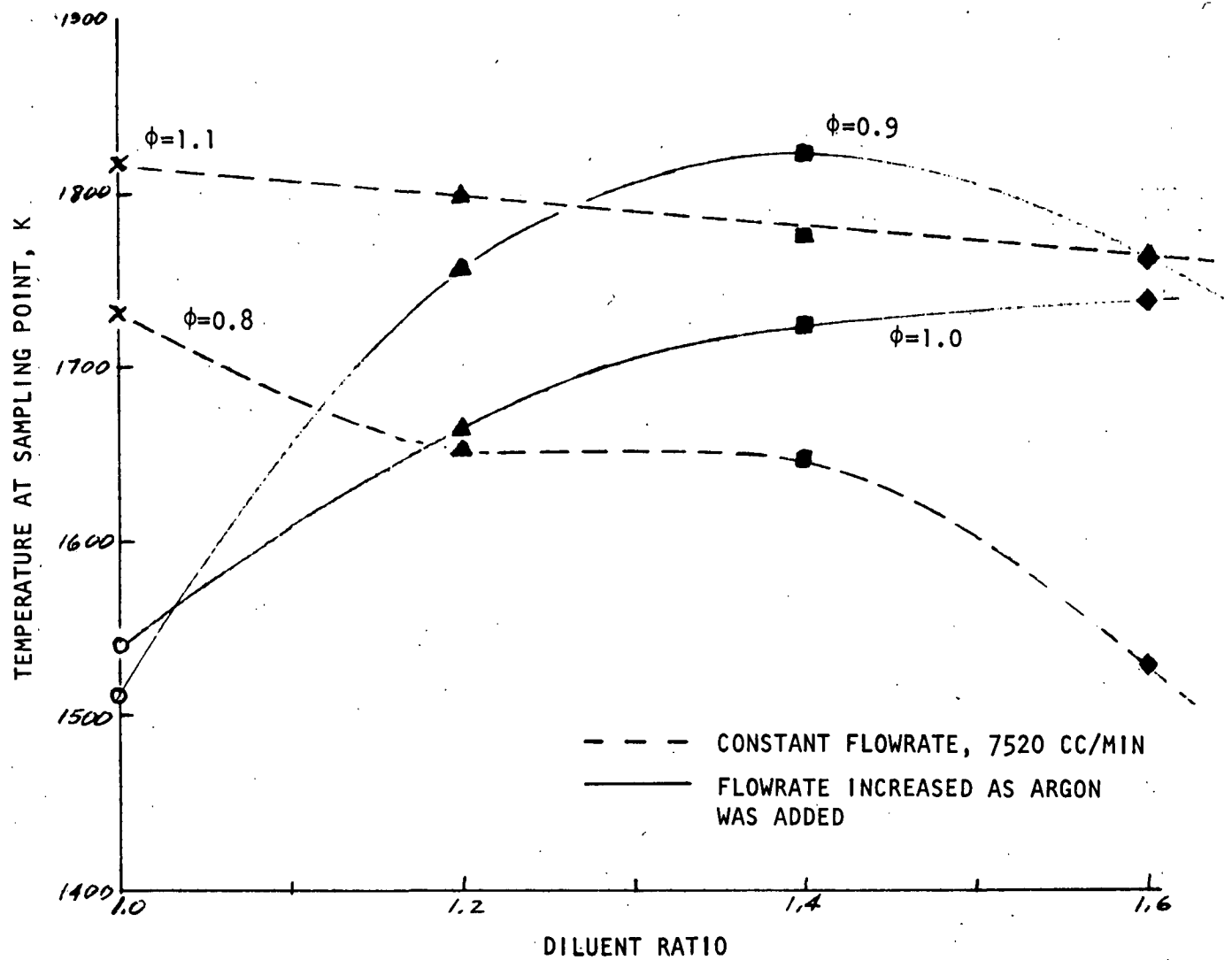


Figure 48. Effect of Argon Dilution on Temperature at Sampling Point ($p = 76$ torr, $d = 80$ mm)

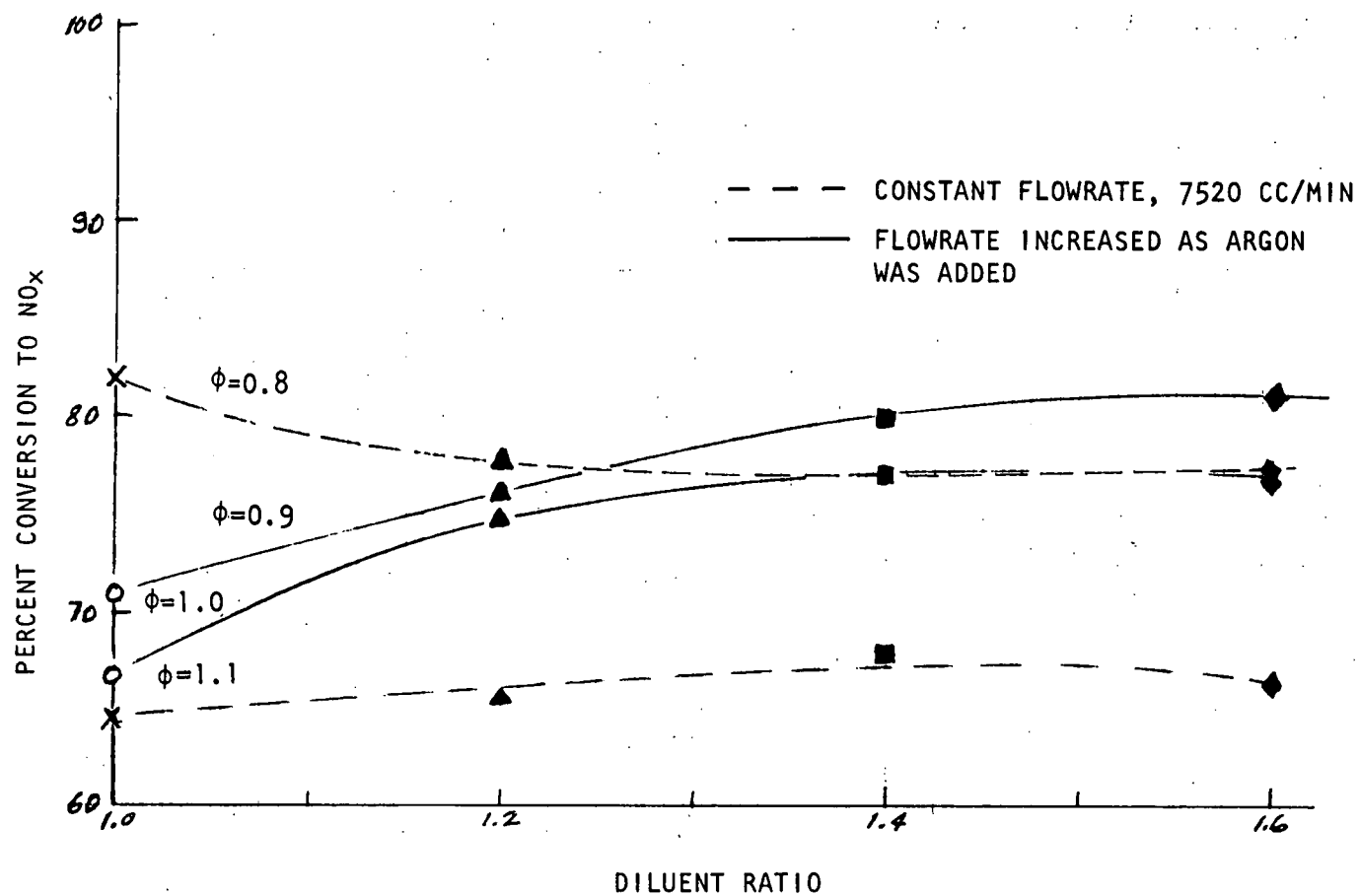


Figure 49. Effect of Argon Dilution on NO_x Yield
(p = 76 torr, d = 80 mm)

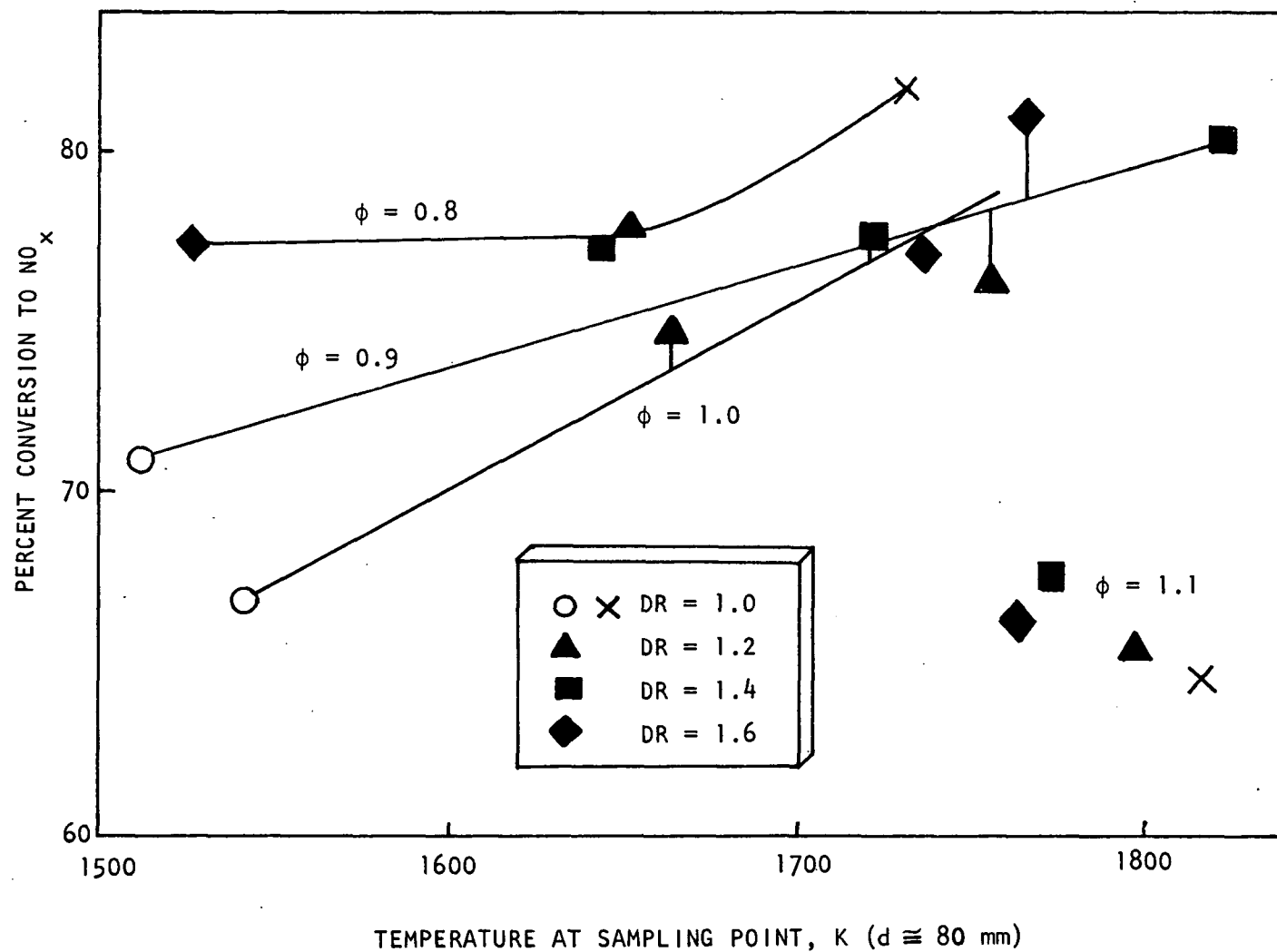


Figure 50. Comparison of NO_x Yield from NH_3 and Temperature (measured approximately 80 mm above burner) For Argon Dilution Screening Experiments

sampling point is far enough behind the flame front, the decrease in reaction rates accompanying argon addition is of no importance to the NO_x yield because the competing reactions for the formation of NO_x and N_2 are affected equally (i.e., are of the same order--probably second).

TABLE 22. EFFECT OF ARGON DILUTION ON OXYGEN CONCENTRATION OF REACTANT MIXTURE AND COMBUSTION PRODUCTS

		Percent Oxygen							
		Reactant Mixture				Combustion Products*			
DR \ ϕ		0.8	0.9	1.0	1.1	0.8	0.9	1.0	1.1
1.0		19.3	19.2	19.0	18.8	4.06	2.71	1.66	0.89
1.2		16.9	16.8	16.6	16.5	3.38	2.13	1.18	0.53
1.4		15.0	14.9	14.8	14.7	2.88	1.69	0.81	0.27
1.6		13.5	13.4	13.3	13.2	2.52	1.36	0.52	0.11

*Assuming adiabatic combustion and equilibrium products

Effect of NH_3 Concentration. There is ample information in the literature to establish that the percent conversion of nitrogen additives to NO decreases as additive concentration is increased (e.g., Ref. 59, 60, and 62). Limited evidence from the screening tests made in this study, however, are ambiguous with respect to the effect of additive concentration. Most of the screening tests were conducted using about 2500-ppm NH_3 addition. This is equivalent to adding 1.6 weight percent nitrogen to the CH_4 (as NH_3) at $\phi = 1.6$ and 2.8 weight percent at $\phi = 0.8$. At $\phi = 0.9$ and 1.0, during experiments where the argon feed rate to the burner was increased (Series D in Table 21), tests were made with the NH_3 feed rate adjusted to 2500 ppm of the total burner feed including the additional argon, and then to 2500 ppm of the feed rate without the additional argon. Of the six sets of data taken in this manner (three sets at $\phi = 0.9$ and three at $\phi = 1.0$), four sets show an increase in NO_x yield at the higher NH_3 concentration. For $\phi = 0.8$, experiments were made at 2517, 3390, and 4909 ppm NH_3 , with a DR of 1.6 and the probe set 20 mm from the burner (Series F in Table 22). The NO_x yields were 80.1, 77.9, and 70.0 percent, respectively. The results of this series (Series F) are in agreement with the expected decrease in NO_x yield at higher additive concentrations.

Effect of Sampling Position. It was noted previously that the Series C NH_3 experiments demonstrated that in fuel-lean flames the NO_x concentration decreases with distance above the burner as the post-flame gases flow from the flame front to the normal sampling point (80 mm above the burner). This effect, which is attributed to thermal decomposition of NO, is shown in Fig. 51. A similar effect is demonstrated by the Series G experiments (Table 21 and Fig. 51) which were conducted at $\phi = 0.7$ at a rather high feed rate of 8763 cc/min. Since the thermal decomposition of NO has a moderately large activation energy, the rapid decrease in NO_x yield with distance in the Series G experiments must result from the higher temperatures attained at these high flowrates (because of lower heat loss rates to the burner). The NO_x yields obtained in the Series H experiments with added Argon at $\phi = 0.8$ (Fig. 51) were essentially independent of sampling distance. This indicates that NO decomposition is slow at the low temperatures obtained under these conditions. The NO_x yield in Experiment I-1 ($\phi = 1.5$) would lie on the extension of the solid curve if plotted in Fig. 47. Thus the yield from the fuel-rich flames is apparently not strongly dependent on sampling position.

Effect of Pressure. The effect of pressure on NO_x yield from NH_3 was measured for $\phi = 0.9$ and 1.2 and a diluent ratio of 1.0 using burner feed rates of 7520 and 15,040 cc/min (plus NH_3) primarily, and 10,450 cc/min in one experiment. Above a certain pressure, the flame, which is normally stabilized above the 8-mesh screen located about 1/8 inch above the porous plate, flashed back through the screen and stabilized on the porous plate. Because of the possibility of damage to the porous plate by overheating, input-output experiments were not performed under these conditions. Thus, the pressure at which flashback occurred, listed in the following table, determined the maximum pressure for the flowrate and value of ϕ being used:

ϕ	Flowrate, cc/min	Flashback Pressure, atm
0.9	7,520	0.5+
0.9	15,040	≈ 0.35
1.2	7,520	0.4+
1.2	15,040	≈ 0.38

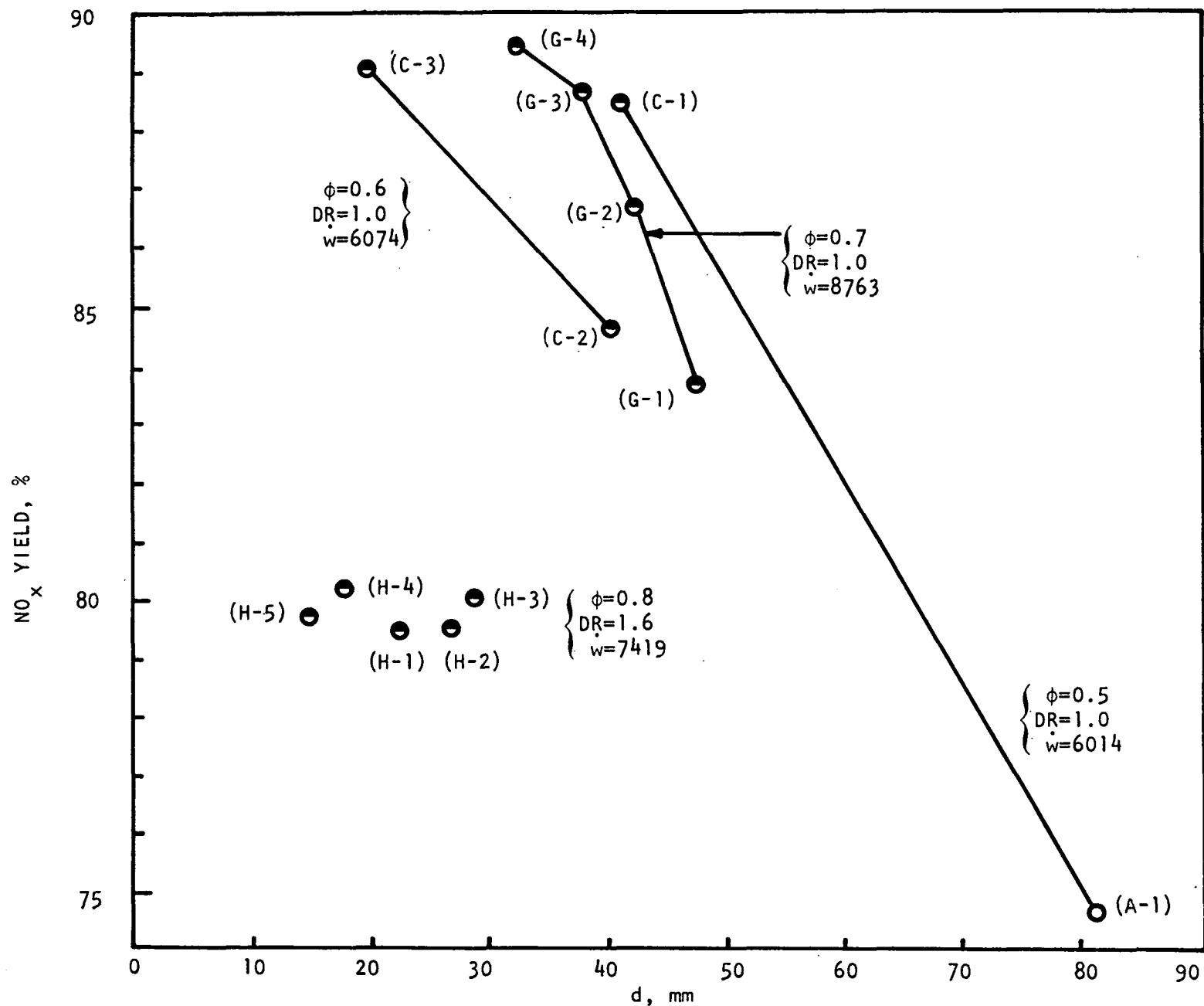


Figure 51. Effect of Sampling Distance on NO_x Yield From NH_3 at a Pressure of 76 Torr

While a higher burner feed rate might be expected to keep the flame from flashing back to the porous plate until a higher pressure was achieved, just the opposite was found to be true. This result suggests flashback is dependent on the temperature of the burner top. The higher feed rate (and, hence, greater energy release rate) could heat the burner face to a higher temperature than did the lower feed rate, resulting in flashback at a lower pressure.

The pressure effect data are given in Table 23 and plotted in Fig. 52. It can be seen from Fig. 52 that the NO_x yield was much smaller at $\phi = 1.2$ than at $\phi = 0.9$, and the difference persisted over the entire pressure range evaluated. It can be seen also that at 7520 cc/min, the NO_x yield at both $\phi = 0.9$ and 1.2 declined as pressure was increased (dashed lines). However, this decline cannot necessarily be attributed to a pressure effect, since the measured temperature also decreased (Table 23). To reduce the heat loss to the burner, the feed rate was doubled. Doubling the feed rate, to 15,040 cc/min, resulted in a smaller variation of NO_x yield with pressure (Fig. 52): the measured temperatures were higher but still decreased with increasing pressure. In general, the higher NO_x yield at the 15,040 cc/min feed rate is believed to be due to a lower percentage heat loss to the burner and a resultant higher reaction zone temperature.

Interpretation of the effect of pressure on NO_x formation reactions is complicated by the fact that temperature, gas density (and therefore gas velocities), and heat loss to the burner also vary as the pressure is changed. The final NO_x concentration is affected by the temperature-time history of the gas in the zone where the temperature is high enough to result in significant reaction rates. Obtaining the data to evaluate this temperature-time history was beyond the objectives of the input-output screening tests. The measured temperatures listed in Table 23 were those at the location of the microprobe (about 80 mm above the flame holder in most experiments). It may be that the temperatures in the reaction zone did not vary to the same extent with pressure as did these measured temperatures.

Because of these complicating factors, a more detailed interpretation of the pressure effect data does not appear to be warranted. It may be that the direct effect of pressure is small, as was apparently the case with argon dilution, because

TABLE 23. SUMMARY OF PRESSURE EFFECT SCREENING EXPERIMENTS
WITH NH₃ ADDITIVE (DR = 1.0)

Experiment No.	ϕ	Symbol in Fig. 52	Distance From Burner, mm	Temperature,* K	Burner Feed Rate, cc/min	NO _x , ppm,	NH ₃ , ppm	Percent NH ₃ Converted	P, atm
J-1	0.9	○	101.3	2006	15,040	1927	2522	76.4	0.1
J-2	0.9	○	78.3	1960	15,040	2141	2458	87.1	0.2
J-3	0.9	○	78.15	1816	15,040	2093	2490	84.0	0.3
J-4	1.2	△	80.05	1876	15,040	1374	2421	56.7	0.2
J-5	1.2	△	80.15	1726	15,040	1358	2402	56.5	0.3
J-6	1.2	△	80.30	1624	15,040	1265	2421	52.2	0.368
J-7	0.9	●	81.65	1792	7,520	1792	2535	72.5	0.1
J-8	0.9	●	80.70	1785	10,450	1825	2473	73.8	0.2
J-9	0.9	●	80.15	1248	7,520	1402	2523	55.5	0.5
B-7	1.2	▲	80.75	1772	7,520	1339	2484	53.9	0.1
J-10	1.2	▲	80.75	1401	7,520	1030	2402	42.9	0.3
J-11	1.2	▲	52.4	1483	7.520	816	2434	33.5	0.4

*Corrected for radiation

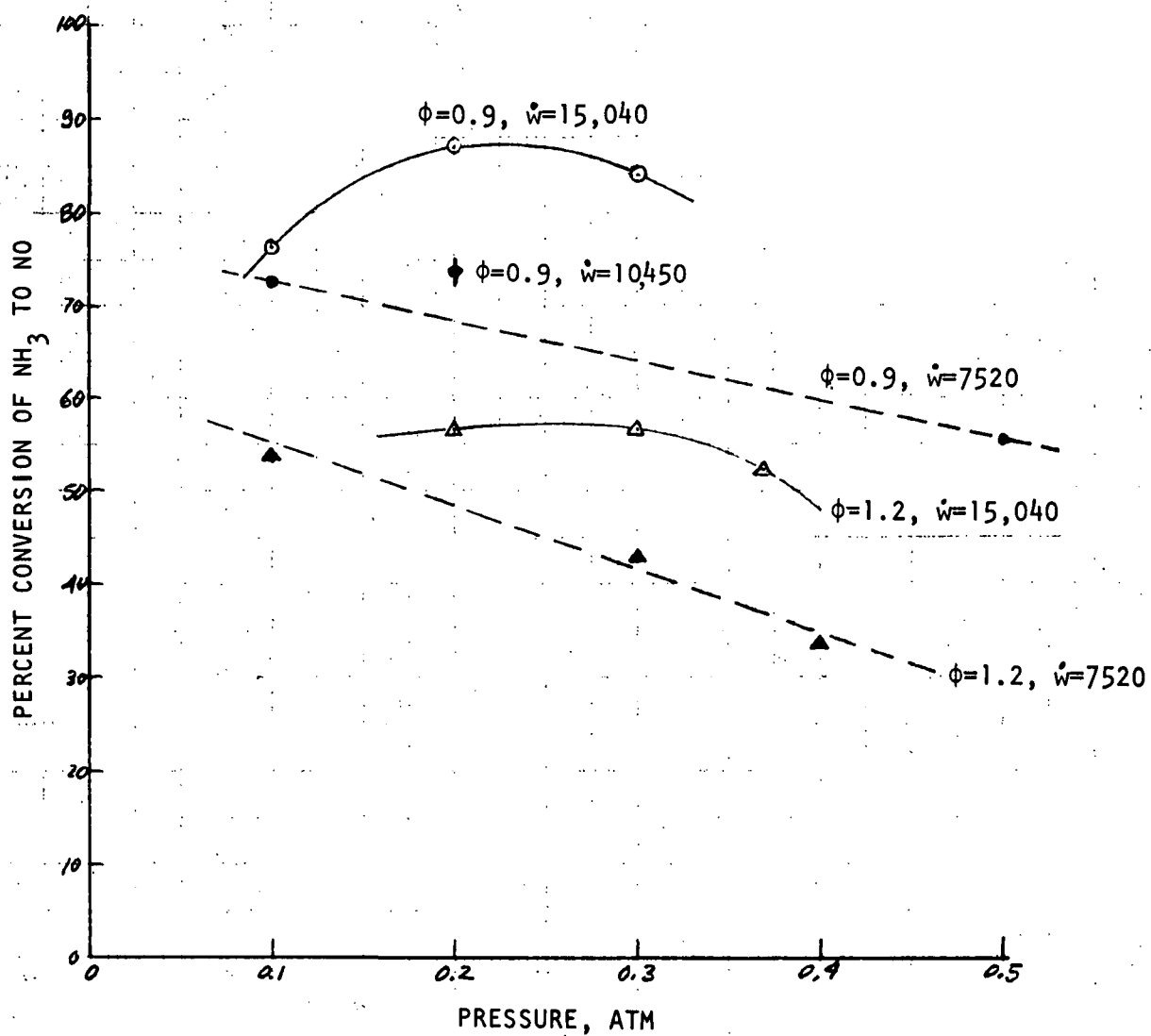


Figure 52. Effect of Pressure on the NO_x Yield From NH_3 (DR = 1)

the rates of formation of NO and N₂ are equally pressure dependent, and the effects shown in Fig. 52 result mainly from the effect of pressure on the flame temperature.

In any event, these pressure screening experiments have shown that the NO yield is not strongly dependent on pressure and indicate that conducting the detailed probing experiments at 0.1 atm (to spread the flame zone) and a feed rate of 7520 cc/min should give NO yields that are comparable to (although somewhat higher than)) those that would be obtained at 1 atm.

Hydrogen Cyanide Addition

Similar types of screening (input-output) experiments were conducted with HCN as the additive. The experience gained with NH₃ permitted conditions to be selected that would give the most meaningful results.

Effect of Equivalence Ratio on NO_x Yield. The percent NO_x yield from HCN additive was determined as a function of the equivalence ratio, ϕ , from 0.5 to 1.5. The data are given in Table 24 and the results are plotted in Fig. 53. These experiments were all conducted at 76 torr. The HCN concentration was approximately 2500 ppm and the diluent ratio was 1.0 (i.e., Ar/O₂ = 3.76). Earlier experience with

TABLE 24. SUMMARY OF NO_x MEASUREMENTS IN SCREENING
EXPERIMENTS WITH HCN ADDITIVE*

Experiment No.	ϕ	Distance From Burner, mm	Measured Temperature**, K	NO _x , ppm	HCN, ppm	Percent HCN Converted
K-1	0.5	79.70	1538	2126	2530	83.8
K-2	0.7	79.70	1722	2115	2515	84.1
K-3	0.9	80.85	1843	2002	2490	80.3
K-4	1.1	80.85	1876	1564	2442	64.1
K-5	1.3	80.25	1678	1017	2377	45.3
K-6	1.5	80.00	1685	652	2314	28.2

*p = 76 torr, DR = 1.0, \dot{w} = 7520 cc/min (7539 cc/min including HCN)

**Corrected for radiation

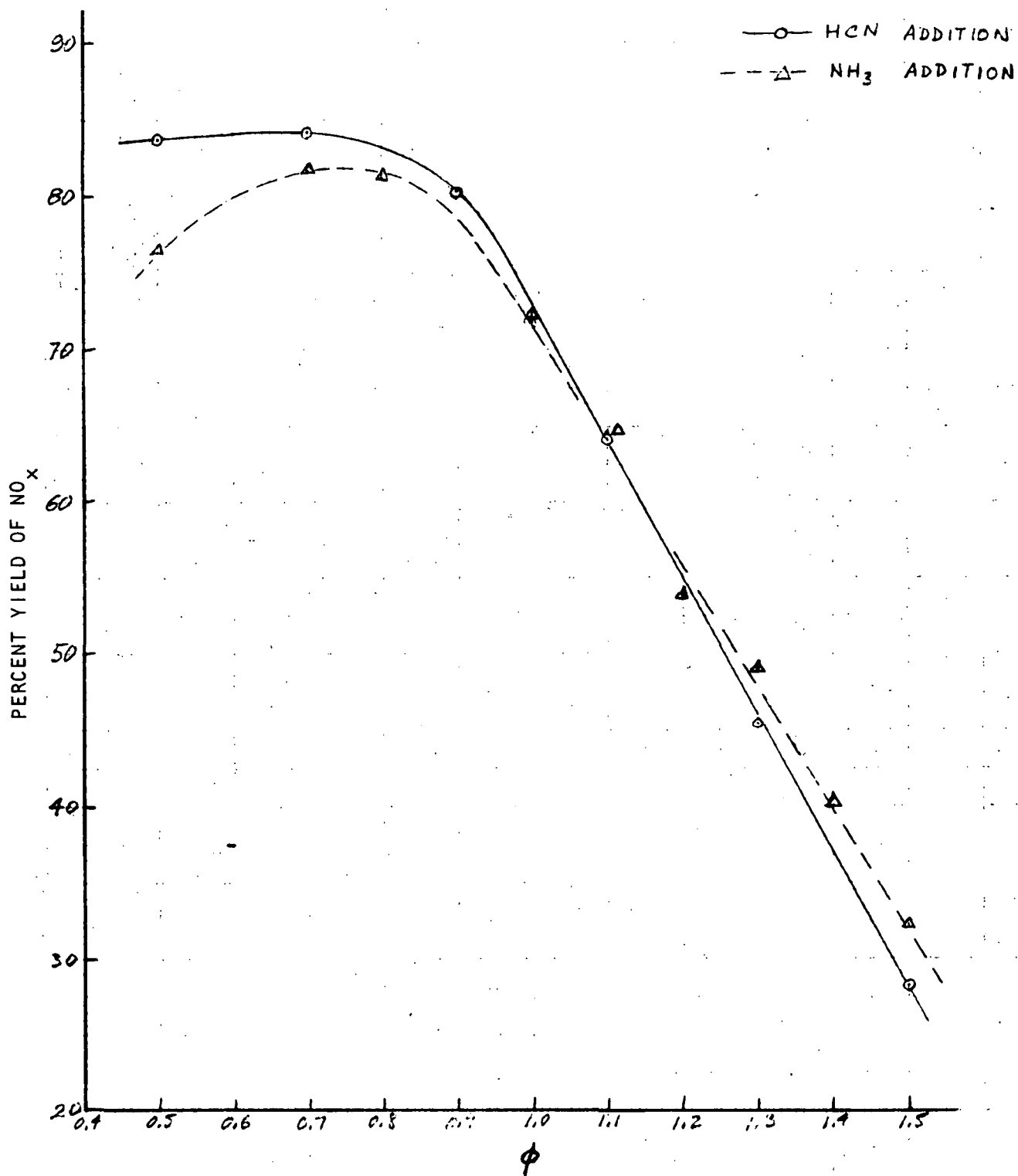


Figure 53. Conversion of Additive to NO_x as a Function of Equivalence Ratio, ϕ , in Screening Experiments ($p = 76$ torr, $DR = 1.0$, $\dot{w} = 7520$ cc/min + Additive, and Additive ~ 2500 ppm)

NH_3 addition indicated that the heat losses to the water-cooled burner varied considerably with the burner feed rate employed since a lower feed rate apparently produced a flame that hovered closer to the burner face. Therefore, a constant burner feed rate was used in the HCN addition screening experiments for the determination of NO_x yield versus ϕ . To permit comparison of the HCN addition experiments with those using NH_3 , a flowrate of 7520 cc/min plus additive was used. The dashed line in Fig. 53 represents the NO_x yields obtained in the NH_3 addition screening experiments under the same conditions. The results for HCN addition are seen to be very similar to those obtained with NH_3 .

The general shape of the NO_x yield versus ϕ curve for NH_3 and HCN (i.e., a high NO_x yield for $\phi < 1$ and a rapid decline in NO_x yield as ϕ is increased beyond 1) closely resembles results obtained in many studies using a wide variety of nitrogen-containing organic compounds as additives (e.g., Ref. 3, 63 through 66). Similar results have been reported for pulverized coal burned in an O_2 -Ar atmosphere, i.e., O_2 -rich conditions produced a higher NO_x yield (Ref. 133). The similarity has been cited as providing strong evidence that the rate-controlling steps in the conversion of fuel-N to NO_x and N_2 are independent of the molecular structure of the fuel-N compound and, hence, involve some common active nitrogen intermediate. The data obtained from these screening experiments indicate that this commonality applies even to the simple nitrogen-containing species, NH_3 and HCN.

Argon dilution was not run as part of the HCN screening experiments. From the screening experiments performed with NH_3 addition, it was determined that the primary effect of argon dilution on the NO_x yield at constant ϕ , was probably manifested through its effect on the flame temperature. The reason for this appears to be that dilution with argon lowers the concentration of all reactants proportionately and, hence, may lower the rates of formation of NO and N_2 in the same proportion. The data from argon dilution tests with the NH_3 additive were judged to be adequate to select conditions for the detailed probing tests with HCN as the additive.

Effect of Pressure. The experimental data obtained on the effect of pressure on NO_x yield from HCN are given in Table 25 and Fig. 54. The pressure effect on NO_x yield from HCN was measured primarily at a burner feed rate of 15,040 cc/min (plus 2500 ppm HCN) with one experiment (No. K-3, reproduced from Table 24) being conducted at a feed rate of 7520 cc/min. The maximum pressure used was 185 torr, or 0.243 atm. Higher pressures were unattainable without apparatus modification because the HCN supply line pressure was limited to 264.4 torr, the vapor pressure of HCN at 0 C. If pressure were found to have a large effect on NO_x yield, the HCN supply system would have been modified to provide the higher pressure required.

TABLE 25. SUMMARY OF PRESSURE EFFECT SCREENING EXPERIMENTS,
 NO_x YIELD WITH HCN ADDITIVE ($\phi = 0.9$, DR = 1.0)

Experiment No.	Pressure, torr/(atm)	Distance From Burner, mm	Burner Feed rate, cc/min	Measured Temperature,* K	NO_x , ppm	HCN, ppm	Percent HCN Converted
K-3	76(.1)	80.85	7,520	1843	2002	2490	80.3
L-1	76(.1)	106.70	15,040	1965	1916	2458	78.0
L-2	114(.15)	106.70	15,040	1856	2069	2458	84.2
L-3	152(.2)	79.90	15,040	1876	2106	2458	85.7
L-4	185(.243)	65.05	15,040	1876	2102	2458	85.5
L-5	185(.243)	79.90	15,040	1808	2095	2458	85.2

*Corrected for radiation

Screening experiments conducted with NH_3 had indicated that at constant ϕ the flame reaction zone temperature had a sizable effect on NO_x yield. If the rate of heat loss from the flame changes as the pressure is varied, the changing of flame reaction zone temperature could mask the true effect of pressure on the NO_x yield. Experience from similar screening experiments with NH_3 , led to the use of a burner feed rate of 15,040 cc/min to minimize the effect of heat loss to the burner on the NO_x yield. The data for HCN plotted in Fig. 54 show a slight increase in NO_x yield with increasing pressure.* The dashed line in Fig. 54 is the correlation obtained previously for NH_3 , also at $\phi = 0.9$. The results for HCN and NH_3 are seen to be quite similar.

*The solid curve in Fig. 54 is drawn through experiment 66 rather than 70 because it was obtained at the same residence time.

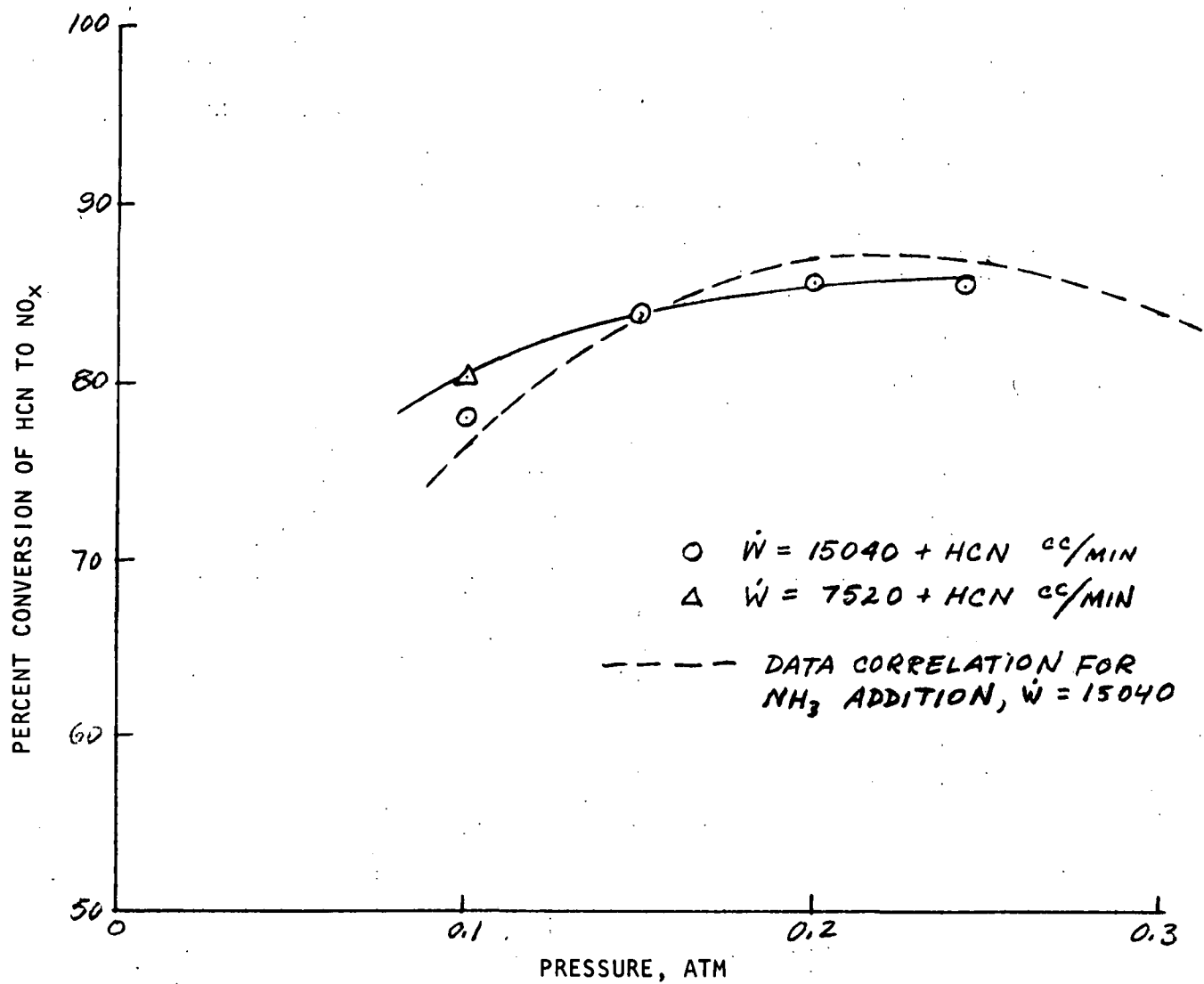


Figure 54. Effect of Pressure on NO_x Yield from HCN
 ($\phi = 0.9$, DR = 1.0)

CONCLUSIONS - SCREENING EXPERIMENTS

The following conclusions have been drawn from the screening (input-output) experiments with NH_3 and HCN addition:

1. NH_3 and HCN give nearly identical yields of NO_x under all conditions tested.
2. Less than 1 percent of the NO_x is NO_2 at the downstream probe position.
3. The NO yield is high (> 80 percent) at equivalence ratios of less than 0.9 but falls off rapidly under fuel-rich conditions.
4. Increasing the burner feed rate increases the NO yield slightly apparently by reducing the heat loss to the burner face.
5. Increasing the argon feed rate by 60 percent has only a small effect on the NO yield from NH_3 .
6. The results were inconclusive on the effect of additive concentration on NO yield but this variable was not studied in any detail.
7. At the higher temperature conditions, some of the fuel NO that forms decomposes thermally before reaching the probe in these input-output experiments.
8. The effect of pressure on NO_x yield is relatively small over the pressure range of 0.1 to 0.4 atm. However, at the feed rates selected to be used in the detailed probing experiments (6247 and 7520 cc/min), the NO_x yield at 0.1 atm will be somewhat higher than it would be at 1 atm (assuming that the trend in NO_x yield versus pressure does not reverse above 0.4 atm).

The screening experiment results were quite useful in planning the detailed probing experiments. In particular, information was provided on the effects of flow-rate, equivalence ratio, diluent ratio, additive concentration, and pressure that permitted conditions to be selected for the conducting of meaningful probing experiments. In addition, the input-output results form part of the data base required for an understanding of the mechanism of fuel NO_x formation. The similarity in

the NO yields from HCN and NH_3 suggests that it may be difficult to establish whether CN or NH_x mechanisms predominate in the formation of fuel NO_x from fossil fuels. For a fuel NO_x mechanism to be definitive, it will have to account for the similarity in NO_x yields from HCN and NH_3 under various conditions.

RESULTS AND DISCUSSION - DETAILED PROBING EXPERIMENTS

The screening experiments were quite informative but detailed probing experiments were required to determine where in the flame front the NO forms and the NH_3 and HCN react under various conditions, and to measure the rates of these processes. The probing experiments were carried out to obtain information on the following:

1. Does fuel NO form rapidly (in the CH_4 combustion zone)?
2. Do the similar NO yields from NH_3 and HCN result from the formation of a common intermediate in the combustion zone?
3. Do the additives react in the same zone that the NO forms, suggesting direct conversion to NO, or react well ahead of the formation of NO indicating the formation of large concentrations of reaction intermediates?

Based on the results of the screening experiments, it was decided to conduct detailed probing experiments at fuel-air equivalence ratios, ϕ , of 0.8 and 1.5 with the additive concentration at 2500 ppm molar based on total feed to burner. Equivalence ratios closer to stoichiometric would have produced maximum flame temperatures that could not be tolerated by the apparatus used (coated thermocouple and uncooled quartz probe) unless nitrogen were used as diluent rather than argon.

Eight premixed $\text{CH}_4\text{-O}_2\text{-Ar}$ flames were studied at the conditions listed in Table 26. The experimental data are tabulated in Appendix G. Both NH_3 and HCN were used at each equivalence ratio in the first four flame experiments. Argon dilution ($\text{DR} = 1.4$) was used in one HCN addition experiment at $\phi = 0.8$ to lower the flame zone temperature (flame 5). The next two detailed probing experiments (flames 6 and 7) were conducted at $\phi = 0.8$ and 1.5, respectively, with 625-ppm NO being added initially along with the HCN. The final detailed probing experiment was performed at

TABLE 26. CONDITIONS FOR PROBING EXPERIMENTS

Flame No.	Nominal Additive Concentration, ppm ¹	Equivalence Ratio, ϕ	Diluent Ratio ²	Burner Feed Rate ³ , cc/min	Calculated Adiabatic Flame Temperature, K	Measured Temperature Maximum ⁴ , K	Distance From Burner at T_{max} , mm
1	NH ₃ (2500)	0.8	1.0	7520	2295	2078, 1978 ⁵	6.0
2	HCN (2500)	0.8	1.0	7520	2306	2050	6.5
3	HCN (2500)	1.5	1.0	6247	2231	2012	8.3
4	NH ₃ (2500)	1.5	1.0	6247	2227	2080	8.0
5	HCN (1793)	0.8	1.4	5851	2097	1890	6.7
6	HCN (2500) +NO (625)	0.8	1.0	7520	~2306	1992	6.3
7	HCN (2500) +NO (625)	1.5	1.0	6247	~2231	2030	8.3
8	NO (675)	1.5	1.0	6247	~2230	1976	7.3

¹ Based on total feed gas to burner² Ar/O₂ molar ratio divided by 3.76³ Excluding additive flowrate⁴ Corrected for thermocouple radiation⁵ Rerun - Temperature difference attributed to higher flowrate of coolant caused by increased water pressure.

$\phi = 1.5$ with NO addition only. The experiments were conducted at 76 torr with a total burner feed rate of 6247 cc/min, excluding the nitrogen additive, at $\phi = 1.5$ and of 7520 cc/min at $\phi = 0.8$ (except for the dilution experiment in which the feed rate was 5851 cc/min).

The analyses by mass spectrometry of 1-liter batch samples of the collected gas, using the procedures described in the Experimental section, gave the mole fractions of CH_4 , O_2 , CO , CO_2 , Ar , C_2H_6 , C_2H_4 , H_2CO , and H_2 in the flames at various distances from the burner. However, this technique did not give reliable measurements for the concentrations of the species NH_3 , HCN , and N_2 at the low concentrations involved in these experiments.

Except for N_2 , the nitrogen species were measured with a chemiluminescent analyzer (CA) employing a molybdenum converter operated at 800 C. At this temperature, and in the presence of oxygen, the species HCN , NH_3 , $(\text{CN})_2$, and NO_2 are all converted to NO to some extent. Calibration experiments (Fig. 46) have shown that if sufficient oxygen is present, this converter is quite efficient for the conversion of NO_2 and HCN to NO, but only about 50 percent of the NH_3 is converted*. It was also demonstrated that $(\text{CN})_2$ will form NO in this converter at 800 C, but calibration experiments were not conducted with $(\text{CN})_2$. If the converter temperature is reduced to 400 C, only NO_2 is converted to NO permitting NO_2 to be distinguished from oxidizable nitrogen species. NO_2 measurements were made in the flame 2 and 4 experiments only. The amounts formed were quite small and NO_2 was detectable only in the early stages of the flame. The concentration of molecular nitrogen in the flames was not determined because of high nitrogen blanks that were encountered in the mass spectrometric results.

Data Interpretation

In reviewing the data obtained in these flame-probing experiments, it should be noted that when a species is reported as "HCN" or " NH_3 ," its mole fraction was obtained by dividing the measured concentration of NO formed in the converter by

*Perhaps the remainder decomposes to N_2 before it can be oxidized.

the converter calibration factor for the denoted species. It will be seen that, despite the limitations that this inability to distinguish directly between HCN and NH_3 puts on the interpretation of the data, considerable new information was obtained in this study regarding the chemical processes involved in the conversion of nitrogen species to NO in flames. In probing atmospheric flames, DeSoete was able to measure HCN and $(\text{CN})_2$ by specific chemical methods but did not measure NH_3 or N_2 . Merryman and Levy measured NO_2 and convertible nitrogen, which would include both NH_3 and HCN, but did not measure N_2 . Modifications are planned for the chemical analysis system of the apparatus used in the present study that will permit NH_3 and HCN to be measured independently and may allow N_2 to be measured directly.

It will be seen that all of the nitrogen introduced into a flame via the additive is not recovered in the measured products once the reaction temperature has been reached. Most of the missing nitrogen is undoubtedly in the form of N_2 in the later stages of the flame but it will be seen that under certain conditions (Flame 1: NH_3 , $\phi = 0.8$) nearly all of the additive-N is not recovered in the measured products of samples drawn from near the top of the luminous zone but later forms NO in high yield above the luminous. Since N_2 is not likely to be converted to NO in high yield via the Zeldovich mechanism*, it appears that another nitrogen product or intermediate forms that is not converted to NO on passing through the molybdenum converter. Therefore, the "missing" nitrogen required for a nitrogen balance will be referred to in this report as "N-BAL." It should be noted that part of the N-BAL that is observed *could* be an artifact. For example, *if* HCN were to be converted to $(\text{CN})_2$ and *if* $(\text{CN})_2$ underwent a smaller extent of conversion to NO than did HCN, this would appear as an increase in the calculated flux of N-BAL at that point in the flame.

For a nitrogen species other than N_2 to accumulate in the flame front and not be converted to NO when it reaches the molybdenum converter, it must almost certainly react in the probe to form N_2 . The only species likely to do this are free radicals such as N atom or NCO. CN radicals would more likely form HCN in the probe and

*Since the rate of formation of thermal NO is first-order in N_2 , the fraction of N_2 converted to NO should be the same at all N_2 concentrations. The possibility that N_2 can form and then oxidize to NO will be checked experimentally in the next study to be carried out in this apparatus.

then be converted to NO in the converter. This leads to the interesting conclusion that even if the small quantities of N_2 present in the gas samples had been measured, there is no assurance that all of it existed as N_2 in the flame front. This is, of course, the classic problem associated with flame-sampling experiments.

The temperature and mole-fraction profiles obtained in these probing experiments were used to calculate flux profiles for the various species of interest through the flame, and the flux profiles were used, in turn, to calculate the rates of production and depletion of these species at various points in the flame. It will be seen that to do this properly, the diffusion of the species must be taken into account. If this is not done, erroneous conclusions can be drawn. For example, NO may appear to form earlier in the flame than it actually does because it diffuses upstream from the zone in which it first starts to form from chemical reaction. Also, the N-additive would appear to start reacting earlier in the flame than it actually does because it diffuses downstream.

The rate of reaction of a species i in a 1-dimensional flow is given by the expression:

$$R_i = \mathcal{D}_{i,j} \frac{d^2 C_i}{dx^2} - v \frac{dC_i}{dx} \quad (127)$$

which is derived as shown in Appendix H. R_i is the rate of reaction (loss) of species i in moles/cm³-sec, v is the gas velocity in cm/sec, and $\mathcal{D}_{i,j}$ is the diffusion coefficient for i in excess j in cm²/sec. If the diffusion velocity of species i is defined as:

$$V_i = -\mathcal{D}_{i,j} \left(\frac{1}{C_i} \right) \frac{dC_i}{dx} \quad (128)$$

Then, Eq. 127 becomes:

$$R_i = - \frac{d}{dx} \left[C_i (v + V_i) \right] \quad (129)$$

The quantity $C_i (v + V_i)$ is the molar flux of species i in moles/cm²-sec. Because of diffusion, the velocity of species i is not the same as that of the bulk gas.

It can be seen that a plot of the flux for each species is very informative because the flux only changes as the result of chemical reaction whereas species mole fractions change as the result of both diffusion and chemical reaction. The slope of the flux (on a distance plot) gives the reaction rate for each species, as shown in Eq. 129.

The diffusion velocity was calculated from the slopes of plots of measured species mole fraction, f_i , versus distance using the following equation which is a modification of Eq. 128 (the change in C_i with T was neglected in making the transformation, Ref. 131):

$$v_i = -D_{i,j} \left(\frac{1}{f_i} \right) \frac{df_i}{dx} \quad (130)$$

Thermal diffusion was ignored because, generally, it is of negligible importance for the components considered in this study (only the low molecular weight species such as H or H_2 might require its use). As is usual for these conditions, the diffusion coefficients were calculated using Lennard-Jones potential parameters obtained from viscosity measurements and an empirically fitted expression for the Lennard-Jones collision integral (Ref. 131). The diffusion coefficients were calculated for the minor species NO, HCN, NH_3 , O_2 , CH_4 , and CO_2 diffusing through the major species, Ar. The final expressions for the diffusion coefficients resulting from the above considerations are shown below at $P = 0.1$ atm:

$D_{i,j} = AT^{1.67} \text{ cm}^2/\text{sec}$			
Species (i)	Species (j)	A	$T_{\min}^*, \text{ K}$
NO	Ar	0.1463×10^{-3}	308
NH_3	Ar	0.1854×10^{-3}	763
HCN	Ar	0.1282×10^{-3}	771
CO_2	Ar	0.1282×10^{-3}	472
CH_4	Ar	0.1631×10^{-3}	388
O_2	Ar	0.1467×10^{-3}	

*Minimum Temperature for which calculated $D_{i,j}$ are recommended.

The gas velocity as a function of distance through the flame was determined from the known mass feed rate to the burner, \dot{w} , by the equation

$$v = \frac{\dot{w}}{A_p} = \frac{\dot{w}RT}{APM} \quad (131)$$

where T is the measured temperature, P the pressure, A the burner area*, and M the molecular weight of the gas. Gas molecular weight was determined from the mass spectrometric analyses of the composition of the gas samples.

Values of the species flux, $C_i(v+V_i)$, moles/cm²-sec, were calculated as a function of distance through the flame. The slope of the flux versus distance correlation, or the reaction rate, was measured as a function of distance to obtain the species reaction rate profiles through the flame. The average gas residence time was calculated as a function of distance by integrating Eq. 131.

The importance of the diffusion calculations to the interpretation of the detailed probing results is illustrated in Fig. 55 which presents some of the Flame 1 results that will be discussed further in the next section. In Flame 1, 2500 ppm NH₃ was added to a CH₄-O₂-Ar flame at an equivalence ratio of 0.8. The CH₄ mole fraction curve in Fig. 55 shows that by the time the gases had reached the first CH₄ sampling point, which was only 0.5 mm above the top of the flame holder (screen), the CH₄ mole fraction had dropped to about one-half of its initial value. However, the calculated CH₄ flux curve demonstrates that the decrease in mole fraction up to that point resulted only from the downstream diffusion of CH₄ into the luminous zone. Virtually none of the CH₄ reacted below the bottom of the luminous zone. The NO mole fraction is appreciable and increasing below the bottom of the luminous zone and has reached about three-quarters of its final value at the top of the luminous zone. However, the calculated NO flux curve, which was obtained from the mole fraction curve by correcting for diffusion, indicates that nearly all of the NO present in the post-flame gases forms just above the top of the luminous zone. The rather large concentrations of NO that are present in the luminous zone result

*Sufficient purge argon flows around the burner to minimize divergence of the flame

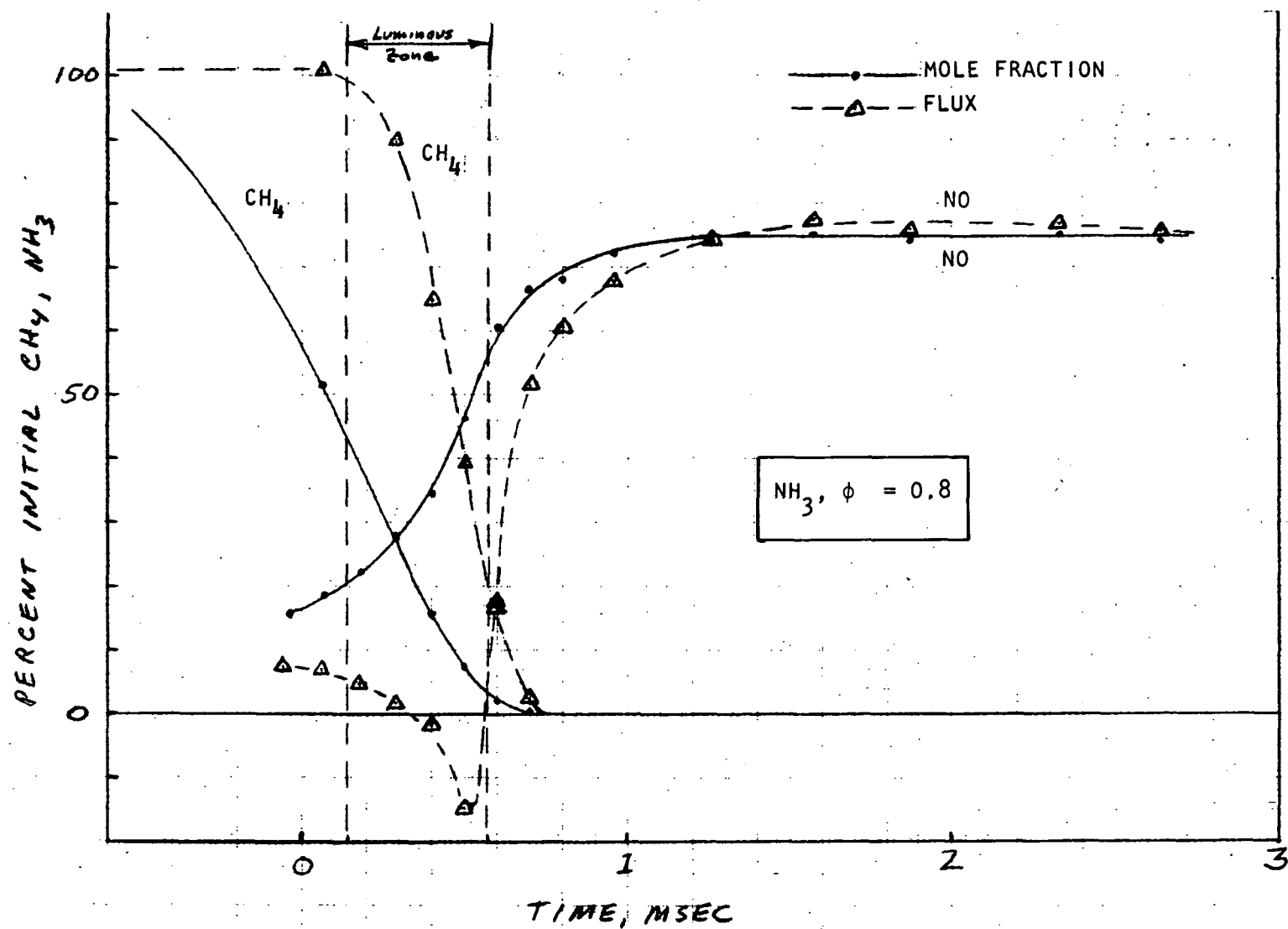


Figure 55. Comparison of Mole Fraction and Flux Curves, Flame 1, NH_3 Addition With $\phi = 0.8$

from the upstream diffusion of NO. A net consumption of NO occurs in the luminous. Most of the NO consumed was formed at the top of the luminous zone but part was formed below the luminous zone. Of course, additional NO could be simultaneously formed and consumed at points in and below the luminous zone giving no net effect on the flux and mole fraction curves.

Comparison of NO_x Flux Profiles

Before presenting the detailed results that were obtained under each condition, the NO flux profiles will be compared. The NO yields are plotted in Fig. 2 (which may be found in the Report Summary) relative to the top of the luminous zone (because the luminous zone is thinner in fuel-lean flames, the time scales were adjusted for this comparison so that the tops of the luminous zone coincide). Because these NO yields were calculated from the NO flux curves (to be presented) the correction for diffusion has been taken into account. It can be seen that relatively little NO is produced in or below the luminous zone. At $\phi = 0.8$, where NO forms in high yield, the NO forms rapidly just above the top of luminous zone (particularly with NH₃ as the additive). Under fuel-rich conditions, $\phi = 1.5$, much of the NO forms slowly in the post-flame gases far above the luminous zone.

Temperature Profiles

Compared in Table 27 are the temperature profiles obtained under the conditions employed in the detailed probing experiments to be discussed. The listed temperatures were taken from Tables 21 and 26. The maximum measured temperatures, which occurred about 6 to 8 mm above the burner, were 200 to 300 degrees lower than the adiabatic flame temperatures. The primary reason was heat loss to the water-cooled burner with heat losses to the rest of the surroundings also taking a toll. The maximum temperature was reached closer to the burner at $\phi = 0.8$ than at $\phi = 1.5$ even though the burner feed rate was larger. It will be seen that reaction occurs over shorter distances in the presence of excess oxygen. Increasing the diluent ratio to 1.4 moved the position of maximum temperature further from the burner even at a lower feed rate. This presumably results from lower reaction rates, resulting from lower temperatures and species concentrations. The measured

TABLE 27. TEMPERATURE PROFILES (P = 0.1 atm)

Equivalence Ratio, ϕ	0.8	1.5	0.8
Diluent Ratio, DR	1.0	1.0	1.4
Burner Feed Rate, cc/min	7520	6247	5851
Adiabatic Flame Temperature, K	2300	2229	2097
Maximum Measured Temperature, K			
Range	1978-2028	1976-2080	1885
Average	2025	2025	1885
Distance above burner, mm	6.3	8.0	6.7
Screening Experiment Temperature, K			
d = 49.4 mm	--	1776	--
d = 80.7 mm	1731	--	--

temperature decreased by about 250 degrees at distances far above the burner giving temperatures 50 to 80 mm above the burner that were lower than the adiabatic flame temperature by about 450 to 550 degrees.

In the following discussion of results, plots are presented as a function of time through the flame for: (1) temperature, (2) species mole fraction, (3) species flux, and (4) species reaction rate. Time zero was taken to be 1550 K for $\phi = 0.8$ and 1250 K for $\phi = 1.5$ because measurable reaction occurred at lower temperatures in fuel-rich flames. The data from each flame study are accompanied by a discussion of their interesting features and implications.

Fuel-Lean Flames ($\phi = 0.8$)-- Detailed Probing

The first two flames studied (Table 26) were with NH_3 and HCN addition at 2500 ppm, DR=1, $\phi = 0.8$, and feed rate = 7520 cc/min. The expected NO yields based on the screening experiments (Fig. 53) were about 82 percent for NH_3 and 83 percent

for HCN.* The reactant gas composition under these conditions (in mole percent) was: CH₄, 7.73; O₂, 19.33; Argon, 72.69; and additive 0.25. The nitrogen content of the mixture was that which would be obtained if 2.83 percent nitrogen were added to the CH₄ (as NH₃ or HCN).

Flame 1--Ammonia Addition With $\phi = 0.8$. The data acquired from the detailed probing of Flame 1 are given in Tables G-1, G-2, and G-12 in Appendix G and in Fig. 56 and 57. Temperature and ppm NO profiles are given for the initial Flame 1 experiment and a temperature profile and ppm profiles for all major species are presented for a complete rerun. The two temperature profiles plotted in Fig. 56 show an almost constant difference of about 100 K on a plot of T versus distance from the burner. The temperature difference is believed to have been caused by a change in the flowrate of cooling water to the burner.

The ppm NO profiles from each run, plotted in Fig. 57, are quite similar. The somewhat steeper ppm curve for the rerun caused some minor differences in the calculated NO flux profiles. The NO flux from the rerun experiment (Fig. 58) goes negative near the top of the luminous zone and then rises rapidly just past the luminous zone. An NO flux profile calculated from the initial Flame 1 experiment (not shown) also had a value of 4×10^{-8} below the luminous zone but then remained constant through the luminous zone increasing rapidly just above the luminous zone. These differences do not, however, affect the major conclusion that under fuel-lean conditions nearly all of the NO forms just above the luminous zone in the region where most of the CO₂ forms. This demonstration of the sensitivity of the flux profiles to the slopes of the mole fraction curves is one of several that will be encountered.

The NO flux curve in Fig. 58 indicates that some NO, about 10 percent of the total NO, forms below the first measurement point, i.e., at or below the flame holder.** However, all of this NO plus the NO that forms just below the top of the luminous zone react in the luminous zone giving no net NO flux at the top of the luminous

*Even higher yields might be expected because the screening experiments indicated that at $\phi = 0.8$ (excess oxygen) some NO decomposed before reaching the downstream probe positions in the higher temperature screening experiments.

**The possibility that the flameholder screen catalyzes the oxidation of part of the NH₃ to NO cannot be ruled out.

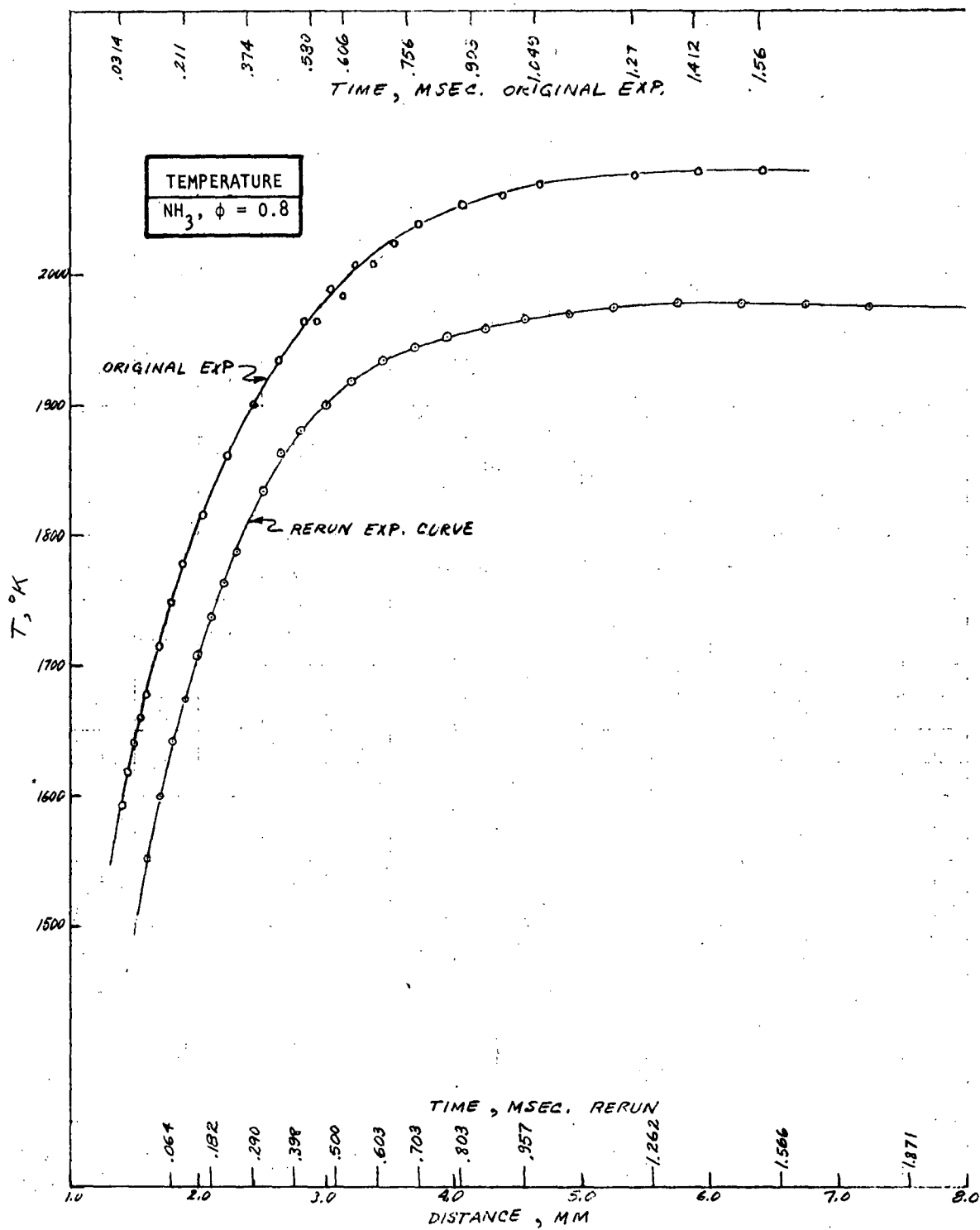


Figure 56. Flame Temperature vs Time, Flame 1, NH₃ Addition With $\phi = 0.8$

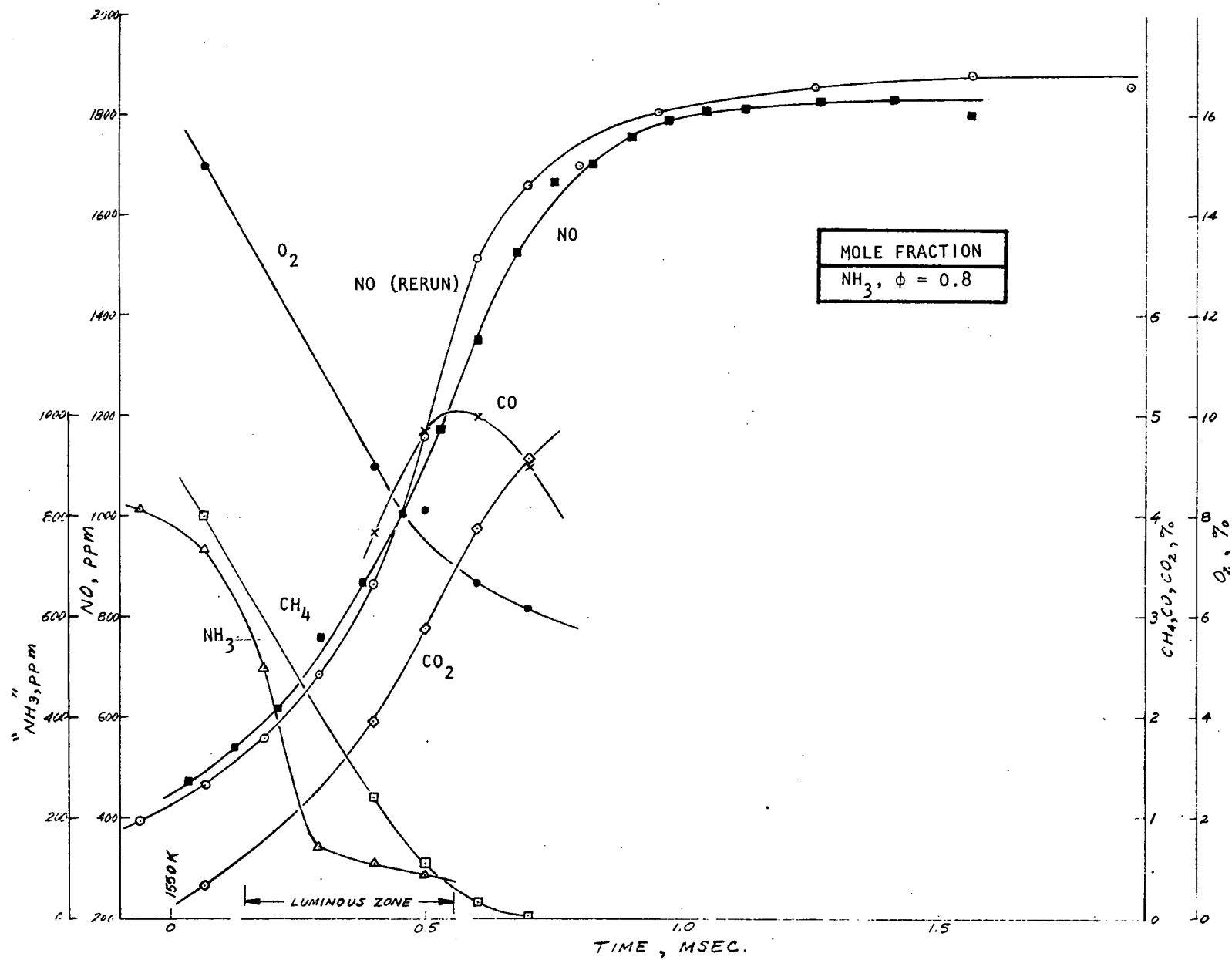


Figure 57. Species Mole Fraction vs Time, Flame 1, NH_3 Addition With $\phi = 0.8$

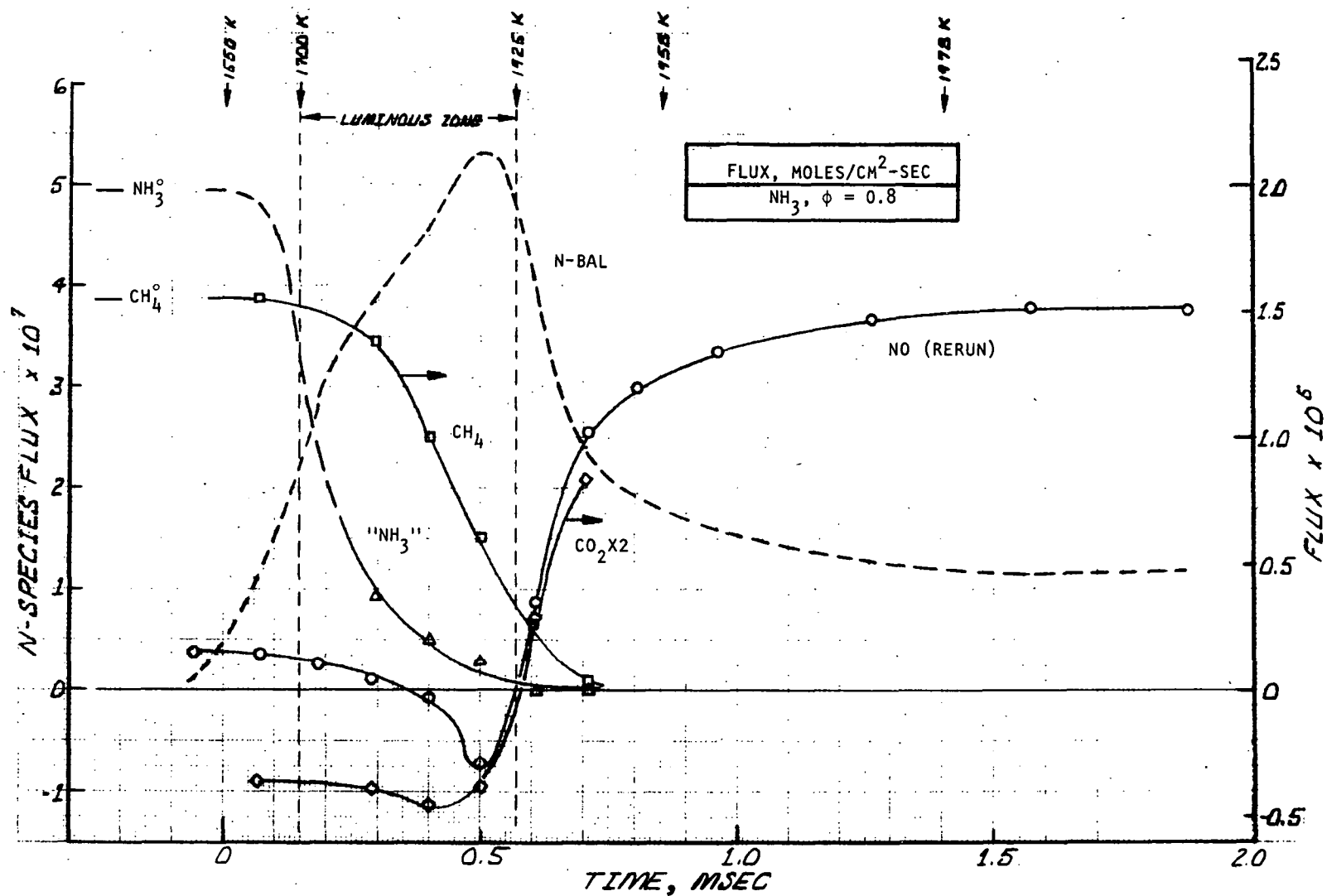


Figure 58. Species Flux vs Time, Flame 1,
 NH_3 Addition With $\phi = 0.8$

zone. The upstream diffusion of NO reaches its maximum at about the position (0.5 msec) where the inflection point in the NO mole fraction curve occurs (maximum slope). This gives rise to a negative NO flux in that region of the flame.

Species mole fractions change both from diffusion and chemical reaction whereas the flux for each species is constant unless chemical reaction is occurring. For this reason, the flux plots will be emphasized in the analysis of the data obtained in these flame probing experiments. From Eq. 129, the slope of the flux curve (on a distance plot) gives directly the reaction rate of a given species (in units of moles/cm³-sec). Reaction rates calculated in this manner for Flame 1 are plotted in Fig. 59. The maxima in the reaction rate plots indicate the region in the flame at which each reactant and product is lost or formed most rapidly. Because the rates are plotted as a function of time, the area under a given rate curve represents the extent of reaction (in moles/cm³) that occurs in that region of the flame. (The reaction rate is defined in Eq. 127 as positive when concentration decreases with increasing distance from the burner; this definition is retained in the rate plots presented for each flame.)

Denoted on each flux plot (e.g., Fig. 58) for comparison, are the position of the observed luminous zone and the points in the flame at which selected temperatures are reached. These five temperatures are, respectively, the temperature at zero on the time scale (1250 K for $\phi = 1.5$ and 1550 K for $\phi = 0.8$), those at the bottom and top of the luminous zone, the temperature that is 20 degrees below the maximum temperature, and finally, the maximum temperature. Because the temperature profile is quite flat near the maximum temperature (e.g., Fig. 56), the point where the temperature is 20 degrees below the maximum is identified on the flux plots to indicate where the temperature begins to approach the maximum value. Also included on the flux plots, at the left edge, are the initial fluxes of CH₄ and the nitrogen additive(s). These fluxes are calculated from the metered reactant flowrates and the area of the burner.

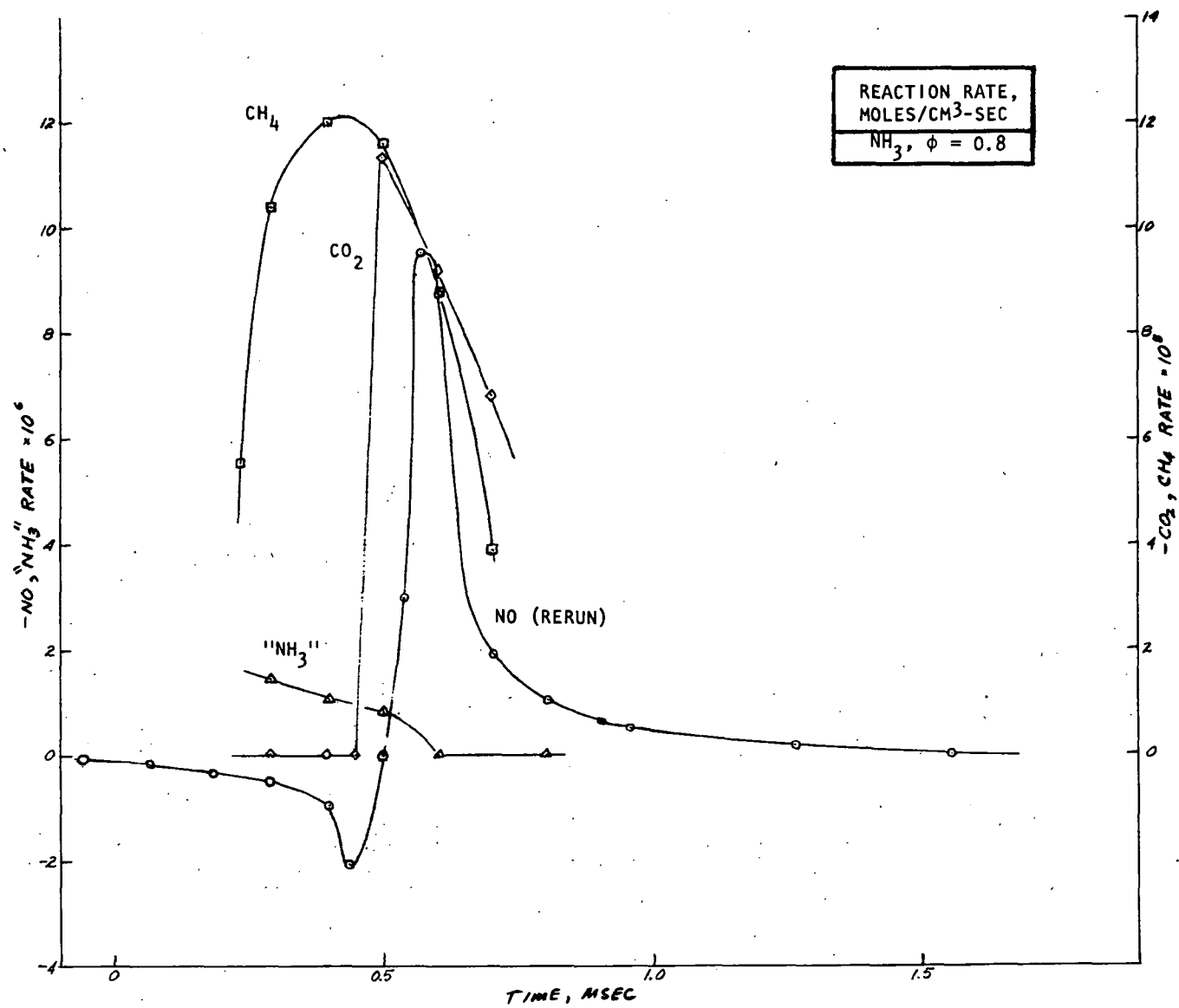


Figure 59. Species Reaction Rate vs Time, Flame 1,
NH₃ Addition With $\phi = 0.8$

The NO flux in Flame 1 reached its maximum value in about 1.5 msec on the assigned time scale* and then remained constant (Fig. 2 and 58). The final NO flux was 77 percent of the metered NH_3 flux. This is slightly lower than the 82 percent (or greater) yield that would have been predicted from Fig. 53. Between 0.5 msec and 0.85 msec, the point at which the temperature reached 1958 K or within 20 degrees of the maximum, the NO flux increased from 10 percent of its final value to 76 percent of the final value. Thus, two-thirds of the NO formed just above the luminous zone in a region 0.35 msec "thick" where the temperature range was 1925 to 1960 K. This is the same region or the flame in which most of the CO_2 is formed (Fig. 58). The NO reached its maximum rate about 0.1 msec after the CO_2 (Fig. 59).

The nitrogen species that were oxidized to NO in the molybdenum converter at 800 C were measured and plotted as " NH_3 " in Fig. 57 and 58. This is probably NH_3 but some of the NH_3 could conceivably have been converted to HCN (or cyanogen, but this is less likely). The " NH_3 " mole fraction and flux curves were calculated using the converter calibration factors and the diffusion coefficients for NH_3 . The NH_3 reacted so early in the flame that the " NH_3 " mole fraction had decreased to one-third its initial value (by reaction and/or diffusion) by the time the first sampling point had been reached despite the fact that this point was only about 0.1 mm above the top of the flame holder (Table G-2). Because of the limited number of data points taken and the steepness of the " NH_3 " mole fraction curve, the " NH_3 " fluxes calculated at the first three data points were erratic. It was established, however, that the " NH_3 " flux was less than 20 percent of its initial value at the fourth sampling point (0.3 msec) and decreased to nearly zero at the top of the luminous zone. Even if the " NH_3 " measured in the luminous zone were actually HCN formed from the added NH_3 , the HCN flux would also be near zero at the top of the luminous zone. Because it was not possible to determine from the data exactly where most of the NH_3 reacted and how much, if any, was converted to HCN, the additive flux curve was dotted up to fourth sampling point and labeled " NH_3 ."

*It can be seen from the time-distance correlations in Fig. 56 and Table G-2 that this point is at a distance of 6.3 mm above the burner. Since the distance zero was taken at the bottom of the flame holder screen and this screen is 1.3 mm thick, the NO reaches its maximum concentration about 5.0 mm above the flame-holder.

The observations that (1) all of the added NH_3 and any measurable nitrogen species formed react before reaching the top of the luminous zone and (2) no net formation of NO occurs below this point in the flame lead to the very interesting conclusion that, at $\phi = 0.8$, all of the added NH_3 is converted to nitrogen species that are not measurable by the converter-CA technique before the rapid formation of NO begins. This results in the "N-BAL" flux in Fig. 58 being equal to the initial NH_3 flux near the top of the luminous zone. The nitrogen balance flux curve, N-BAL, was obtained at each point by subtracting the " NH_3 " and NO fluxes from the initial NH_3 flux.

It can be seen from Fig. 58 that the nitrogen intermediate(s) that apparently forms quantitatively from the NH_3 reacts rapidly just above the luminous zone to form NO in high yield. It may react with O or OH radicals, which increase rapidly in concentration in this region, or with O_2 which is still present at a concentration of more than 6 percent in this fuel-lean flame.

Only small amounts of NO_2 were detected in and just above the luminous zone (Table G-1). The maximum mole fraction of NO_2 was about 8 ppm or 0.3 percent of the added NH_3 . NO_2 was not detected in the later stages of the flame. Early NO_2 has been detected by others (Ref. 101, 134, and 135). Whether it is present in the flame, or the result of reactions occurring in the microprobe during quenching, is apparently still a moot point (Ref. 135).

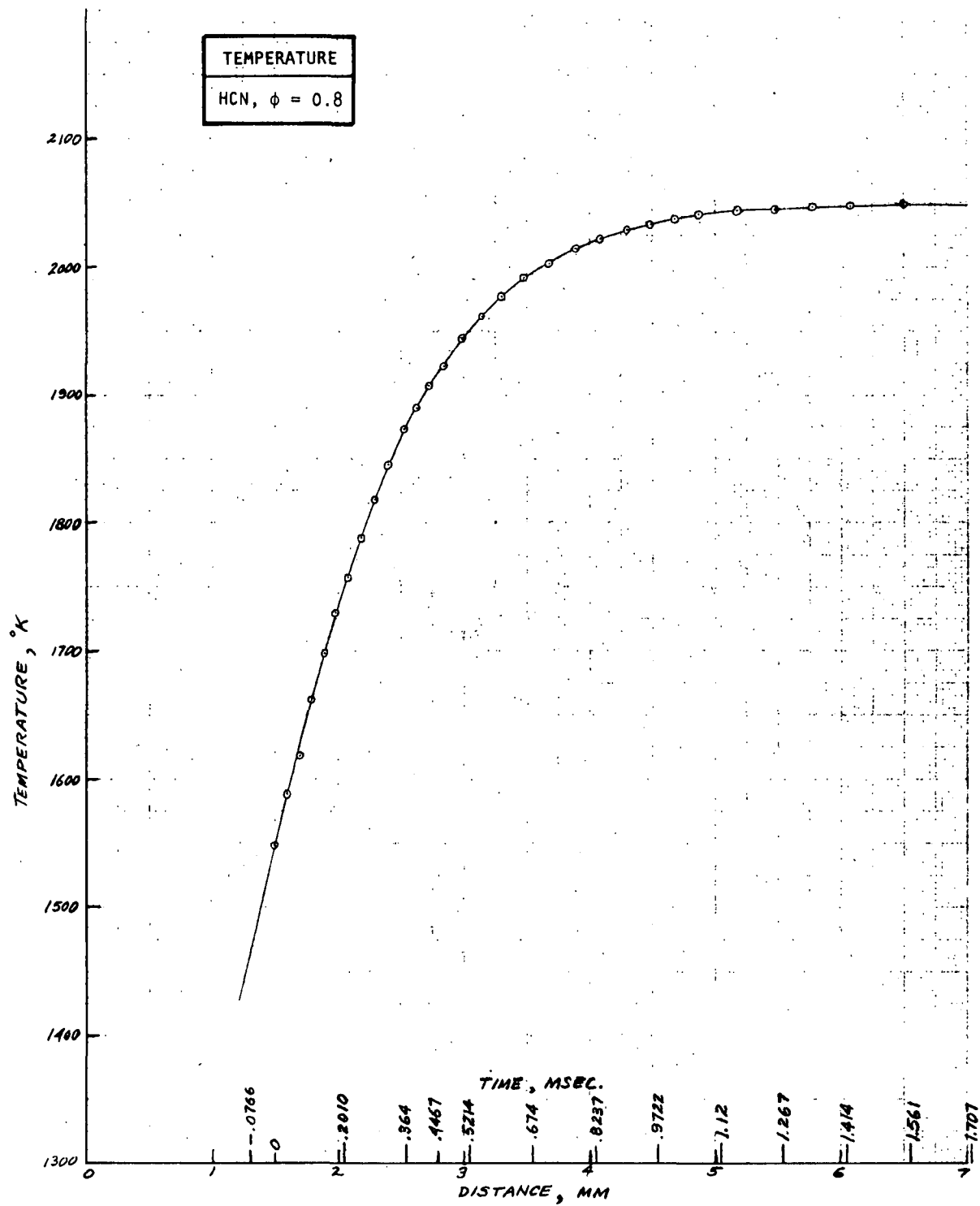
It will be seen that under both lean and rich conditions nearly all of the CH_4 reacts in the visual luminous zone. The time required for the gases to travel through the luminous zone is about 0.4 msec at $\phi = 0.8$ and 0.9 msec at $\phi = 1.5$ (see Fig. 2). The oxygen reacts in the luminous zone with the CH_4 and in the near post-flame gases where CO is converted to CO_2 . The flux curves for O_2 and CO were not calculated. The CO_2 flux was used to determine the rate of CO oxidation. In several of the flames, including Flame 1, the CO_2 flux curve goes negative in the luminous zone. This is not believed to be a real effect because it does not occur

in all flames of the same ϕ and, should some CO_2 be consumed in the luminous zone, the flux curve should attain a negative slope in that region as a result of this reaction.

To check the carbon balance, the CO flux can be calculated readily at the point where CO reaches its maximum mole fraction (about 0.58 msec in Fig. 57) because the diffusion velocity of CO is zero at that point (Eq. 130) and the CO flux is simply the product of its concentration and the bulk gas velocity. The concentration of CO is 3.18×10^{-8} moles/cm³ and the velocity is 321 cm/sec giving a CO flux of 1.02×10^{-5} moles/cm²-sec. At this point, the CH_4 flux is 0.25×10^{-5} and the calculated CO_2 flux is about zero giving a total measured flux of carbon species of 1.27×10^{-5} which is 83 percent of the initial CH_4 flux of 1.54×10^{-5} . If the CO_2 flux curves in Fig. 58 were shifted upward so that the flux at 0.7 msec were zero, the carbon balance would become 106 percent again indicating that the negative CO_2 fluxes are not real.

Flame 2--HCN Addition With $\phi = 0.8$. The data obtained from this experiment are listed in Tables G-3 and G-13 in Appendix G. The measured temperatures and species mole fractions are plotted in Fig. 60 and 61. The calculated fluxes and reaction rates are plotted in Fig. 62 and 63.

The NO flux (Fig. 62) has a slight positive value at the first sampling point and then remains constant through the luminous zone. NO formation occurs rapidly above the luminous zone as was the case when NH_3 was added to the fuel-lean flame. It can be seen from Fig. 2, however, that the maximum rate of NO formation occurs about 0.24 msec later when the additive is HCN. The NO measurements were carried out to 1.7 msec (7 mm above the burner) but the NO flux had not yet reached its maximum value (Fig. 2). The NO yield at 1.56 msec was 63 percent and was increasing at a rate that indicated that it would have reached a maximum value in the range of 80 percent near the value of 83 percent that was obtained in the HCN screening experiments (Fig. 53). As discussed, values greater than 83 percent should have been obtained in the probing experiments because some NO apparently decomposed (at $\phi = 0.8$) before reaching the screening probe position.



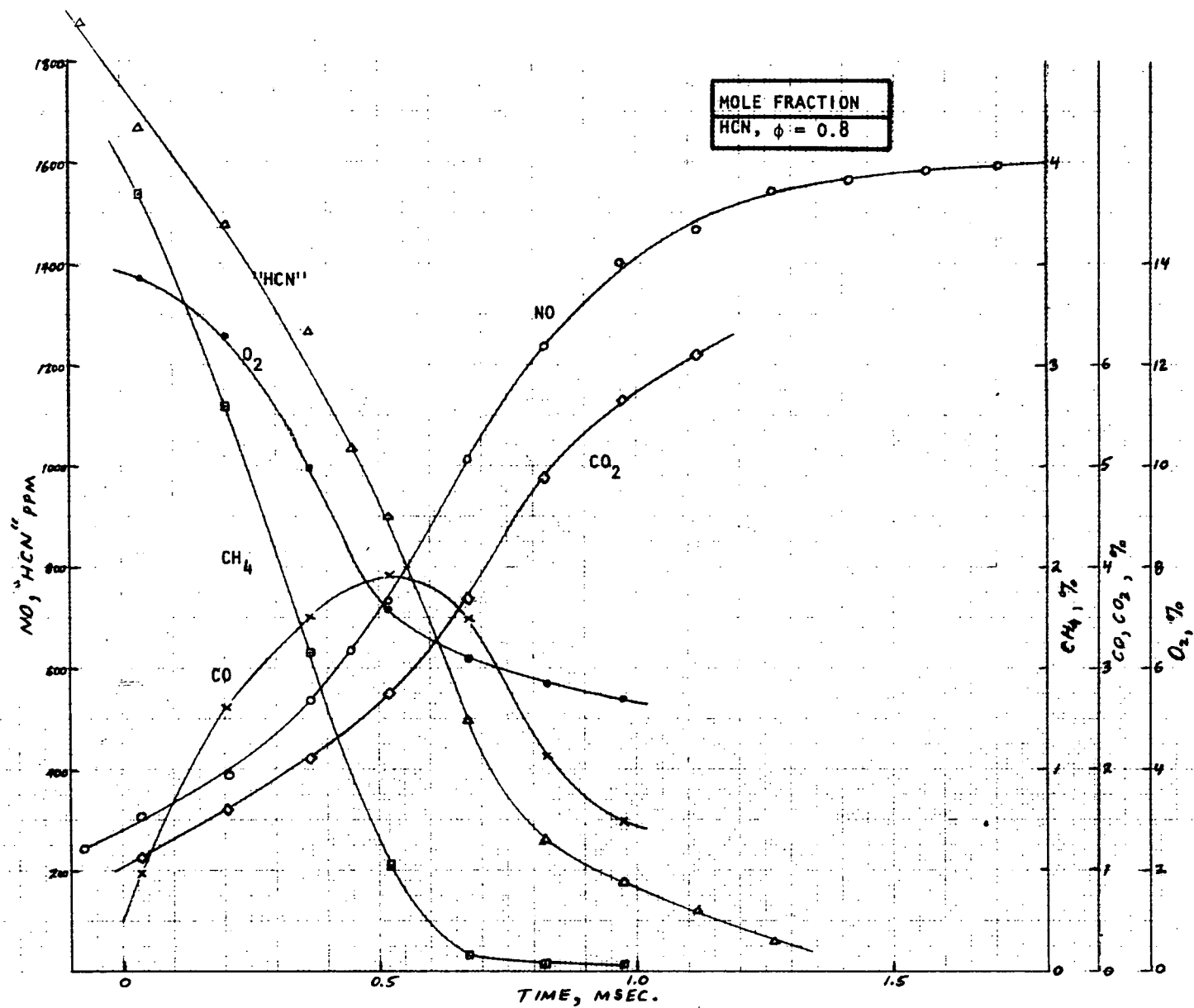


Figure 61. Species Mole Fraction vs Time, Flame 2, HCN Addition With $\phi = 0.8$

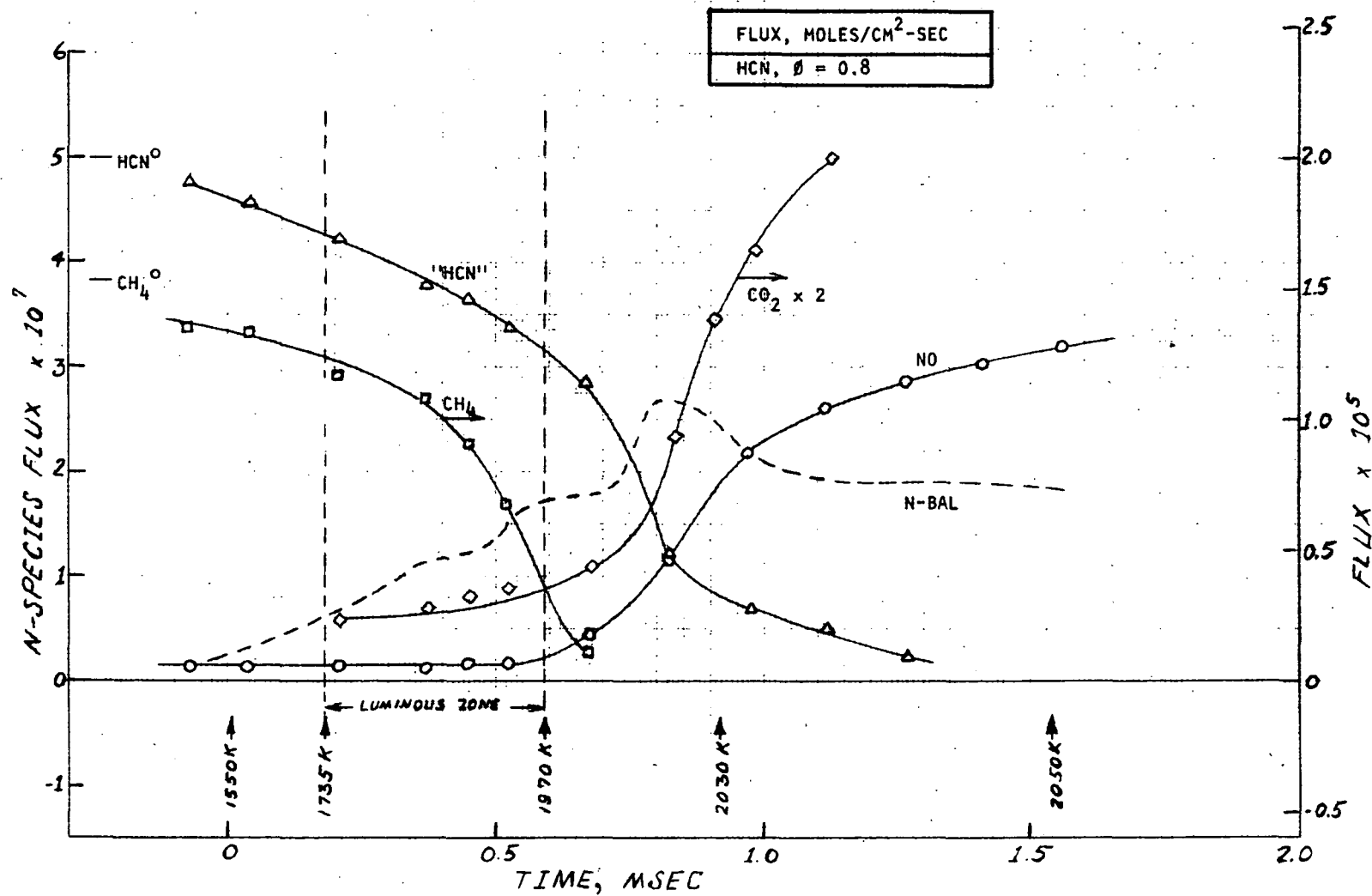


Figure 62. Species Flux vs Time, Flame 2,
HCN Addition With $\phi = 0.8$

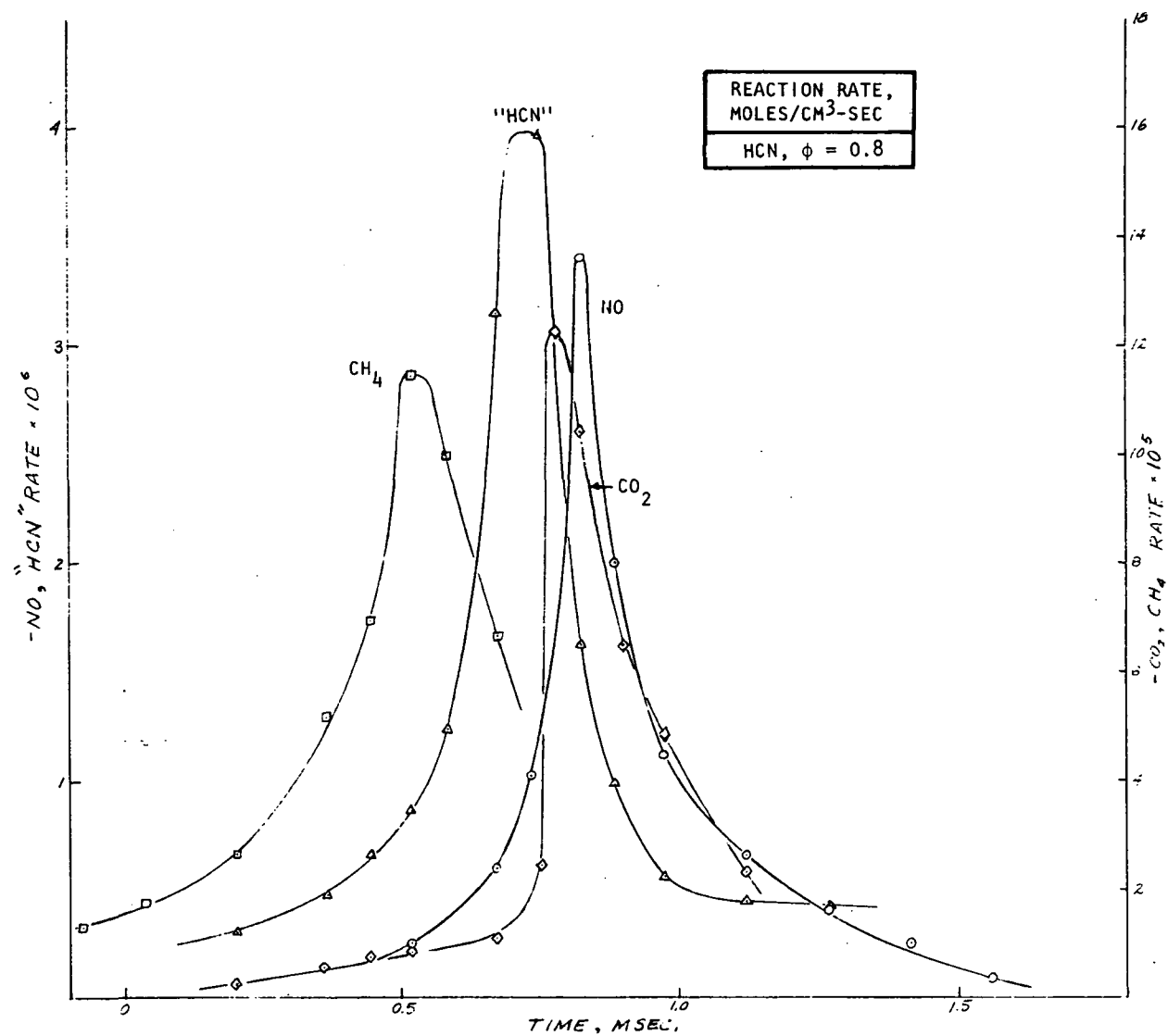


Figure 63. Species Reaction Rate vs Time, Flame 2,
HCN Addition With $\phi = 0.8$

Mole fractions and molar fluxes were calculated for the nitrogen species that were oxidized to NO in the molybdenum converter using the calibration factors and diffusion coefficients for HCN. It can be seen from the "HCN" flux curve in Fig. 62 that more than 60 percent of the added HCN survives the luminous zone. The HCN reacts gradually below and through the luminous zone and then more rapidly above the luminous zone. It is apparently the low reactivity of the HCN that causes the NO to form farther above the luminous zone in Flame 2 than in Flame 1.

It is likely that the curves labelled "HCN" actually do represent HCN because if any NH_3 were to form it would have reacted very rapidly as in the Flame 1 experiments. The formation of $(\text{CN})_2$ is not likely because any CN radicals formed should abstract a hydrogen atom and reform HCN rather than combine to form cyanogen. In addition, DeSoete (Ref. 64) has shown that cyanogen forms HCN in a hydrocarbon flame.

The rate maxima in Fig. 63 indicate that NO forms from HCN in the same region of the flame in which CO is oxidized to CO_2 (suggesting that OH radicals may be involved as was proposed by Fenimore, Ref. 66). The rate of maximum NO formation lags the maximum rate of HCN reaction by about 100 microseconds (Fig. 63) indicating that an intermediate species forms from the HCN. The formation of an intermediate from HCN is also demonstrated by the flux profiles. The N-BAL flux reaches a maximum that represents nearly 50 percent of the added HCN and then decreases. Nitrogen species other than N_2 must be present because the N-BAL flux must finally decrease to 1.0×10^{-7} if an 80 percent yield of NO is obtained. An even stronger related argument for the hypothesis that much of the NO does not form from the direct oxidation of HCN is that from 0.8 to 1.6 msec on the assigned time scale, the NO flux increases by 2.0×10^{-7} while the HCN flux decreases by only 1.3×10^{-7} . In fact, if an 80 percent NO yield is obtained, the NO flux would increase by 2.8×10^{-7} from its value at 0.84 msec and yet the HCN flux is only 1.2×10^{-7} . The maximum rate of NO formation (Fig. 63) occurs at 0.85 msec and is larger than the HCN decay rate at that point by a factor of 2.3

Comparison of the Flame 1 and Flame 2 results demonstrates that although NH_3 and HCN form similar amounts of NO at $\phi = 0.8$, their rates of reaction in the flame are quite different. A significant fraction of the HCN remains unreacted up to as much as 1 msec longer than does NH_3 . The results indicate that neither NH_3 nor HCN form NO directly at an equivalence rate of 0.8 but rather the NO forms from a moderately long-lived nitrogen intermediate. The intermediate cannot be NH_3 , HCN or $(\text{CN})_2$ because these would be measured by the converter-CA technique. It is not likely to be CN or NH_x radicals, because these would probably form NO in the probe-converter system; or N atom, because it would be too short lived; or N_2 , because its (fractional) rate of conversion to NO is probably too slow. We postulate that this intermediate is the NCO radical. To explain the results obtained from Flames 1 and 2, the intermediate would have to (1) form quantitatively from NH_3 and in at least 50 percent yield from HCN, (2) be oxidized later in the flame to form NO in high yield, and (3) recombine in the probe to form N_2 so that it could not be converted to N_2 in the molybdenum converter.

Fuel-Rich Flames ($\phi = 1.5$)-- Detailed Probing

Flames 3 and 4 (Table 26) were with HCN and NH_3 addition at 2500 ppm under fuel-rich conditions ($\phi = 1.5$, DR=1, and feed rate = 6247 cc/min. The reactant gas composition under these conditions (in mole percent) was: CH_4 , 13.58; O_2 , 18.10; Argon, 68.07; and additive 0.25. The nitrogen content of the mixture was that which would be obtained if 1.61 percent nitrogen were added to the CH_4 (as NH_3 or HCN).

Flame 3--HCN Addition With $\phi = 1.5$. The data obtained from the detailed probing of Flame 3 (Tables G-4, G-5, and G-14) are plotted in Fig. 64 through 67. The NO and HCN data were obtained in a partial rerun because experimental difficulties were encountered with the CA measurements in the first Flame 3 experiment.

The NO flux curve in Fig. 66 is near zero at the top of the luminous zone, increases slightly just above the luminous zone and then increases gradually with a small inflection starting at 2.7 msec. The Flame 3 flux yield is plotted in Fig. 2 for comparison with the other conditions. It can be seen that for fuel-rich flames

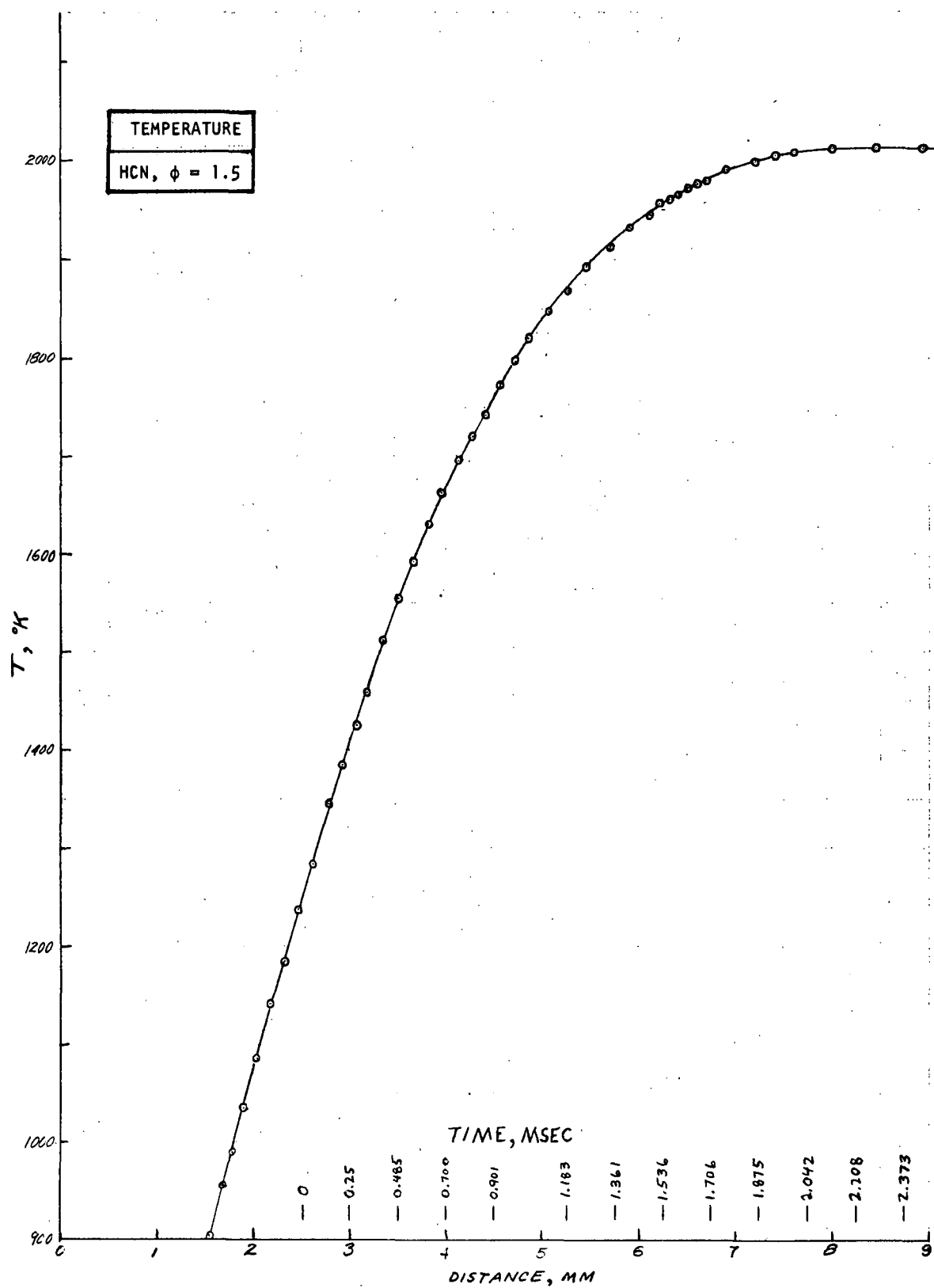


Figure 64. Flame Temperature vs Time, Flame 3, HCN Addition With $\phi = 1.5$

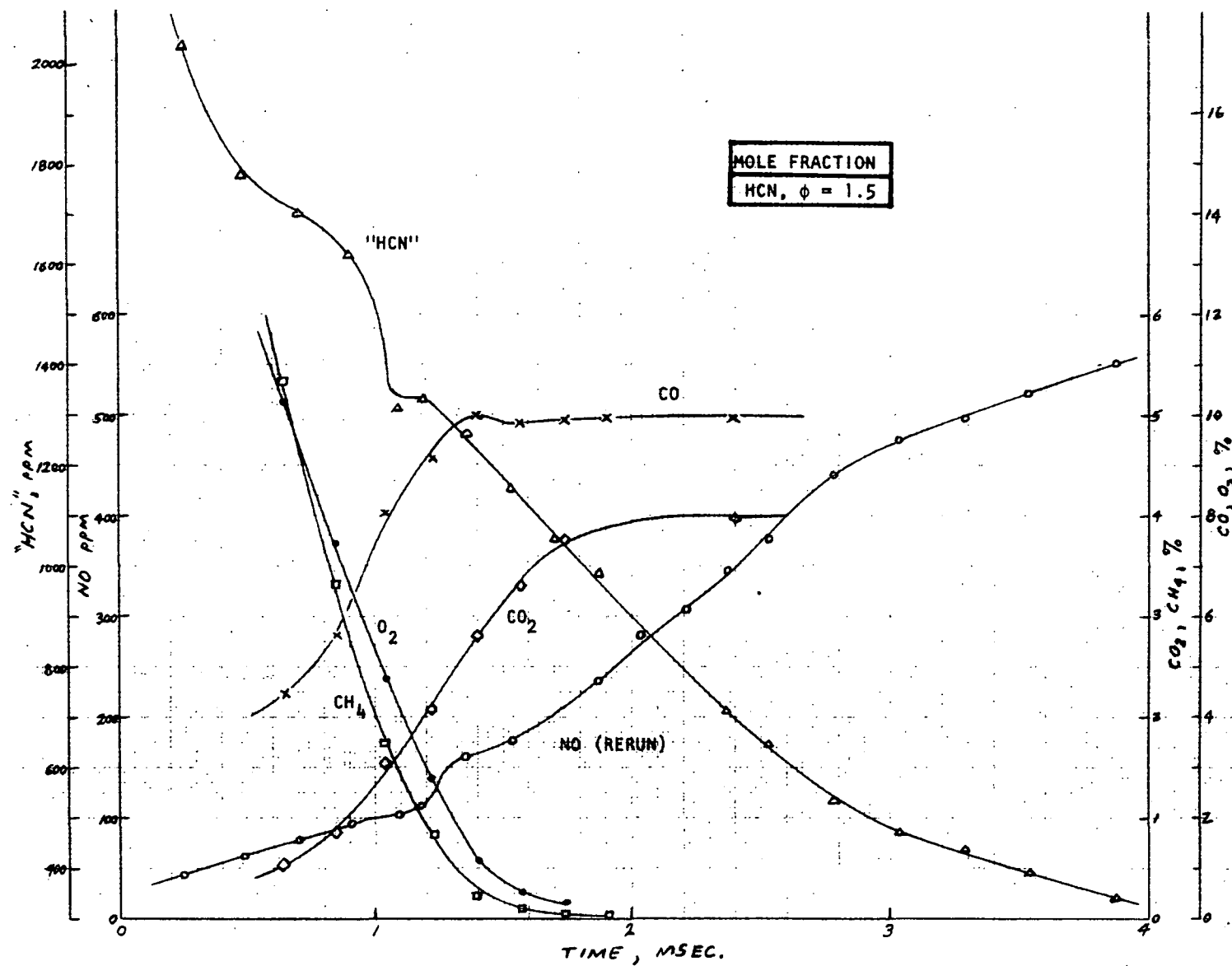


Figure 65. Species Mole Fraction vs Time, Flame 3, HCN Addition With $\phi = 1.5$

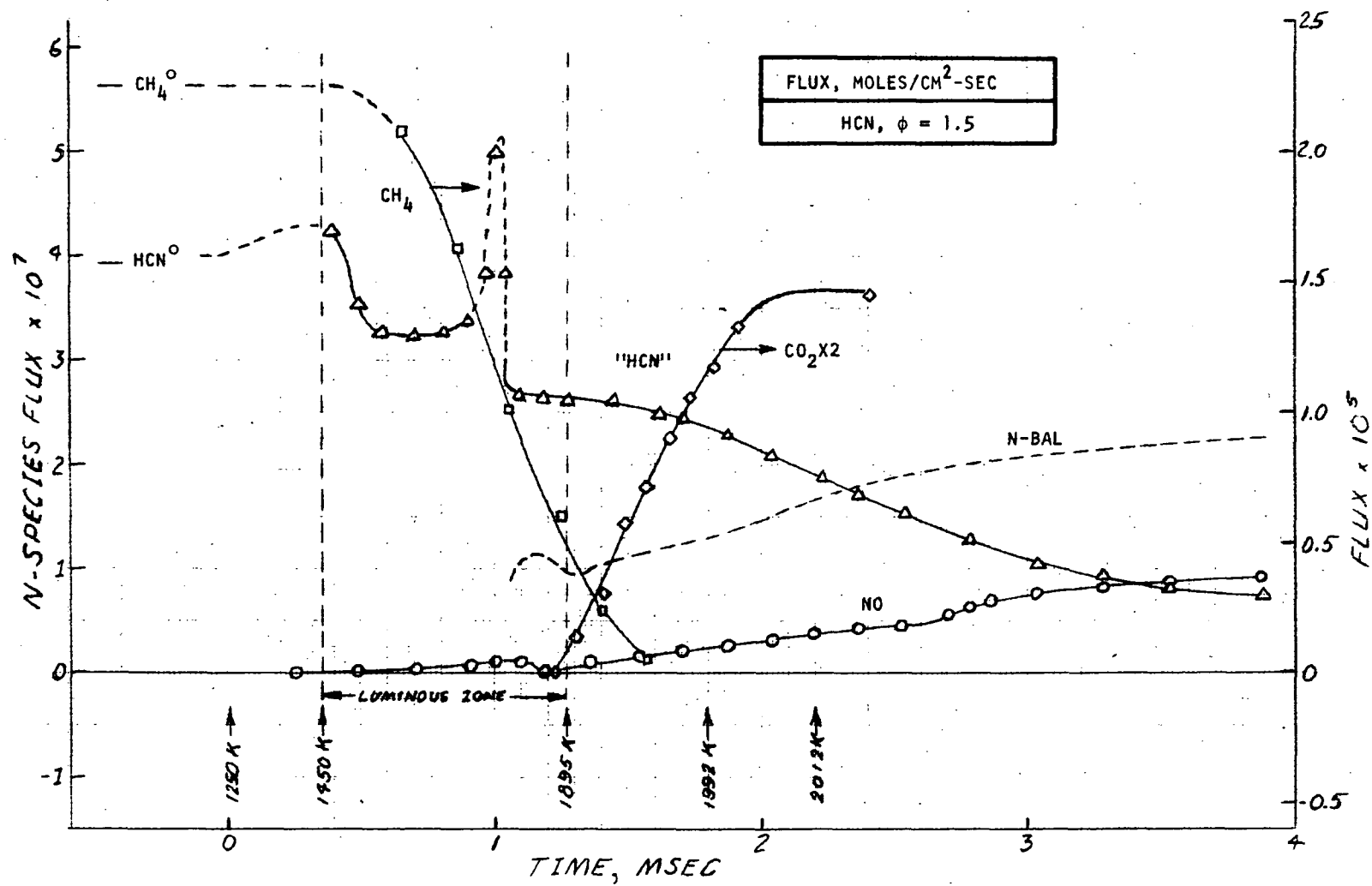


Figure 66. Species Flux vs Time, Flame 3, HCN Addition With $\phi = 1.5$

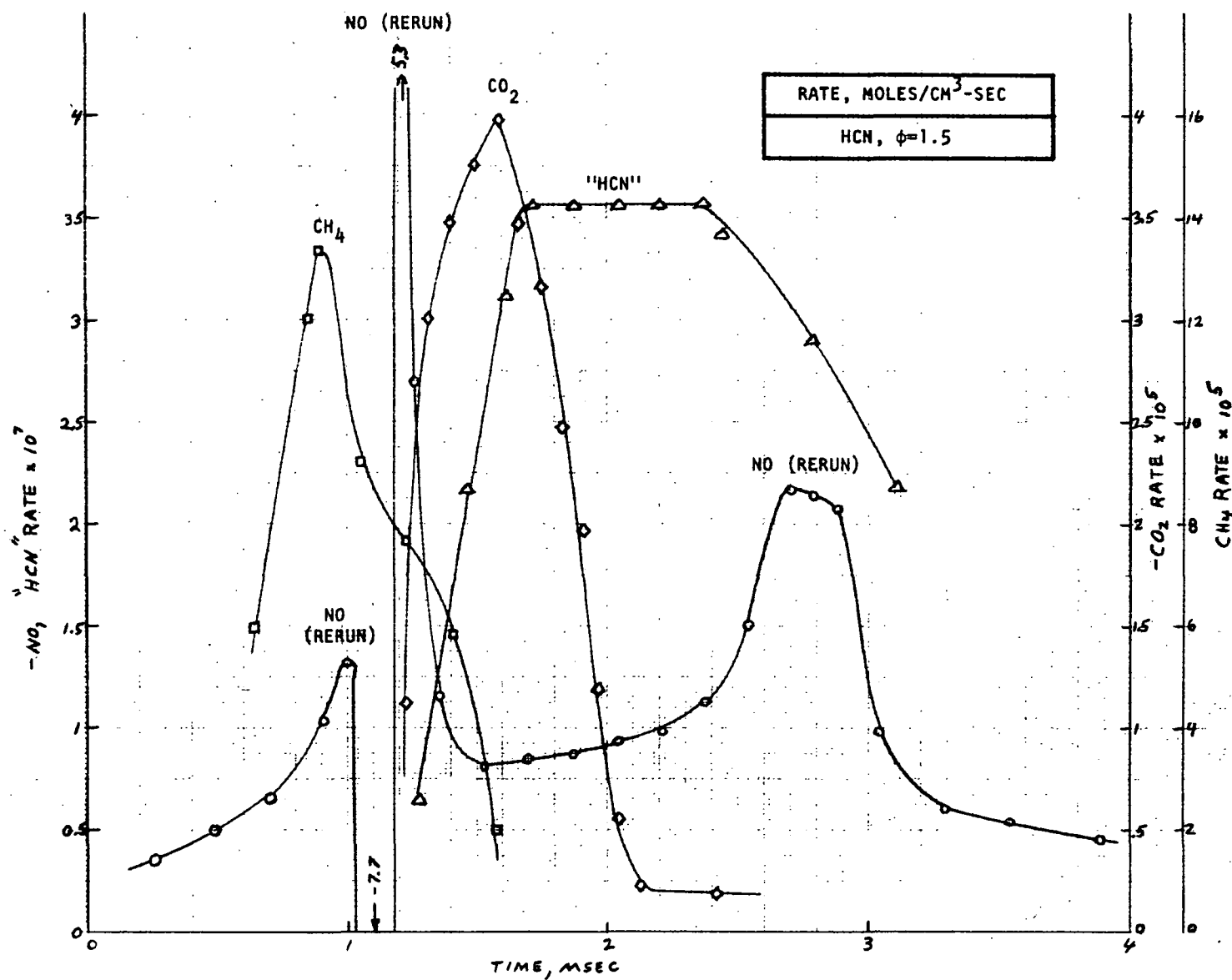


Figure 67. Species Reaction Rate vs Time, Flame 3, HCN Addition With $\phi = 1.5$

most of the NO forms far above the luminous zone and well above the region where CO is oxidized. The NO flux at the last measurement point in Flame 3 was 23.4 percent of the initial HCN flux and was increasing slowly. The screening results suggest that the NO yield would have reached about 32 percent if additional data points had been taken further above the burner. HCN experiments were not conducted at this lower flowrate but NH_3 gave 32 percent NO yield (Run I-1 in Table 21) and HCN gave about the same yields under all conditions.

The "HCN" mole fraction in Fig. 65 decreased gradually and almost linearly through and after the luminous zone except for a dip near the top of the luminous zone. The "HCN" flux (Fig. 66) calculated beyond this dip in the mole fraction curve remained nearly constant for about 0.4 msec at the top of the luminous zone and then decayed very slowly. The "HCN" flux was only slightly less than the NO flux at the last measurement point. About two-thirds of the added HCN apparently survives the luminous zone and then reacts very slowly with 20 percent of the initial HCN remaining unreacted well above the flame front (at about 4 msec on the assigned time scale). This suggests that considerable HCN may pass through the burner under these fuel-rich conditions. The moly converter was not operated at 800 C in the screening experiments in which the probe was 80 mm above the burner. Such "exhaust" measurements of HCN will determine the amount of HCN that survives under these conditions.

The "HCN" flux calculated in the luminous zone (Fig. 66) dropped slightly at the bottom of the zone and then remained constant until just above the middle of the zone where it increased to a sharp maximum before dropping abruptly to its lower constant value below the top of the luminous zone. The shape of the "HCN" flux curve in the region where it apparently increases to a maximum value depends on the shape of the mole fraction curve near its dip. More data points in this region are required to determine if this spike in the flux "HCN" curve is real. In any event, it cannot be as large as shown in Fig. 66 because the top of the spike is well above the initial HCN flux. These conditions were repeated in a later experiment, Flame 7, except that some NO was added initially with the HCN. It will be seen (Fig. 83) that the "HCN" flux curve again dropped abruptly near the center of the luminous zone and then leveled off. No spike in the flux curve was obtained in Flame 7.

The CO_2 reaches its maximum rate of formation at 1.6 msec. At this point, only one-third of the HCN has reacted and only 17 percent of the final NO has formed. It is apparent, therefore, that under fuel-rich conditions, fuel NO forms from HCN slowly over a considerable distance above the luminous zone. Because of the low NO yields obtained under fuel-rich conditions, it is not possible to determine if most of the NO forms directly from HCN or if an intermediate is involved. The NO formation rate (Fig. 67) never exceeds the decay rate of HCN except just above the top of the luminous zone at which point the NO must form from an intermediate.

Flame 4--Ammonia Addition With $\phi = 1.5$. The data acquired on Flame 4 are listed in Tables G-6, G-7 and G-15 in Appendix G. The initial experiment with the fuel-rich Flame 4 gave the temperature profile shown in Fig. 68 and the species mole fractions plotted in Fig. 69 for those species measurable by mass spectroscopy. A partial rerun of Flame 4 was carried out (Table G-7) in which the NO concentration measurements were made and the NO formed in the molybdenum converter at 800 C was measured. For reasons that will be discussed, the NO formed in the converter was plotted in the mole fraction figure (Fig. 69) both as " NH_3 " and as "HCN" by using the converter calibration factors for NH_3 and HCN, respectively, and two flux are presented for this flame (Fig. 70 and 71).

The NO flux profile for Flame 4 shown in Fig. 70 shows an apparent inflection at a point 6 mm above the burner or at about 1.45 msec on the assigned time scale. This inflection in the NO flux curve indicates the rapid formation of NO near the top of the luminous zone followed by a region of little NO formation and then a second stage of NO formation as the maximum temperature is approached. The apparent two-stage nature of NO formation in this flame is indicated by the two rate maxima in Fig. 72. It should be noted, however, that the first peak results from a small inflection in the NO concentration curve. The inflection in the NO flux profiles cannot result from the formation of NO_2 because only small amounts of NO_2 were formed (Table G-7) and this was in the preflame and luminous zones.

The NO flux at the last measurement point represents 23 percent of the added NH_3 (Fig. 2) but appears to be increasing. This is in agreement with the prediction from the screening experiments that 32 percent of the NH_3 should form NO at $\phi = 1.5$

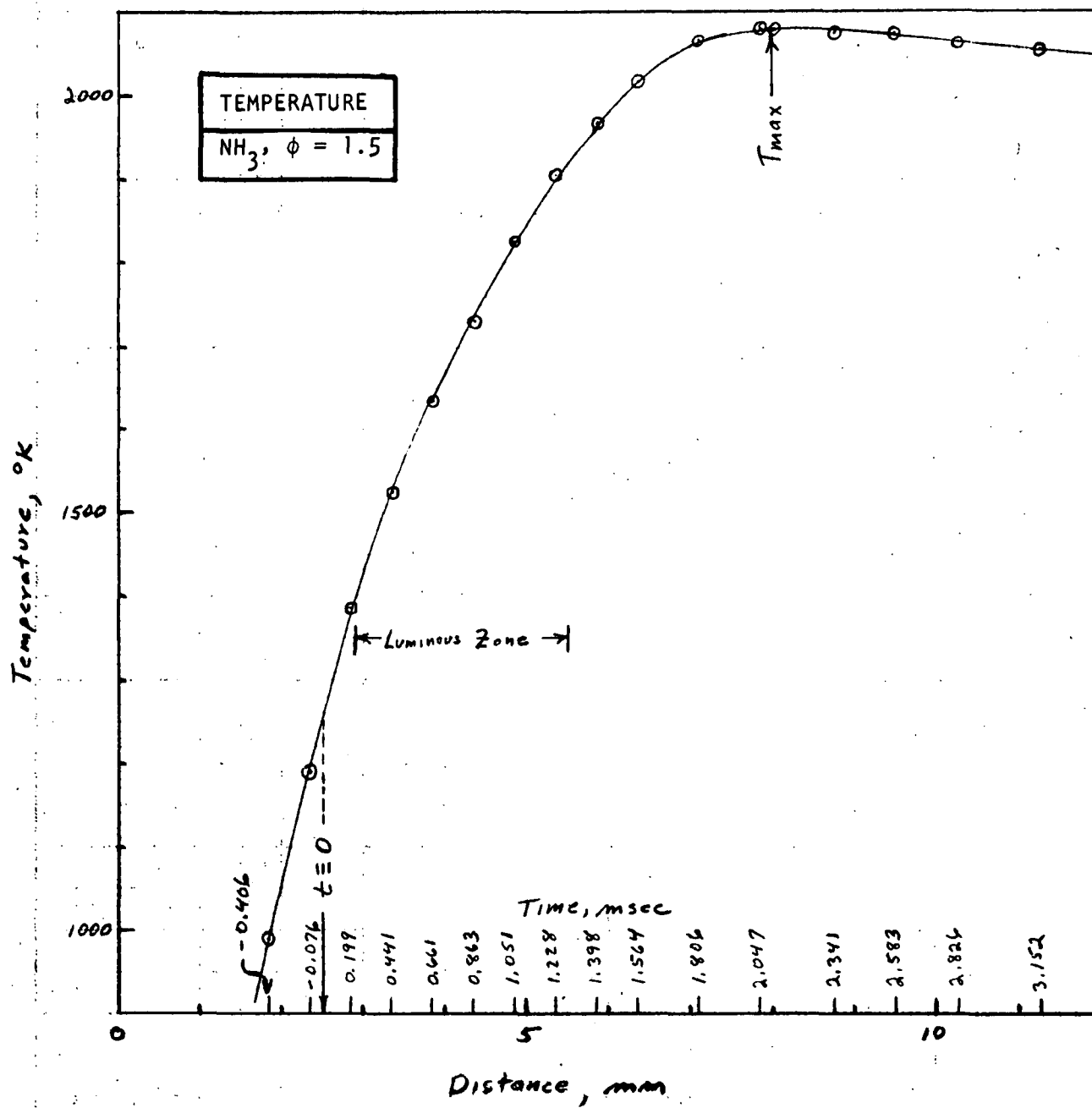


Figure 68. Flame Temperature vs Time, Flame 4,
NH₃ Addition With $\phi = 1.5$

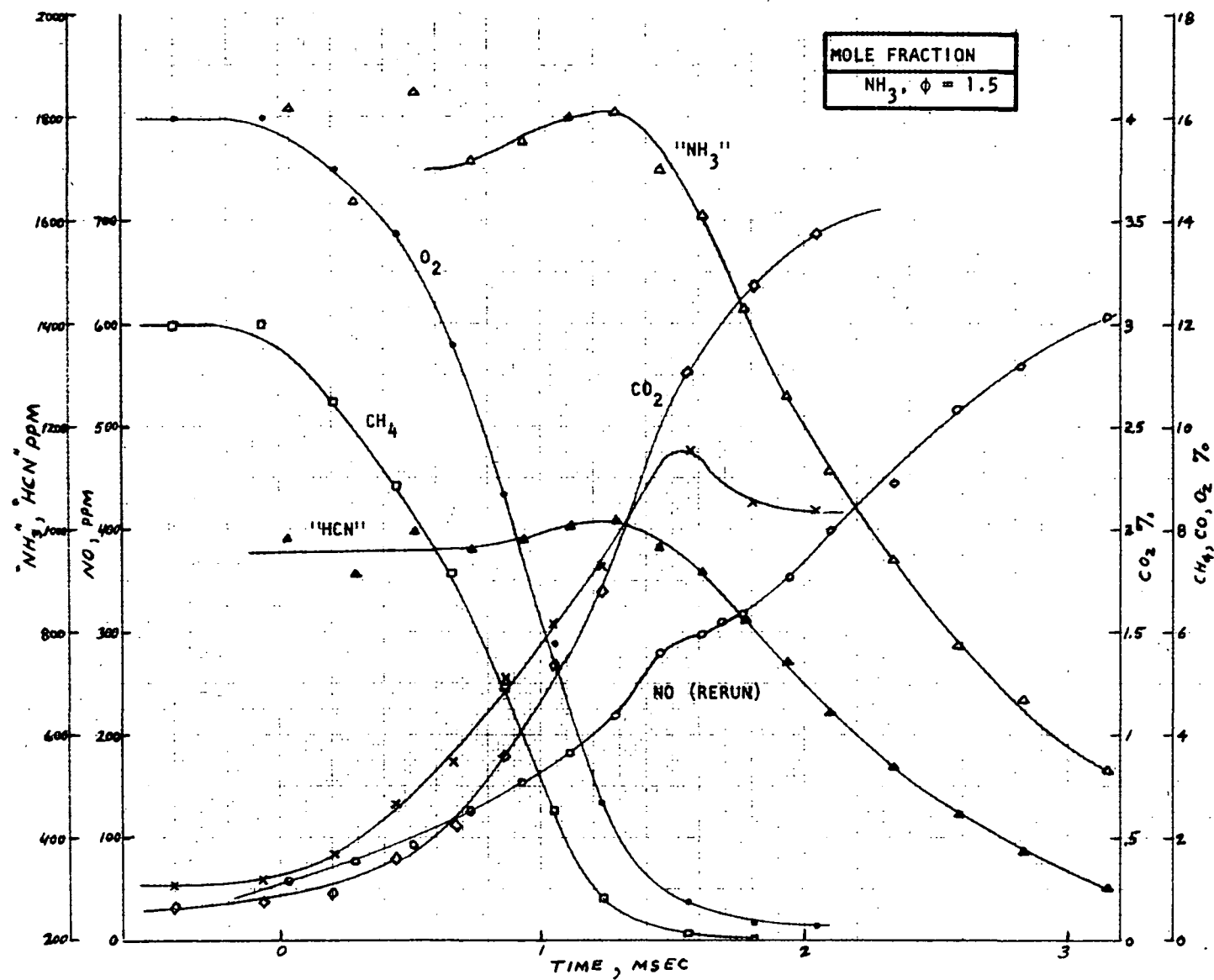


Figure 69. Species Mole Fraction vs Time, Flame 4, NH_3 Addition With $\phi = 1.5$

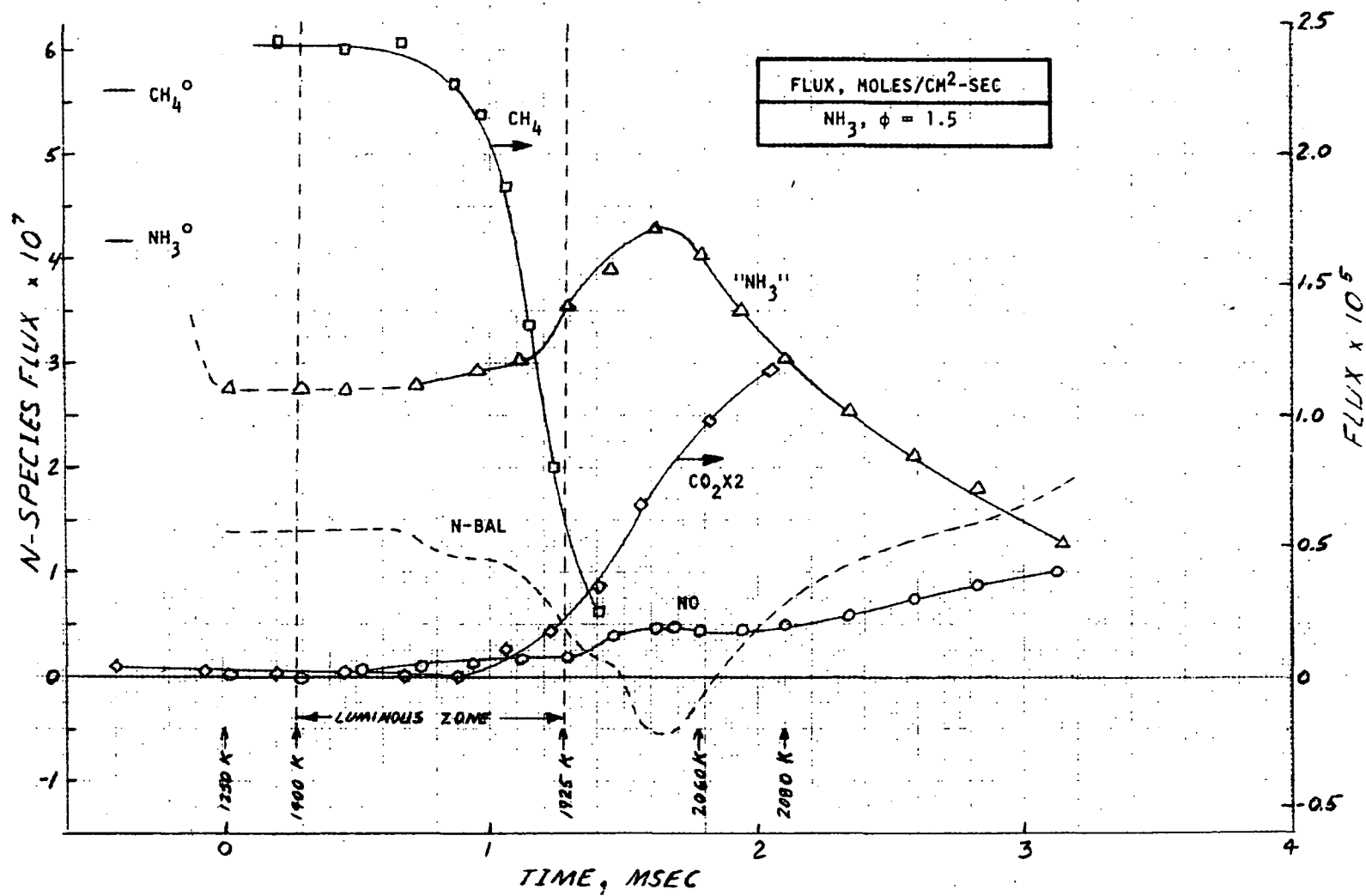


Figure 70. Species Flux vs Time, Flame 4, NH_3 Addition With $\phi = 1.5$
(Assuming Additive Remains as NH_3)

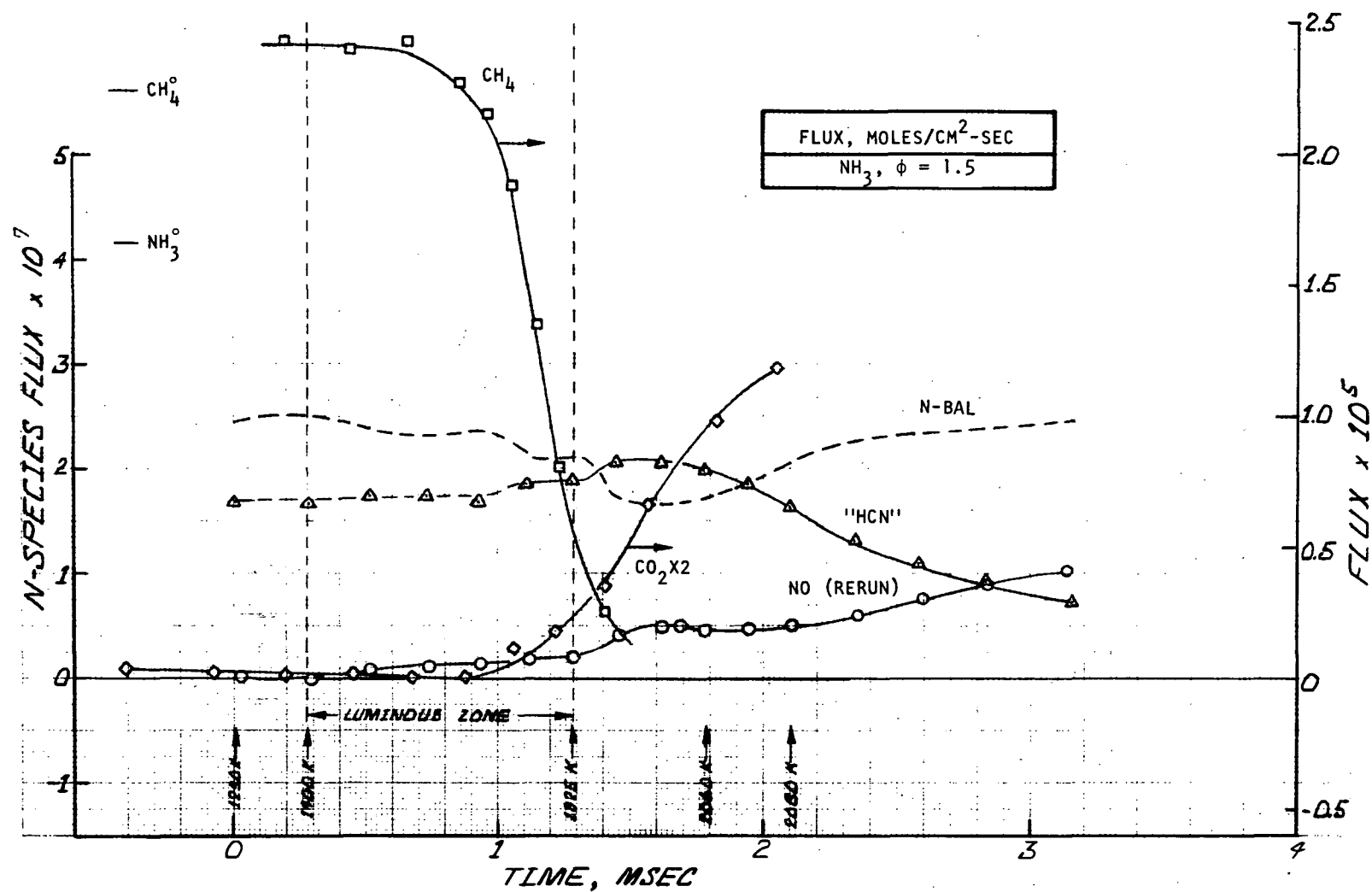


Figure 71. Species Flux vs Time, Flame 4, NH_3 Addition With $\phi = 1.5$
(Assuming Additive Forms HCN)

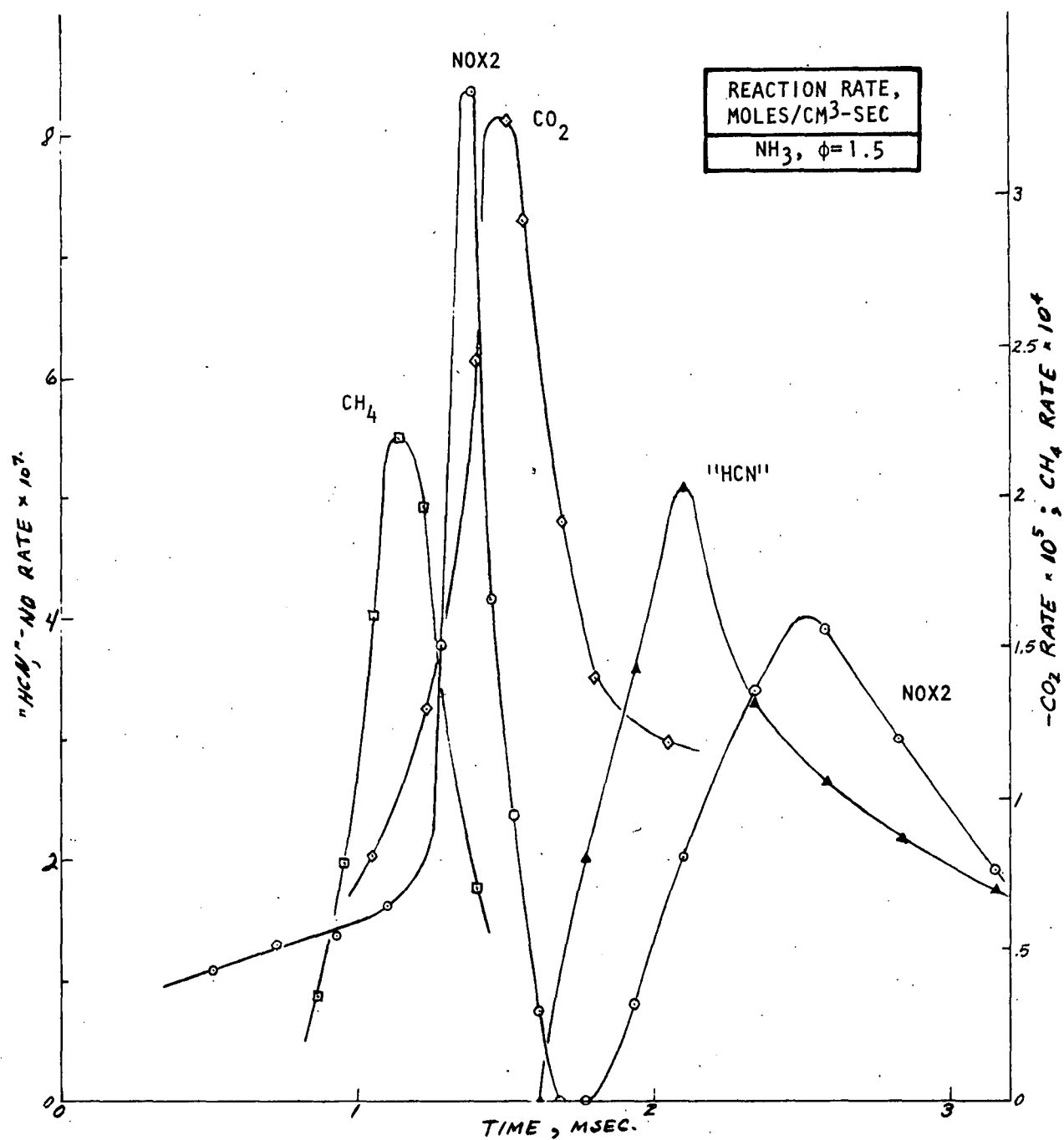


Figure 72. Species Reaction Rate vs Time, Flame 4,
NH₃ Addition With $\phi = 1.5$
(Assuming Additive Forms HCN)

and this feed rate (Run I-1, Table 21). Whether or not the NO actually forms in two discrete stages, it is apparent that in this fuel-rich flame most of the NO forms late in the combustion process, as was the case with added HCN in Flame 3. Assuming that the final extent of conversion of the additive nitrogen to NO reached 30 percent (above the last measurement point), only 15 percent of the total NO was formed in the luminous zone and only one-third was formed by the end of the first reaction stage (1.7 msec).^{*} Thus, about two-thirds of the NO was formed in the post-flame gases in the approximate temperature range 2055 to 2075 K (actually, the 25 percent of the NO estimated to form beyond 3.1 msec formed at somewhat lower temperatures because the temperature begins to decrease at this distance from the burner). The maximum rate for this second stage of NO formation occurred 1.2 msec above the top of the luminous zone and 1.0 msec above the point where CO₂ formation reached its maximum rate. Only about one-half of the final NO had formed even at this late point in the flame.

Consider next the "NH₃" concentration curve in Fig. 69. NH₃ was added at 2500 ppm and the measured "NH₃" concentration was about constant at 1800 ppm until the top of the luminous zone beyond which it decayed rapidly. It can be seen from Fig. 70, however, that if all of the nitrogen measured by the converter were NH₃, the sum of the fluxes for NH₃ and NO at 1.6 msec would be 4.7×10^{-7} which is in excess of the initial NH₃ flux of 4.1×10^{-7} (giving a negative value to the N-BAL curve). Also, the calculated "NH₃" flux increases in the luminous zone reaching a maximum at 1.6 msec. It is apparent, therefore, that all of the nitrogen species that is oxidized to NO in the converter is not NH₃.

DeSoete (Ref. 63) reported the formation of significant amounts of HCN "early in the flame" when NH₃ or amines were added to sufficiently fuel-rich ethylene flames. The converter-formed NO measured from Flame 4 was recalculated using the converter calibration factor for HCN and plotted as "HCN" in Fig. 69, 71 (using the diffusion coefficient for HCN) and Fig. 72. The calculated "HCN" mole fractions and fluxes are smaller than those for "NH₃" because, with air addition to the sampled gas, the extent of conversion of HCN to NO in the molybdenum catalyst is greater than with NH₃.

^{*}The area under the second NO peak in Fig. 72 will be twice that of the first peak when a 30 percent yield is attained.

Considering first the situation below the luminous zone at the point where the temperature is 1250 K (defined as zero on the time scale), it can be seen that the "NH₃" and "HCN" fluxes are not sufficient to account for the NH₃ that was added to the flame. Therefore, significant amounts of the added NH₃ must have been converted to other forms of nitrogen very early in the flame before the temperature exceeded 1250 K. If the NO formed in the converter at this point in the flame is from unreacted NH₃, about one-third of the NH₃ has been converted to other species (N-BAL curve in Fig. 70). Assuming that all of the NO formed in the converter were from HCN only at this early point in the flame, i.e., that no NH₃ remained unreacted, gives an "HCN" flux (Fig. 71) that represents 40 percent of the added NH₃.

As discussed previously, all of the nitrogen species measured with the converter cannot be NH₃ at 1.6 msec where the calculated "NH₃" and "HCN" flux curves reach their maxima. The sum of the calculated NH₃ flux (4.3×10^{-7}) and the NO flux (0.4×10^{-7}) exceeds the initial NH₃ flux of 4.15×10^{-7} . Also, the NH₃ flux cannot increase from its value at zero on the assigned time scale ($\cong 2.7 \times 10^{-7}$) unless it reforms from other nitrogen species and this does not seem likely. If the measured nitrogen species were entirely HCN at this point in the flame (1.6 msec) its flux would be 2.06×10^{-7} and one-half of the nitrogen would be present as N₂ or other nitrogen species (N-BAL).

It can be seen from the "NH₃", "HCN" and N-BAL flux curves in Fig. 70 and 71 that at least one-third of the NH₃ reacts in the preflame zone to form nitrogen species that are not oxidized to NO in the probe-converter system (i.e., "N-BAL" species). The conversion of any or all of the remaining NH₃ to HCN (and some N-BAL) in the preflame zone would also be compatible with the results obtained. At 1.6 msec, above the top of the luminous zone, about one-half of the added nitrogen is present as HCN or some other nitrogen species that gives a much higher response in the converter-CA analysis technique than does NH₃. The conversion of NH₃ to HCN in the luminous zone appears to be a reasonable process but the reaction of significant amounts of NH₃ in the preflame region was unexpected. One possibility would

be that one-third of the NH_3 decomposes to N_2 and H_2 on passing through the heated screen at the top of the burner. This does not appear likely, however, since NH_3 undergoes nearly complete conversion to NO at $\phi = 0.8$ after passing through the same flame holder and HCN and NH_3 undergo similar extents of conversion to NO at $\phi = 1.5$. It was established (Flames 2 and 3) that HCN definitely survives passing through the screen at $\phi = 1.5$ and 0.8. The nature and fate of the "N-BAL" species, that are calculated to form on the basis of nitrogen flux balances, cannot be determined from the measurements that were made. One-third of the NH_3 -N could have formed N_2 in the preflame zone or could have produced a species that does not form NO in the probe-converter system but forms NO and N_2 later in the flame.

The similarities at $\phi = 1.5$ of the "HCN" flux curves above the luminous zone for added NH_3 (Fig. 71) and for added HCN (Fig. 66) strongly indicate that most of the added NH_3 is converted to HCN in or below the luminous zone. Once formed, much of the "HCN" survives the luminous zone as it did when HCN was added initially. As discussed in the case of Flame 3, it is not possible to determine from the data if most of the NO forms directly from "HCN" in fuel-rich flames or via a long-lived intermediate because the rate of NO formation does not exceed the rate of "HCN" decay except in a region just above the luminous zone.

It appears from Fig. 71 that some of the HCN will still be present in the exhaust gas. How much will depend on the downstream decomposition rate of the HCN and the rate of temperature quenching. Fenimore (Ref. 66) demonstrated that under fuel-rich conditions, at sufficiently high additive concentration, some NH_3 -N survives the flame in a form that can be converted to NO in another (fuel-lean) flame. The results obtained from Flames 3 and 4 of this study indicate that the surviving fuel-N must have been in the form of HCN rather than NH_3 .

Flame 5--HCN Addition With $\phi = 0.8$ and Added Argon. In all of the other probing experiments, the diluent ratio was 1 ($\text{Ar}/\text{O}_2 = 3.76$ molar ratio). For Flame 5, however, the DR was increased to 1.4 ($\text{Ar}/\text{O}_2 = 5.26$ molar ratio). The purpose of the additional argon was to lower the flame zone reaction temperature. Screening experiments had indicated that added argon affected the NO_x yield from NH_3 and HCN

via its effect on the flame temperature but was not very effective in reducing temperature. In an attempt to obtain even lower temperatures, the burner feed rate was reduced to 5851 cc/min, a rate lower than used in any of the screening experiments.

The pertinent data obtained from the detailed probing of Flame 5 are plotted in Fig. 73 through 76. A comparison of the flame temperature profiles given in Table 27 indicates that the flame temperature was lowered about 140 K by argon dilution, and the reaction zone shifted slightly further from the burner in spite of the fact that the burner feed rate was lowered from 7520 cc/min for Flame 2 to 5851 cc/min for Flame 5. The temperature decrease should have been about 200 K (based on adiabatic calculations), but the movement of the flame front away from the water-cooled burner apparently lowered the heat loss to the burner.

The final NO flux was 84 percent of the metered HCN flux and had nearly leveled off. This is about the same as the values obtained in the screening experiments at $\phi = 0.8$ but they were not conducted at this feed rate and additive concentration. About 4 percent of the HCN remained unreacted at this point. The position of the luminous zone was not measured but, based on the CH_4 flux, the top must have been at about 0.9 msec. Comparison of Fig. 75 and 62 demonstrates the similarities in the flux profiles obtained at DR of 1.0 and 1.4. The NO and CO_2 form in the same region, the HCN flux decays rapidly just above the luminous zone, and a peak appears in the N-BAL curve just above the luminous zone.

The reaction rate curves, Fig. 76 and 63, indicate that the reaction rates reach their maxima in the same sequence in Flames 5 and 2. Perhaps more data points would be required to establish the exact maximum for each rate curve. As a consequence of the lower temperature and somewhat diluted gas, the maximum reaction rates for NO, HCN, CH_4 , and CO_2 for Flame 5 are all smaller than the corresponding maximum rates in Flame 2. The reaction rate ratios are 0.70, 0.92, 0.58 and 0.71, respectively. This is in approximately agreement with the observation that the position of maximum temperature increased slightly even though the feed rate was

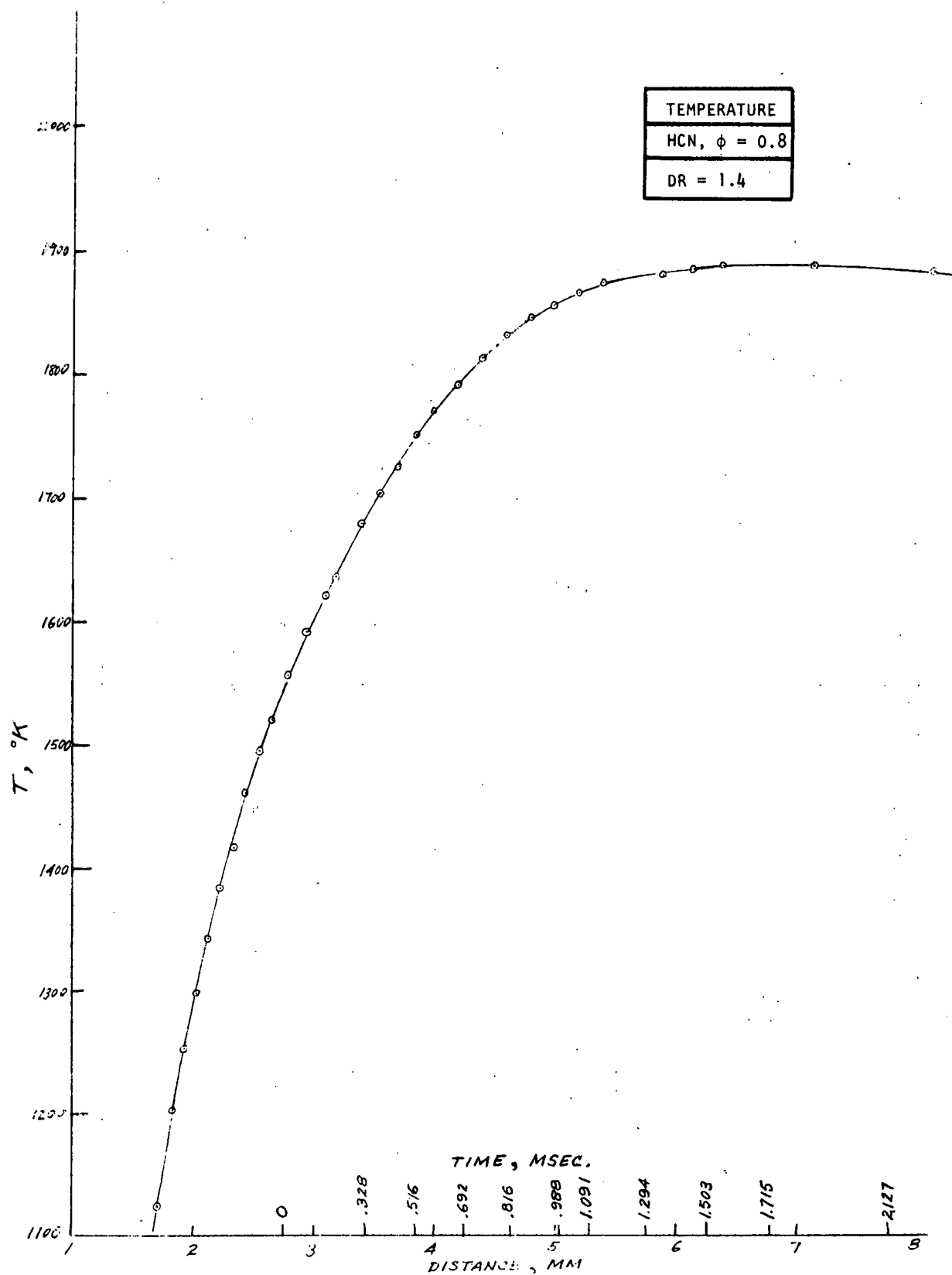


Figure 73. Flame Temperature vs Time, Flame 5,
HCN and Argon Addition With $\phi = 0.8$

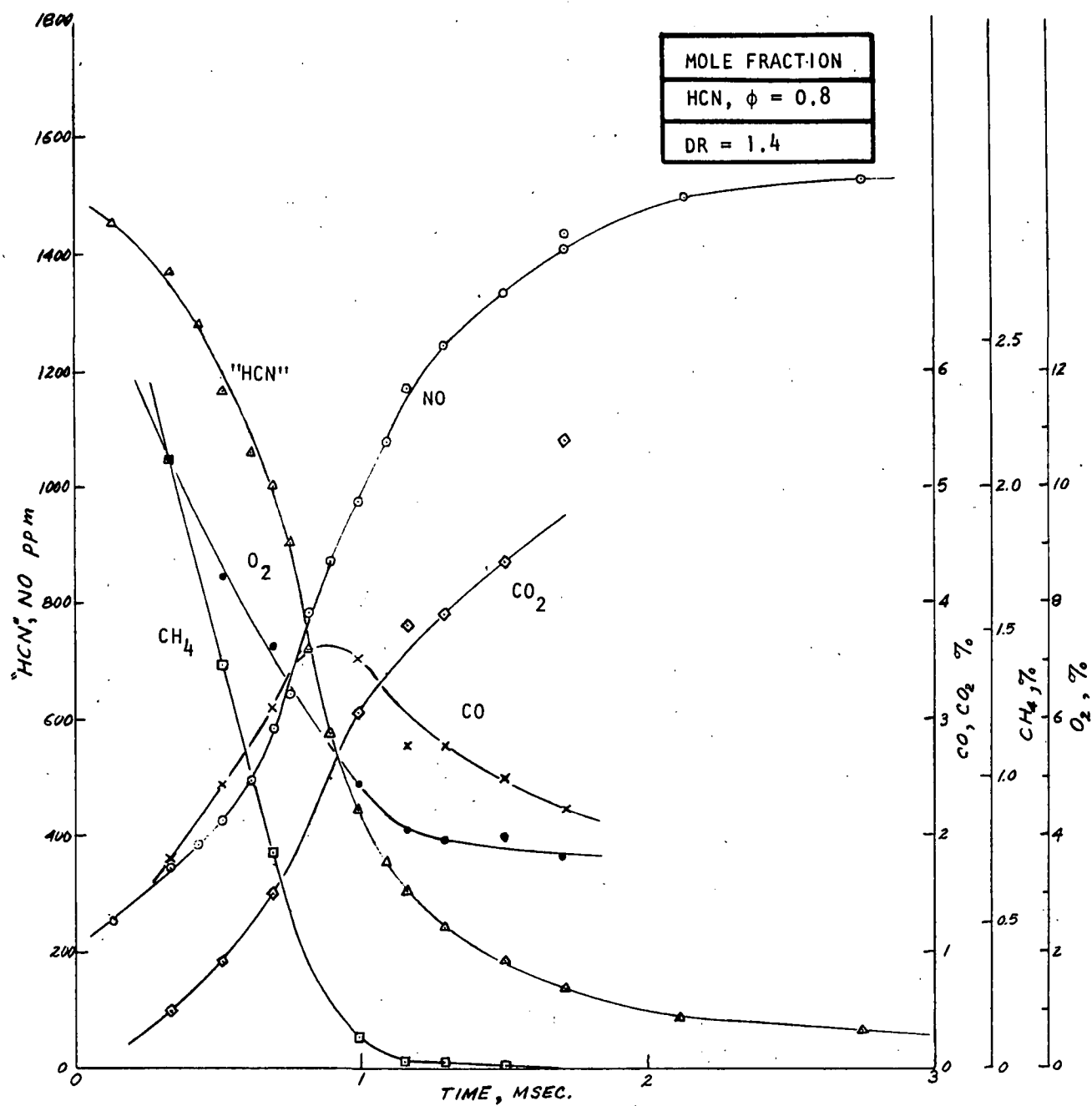


Figure 74. Species Mole Fraction vs Time, Flame 5, HCN and Argon Addition With $\phi = 0.8$

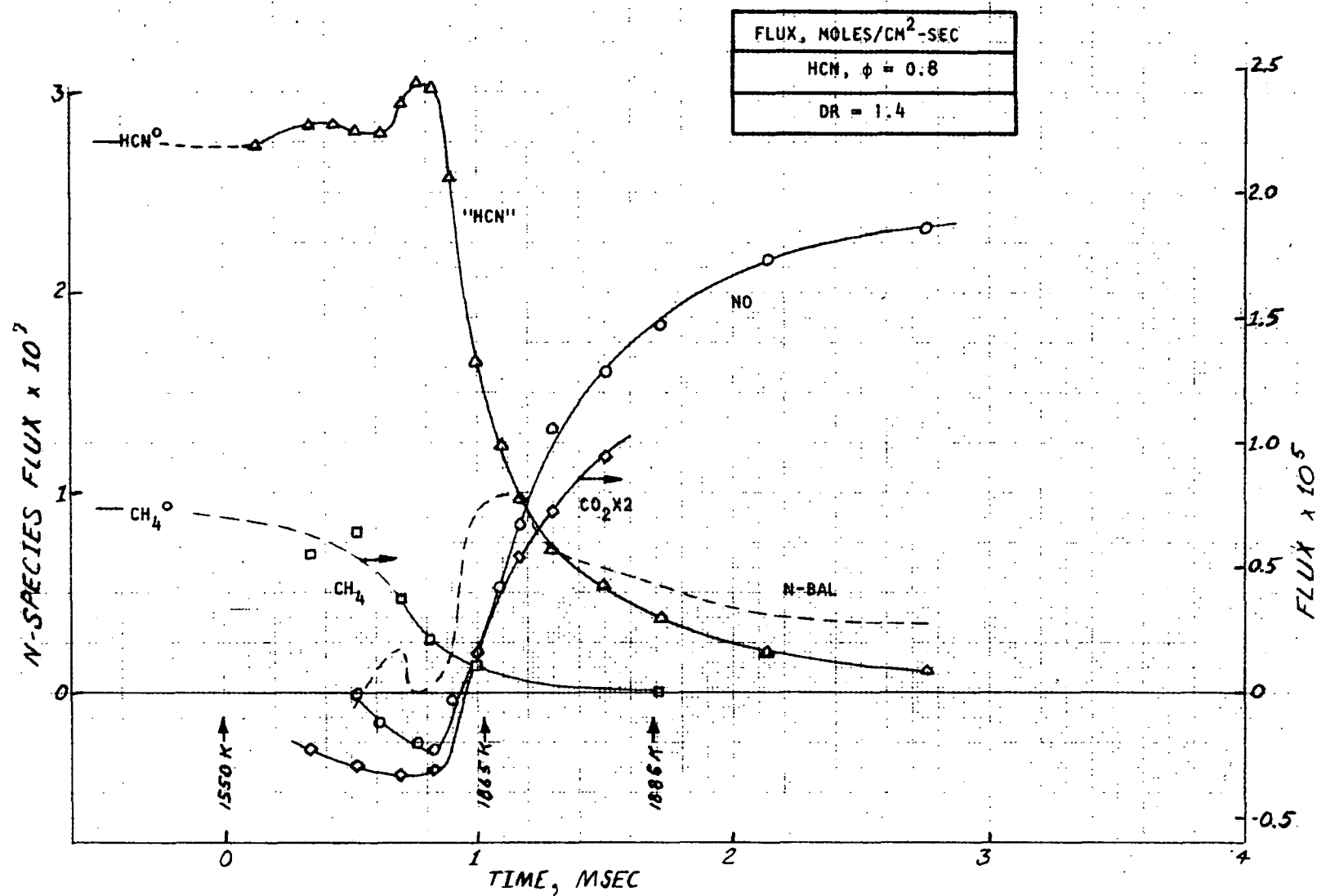


Figure 75. Species Flux vs Time, Flame 5, HCN and Argon Addition With $\phi = 0.8$

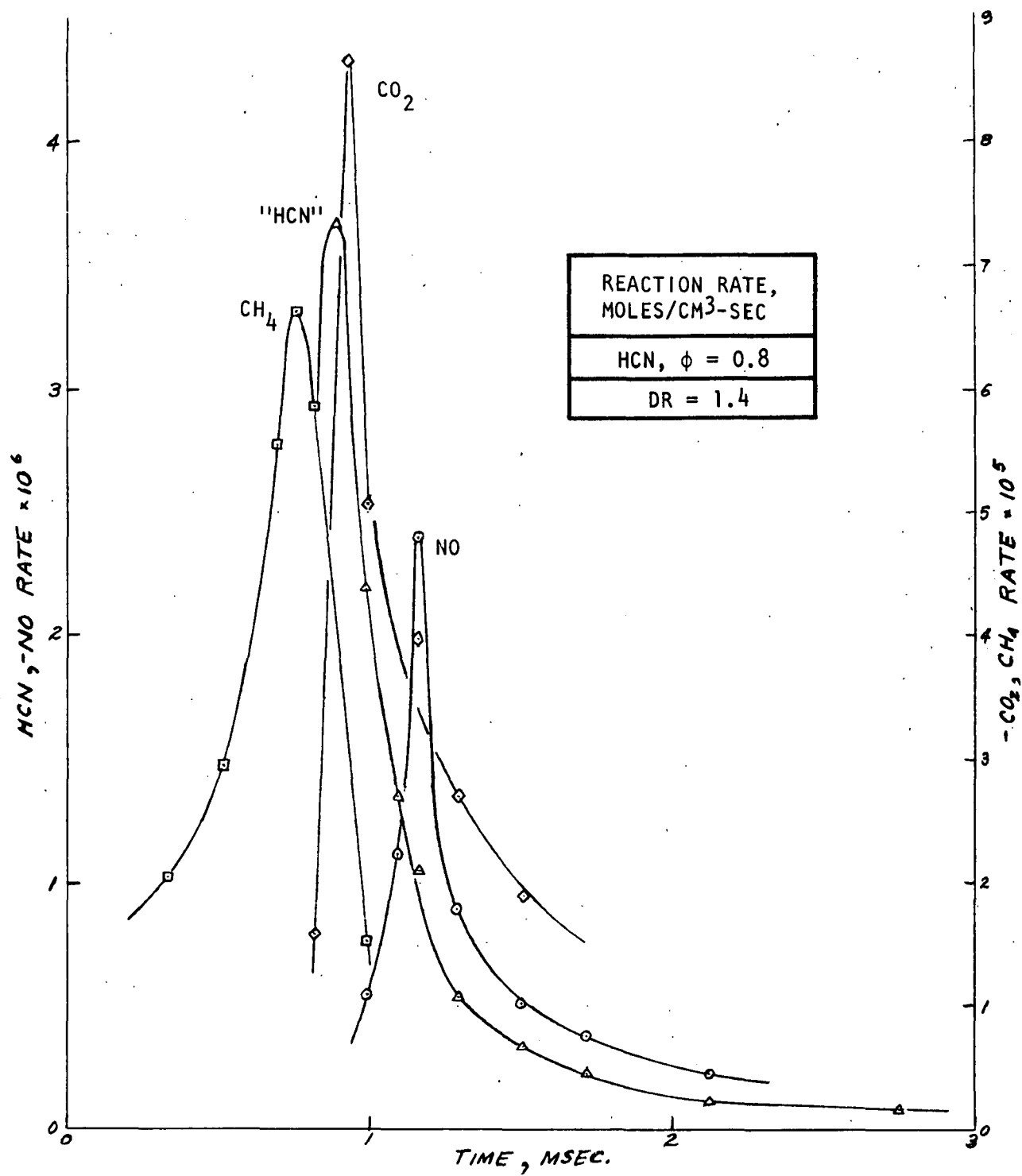


Figure 76. Species Reaction Rate vs Time, Flame 5,
HCN and Argon Addition With $\phi = 0.8$

decreased by 22 percent in Flame 5. The effect of argon dilution on reaction rates is analyzed in more detail later in the report. There are several factors involved some of which are compensating.

Because of a change in the HCN flowmeter calibration, the HCN mole fraction in the burner feed gas was 1793 ppm rather than 1936, the ppm that would have been required to keep the HCN/O₂ ratio equivalent to 2500 ppm in an undiluted burner feed stream (DR=1). The HCN flux correlation curve in Fig. 75 exceeds the metered HCN flux in the region just before the HCN flux begins to decline. It is possible that these high values of HCN flux are somehow related to the negative NO flux values occurring in the same region since an experimental determination of the HCN mole fraction depends on the measurement of two mole fractions, i.e., NO mole fraction with and without the molybdenum catalyst. It should be noted that the N-BAL curve is quite close to zero in this region, indicating that an error in the measurement of NO could cause the increase in the "HCN" flux curve. A plausible explanation, that does not involve experimental error, might be that in this region of the flames, small amounts of NO₂ are formed by the reaction of HO₂ or OH with NO. The presence of NO₂ would lead to higher apparent HCN readings on the CA because the conversion efficiency of the catalyst for NO₂ at 800 C is greater than for HCN. NO₂ measurements were not carried out for the HCN flames but the amounts of NO₂ formed in the NH₃ flames were much smaller than this explanation would require.

NO Addition With and Without HCN--Detailed Probing

Three flames were investigated using NO addition. The first two (flames 6 and 7) were conducted with HCN and NO added simultaneously at $\phi = 0.8$ and 1.5, respectively, while the last detailed probing experiment (flame 8) involved NO addition only at $\phi = 1.5$. These experiments were carried out to determine whether there was an interaction between HCN and NO that would not be readily apparent unless NO were present at a greater initial concentration.

Flame 6--HCN and NO Addition with $\phi = 0.8$. The data taken on flame 6 have been plotted in Fig. 77 through 80. The HCN flux profile obtained for this flame has some very unusual features that indicate that either (1) the added NO has a marked effect on the rate of HCN reaction in the region of the flame holder or (2) some unidentified experimental error is involved. When HCN alone was added at a concentration of 2500 ppm and $\phi = 0.8$ (flame 2), the measured "HCN" concentration just above the flame holder (Fig. 61) was about 1900 ppm dropping almost linearly to about 900 ppm at the top of the luminous zone. The flux curve derived from that ppm profile (Fig. 62) was nearly equal to the initial HCN flux (based on the added HCN feed rate) at the first sampling point and then decreased gradually to about 63 percent of the initial flux at the top of the luminous zone. In flame 6, 2500 ppm HCN and 625 ppm NO were contained in the feed gas to the burner. The "HCN" concentration at the first measurement point in this experiment was only 1235 ppm dropping to 300 ppm at the top of the luminous zone. The "HCN" flux curve obtained for this flame had an initial value of only 60 percent of added HCN flux at the first sampling point, and remained nearly constant until just below the top of the luminous zone.

The lower initial measured flux in flame 6 could result from an error in metering or measurement of the HCN. However, a calibration check of the molybdenum catalyst for the determination of HCN was made the day after the experiment and the HCN flowmeter had been calibrated the day before. In addition, incorrect metering of HCN would not account for the difference in the shapes of the "HCN" flux curves. Precluding experimental error, the initial low value for the "HCN" flux indicates that the added NO somehow catalyzes the reaction of HCN in the region of the

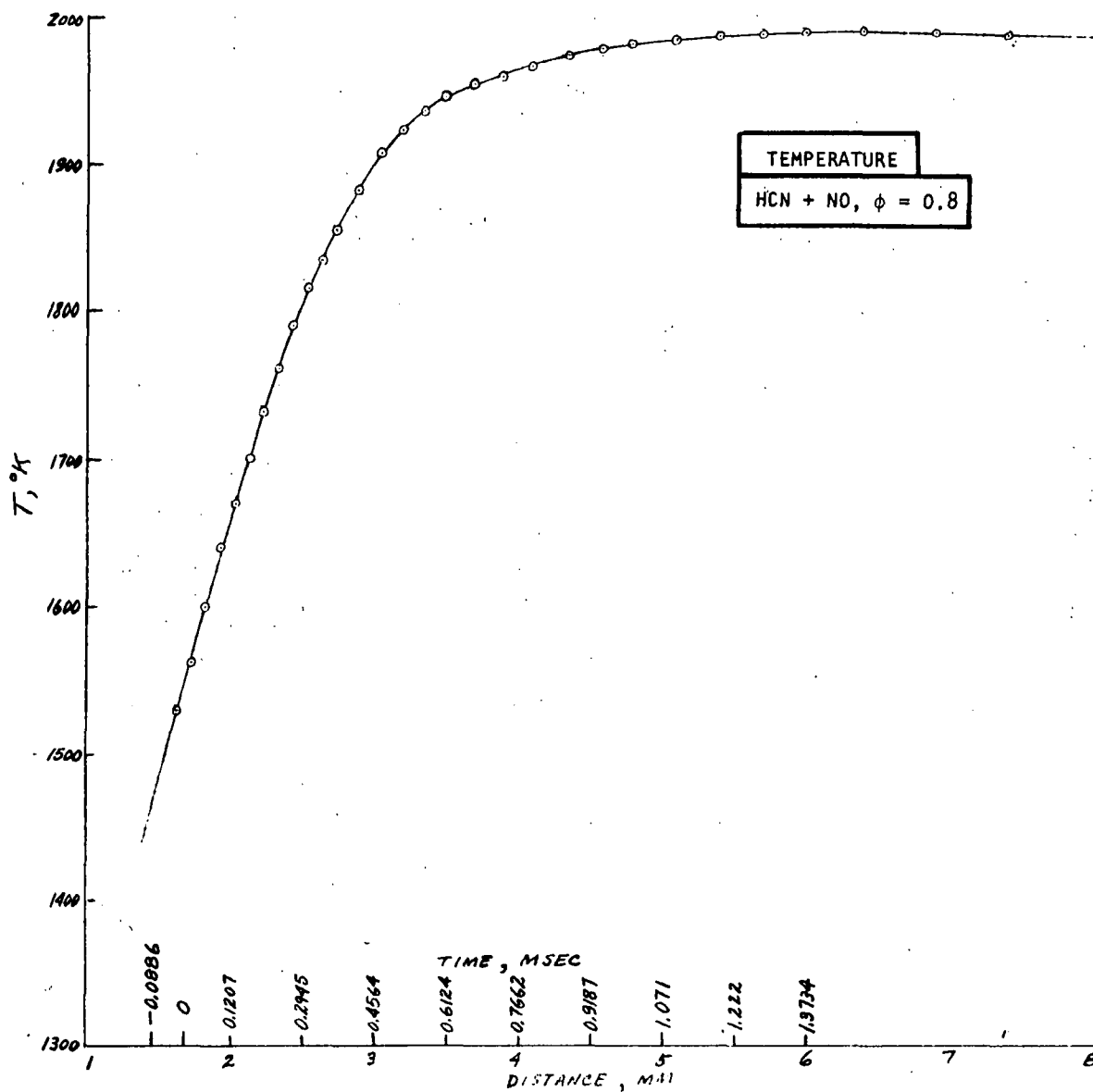


Figure 77. Flame Temperature vs Time, Flame 6,
HCN and NO Addition With $\phi = 0.8$

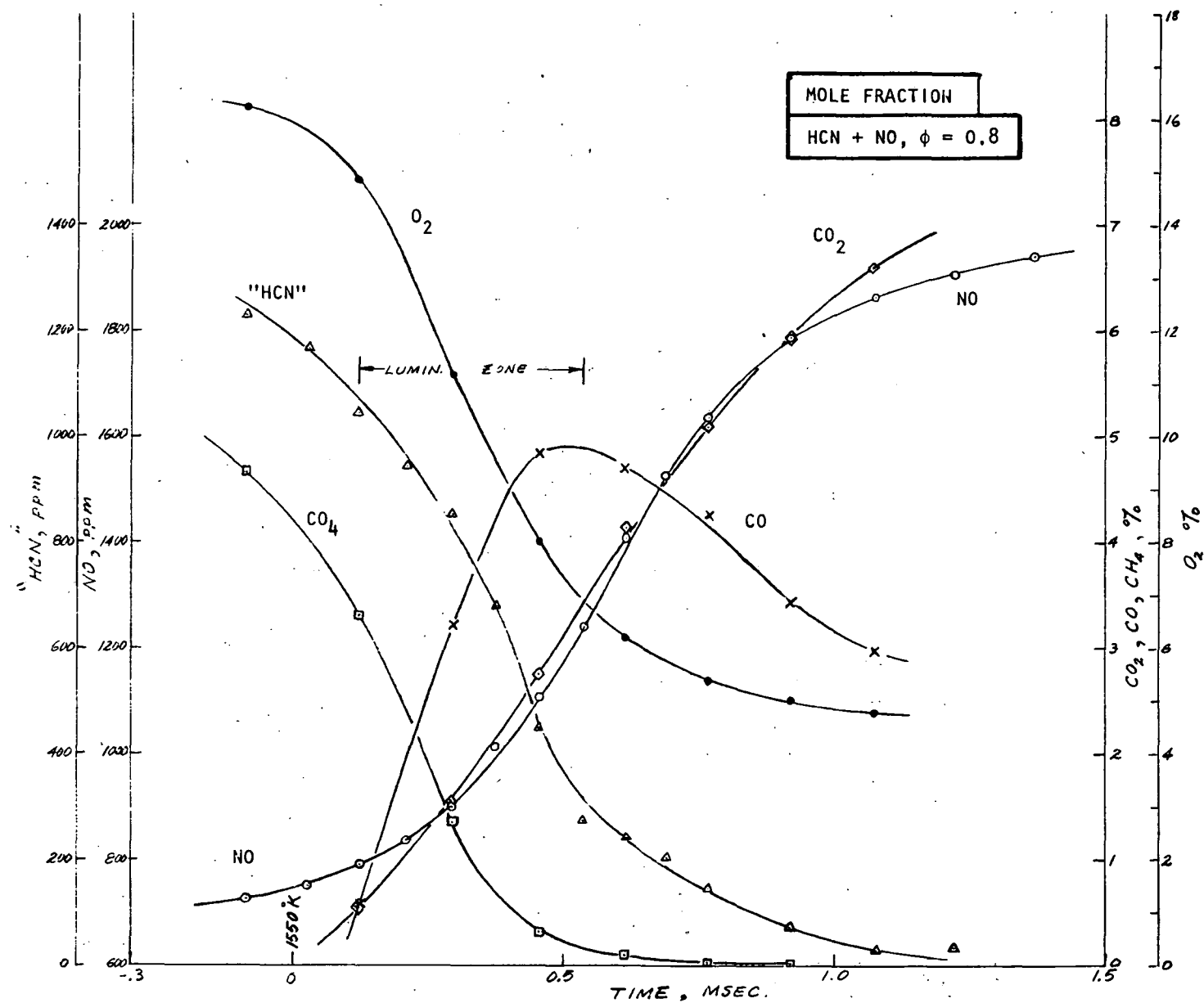


Figure 78. Species Mole Fraction vs Time, Flame 6, HCN and NO Addition With $\phi = 0.8$

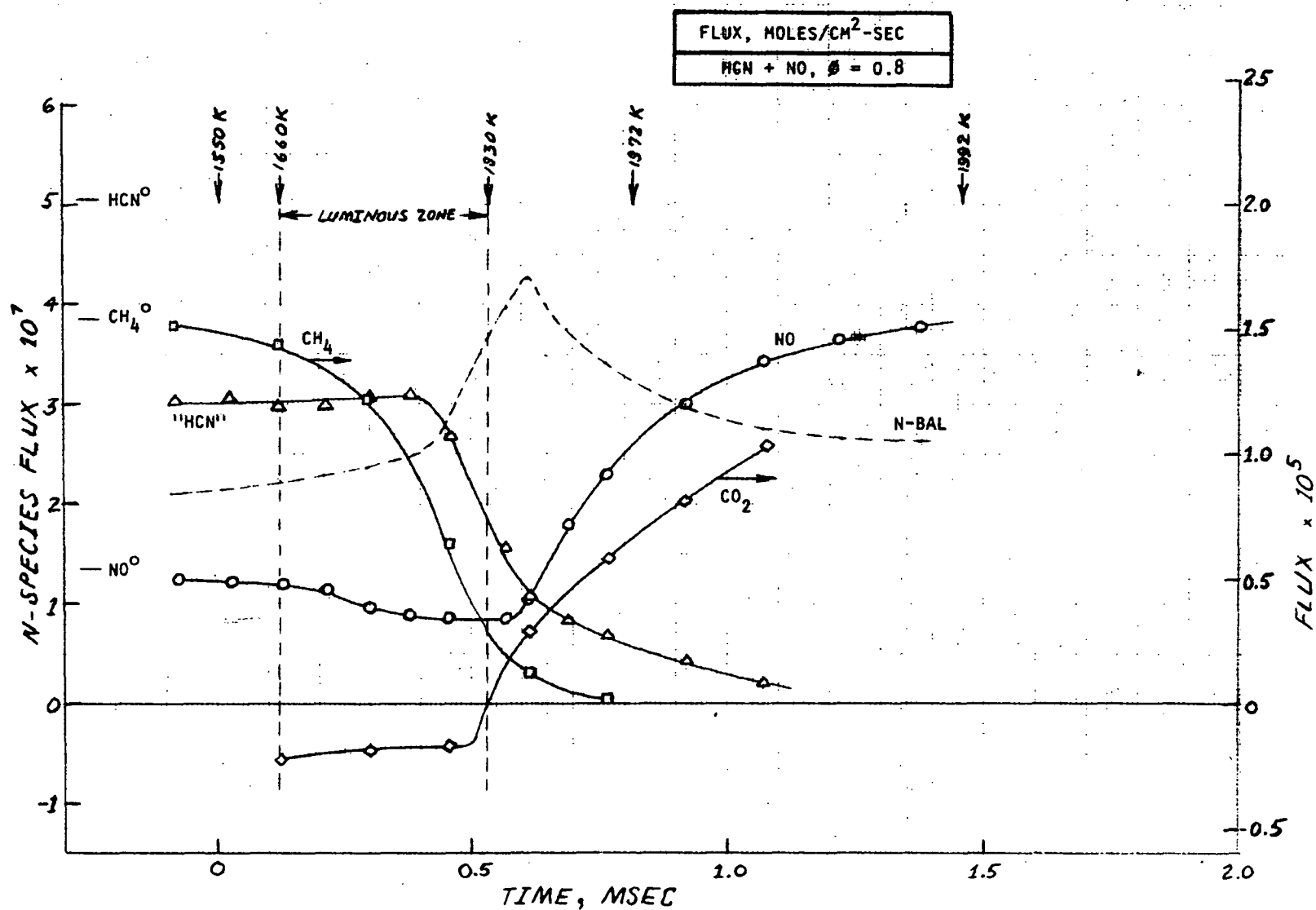


Figure 79. Species Flux vs Time, Flame 6,
HCN and NO Addition With $\phi = 0.8$

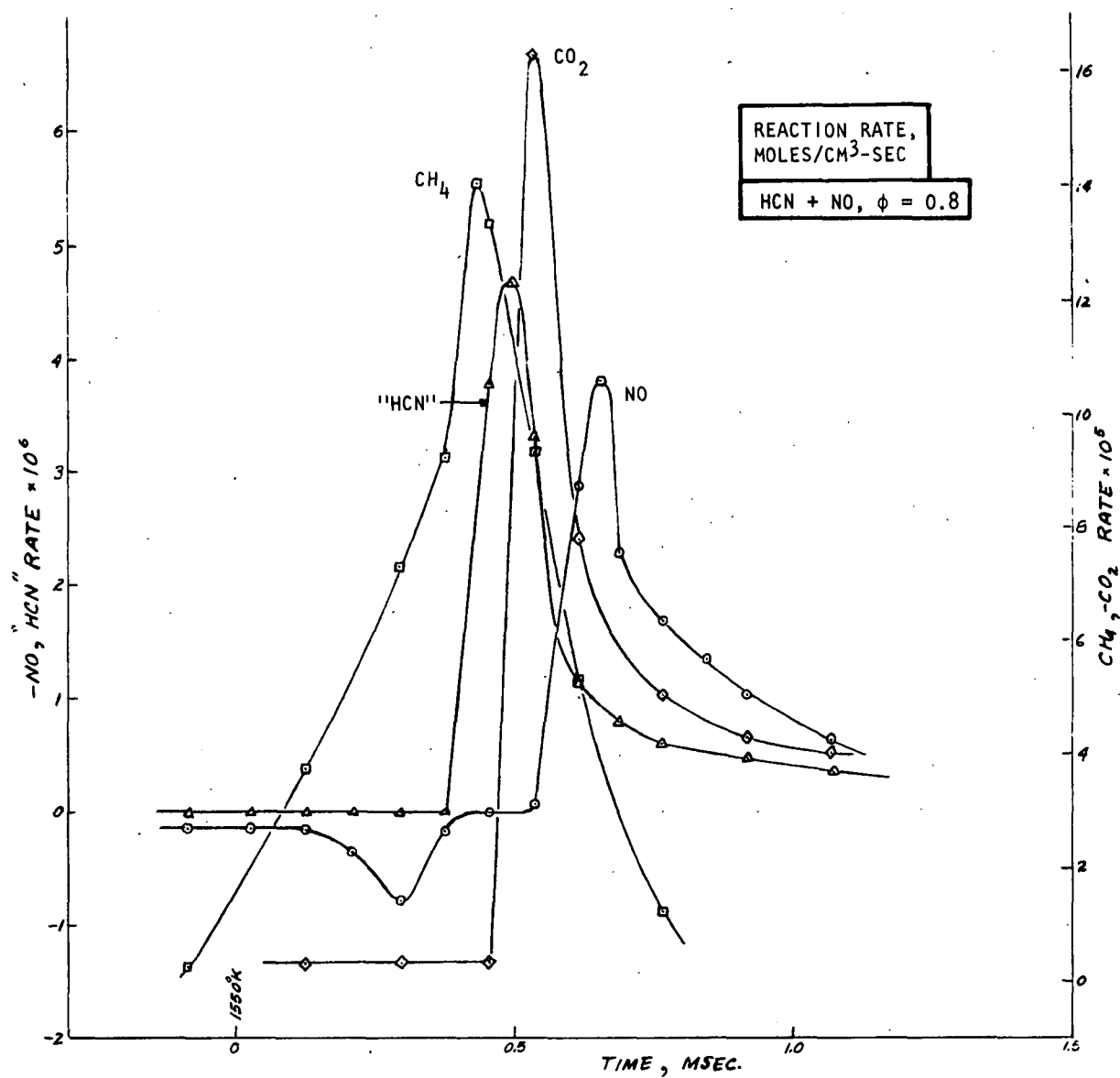


Figure 80. Species Reaction Rate vs Time, Flame 6,
HCN and NO Addition With $\phi = 0.8$

flameholder. If this turns out to be the case, the nitrogen species formed must be later converted to NO in high yield (above the luminous zone) because it will be shown that the NO yield curves for flames 2 and 6 are nearly identical and the HCN consumed initially represents 32 percent of the added nitrogen compounds.

The NO flux begins to decrease below the center of the luminous zone while the "HCN" flux does not start to decrease from its initially measured value until well above this point (Fig. 79). These flux profiles as well as the rate profiles (Fig. 80) suggest that the removal of the added NO by chemical reaction precedes the luminous-zone depletion reaction of HCN. When the depletion of "HCN" begins, the destruction of NO has ceased. Because NO₂ measurements were not made for this flame, the point at which HCN reaction began cannot be established for certain. The constant portion of the "HCN" flux curve could result from the depletion of HCN being compensated for by the conversion of NO to NO₂. Further data are required to resolve this point and to determine if added NO does catalyze the early reaction of HCN.

The point at which NO depletion reaches its maximum rate in flame 6 (about 0.3 msec, Fig. 80) is the same region of the luminous zone in which NO reached its maximum rate of consumption in Flame 1 (0.4 msec, Fig. 59). Therefore, at $\phi = 0.8$, any NO that forms below or in the luminous zone, or is added initially, can react near the center of the luminous zone. Because the added NO that is lost before the NO flux begins to increase represents only 7 percent of the added nitrogen species (HCN + NO), the consumed NO could form either N₂ or a reactive nitrogen intermediate and be compatible with the NO yields obtained.

Farther into the flame reaction zone, where the "HCN" flux rapidly declines, the N-BAL flux becomes quite large before NO formation begins. As in the other flames studied at $\phi = 0.8$, NO and CO₂ production occur in the same region of the flame. Based on the total metered additive flux of 6.3×10^{-7} , the NO flux in Fig. 79 gives the following percent yields:

t(msec)	0.69	0.76	0.92	1.07	1.22	1.37
%NO	28.2	35.7	47.1	53.8	57.0	59.0

Comparison of these yields with the flame 2 yields plotted in Fig. 2 demonstrates that the yields obtained at 1.37 msec (2.07 msec on the shifted time scale of Fig. 2) were identical in the two experiments although the NO formed earlier in Flame 6 and the yield appeared to be leveling off more rapidly. Assumption that the HCN was inadvertently added initially at a flux of only 3.0×10^{-5} gives a calculated yield at 1.37 msec that is 86.2 percent and still increasing rapidly. This is a much higher yield than was obtained in Flame 2 indicating the metered HCN flux in flame 6 was actually about 5×10^{-7} as planned.

Flame 7--HCN and NO Addition with $\phi = 1.5$. The data for flame 7 are given in Fig. 81 through 84. From the flux curves in Fig. 83, it can be seen that destruction of the added NO occurs near the top of the luminous zone but, under these fuel-rich conditions, NO consumption does not occur until after much of the HCN has reacted. Just above the luminous zone, after more than one-half of the added NO has been consumed, NO reforms reaching its metered flux and then is consumed again. This regeneration of the consumed NO occurs in the same region where the rate of CO_2 formation is at its maximum. Beyond the minimum at 1.8 msec, NO forms gradually much as in flame 3 in which only HCN was added (at $\phi = 1.5$). The NO yield at the last data point was 16.3 percent, based on the added HCN + NO, and was increasing. This is in agreement with the NO yield obtained in flame 3 at 2.7 msec (Fig. 2).

The "HCN" flux remains nearly constant over the region of the flame in which the added NO is consumed, reforms and then is consumed again. Therefore, the N-BAL flux curve is nearly a mirror image of the NO curve in this region. The NO is apparently converted first to a nitrogen species that forms NO in high-yield just above the luminous (much as did the intermediates formed from HCN and, particularly, NH_3 in the fuel-lean flames) and then is converted to nitrogen species that may form NO but in low yield. Much of the NO could be converted to N_2 in the second stage of NO consumption.

In flame 7, the "HCN" flux remains constant approximating the initial flux of added HCN, until near the center of the luminous zone where about one-third of the "HCN" is suddenly consumed just before the consumption of the added NO begins.

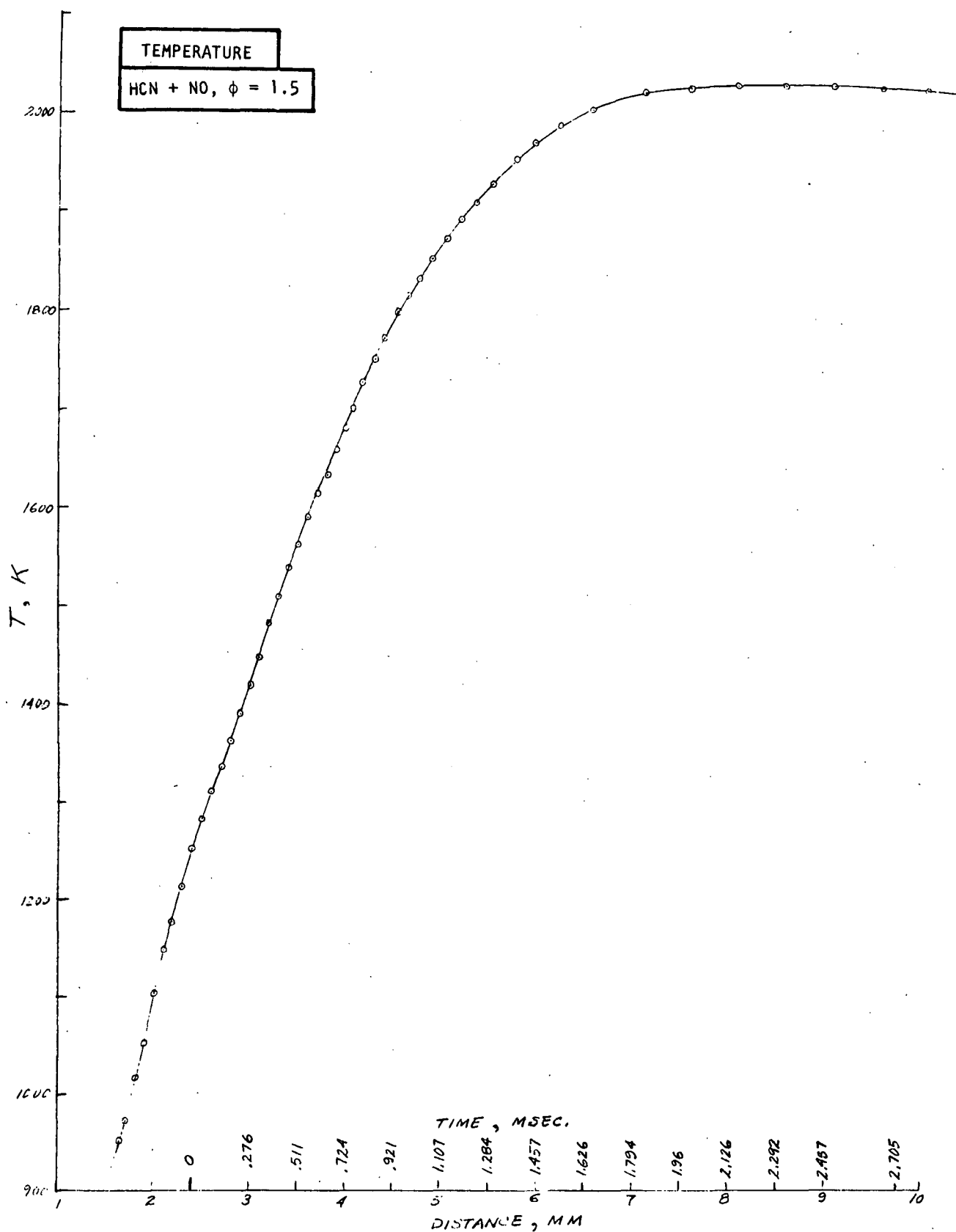


Figure 81. Flame Temperature vs Time, Flame 7,
HCN and NO Addition With $\phi = 1.5$

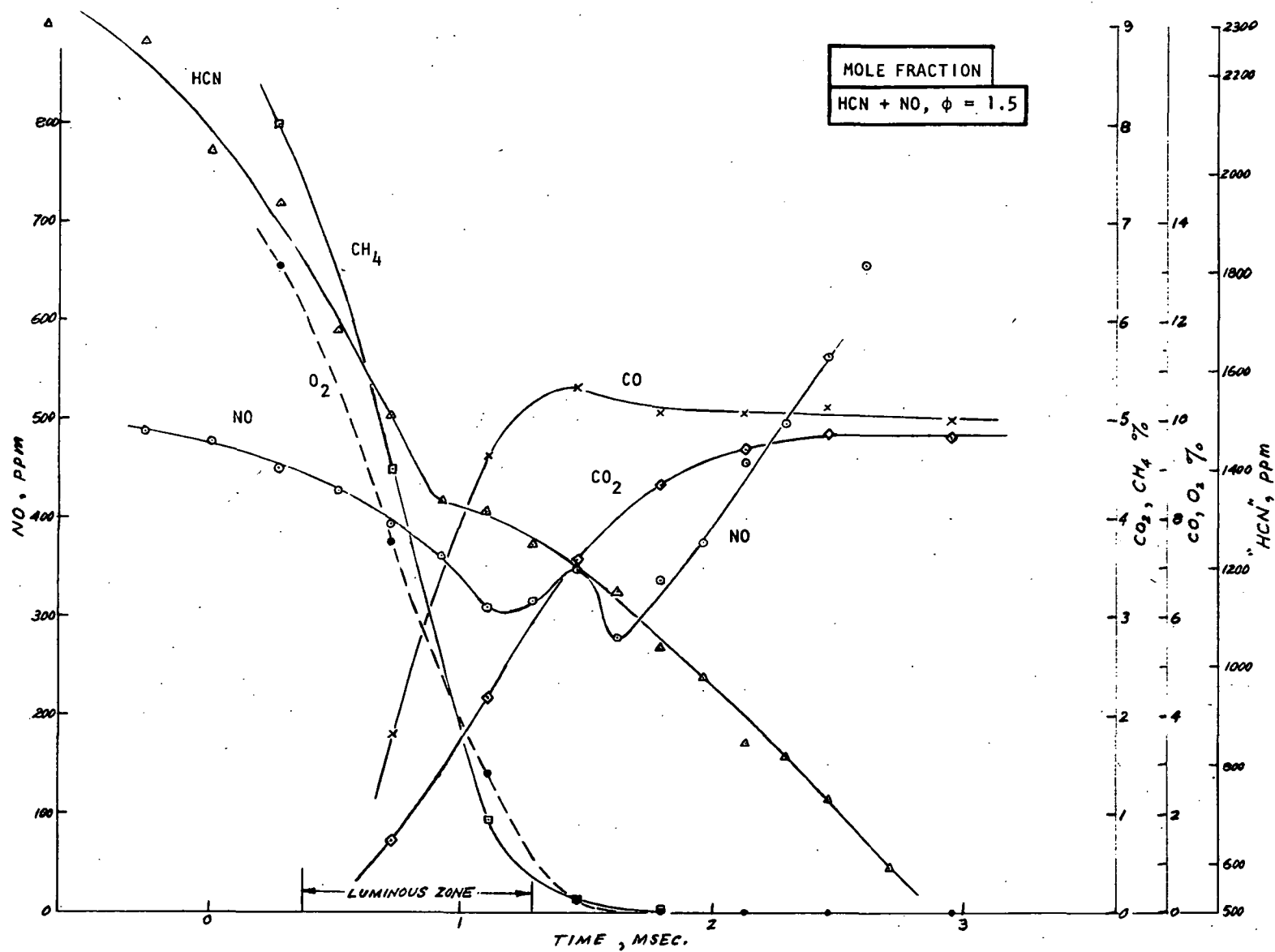


Figure 82. Species Mole Fraction vs Time, Flame 7, HCN and NO Addition With $\phi = 1.5$

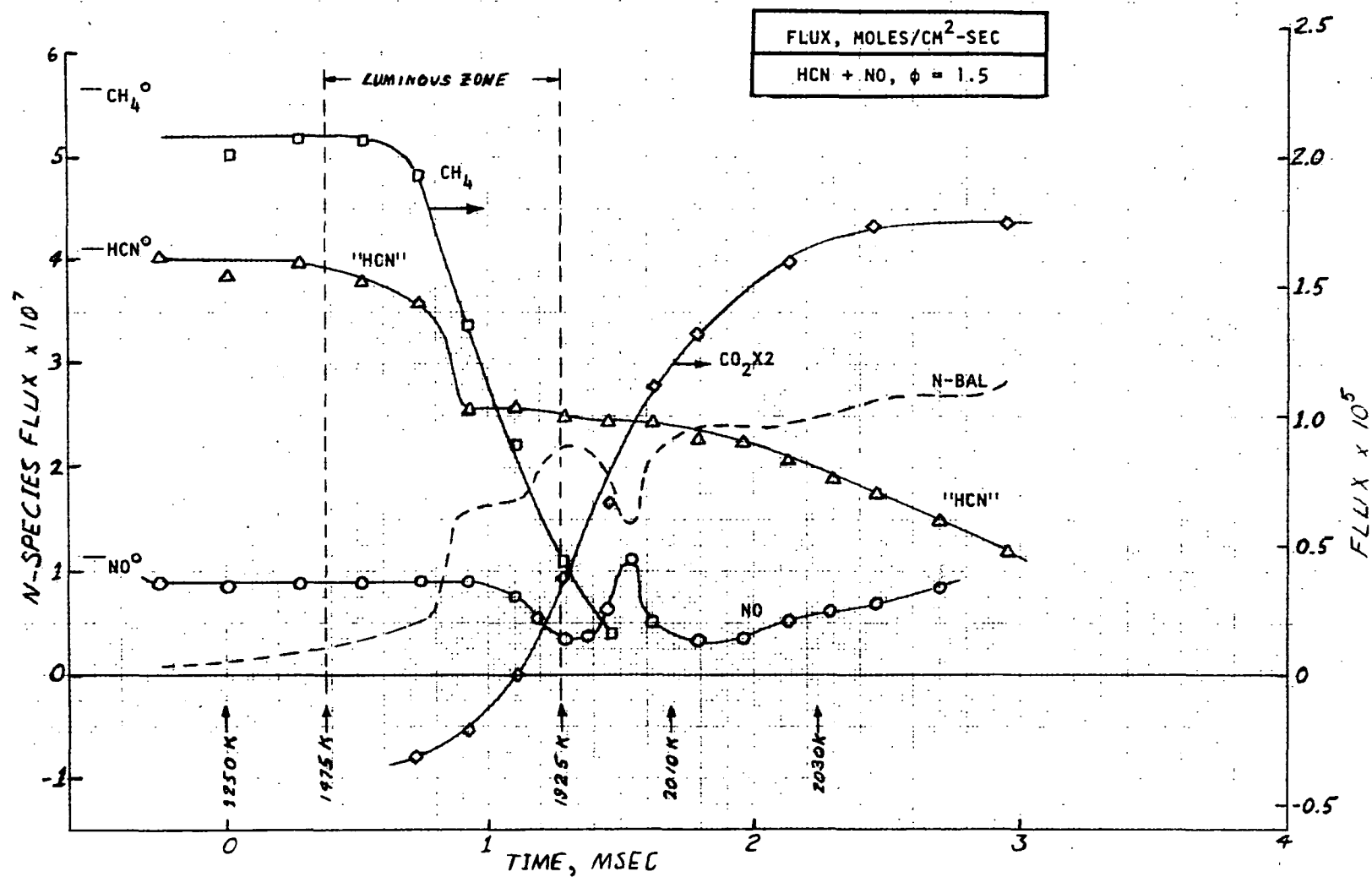


Figure 83. Species Flux vs Time, Flame 7, HCN and NO Addition With $\phi = 1.5$

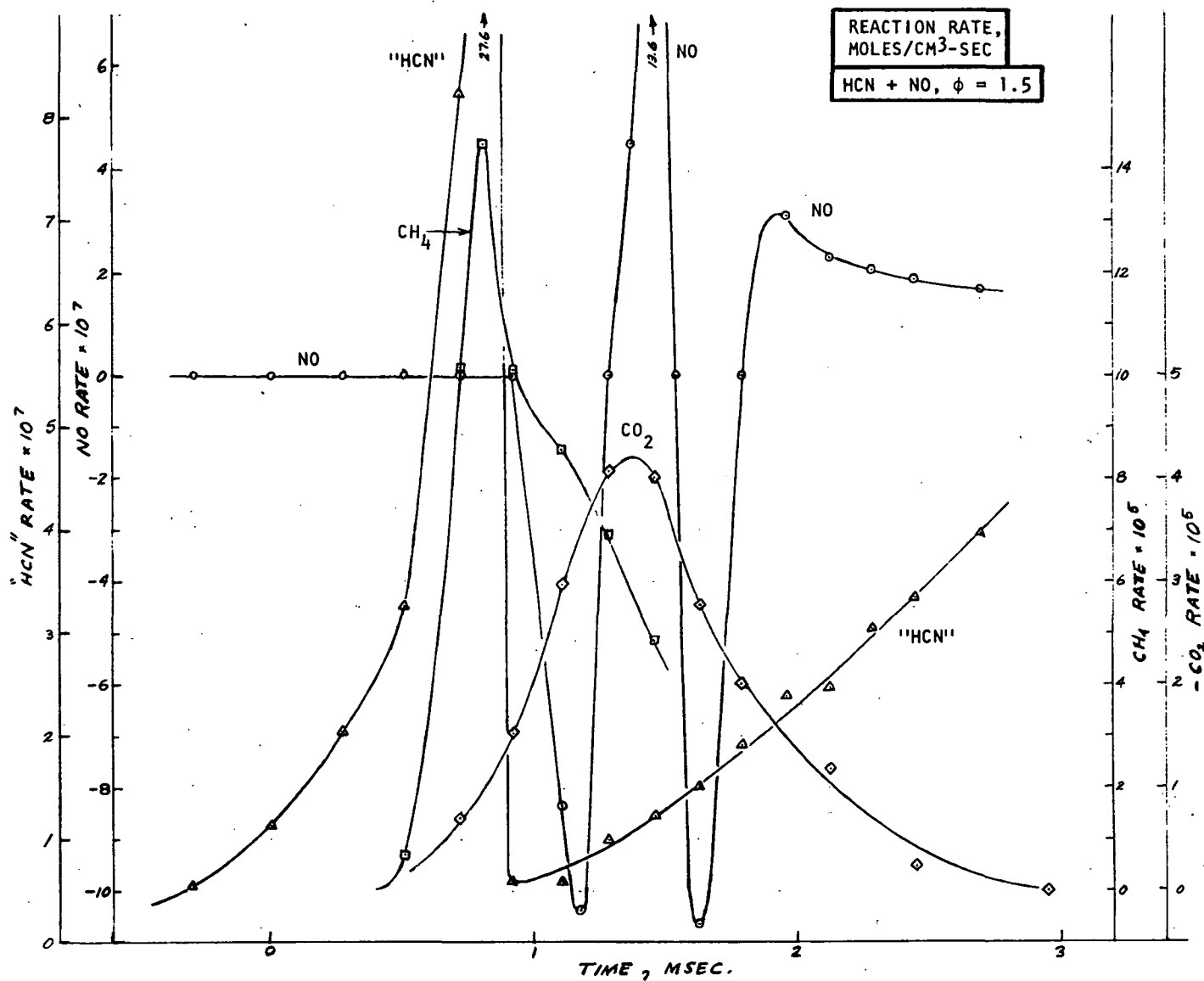


Figure 84. Species Reaction Rate vs Time, Flame 7, HCN and NO Addition With $\phi = 1.5$

The "HCN" flux then remains nearly constant until well above the luminous zone where it decays slowly at a rate that is more than twice the rate of NO formation. At the last measurement point, 28 percent of the "HCN" still remained unreacted. In flame 3, the "HCN" flux also dropped suddenly near the middle of the luminous zone and then remained constant before beginning its gradual decay. The duration of the constant "HCN" flux plateau at the top of the luminous zone was somewhat longer in flame 7. It will be seen that the results of flame 8, in which only NO was added at $\phi = 1.5$, demonstrate that part of the added NO is converted to "HCN" in the region of the "HCN" flux plateau. This could account for the longer plateau in flame 6 than in flame 3, i.e., HCN is being consumed and formed simultaneously.

Flame 8--NO Addition With $\phi = 1.5$. The data obtained from the detailed probing of flame 8 are presented in Fig. 85 through 88. The sole nitrogen additive for this fuel-rich flame was NO. The NO flux profile displayed in Fig. 87 is very similar to that determined for flame 7 except that in flame 7, the final stage of NO formation is 4 times faster and, of course, yields greater amounts of NO since the nitrogen additive concentration was much higher. The similarities include the time, or distance from the burner, at which (1) NO destruction begins, (2) NO reforms and (3) NO is again consumed. In this flame, however, the NO consumed near the top of the luminous zone is not completely reformed. The NO flux at the last measurement point was 0.47×10^{-7} and appeared to be increasing slightly. This represents 45 percent of the metered NO flux. This higher NO "yield" might indicate that under these conditions NO behaves differently than other nitrogen additives. However, the higher "yield" of NO from NO probably resulted from the lower additive concentration employed in this experiment.

As the NO disappeared, the formation of small amounts of nitrogen compound was detected by the use of the catalytic converter and the CA. The data on this measured nitrogen compound have been reduced using the assumption that it is HCN. A nitrogen flux balance revealed that 40 percent of the reacted NO was converted to "HCN" while the rest was converted to N-BAL (probably N_2). It is not likely that the "HCN" formed was NO_2 . The "HCN" mole fraction was over 100 ppm at the top of the luminous zone and less than 10 ppm NO_2 was formed in flame 4 even though the NO mole fractions were similar in this region of each flame. The

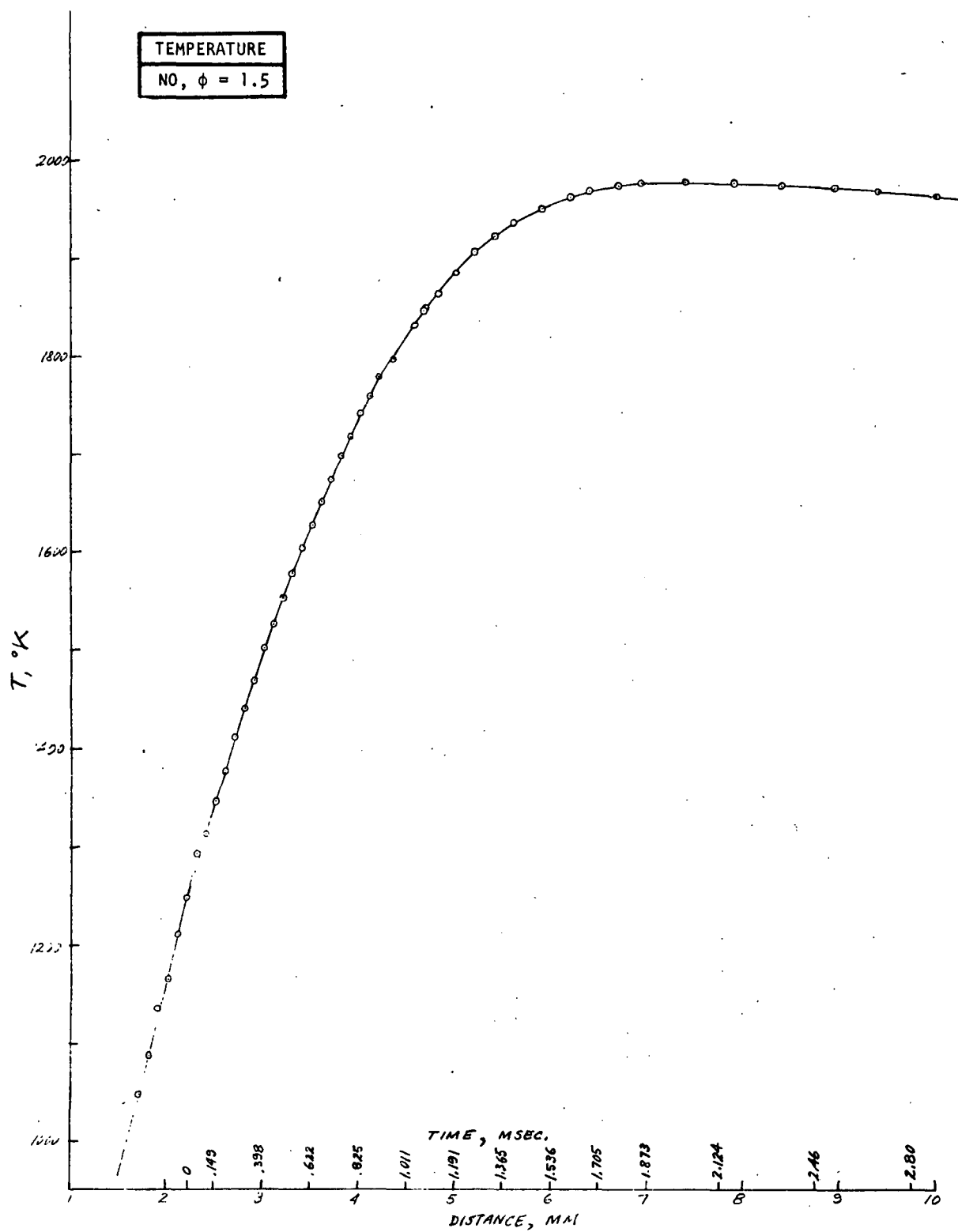


Figure 85. Flame Temperature vs Time, Flame 8
NO Addition With $\phi = 1.5$

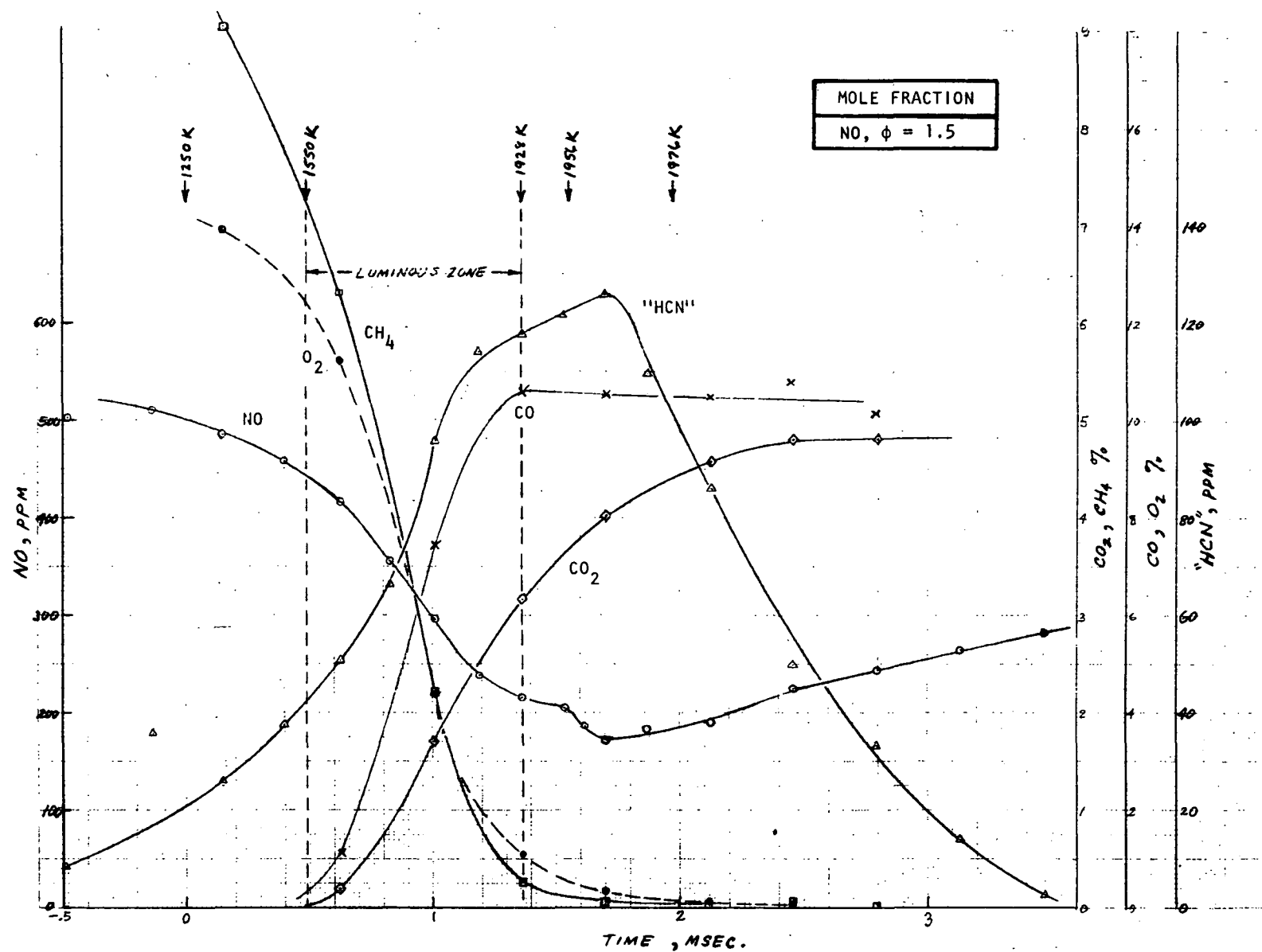


Figure 86. Species Mole Fraction vs Time, Flame 8, NO Addition With $\phi = 1.5$

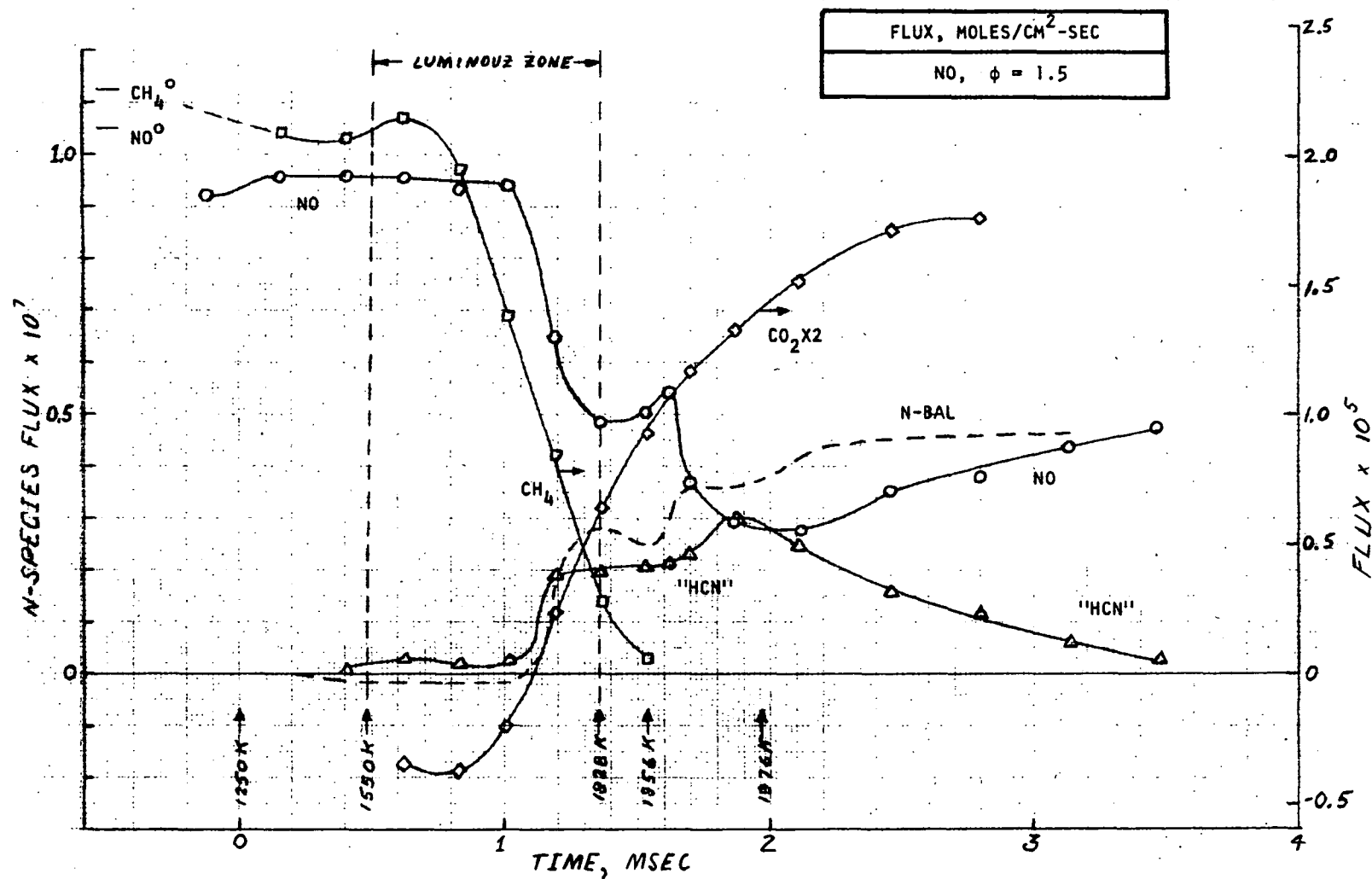


Figure 87. Species Flux vs Time, Flame 8, NO Addition With $\phi = 1.5$

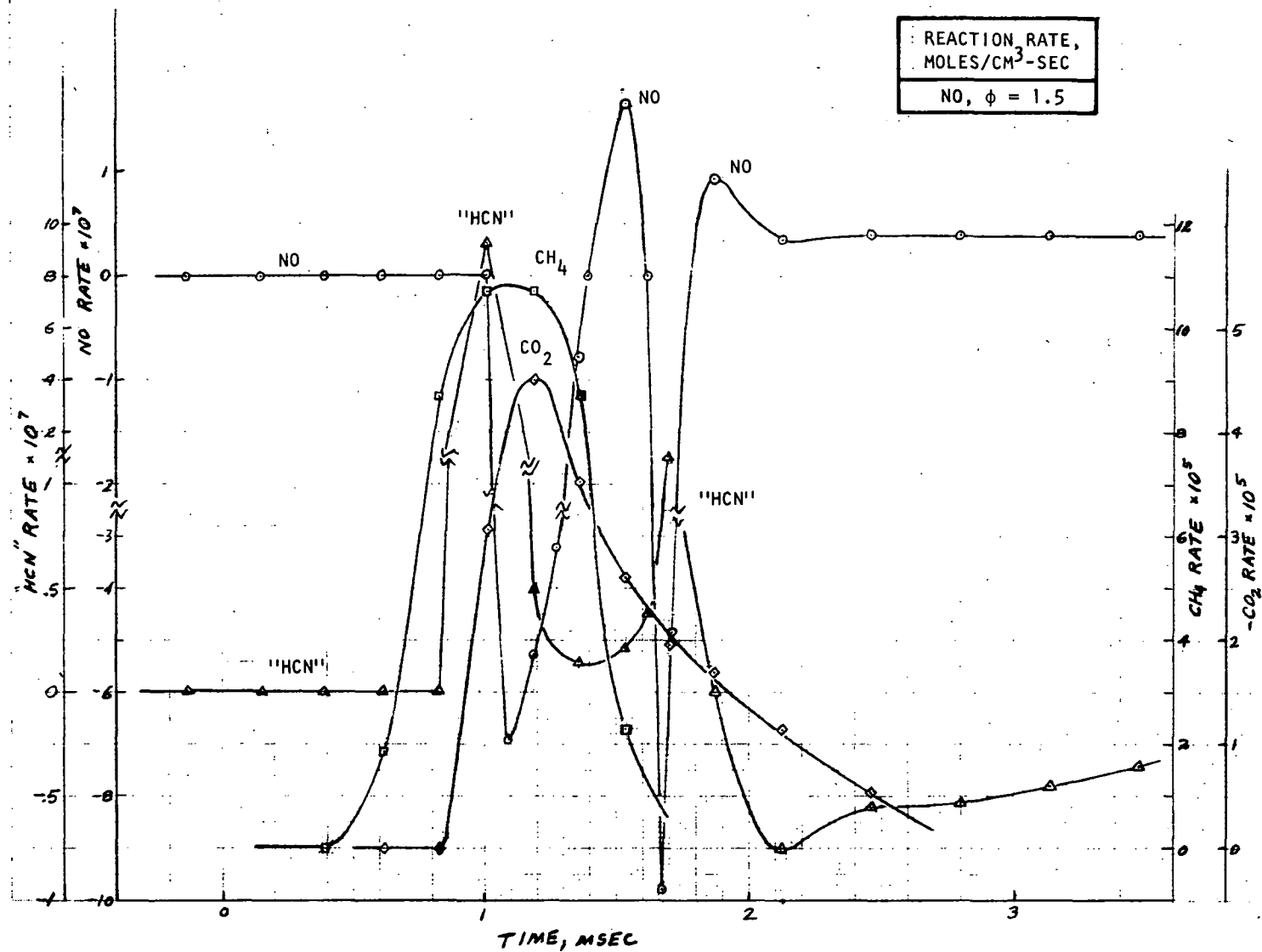


Figure 88. Species Reaction Rate vs Time, Flame 8,
NO Addition With $\phi = 1.5$

small amount of NO formed just above the luminous zone does not cause a decrease in the "HCN" flux curve indicating that this NO is not formed from HCN but rather from an N-BAL species, or if the NO is formed from HCN, an equal amount of HCN is formed from an N-BAL species.

After a further decline in NO flux, accompanied as before by rises in the "HCN" and N-BAL flux curves, the accumulated HCN produced from the NO additive gradually reacts reforming NO. Beyond 2.2 msec, the rate of NO formation is about equal to the rate of HCN consumption (giving a nearly constant N-BAL flux curve) indicating a 100 percent yield of NO from "HCN" in this region of the flame. In this region of flames 3 and 7, the yield of NO from the reacting "HCN" was only on the order of 50 percent. This demonstrates that at lower concentrations of "HCN" and NO, the yield of NO from "HCN" in the post-flame gases is greater (in flames 3 and 7, the NO and "HCN" were present at 450 to 650 ppm at 2.8 msec while in flame 8 they were each only at 240 ppm). However, even when the yield of NO from HCN is near 100 percent, it is not possible to establish that the NO forms from the HCN directly. The HCN could form an N-BAL species, (e.g., NCO) and the NO could be forming from the N-BAL species still giving a constant N-BAL flux in this region.

Comparison of Flames 3, 7 and 8. The NO flux profiles for the fuel-rich flames 3 (HCN additive) and 8 (NO only added) are compared in Fig. 89. In both flames, the rapid consumption of NO occurs somewhat below the top of the luminous zone (at about 1.13 msec on the assigned time scale). The depletion of NO is followed by a region of rapid NO formation in both flames but this occurs later in flame 8 (above the luminous zone). At about 1.65 msec, NO is consumed rapidly in flame 8 while NO forms slowly in flame 3 at this point. It is possible, therefore, that NO forms faster from flame 8 in this region of the flame than the observed rate but part of the NO is consumed as it forms giving a lower net rate of NO formation.

The NO flux of flame 7, in which HCN and NO were both added (at $\phi = 1.5$), is compared in Fig. 90 with the sum of the NO fluxes measured in flames 3 and 8 to test additivity. The flame 8 NO flux profile was decreased by 6.6 percent before adding to the flame 3 profile (to make the curves in Fig. 90 coincide below the luminous

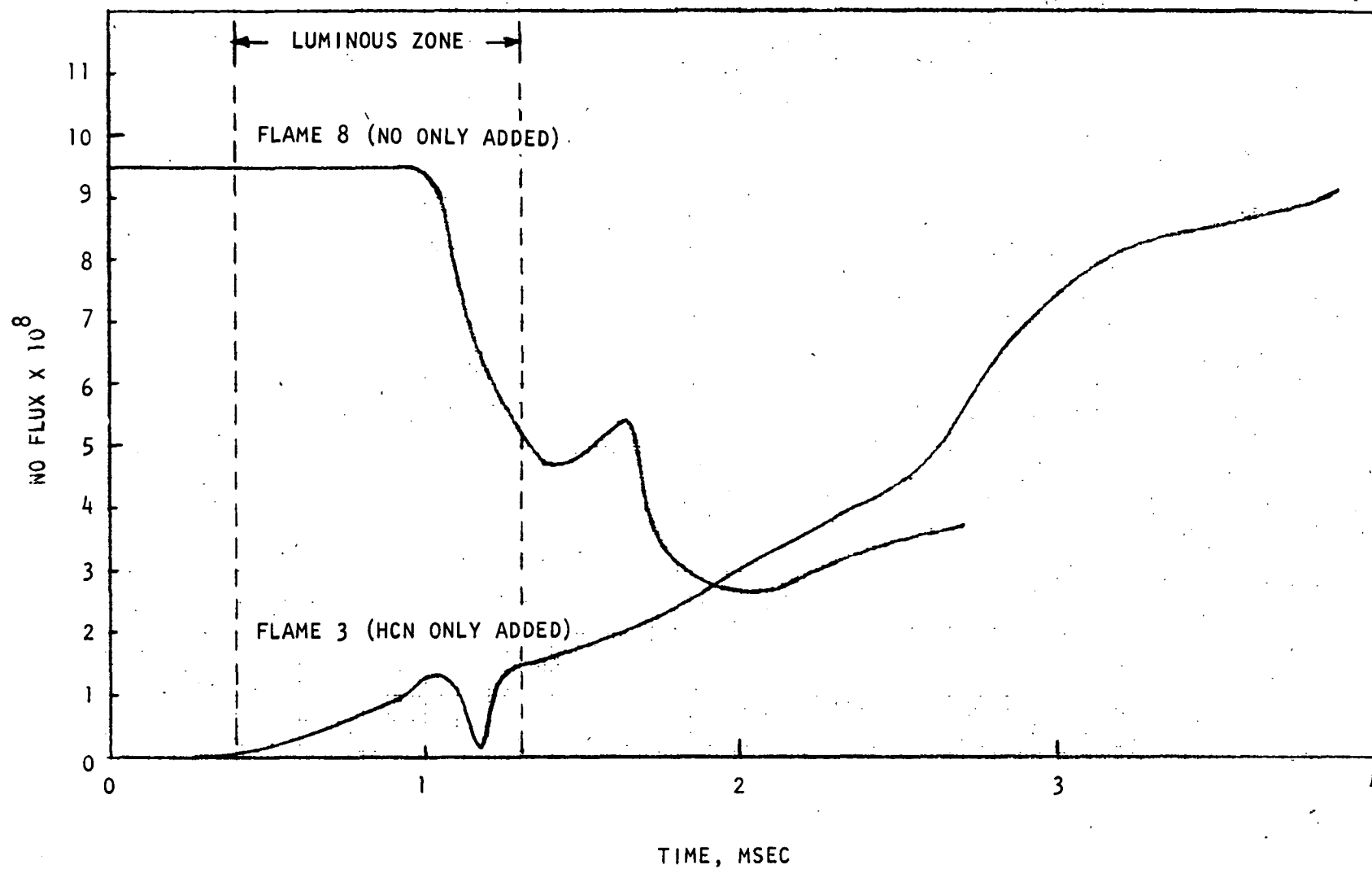


Figure 89. Comparison of NO Flux Profiles for the Fuel-Rich Flames 3 and 8

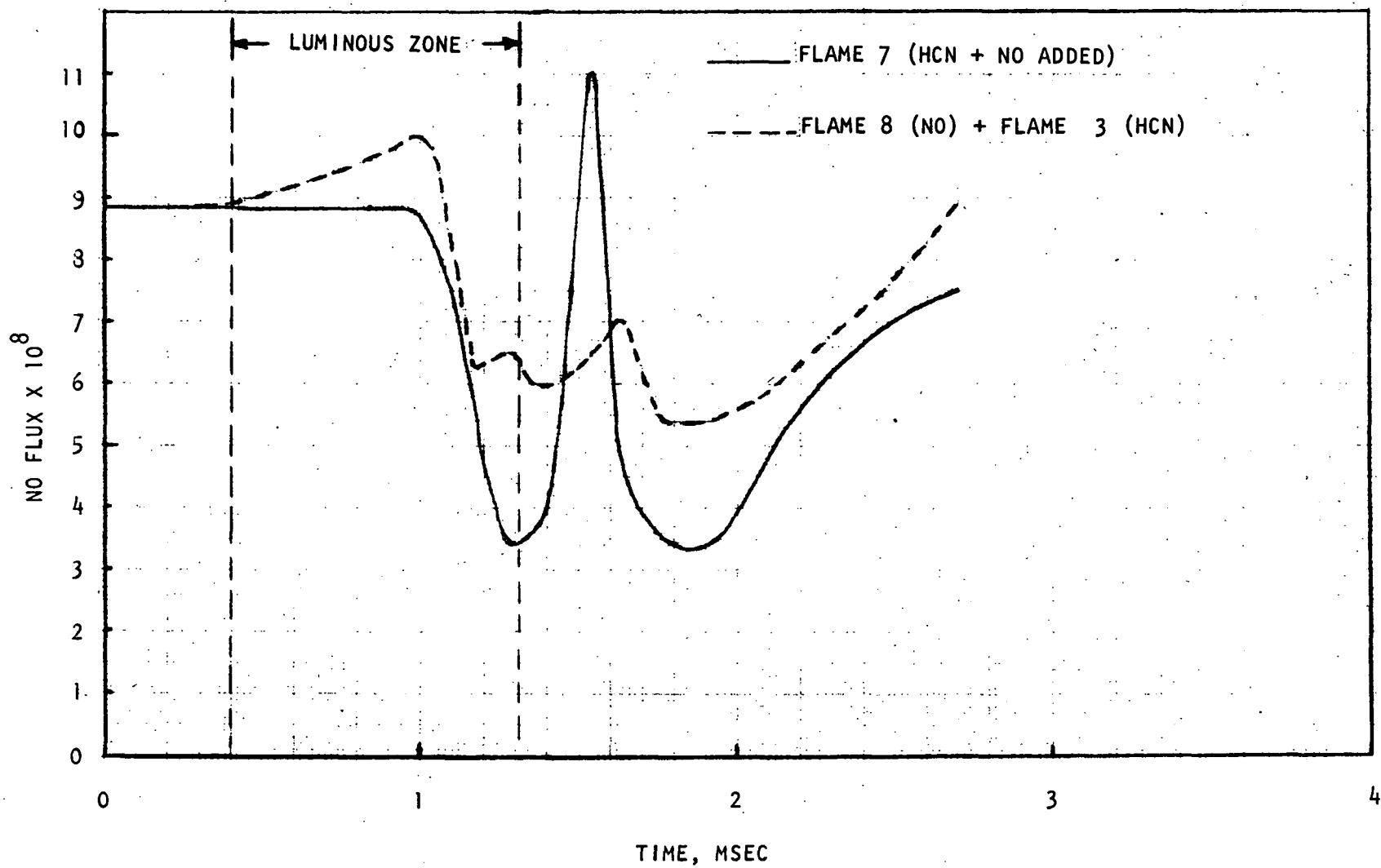


Figure 90. Comparison of Flame 7 NO Flux Profile With Sum of NO Fluxes From Flames 3 and 8

zone) because the added NO flux was slightly higher in flame 8 than in flame 7. The formation of NO around the center of the luminous zone in flame 3 is not reflected in flame 7. One possibility is that NO is in quasi-equilibrium with the other species in flame 7 and forms in this region of the flame in flame 3 because it is below this "equilibrium" concentration.

Above the luminous zone, both curves in Fig. 90 increase, decrease and then increase again. The larger inflection in the solid curve indicates that the presence of "HCN" and its reaction products (N-BAL species) has an effect on the amounts of NO that are consumed and formed above the luminous zone. As discussed previously, the shapes of the calculated flux profiles are quite sensitive to the slopes measured at various points on the mole fraction curves (because these determine the calculated species diffusion velocities, Eq. 130). Therefore, the differences between the Fig. 90 curves above the luminous zone might not be as great as the measured results indicate.

Comparison of NO Addition Experiments With Those of De Soete. De Soete (Ref. 65) added NO to premixed ethylene-O₂-Ar flames at atmospheric pressure and measured the NO concentration profile in the flame. He reported NO "yields" from added NO of the same magnitude as from amines and cyanides. Under fuel-lean conditions ($\phi = 0.7$), the NO decreased rapidly with distance from the burner from its initial concentration of 215 ppm to 160 ppm and then increased to 210 ppm and remained constant (98 percent yield). This occurred at temperatures between 2300 and 2400 K in his experiments. The dip may be the same as was observed at 0.3 msec in the flame 6 flux curve (Fig. 79)*.

Under fuel-rich conditions ($\phi = 1.47$), De Soete reports the added NO decreased from its initial concentration of 200 ppm to 50 ppm and then increased to its final concentration of about 75 ppm (38 percent yield). In another experiment at $\phi = 1.5$, shown in Fig. 91, the NO decreased from 265 ppm to 59 ppm and then

*Because of diffusion in the low-pressure flames studied here, the mole fraction of NO did not show a dip in flame 6 (Fig. 78) but the calculated flux curve did. De Soete did not make diffusion corrections to his atmospheric flame results.

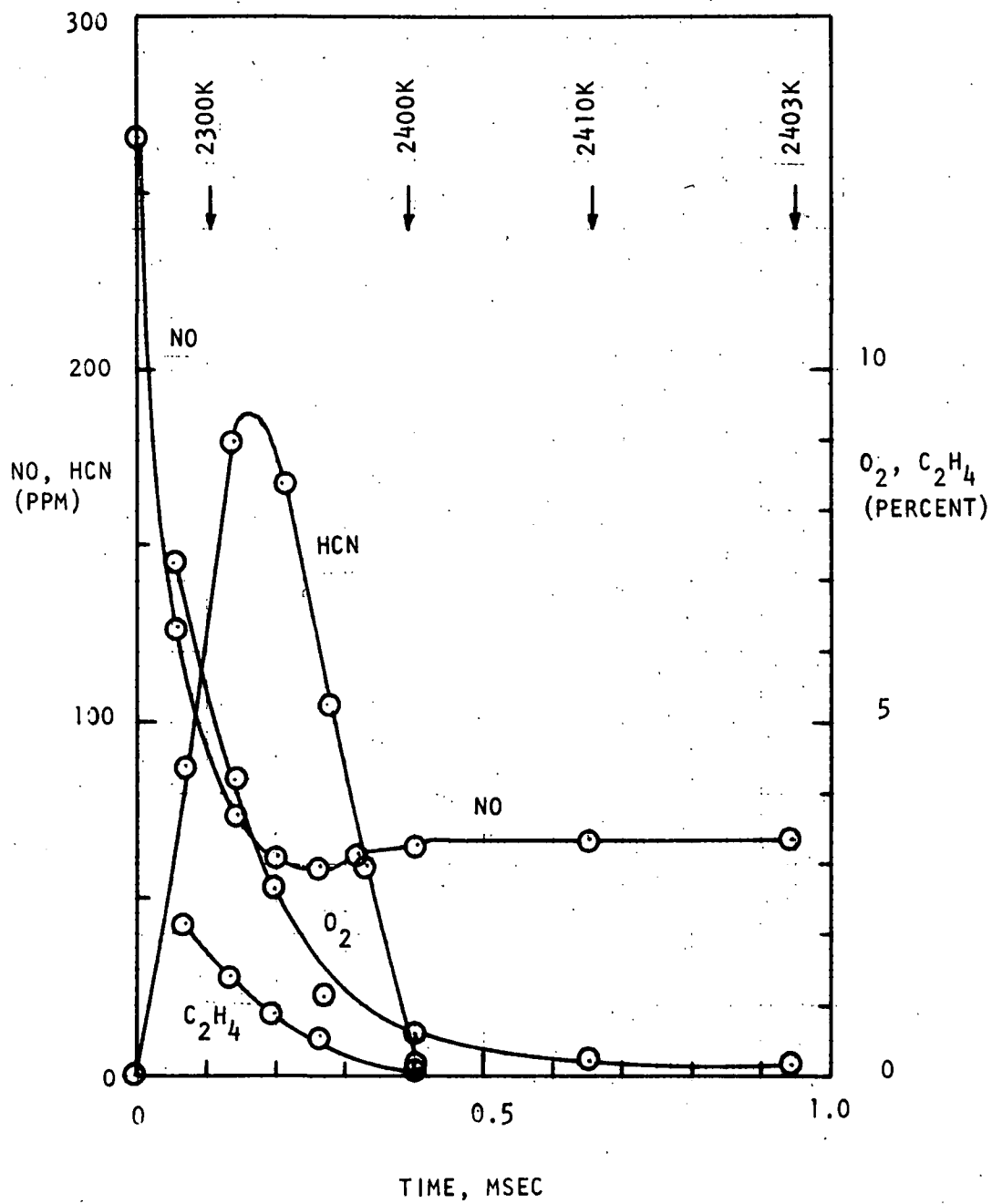


Figure 91. Species Mole Fractions in C₂H₄-O₂-Ar Flame at Atmospheric Pressure, NO Added Initially at 265 PPM, $\phi = 1.5$ (Ref. 65)

increased slightly to a final value of 67 ppm (25 percent yield). HCN was measured in this experiment and it reached a maximum concentration of about 188 ppm near the point in the flame where the NO was at a minimum and then decayed rapidly. This point was well beyond the point in the flame where most of the C_2H_4 had reacted. The HCN at its maximum mole fraction represented 96 percent of the NO that had been consumed. These concentration profiles obtained by De Soete are almost identical to those from flame 8 (Fig. 86) except that his HCN yield was higher and his flames were not as spread out. The higher yields of HCN from NO in De Soete's experiments may result from the higher flame temperatures (Ar/O₂ molar ratios of only 2.6 to 3.3) or from the use of ethylene as the fuel.

ANALYSIS OF RESULTS OF FLAME-PROBING EXPERIMENTS

The results of the detailed flame-probing experiments will be analyzed and reviewed briefly before considering the possible chemical mechanisms involved in the formation of NO from NH_3 and HCN in these flames.

Fuel-Lean Flames

The flame 1 results definitely establish that with NH_3 addition in the presence of excess oxygen (1) NH_3 is converted to NO almost exclusively via a relatively long-lived nitrogen intermediate and (2) most of the NO forms rapidly and in high yield from the intermediate just above the luminous zone (Fig. 58). The fluxes of all of the measurable nitrogen species (which include NO, NO_2 , HCN and cyanogen) are near zero at the top of the luminous zone indicating that in fuel-lean premixed flames all of the NH_3 is converted to an intermediate species before the production of most of the NO begins*. The flux of the nitrogen species that are not measurable by the probe-converter-CA technique employed was calculated by subtracting the fluxes of the measured nitrogen species from the initial additive flux (i.e., by nitrogen mass-balancing). In this report, therefore, these are referred to as "N-BAL" species. The N-BAL species include any N_2 that has formed plus any radicals or other nitrogen intermediates present in the sample entering the probe that form a species in the probe (probably N_2) that will not convert to NO over the molybdenum catalyst at 800 C (or is converted to a smaller extent than the species NH_3 or HCN).

The results obtained in flame 2 on the formation of NO from HCN under fuel-lean conditions also establish that most of the NO is formed via a nitrogen intermediate. This conclusion cannot be reached as directly as in the case of NH_3 addition because the much slower rate of reaction of HCN in the flame prevents more than about one-half of the HCN-N from being present as N-BAL species at any point in the flame (Fig. 62). The final flux of N_2 in flame 2 was 1.0×10^{-7} (if an 80 percent yield of NO were obtained). Therefore, the maximum value of the N-BAL flux, obtained at about 0.8 msec, establishes that at that point in

*This conclusion is based on a rather large correction for the upstream diffusion of NO but is within the expected error for this type of correction.

the post-flame gases at least one-third of the added HCN-N is present as an (unmeasurable) intermediate that later forms NO (it will be assumed throughout this analysis of the results that N_2 , once formed, will not form NO in these moderate temperature flames). At this point in the flame, which is slightly above the point of maximum "HCN" consumption, the rate of formation of NO is at its maximum. These and other arguments presented in the previous discussion of flame 2 establish that much, and very possibly most, of the NO formed from HCN in the fuel-rich flame forms from a nitrogen intermediate.

The candidates for the nitrogen intermediate(s) that is the precursor to NO formation in fuel-lean flames are probably limited to CN, NH_x , N and NCO. The intermediate, or whatever product it forms when quenched in the sampled gas, has been shown not to be converted to NO by the molybdenum catalyst at 800 C. The very reactive nitrogen atom is expected to be too short-lived to achieve the concentrations attained by the N-BAL species in flames 1 and 2 (the maximum N-BAL mole fraction in flame 1 is about 2000 ppm* of which a maximum of 20 percent can be N_2 because 80 percent later forms NO). CN and NH_x intermediates would probably form HCN, cyanogen and NH_3 in the probe and, therefore, be converted to NO over the catalyst and measured as "HCN" or " NH_3 " (however, NH radicals could conceivably react in the probe to form $N_2 + 2H$). The most likely candidate for the precursor to NO formation in fuel-lean flames is the NCO radical. The probe reaction for this species might be $2 NCO = N_2 + 2 CO$.

Fuel-Rich Flames

When HCN was added to the fuel-rich flame (flame 3, Fig. 66), about two-thirds of the HCN apparently survived the luminous zone and then reacted very slowly in the post-flame gases. The NO formed slowly and in low yield with most of the NO forming far above the luminous zone.

*From Eq. 129, $C = \text{Flux}/(V_i + v)$. V_i of N-BAL species is zero at maximum mole fraction of N-BAL which will be somewhat upstream from the point of maximum flux. Therefore at this point (about 0.3 msec), flux = 4×10^{-7} and $v = 300$ cm/sec giving $C = 1.32 \times 10^{-9}$ moles/cm³. At 0.1 atm and 1816 K, this concentration is 1970 ppm.

The results also strongly indicate that when NH_3 is added to the fuel-rich flame (flame 4) most of the NH_3 reacts in and/or below the luminous zone to form HCN, N-BAL species and a small amount of NO. The measurement method employed could not distinguish directly between NH_3 and HCN but comparison of the flux curves for the fuel-rich flames 3 and 4 (Fig. 66 and 71), over the time range from 1.5 to 3 msec shows a remarkable agreement even though the additives were HCN and NH_3 , respectively. The "HCN," NO and N-BAL curves are very similar in this region. The "HCN" flux is somewhat higher at 1.5 msec in flame 3 than in flame 4 where it represents only 50 percent of the added NH_3 -N. The "HCN" rate curves do not appear as similar as the flux curves but this results from minor differences in the shapes of the "HCN" flux curves in this region. The "HCN" rates for flames 3 and 4 are actually quite comparable. Since De Soete also observed the conversion of NH_3 to HCN in fuel rich flames, it will be assumed in the following discussion that the "HCN" flux plotted in Fig. 71 for the NH_3 addition experiment is actually entirely HCN above the top of the luminous zone. Experiments are planned that will permit the conversion of NH_3 to HCN to be followed through the flame front in the apparatus used in this study.

In both flames 3 and 4, more than one-half of the NO is formed in the region of the flame between 1.5 and 3.0 msec (slowly and in low yield). It is not possible to determine for certain, however, if NO forms in these fuel-rich flames directly from the reacting HCN or, as seems more likely, from a reactive intermediate and, if an intermediate is involved, its relative lifetime. The amounts of NO formed between 1.5 and 3 msec are sufficiently small that, in both flames, the HCN reacted in this flame zone and the amount of N-BAL species present at 1.5 msec are each sufficient to supply more than twice the nitrogen required for the NO that is formed.

Maximum NO Formation Rates

The conditions that existed at the points of maximum NO formation rate in the post-flame gases are compared in Table 28. The maximum NO formation rates in the fuel-rich flames were lower by factors of 20 to 50 than the rates at $\phi = 0.8$.

TABLE 28. CONDITIONS AT POINT OF MAXIMUM
NO FORMATION RATE IN POST-FLAME GASES

	Flame 1	Flame 2	Flame 3	Flame 4
Equivalence Ratio	0.8	0.8	1.5	1.5
Additive	NH ₃	HCN	HCN	NH ₃
Time, msec	0.58	0.82	2.7	2.5
Temperature, K	1956	2040	2010	2075
NO Rate, moles/cm ³ -sec	9.5×10^{-6}	3.8×10^{-6}	2.2×10^{-7}	2.0×10^{-7}
O ₂ Concentration, moles/cm ³	4.3×10^{-8}	2.8×10^{-8}	$<1.5 \times 10^{-9}$	$<1.44 \times 10^{-9}$
NO Rate ÷ (O ₂)	219	136	>148	>139

The maximum NO rates in the fuel-rich flames occurred beyond the last O₂ measurement points (at which the O₂ mole fraction had decreased to about 0.3 percent). It can be seen from the values listed in the last line in Table 28 that the rate of NO formation is, as would be expected, strongly dependent on the O₂ concentration. This does not indicate that molecular oxygen is necessarily involved in the rate-determining step since the concentrations of other oxygen species such as O atom and OH will also be dependent on the O₂ concentration.

Effect of Argon Dilution

The flame 2 and flame 5 experiments were conducted under similar conditions, $\phi = 0.8$ and HCN addition, except that in flame 5 the diluent ratio was increased from 1.0 to 1.4 and the burner feed rate was decreased from 7520 to 5851 cc/min. The additional argon and decreased flowrate lowered the measured maximum temperature from 2050 K to 1890 K. It was noted in the discussion of the flame 5 results that the measured maximum reaction rates of the species NO, HCN, CH₄ and O₂ were decreased by 30, 8, 42 and 29 percent, respectively, by argon dilution (and the reduced flowrate). Analysis of the data for flames 2 and 5, presented in Fig. 60 through 63 and 73 through 76, indicate that a number of factors determine the effect of argon dilution on the maximum rates that are observed. It will be seen, for example, that when a reaction rate is decreased by lowering the temperature and species concentrations, the maximum rate will in general occur at higher reactant concentrations partially offsetting the decrease in the maximum rate relative to the decrease in the average reaction rate of a given species.

Considering first the points in flames 2 and 5 at which the HCN depletion rates are at their maxima, the conditions at these points are, respectively: time (msec) = 0.72 and 0.89; T = 2005 K and 1850 K; (HCN) = 2.37×10^{-10} and 3.77×10^{-10} moles/cm³; (O₂) = 3.65×10^{-8} and 3.62×10^{-8} ; and $-d(\text{HCN})/dt = 4.0 \times 10^{-6}$ and 3.67×10^{-6} moles/cm³-sec. Because the HCN concentration at which the maximum rate of HCN depletion occurs is higher in the argon dilution flame, a decrease of only 8 percent in the maximum HCN rate represents a larger decrease in the rate

constant for the HCN consumption reaction. This can be shown as follows: If the global rate expression for HCN consumption were $R^{\text{HCN}} = k^{\text{HCN}} (\text{HCN})^x (\text{O}_2)^y$, then the ratio of the rates under any two given conditions (selected here are the maximum HCN rates in flames 5 and 2 defined as R_5^{HCN} and R_2^{HCN}) is given by:

$$\frac{R_5^{\text{HCN}}}{R_2^{\text{HCN}}} = \frac{k_5^{\text{HCN}}}{k_2^{\text{HCN}}} \left[\frac{(\text{HCN})_5}{(\text{HCN})_2} \right]^x \left[\frac{(\text{O}_2)_5}{(\text{O}_2)_2} \right]^y \quad (132)$$

Since the O_2 concentrations were nearly the same at these maxima, $(k_5^{\text{HCN}}/k_2^{\text{HCN}}) = (R_5^{\text{HCN}}/R_2^{\text{HCN}}) \cdot (0.63)^x = 0.92(0.63)^x$. If the consumption of HCN is first-order in HCN ($x=1$), then $k_5^{\text{HCN}}/k_2^{\text{HCN}} = 0.58$ and the rate constant decreased by 42 percent even though the rate only decreased by 8 percent. A 42 percent decrease in a rate constant from 2005 K to 1850 K would require an activation energy for HCN consumption of 26 kcal/mole. This activation energy was obtained assuming that the reaction consuming HCN is first-order in HCN. If $x=0.5$, for example, the calculated decrease in the rate constant is only 27 percent and the activation energy obtained is 15 kcal/mole.

Considering next the points in flames 2 and 5 at which the CH_4 depletion rates are at their maxima, the conditions are, respectively: time (msec) = 0.52 and 0.75; $T = 1950$ K and 1820 K; $(\text{CH}_4) = 3.44 \times 10^{-9}$ and 3.62×10^{-9} ; $(\text{O}_2) = 4.5 \times 10^{-8}$ and 4.35×10^{-8} ; and $R^{\text{CH}_4} = 1.14 \times 10^{-4}$ and 6.62×10^{-5} . Because the concentrations of CH_4 and O_2 remained nearly unchanged, the decrease in CH_4 oxidation rate of 42 percent must have resulted mainly from the decrease in temperature. This gives an activation energy for CH_4 oxidation of 30 kcal/mole.

At the points in flames 2 and 5 where CO oxidation is at its maximum: time (msec) = 0.78 and 0.93; $T = 2015$ K and 1853 K; $(\text{CO}) = 1.57 \times 10^{-8}$ and 2.37×10^{-8} ; $(\text{O}_2) = 3.52 \times 10^{-8}$ and 3.49×10^{-8} ; $(\text{H}_2\text{O}) = 9.2 \times 10^{-8}$ and 6.6×10^{-8} ; and $R^{\text{CO}} = 1.22 \times 10^{-4}$ and 8.65×10^{-5} . The global rate expression for the oxidation of CO is well established to be first-order in CO and one-half-order in H_2O . Since the O_2 concentration remained unchanged, the 29 percent decrease in the maximum rate of

oxidation of CO can be calculated to represent a decrease of 45 percent in the rate constant for CO oxidation. The accepted activation energy for CO oxidation of 27 kcal/mole would predict a rate constant decrease of 45 percent from 2015 K to 1853 K in exact agreement with the measured rates.

At the points of maximum NO formation rate in flames 2 and 5: time (msec) = 0.82 and 1.16; $T = 2020$ K and 1875 K; $(\text{NO}) = 7.45 \times 10^{-10}$ and 7.47×10^{-10} ; $(\text{O}_2) = 3.44 \times 10^{-8}$ and 2.70×10^{-8} ; $(\text{HCN}) = 1.57 \times 10^{-10}$ and 1.98×10^{-10} ; N-BAL Flux = 2.7×10^{-7} and 1.0×10^{-7} moles/cm²-sec; $v = 336$ and 239 cm/sec; and $R^{\text{NO}} = 3.40 \times 10^{-6}$ and 2.37×10^{-6} . The effect of argon dilution on the maximum rates of NO formation cannot be analyzed directly because the rate-determining step involves unidentified nitrogen and oxygen species whose concentrations are unknown.

Consider first the possibility that the rate of NO formation is first order in oxygen and first order in N-BAL species. Because the N-BAL fluxes are at their maxima in the region where the NO formation rates are at their maxima, the diffusion velocity of the N-BAL species is near zero (assuming that N-BAL represents a single species) permitting the N-BAL concentrations to be calculated. Thus the N-BAL concentrations, obtained by dividing the fluxes by the gas velocities, are 8.0×10^{-10} and 4.2×10^{-10} in flames 2 and 5, respectively. If it is assumed, as a first approximation, that the rate of NO formation is proportional to the concentrations of the N-BAL species and of O_2 , the rate should decrease by a factor of 0.52 for the decrease in N-BAL concentration and a factor of 0.78 for the decrease in O_2 concentration. Therefore the maximum rate of NO formation should have decreased by 60 percent because of concentration factors alone, not taking into account any effect of the lower temperature, but the maximum NO rate actually only decreased by 30 percent between flames 2 and 5.

If the rate of NO formation were proportional to both the O_2 concentration and the HCN concentration, which is actually larger by 26 percent in flame 5 than in flame 2 at the point of maximum NO formation rate, the concentration effects cancel and

the 30 percent decrease in rate can be attributed to the effect of temperature on the rate constant. This would give an effective activation energy for NO formation of 19 kcal/mole. This analysis indicates, therefore, that the rate of maximum NO formation in flames 2 and 5 correlate more closely with the "HCN" concentration than with the concentration of N-BAL species.

NO Addition

The fuel-lean flames 2 and 6 were conducted under similar conditions, $\phi = 0.8$ and HCN additive, except that some NO was also added initially in flame 6. It can be seen from the reaction rate curves in Fig. 63 and 80 that the reaction of CH_4 reaches its maximum at about the same point in each flame. However, HCN, CO_2 and NO reach their maximum rates much earlier in flame 6 than in flame 2. The rate curves for these three species retain their same order and approximate spacing in flame 6 but reach their maxima earlier than in flame 2. About 60 percent of the added HCN has reacted by the top of the luminous zone in flame 6 while more than 60 percent of the HCN survives the luminous zone in flame 2. It is not possible to determine for certain if the added NO contributes to the earlier reaction in this flame or if some unidentified experimental difficulty is involved. The maximum CO_2 formation rate occurs much closer to the luminous zone when NO is added initially but the presence of NO should not affect the rate of oxidation of CO. An experimental discrepancy is, therefore, suspected.

Some consumption of NO in the luminous zone was indicated in the fuel-lean flames 6 and 1. However, no such effect was observed in flame 2 even though the NO mole fraction was about two-thirds of that of the other two flames in this region. In each case, the calculated consumption of NO (decrease in the flux curve) occurs in a region of the flame where, because of upstream diffusion of NO, the NO mole fraction is increasing steadily. Therefore, the magnitude of NO consumption in the luminous zone of the fuel-lean flames is not well established.* Also, the addition of NO alone was not investigated under fuel-lean conditions.

*It should be noted that in flame 1, one of the two NO profiles that were measured did not give a negative calculated flux or rate in the luminous zone.

Under fuel-rich conditions, NO was added alone (flame 8) and with HCN (flame 7). In each case, about one-half of the added NO is suddenly consumed just below the top of the luminous zone. The NO flux at one point in flame 8 decreases to about one-fourth of its initial value. The consumption of NO in and above the luminous zone is well established under fuel-rich conditions. In addition to a decrease in the calculated flux, the measured mole fractions of NO actually decrease in both flames (because the downstream NO concentration gradients are so small that little NO diffuses upstream).

These results with added NO demonstrate that, in fuel-rich flames with HCN or NH_3 added, more NO could form than the flux curves indicate because both NO formation and consumption are occurring simultaneously. In flames 7 and 8, the maximum rates of NO consumption are 10×10^{-7} and 7×10^{-7} , respectively, at NO mole fractions of 305 and 250 ppm ($t = 1.16$ msec). In flame 3 (HCN addition), the maximum in the NO consumption rate is 8×10^{-7} at an NO mole fraction of 100 ppm. In flame 4, however, the NO flux is increasing in this region of the flame even though the NO mole fraction is 200 ppm. Apparently some NO is being formed in the luminous zone as part of the added NH_3 is being converted to HCN. Most of this NO is being consumed by the reactions that consumed added NO in flame 8. The net effect in flame 4 is a positive NO formation rate (at 1.16 msec) of 2×10^{-7} .

Reaction Mechanism

The elementary reactions that may be involved in the formation of NO from NH_3 and HCN are discussed in this section and compared with the experimental results. More data and theoretical analysis are required before a detailed mechanism can be established. Computer calculations need to be carried out to determine if the reactions that are considered can predict the reaction rates observed for each of the measured species in various regions of the flame as well as the overall yields of NO.

The reactions under consideration are listed in Table 29.* The tabulation is not all inclusive but contains most of the elementary reactions that would appear to be of importance in the production of NO and N₂ from NH₃ and HCN in hydrocarbon flames. According to this mechanism, the major path for the formation of NO involves the reaction of CN radical with O₂ or OH to form NCO which is postulated to be relatively stable and can eventually react with oxygen atom to form NO:



As discussed previously, the NCO radical is proposed as the principal intermediate in the formation of NO from NH₃ and HCN because it could have the characteristics required by the experimental results obtained in this study; namely, of not forming NO in the probe-converter system and of being sufficiently non-reactive to have a relatively long lifetime in the region of the luminous zone. It does not appear that the NCO radical can undergo reactions other than Reaction 28, and possibly, Reactions 29 and 30. Reaction 28 will not occur rapidly until above the luminous zone where the oxygen atom concentration is high. Davies and Thrush (Ref. 136) have proposed that NCO is an intermediate in the formation of NO from the reaction of oxygen atom with HCN. More recently, Mulvihill and Phillips (Ref. 137) have proposed NCO as the precursor to NO formation from cyanogen added to a low-temperature H₂-N₂-O₂ flame.

According to the proposed reaction scheme listed in Table 29, molecular nitrogen can form in the following four reactions:



*Reactions 1 through 30, as listed in Table 29, are numbered here out of sequence with those in the rest of the report for simplification of the discussion.

TABLE 29. REACTION SCHEME FOR FUEL NO FORMATION
FROM AMMONIA AND HYDROGEN CYANIDE

	<u>ΔH_{298}, KCAL/mole</u>
1. $\text{NH}_3 + \text{O} \rightarrow \text{NH}_2 + \text{OH}$	+1.0
2. $\text{NH}_3 + \text{OH} \rightarrow \text{NH}_2 + \text{H}_2\text{O}$	-16.2
3. $\text{NH}_3 + \text{H} \rightarrow \text{NH}_2 + \text{H}_2$	-1.1
4. $\text{NH}_2 + \text{O} \rightarrow \text{NH} + \text{OH}$	0.0
5. $\text{NH}_2 + \text{OH} \rightarrow \text{NH} + \text{H}_2\text{O}$	-17.2
6. $\text{NH}_2 + \text{H} \rightarrow \text{NH} + \text{H}_2$	-2.0
7. $\text{NH} + \text{O} \rightarrow \text{N} + \text{OH}$	-27.3
8. $\text{NH} + \text{OH} \rightarrow \text{N} + \text{H}_2\text{O}$	-44.5
9. $\text{NH} + \text{H} \rightarrow \text{N} + \text{H}_2$	-29.3
10. $\text{NH} + \text{O} \rightarrow \text{NO} + \text{H}$	-76.0
11. $\text{NH} + \text{OH} \rightarrow \text{NO} + \text{H}_2$	-78.1
12. $\text{NH} + \text{O}_2 \rightarrow \text{NO} + \text{OH}$	-59.1
13. $\text{NH} + \text{NO} \rightarrow \text{N}_2 + \text{OH}$	-102.2
14. $\text{N} + \text{O}_2 \rightarrow \text{NO} + \text{O}$	-31.8
15. $\text{N} + \text{OH} \rightarrow \text{NO} + \text{H}$	-48.8
16. $\text{N} + \text{NO} \rightarrow \text{N}_2 + \text{O}$	-75.0
17. $\text{N} + \text{CH}_3 \rightarrow \text{HCN} + 2 \text{H}$	-11.3
18. $\text{N} + \text{CH}_2 \rightarrow \text{CN} + 2\text{H}$	+2.9
19. $\text{N} + \text{CHO} \rightarrow \text{NCO} + \text{H}$	-33.2
20. $\text{N} + \text{RH} \rightarrow \text{NH} + \text{R}$	
21. $\text{HCN} + \text{O} \rightarrow \text{CN} + \text{OH}$	+21.6
22. $\text{HCN} + \text{O} \rightarrow \text{NCO} + \text{H}$	-1.7
23. $\text{HCN} + \text{OH} \rightarrow \text{CN} + \text{H}_2\text{O}$	+4.4
24. $\text{HCN} + \text{H} \rightarrow \text{CN} + \text{H}_2$	+19.6
25. $\text{CN} + \text{O}_2 \rightarrow \text{NCO} + \text{O}$	-6.3
26. $\text{CN} + \text{OH} \rightarrow \text{NCO} + \text{H}$	-23.3
27. $\text{CN} + \text{O} \rightarrow \text{CO} + \text{N}$	-77.0
28. $\text{NCO} + \text{O} \rightarrow \text{NO} + \text{CO}$	-102.5
29. $\text{NCO} + \text{NCO} \rightarrow \text{N}_2 + 2 \text{CO}$	-129.0
30. $\text{NCO} + \text{N} \rightarrow \text{N}_2 + \text{CO}$	177.5

Reaction 16 is part of the reverse Zeldovich mechanism. It will be seen that the amount of N_2 that can form via Reaction 16 is limited by the competing Reaction 14 from the forward Zeldovich mechanism:



The experimental procedure did not permit the molecular nitrogen flux profile to be obtained and N_2 had to be included in the N-BAL species. The final measured yields of NO establish, however, that N_2 is formed in low yield in the fuel-lean flames and in high yield in the fuel-rich flames.

A probable reaction mechanism for NH_3 would first involve the progressive stripping of H atoms by reaction of NH_3 , NH_2 , and NH with H, OH, and O to produce N and NH (Reactions 1 through 9). Reaction of N atom with hydrocarbon fragments such as CH_3 and CH_2 via Reactions 17 and 18 is known to be fast (Ref. 138). About one-half of the NH_3 forms HCN in fuel-rich flames (flame 4) while all of the NH_3 is apparently converted to NCO in fuel-lean flames (flame 1). This may be partially due to the lower concentrations of hydrocarbon fragments in the fuel-lean flames. Also, the presence of intermediate oxidation products in the lean flames such as CH_2O and CHO could lead to the direct formation of NCO by, for example, Reaction 19. Any CN radicals formed in reactions such as Reaction 18 could form NCO in fuel-lean flames via Reaction 25 but would form HCN in fuel-rich flames by the reverse of Reactions 21 and 24.

NO Formation From NH_3 in Fuel-Lean Flames. According to the mechanism being considered, NH_3 reacts at $\phi = 0.8$ (flame 1) to form N and NH which react with hydrocarbon fragments and partially oxidized species to form CN and possibly some NCO directly. Nearly all of the CN formed then reacts with O_2 to form NCO. After the methane reaction rate declines at the top of the luminous zone, the O atom concentration rises and the NCO is converted to NO rapidly and in high yield via Reaction 28.

NO Formation From HCN in Fuel-Lean Flames. About one-third of the HCN reacts in the luminous zone under these conditions (flame 2) to form CN and then NCO (Reactions 21 through 25). However, most of the HCN does not react until just above the luminous zone where it reacts rapidly, probably through Reactions 22 and 23,

forming CN and then NCO which forms NO in high yield (Reaction 28). All of the reactions that involve the initial breakdown of the HCN molecule are either endothermic or sterically hindered. The results indicate that the reactions of the HCN molecule are much slower than those of NH_3 and, according to the proposed mechanism, the HCN reacts with O atom above the luminous zone more slowly than does NCO giving a somewhat slower rate of NO formation from HCN (Fig. 2). However, once the HCN molecule reacts, Reactions 25 and 28 predominate in the fuel-lean flame giving high yields of NO.

Formation of N_2 in Fuel-Lean Flames. In the fuel-lean flames (1 and 2), about 18 percent of the additive nitrogen ultimately forms N_2 (based on an 82 percent yield of NO) but the region in which most of the N_2 forms cannot be established from the experimental data. Two sources of molecular N_2 are included in the proposed mechanism. Reactions 13 and 16 form N_2 from NO by reactions of the type proposed by Fenimore (Ref. 66). In Reactions 29 and 30, N_2 forms from NCO in competition to Reaction 28.

Consider first the situation if it is assumed that N_2 forms solely from Reaction 16 in these fuel-lean flames where the O_2 concentration is much greater than the NO concentration even at complete reaction. The rate constant ratio k_{16}/k_{14} is not large and has the following values:

Temperature, K	1600	1800	2000	2200	2400
k_{16}/k_{14}	11.2	8.0	6.0	4.8	3.9

The molar ratio $(\text{O}_2)/(\text{NO})$ is about 50 just above the luminous zone dropping to 20 at complete reaction. Therefore the reaction rate ratio R_{14}/R_{16} is 7 above the luminous zone and 3 at complete reaction. Thus if the 18 percent N_2 formed is from Reaction 16 only, nearly all of the NO would have to form via Reaction 14 rather than Reaction 28 as proposed.

If such a Fenimore mechanism were occurring in the fuel-lean flames instead of the proposed "NCO" mechanism, the required maximum mole fraction of N atom can be calculated as follows. The N-atom concentration required for Reaction 14 to occur at a given rate, R_{NO} , is $(\text{N}) = R_{\text{NO}} / [k_{14}(\text{O}_2)]$. It can be seen from Table 28

that at the maximum rate of NO formation in flame 1, $R_{\text{NO}}/(\text{O}_2)=219$ and $T=1956$ K. The value of k_{14} at this temperature is 2.5×10^{12} giving $(\text{N})=8.8 \times 10^{-11}$ mole/ cm^3 or 141 ppm N atom at 0.1 atm. This is a much larger steady-state N-atom concentration than can form from N_2 in hydrocarbon-air flames (via the Zeldovich mechanism). It is possible, however, that the major N-BAL species formed from NH_3 and HCN in fuel-lean flames is actually CN radical rather than NCO and Reaction 27 occurs so rapidly just above the luminous zone that the N atom concentration reaches the high values required for the observed NO and N_2 to form via reactions 14 and 16, respectively. Computer modeling will be required to determine if this mechanism for NO formation is reasonable. Assuming that large concentrations of CN radicals accumulate in the flame front rather than CNO radicals does not appear to be in agreement with the flame 1 results, however, because CN would be expected to form HCN or $(\text{CN})_2$ in the probe and, therefore, be measurable as "HCN" in the converter-CA system.

Consider next the favored mechanism in which all of the NO forms from NCO through Reaction 28. The N_2 now cannot form from Reaction 16* but must form from NCO. Reaction 29 then appears to be the most likely path for N_2 formation from NCO (see page 18 of Ref. 2). This mechanism predicts a lower NO yield at higher additive concentrations because R_{29}/R_{28} increases with increasing NCO concentration. At the point in Flame 1 where NO is forming at its maximum rate (0.58 msec), $R_{\text{NO}} = 9.5 \times 10^{-6}$ and R_{N_2} is presumably about 2×10^{-6} . If the NCO mole fraction is estimated to be 1000 ppm** at that point and O atom is assumed to be in equilibrium with O_2 which is present at a concentration of 4.3×10^{-8} (Table 28), then $(\text{NCO}) = 6 \times 10^{-10}$ and $(\text{O}) = 2.6 \times 10^{-10}$ moles/cc***. Therefore, to be compatible with this reaction scheme under these conditions, k_{28} would have to equal 6×10^{13} and k_{29} would be 5.5×10^{12} $\text{cm}^3/\text{mole-sec}$. An oxygen-atom overshoot of a factor of 6 at this point just above the luminous zone would reduce the required value of

*Similar arguments can probably be made against the other Fenimore-type reaction, Reaction 13.

**The N-BAL flux at 0.58 msec in Fig. 58 is about 90 percent of NH_3° which was 2500 ppm. However, the N-BAL mole fraction is about one-half of the initial NH_3 mole fraction because of diffusion (compare with methane in Fig. 55 which diffuses somewhat faster).

***Log $K_p = -6.6$ for $\text{O}_2 = \text{O} + \text{O}$. $K_C = K_p/RT = 1.5 \times 10^{-12}$ moles/cc. $(\text{O}) = K_C^{1/2} (\text{O}_2)^{1/2} = 2.59 \times 10^{-10}$.

k_{28} to 1×10^{13} making the proposed NCO mechanism quite reasonable (the values of k_{16} and k_{14} at this temperature are, for example, 1.6×10^{13} and 2.6×10^{12} , respectively).

Reactions in Fuel-Rich Flames. Under fuel-rich conditions (flames 3 and 4) most of the NO forms slowly and in low yield far above the luminous zone although some NO does form in the luminous zone and a surge of NO formation occurs just above the luminous zone. When the additive is HCN (flame 3) about one-third of the HCN reacts in the flame front forming mainly N-BAL species which could be either N_2 or NCO. With NH_3 addition at $\phi = 1.5$ (flame 4), about one-half of the NH_3 appears to form HCN in the flame front by the mechanism that has been discussed and the remainder forms N-BAL species.

With either additive the HCN reacts very slowly above the luminous zone. Because the final overall yield of NO is about 30 percent, the rate of NO formation in the post-flame gases is about one-half of the rate of HCN consumption. The slower rate of "HCN" consumption in fuel-rich flames compared with the fuel-lean conditions could result from several factors: (1) the slower rate of Reaction 22, (2) CN formed in Reaction 23 may be converted back to HCN by the reverse of Reaction 24, and (3) the reduced rate of Reaction 25 could permit the CN concentration to build up (the CN radical is expected to be measured as "HCN" in the probe-converter-CA system). The major path for NO formation in fuel-rich flames probably involves Reactions 23, 26, and 28. The small amounts of NO formed in the luminous zone could form from Reaction 14 particularly with NH_3 addition.

According to the proposed mechanism, the temporary increase in NO formation rate just above the luminous zone could come about as follows. The NCO reaches a steady-state concentration at the top of the luminous zone that is controlled by the relative rates of Reactions 26 and 28. The O-atom concentration increases rapidly just above the luminous zone as the methane nears complete reaction and the NCO "reservoir" is consumed by Reaction 28 producing a momentary surge in NO production. The rate of NO formation then falls off until NCO achieves a new lower steady-state concentration.

The increase in N_2 yield over NO yield in fuel-rich flames results from an increase in the average ratio R_{29}/R_{28} . This ratio is proportional to $(NCO)/(O)$ at a fixed temperature. Since the post-flame oxygen-atom concentration should decrease by two orders-of-magnitude (not including a reduction in overshoot) in going from $\phi = 0.8$ to $\phi = 1.5$ (see Fig. 8), the increased yield of N_2 appears reasonable in terms of the favored mechanism. Computer modeling will be required to test this conclusion.

Flames With NO Addition. NO was added along with HCN in flames 6 ($\phi = 0.8$) and 7 ($\phi = 1.5$), and NO alone was added in flame 8 ($\phi = 1.5$). The results of these NO addition experiments were discussed in the Results and Discussion section and were compared there with the NO addition experiments of De Soete. These results were also analyzed further earlier in this section of the report. NO appears to be consumed in the luminous zone under both fuel-rich and fuel-lean conditions but NO consumption under the latter condition is not well established because the effect is small and NO was not added alone to a fuel-lean flame. The mechanism of NO consumption in fuel-lean flames will be considered.

The only reactions that are listed in Table 29 that could consume NO are the reverse of the NO formation reactions (i.e., Reactions 10R, 11R, 12R, 14R, 15R and 28R) but all of these are too endothermic to be likely sinks for NO. Taking the reverse Zeldovich reactions, for example, $k_{14R} = 1.8 \times 10^8$ and $k_{15R} = 2.7 \times 10^9 \text{ cm}^3/\text{mole-sec}$ at 2000 K*. The maximum rate of NO consumption in flame 8 (at 1.16 msec) is $7 \times 10^{-7} \text{ moles/cm}^3\text{-sec}$ at an NO concentration of $1.6 \times 10^{-10} \text{ moles/cm}^3$ (250 ppm) and a temperature of 1880 K. The O-atom concentration required for this consumption rate of NO to be given by Reaction 14R is $(O) = R_{NO} \div [k_{14R}(NO)] = 2.4 \times 10^{-5} \text{ moles/cm}^3$ or 3.7 atm**. The required H atom concentration for Reaction 15R is 1.6×10^{-6} or 0.25 atm. These calculations demonstrate conclusively that the reverse Zeldovich reactions cannot be important processes

* $k_{14} = 6.4 \times 10^9 T \exp(-6300/RT)$ giving 2.65×10^{12} at 2000 K and the equilibrium constant is 6.8×10^{-5} . k_{15} is about 4×10^{13} with an equilibrium constant at 2000 K of 6.5×10^{-5} .

**The rate constant at 2000 K was used in these qualitative calculations. Therefore, the required radical concentrations would be even higher at 1880 K.

in the consumption of NO in fuel-rich flames. Similar conclusions can no doubt be drawn for the other endothermic reverse reactions. The proposed reaction scheme is, therefore, deficient in that it does not predict the consumption of added NO. Other reactions will have to be added to account for the hydrocarbon-initiated consumption of NO. These will probably involve the reaction of NO with hydrocarbon fragments. Note that De Soete did not observe consumption of NO added to a $\text{H}_2\text{-O}_2$ flame (Ref. 69).

CONCLUSIONS FROM COMBUSTION EXPERIMENTS

Screening Experiments

1. The NO yields from NH_3 and HCN added to 0.1 atm premixed $\text{CH}_4\text{-O}_2\text{-Ar}$ flames exhibit a similar dependence on equivalence ratio from $\phi = 0.5$ to 1.5. The NO yield is high from $\phi = 0.5$ to 0.8 (about 80 percent at the rather large additive concentrations employed) and declines steadily thereafter as ϕ increases.
2. The flame temperature is a function of the flowrate (burner feed rate) because of heat losses to the water-cooled burner.
3. Increasing the mole fraction of argon in the reactants can either increase or decrease the flame temperature (measured in the post-flame gases) depending on whether or not the flowrate is increased simultaneously. There is a general correlation between the effect of argon dilution on temperature and its effect on NO yield. The NO yield increases with increasing temperature and vice versa.
4. Increasing the total pressure from 0.1 to 0.4 atm causes the yield of NO to decrease somewhat at low flowrates and to remain relatively unchanged at high flowrates. There again appears to be a general correlation between the effect of pressure on temperature and the effect on NO yield.
5. Changing the species concentrations by argon dilution or by varying the total pressure appears to have little effect on NO yield (except for the attendant temperature effect). This suggests that NO and N_2 are formed by reactions of the same order -- undoubtedly second.

Detailed Probing Experiments

1. NH_3 reacts rapidly in or below the luminous zone whereas HCN reacts much more slowly with more than one-half of the HCN surviving the luminous zone in either a rich or lean flame.
2. NH_3 forms an unmeasurable nitrogen species (probably NCO radical) in high yield in the fuel-lean flame. At $\phi = 1.5$, about one-half of the NH_3 apparently forms HCN.
3. In the lean flame, the surviving HCN reacts rapidly just above the luminous zone. HCN (added or formed) reacts slowly in the rich flame with much HCN remaining unreacted far above the luminous zone.
4. Nearly all of the NO that exits the reactor forms above the top of the luminous zone. In the fuel-lean flame, NO forms in high yield just above the luminous zone in the region of the flame where CO is oxidized to CO_2 . The rate of NO formation is somewhat slower from HCN than from NH_3 . In the rich-flame, the NO forms slowly and in low yield with much of it being formed far above the flame front as the remaining HCN continues to react slowly.
5. Reduction of flame temperature and species concentrations by argon dilution does not have a large effect on the NO yield but does reduce the species reaction rates as would be expected.
6. Added NO is rapidly consumed in the luminous zone of the rich flame (forming some HCN) and then partially reforms.
7. NO forms from NH_3 or HCN in the lean flame via a reaction intermediate that is probably NCO.
8. The similarity of the NO yields from the NH_3 and HCN additives can be explained in the rich flame by the observed conversion of the NH_3 to HCN before most of the NO forms. The similarity appears to be more coincidental in the lean flame although a common intermediate, such as NCO, is probably involved.

APPENDIX A

CHEMICAL ANALYSIS TECHNIQUES

CHEMICAL ANALYSIS TECHNIQUES-ORGANIC SPECIES

The organic decomposition products formed from pyrolysis of model nitrogen-containing compounds were identified by temperature-programmed gas chromatography. The 2-foot by 1/8-inch stainless-steel column was packed with Chromasorb 103 that had been screened, rinsed five times with Freon TF, and activated at 275 C for several hours. Pertinent operating conditions for this gas chromatograph are given in Table A-1.

TABLE A-1. INSTRUMENT CONDITIONS FOR ORGANIC PRODUCTS ANALYZER

Instrument: Hewlett-Packard Model 700 Gas Chromatograph
Column: 2-foot by 1/8-inch Chromasorb 103
Column Temperature: Programmed from 60 to 250 C
Heating Rate: 7.5 C/min
Detector: Flame Ionization (H_2 and O_2)
Carrier Gas: Sample gas from pyrolysis tube: He at 43 cc/min and an additional 40 cc/min added at head of column
Recorder: L and N Speedomax W
Integrator: Hewlett-Packard Model 3371B

The procedure used for analyses of the decomposition products was as follows. After injection of the sample into the pyrolysis apparatus, the pyrolysis products and any undecomposed starting materials were entrained in the flowing helium and passed into the gas chromatographic analysis system with the column at 60 C. One minute after injection of the sample, temperature programming of the column from 60 to 250 C was initiated at a rate of 7.5 C/min. The effluent gases were usually split into two streams: 30 percent of the gas was directed to the flame ionization detector for identification of the organic products, and the remaining 70

percent of the gas was passed through the appropriate scrubber solution for inorganic product analyses or to the mass spectrometer for peak identification. In this manner, complete analyses of the effluent gases were performed. Prior to subsequent analyses, the column was backflushed at 250 C for about 5 minutes.

In most cases, the organic products were identified on the basis of their retention times. The retention times of the various materials pyrolyzed and their decomposition products are given in Table A-2. Quantitative analyses for the organic species were obtained by automatic integration of the peak areas using a Hewlett-Packard Integrator, Model 3371B.

TABLE A-2. RETENTION TIMES BY ORGANIC PRODUCTS*

Compound	Retention Time, minutes
Methane	0.5
Acetonitrile	5.7
Acrylonitrile	7.8
Benzene	10.8
Pyridine	12.8
Benzonitrile	19.2
Napthalene	23.4
Quinoline	24.5
Biphenyl	26.6

*The retention times given were obtained under the conditions given in Table A-1.

Gas Chromatograph Calibration

Careful calibration of the GC pyrolysis apparatus was important because under some conditions large losses of pyridine and/or saturation of the flame ionization detector were found to occur. Pyridine, being basic, was absorbed in various parts of the system if certain column packing or materials of construction were

used. A Poropak N column packing and brass and copper fittings caused significant amounts of pyridine to be removed from the carrier gas stream. It was also found that traces of solder flux were detrimental in this respect but they could be removed by flowing warm water through the tubing for several days after assembly. To ensure that pyridine was not being lost in a given series of experiments, special calibrations were made. Mixtures containing equal amounts of pyridine and benzene at various concentrations in benzonitrile were run. The pyridine peak area would decrease with respect to the benzene peak under conditions where pyridine loss was a problem. The pyridine concentration at which this occurred would indicate if the problem was serious enough for corrective action to be taken. Benzonitrile was chosen as the carrier because it has a longer retention time than benzene and pyridine and, therefore, does not interfere with these earlier peaks.

Saturation of the flame ionization detector can occur if: (1) the sample size is too large, (2) the H_2 and O_2 flowrates to the detector are not in the proper range, and (3) if the carrier gas port into the flame becomes partially plugged. If saturation occurs, the peak area will not be proportional to the amount of the material in the flame. Calibration mixtures containing a range of concentrations of the compounds of interest were run periodically to ensure that flame saturation was not occurring.

A standard calibration sample was prepared that was a mixture of the various model compounds and their major reaction products. This was run before and after each series of model compound pyrolysis experiments and the areas measured were inputted to a computer program to calculate the organic product distribution from each pyrolysis experiment.

CHEMICAL ANALYSIS TECHNIQUES-INORGANIC NITROGEN SPECIES

The inorganic species included elemental nitrogen, ammonia, hydrogen cyanide,* and mixed oxides of nitrogen (NO_2 and NO), commonly referred to as NO_x . All of

*Consideration also had to be given to possible interference by any $(CN)_2$ that might form (discussed later under HCN analysis).

these species have previously been determined at the microgram level by several methods in a variety of matrixes, and standard analytical procedures are available in the literature (Ref. 139 through 143). At the outset of this program, the literature methods were critically examined to select the optimum method for each species determination. A number of factors were considered in the selection: (1) sensitivity: sample sizes as small as 0.2 to 1 milligram were to be pyrolyzed, the fuel oil samples contain as little as 0.3-percent N and, therefore, some pyrolysis samples would contain only a few micrograms of nitrogen; (2) interferences: the method had to be capable of sampling and determining the species in a flowing helium stream containing a wide variety of other compounds including unreacted starting material; (3) specificity: the method had to be specific for the species to be determined; and (4) speed of analysis.

As the program progressed, some of the selected methods proved to be satisfactory. Others, however, were found to be deficient and proposed methods were abandoned for alternate methods. In other cases, no adequate method was available and modification of existing procedures was required. A review of the analytical procedures (proposed and used) on this program follow.

Elemental Nitrogen

Elemental nitrogen was determined by gas chromatography (GC) using a molecular sieve 5A column and thermoconductivity detection. The instrument used was an Aerograph 200 with an L&N Model Speedomax W recorder and a Hewlett-Packard Integrator. The GC inlet system was modified so that the helium effluent from either pyrolysis apparatus passed through a 1/4-inch, glass-bead-packed, stainless-steel U-Tube and then into the GC column for N₂ analysis. The column used was a 9-foot by 1/4-inch aluminum tube packed with 40 to 50 mesh Molecular Sieve 5A. This column will separate hydrogen, oxygen, nitrogen, methane, and carbon monoxide. It was originally intended to use the U-tube to cold-trap HCN, NH₃, and NO_x for subsequent chemical analyses. However, its main use was to remove from the helium stream condensible species, i.e., water, undecomposed model compounds, and intermediate decomposition products that would eventually deactivate the chromatographic column. When used as a removal trap, the U-tube was packed

with 60 to 80 mesh glass beads. This minimized dead volume and prevented diffusion of the nitrogen, thus providing a sharp chromatographic peak. Table A-3 lists the instrument conditions for N_2 determination and Table A-4 shows the absolute sensitivity of this method and the sensitivities of the various analytical methods (to be discussed) as percent of nitrogen present in a typical pyrolysis sample.

By increasing the bridge current of the detector, sensitivity of the N_2 analysis was better than originally estimated at the start of the program. Late in the program, a calibration gas containing 0.102 mole percent N_2 in helium was used to calibrate the GC under conditions appropriate to those of the actual fuel pyrolysis experiments. The repeated injection of 0.5 μ g samples of N_2 gave integrated peak areas that were reproducible within 10 percent. However, the quantity of N_2 that was measured was about 30 percent larger than the actual quantity. Since the GC was normally calibrated with 442- μ g N_2 samples, this result indicates that the calibration curve has a positive deviation from linearity for small sample sizes. Thus, the N_2 values obtained from pyrolysis of coals and oils may be as much as 30 percent lower than reported in the Results and Discussion section.

Hydrogen Cyanide

Quantitative determination of hydrogen cyanide present in the pyrolysis products was evaluated using two different methods of analysis: (1) the Orion Research activity electrode that is reported to be specific for cyanide ion, and (2) an ASTM spectrophotometric method that utilized barbituric acid as the color-developing reagent. With the specific electrode, inconsistent HCN analyses were obtained for model compound and fossil fuel pyrolysis. In the case of the fuel pyrolysis experiments, the inconsistent results were attributed to the presence of sulfide ion from H_2S in the pyrolysis gases. Some other type of interfering species was apparently present in the model compound products but its identity could not be established. Very reproducible results were obtained, however, with the spectrophotometric method. The sample collection used for both types of analyses was the same and is briefly described.

TABLE A-3. INSTRUMENT CONDITIONS FOR N₂ DETERMINATION

Instrument:	Aerograph 200
Column:	9-foot by 1/4-inch Molecular Sieve 5A (40 to 50 mesh)
Column Temperature:	43 C
Detector:	Thermoconductivity
Bridge Current:	175 ma
Detector Temperature:	45 C
Carrier Gas:	Sample Gas from Pyrolysis Tube
Sample Gas From Pyrolysis Tube:	He at 20 cc/min
Reference Gas:	Independent He Supply at 20 cc/min
Recorder:	L&N Speedomax W

TABLE A-4. SENSITIVITIES OF THE ANALYTICAL METHODS

Component	Method	Absolute, μg	Sensitivity in Terms of Percent of Sample-N	
			0.2-μl Pyridine	1mg of 0.3%-N Oil
N ₂	Gas Chromatography	0.5	1.2	17
HCN	Cyanide Specific Electrode	0.7	0.5	23
HCN	Barbituric Acid	0.2	0.14	7
NH ₃	Distillation- Titration	34	80	>100
NH ₃	Nessler Colorimetric	1.0	2.4	33
NH ₃	Decomposition to N ₂	0.6	1.4	20
NO _x	Saltzman	0.5	0.7	17

Sample Collection System. All methods investigated required that the hydrogen cyanide be collected in an alkaline solution. The effluent helium stream was bubbled directly into a tube containing 25 cc of NaOH solution with the specific electrode method. The scrubber solution was later changed to sodium carbonate solution for the spectrophotometric determinations along with some other modifications that will be discussed. Quantitative recovery of HCN by the scrubber solution was proved by direct injection of gaseous HCN, with a gas-tight syringe, into the helium stream just before the bubbler. The HCN used for calibration was obtained from Fumico, Inc., Amarillo, Texas.

Specific Ion Electrode Method. The Model 94-06 Cyanide Ion Activity Electrode is one of a family of electrochemical sensors developed by Orion Research. Designed to be used like a conventional pH electrode, it has a solid-state sensing element which is a solid mixture of inorganic silver compounds. This membrane is an ionic conductor which allows silver ions to pass between a sample solution and the internal reference solution, which is kept at a fixed silver ion level. The distribution of silver between the two solutions develops a potential which depends on the silver ion activity in the sample solution:

$$E = E_a + 2.3 \frac{RT}{F} \log A_{Ag^+} \quad (A-1)$$

where

- E = measured total potential
- E_a = potential due to reference electrodes and internal solution
- 2.3 RT/F = Nernst factor, R and F are constants, and T is the temperature in degrees Kelvin
- A_{Ag⁺} = the silver ion activity in the sample solution

The operation of the electrode depends on the reaction of cyanide ion with sparingly soluble silver salts from the membrane surface:



and it can be shown that the potential developed between the two solutions varies with the cyanide ion activity in the sample:

$$E = E_b - 2.3 \frac{RT}{F} \log A_{CN^-} \quad (A-3)$$

where E_b is a new constant. With frequent calibrations, measurements down to 1×10^{-6} M (0.027 $\mu\text{g/ml}$) cyanide ion were attainable. For a 25-ml scrubber solution, the sensitivity was, therefore, 0.7 μg . At the 2.5 μg level, reproducibility was found to be ± 15 percent.

For the fuel oil and coal experiments, however, both sensitivity problems and interferences were encountered when the specific ion electrode was used. For a 1-mg fuel oil sample containing 0.4-percent nitrogen, only 4 μg of nitrogen is in the sample. To see 5-percent conversion to HCN, a sensitivity of 0.14 μg HCN is needed. This is below the sensitivity of the specific ion electrode method. In addition, the electrode will malfunction if ions which form very insoluble salts of silver are present at sufficiently high levels to form a layer of silver salt on the membrane surface. The Orion instruction manual states that sulfide ion, $S^{=}$, must be absent. It was found that sulfide ion at approximately the same level as cyanide ion (5 μg) caused a positive interference ranging from 25 to 50 percent. All of our fuel oil samples contained sulfur at levels equal to or more than the nitrogen level. Because of the problems encountered in analyses of the fuel oil and model compounds pyrolysis products by the specific ion technique, it was necessary to use the following analytical method for both types of materials.

Barbituric Acid Method, D2036-72. A spectroscopic cyanide method, ASTM D2036-72, which uses barbituric acid to develop the color after oxidizing the cyanide with Chloramine-T, was investigated. According to Mr. Bill Fitzgibbons of Sohio Research in Cleveland, with this method calibration curves are repeatable, the reagent solutions are stable for up to 6 months, and a time-consuming distillation step could be eliminated because the method is more interference-free than either the cyanide electrode or the pyridine-pyrazalone procedure recommended in the "Standard Methods for Water Examination," Method 207C. ASTM D2036-72 states only

that sulfides adversely affect a recommended titration method. Good reproducibility was obtained in preliminary calibration experiments at cyanide levels of 0.26 to 5.20 μg . However, at the 1- μg level, it was found that an equivalent amount of sulfide ion caused a significant decrease in the color development (absorbance at 578 $\text{m}\mu$ decreased from 0.10 to 0.035), and a threefold concentration of sulfide completely prevented formation of color.

We learned subsequently, from personnel at Sohio Research, of a method for removal of sulfide interference. It is a time-consuming procedure involving precipitation with lead carbonate, filtration, and distillation from acid solution. The ASTM method suggests precipitation with cadmium carbonate, followed by filtration and distillation. It was obvious that additional development work was required to provide a method that was adequate for our purposes.

Although not stated in either the Standard Methods or ASTM D2036-72, sulfide will react with HCN (Ref. 144). Therefore, the elimination of sulfide interference is a matter of removal of sulfide ion before it can react with cyanide. In most aqueous cyanide analyses, this is not possible because the sample is obtained with the cyanide and sulfide already together. However, our experimental procedure was the scrubbing of a carrier gas containing HCN and H_2S by a Na_2CO_3 solution. By placing cadmium carbonate in the scrubber solution, sulfide may be removed before reaction with cyanide can occur:



Both the Standard Methods and ASTM D2036-72 suggest filtration as the method of removal of CdS and CdCO_3 . From Latimer's Oxidation Potentials, it can be shown that:



This indicates that air oxidation of cyanide could be spontaneous and a filtration procedure which involves a significant mixing of air and the solution would

be deleterious to accurate CN^- determinations. We found that a single, rapid filtration of 1.0- μg cyanide in 30 ml of solution resulted in a loss of 25 percent of the cyanide although the exact cause of this loss was not established. The use of centrifugation to remove CdCO_3 and CdS precipitate avoids the oxidation. The following table shows the recovery of 1.0- μg cyanide in the presence of varying amounts of sulfide ion obtained when CdCO_3 was suspended in the absorbing solution prior to addition of cyanide or sulfide. The recovery was 90 to 100 percent.

RECOVERY OF 1.04 μg CN^- AND $\text{S}^{=}$ (CdCO_3 ADDED BEFORE CN^- AND $\text{S}^{=}$)

μg $\text{S}^{=}$	Percent Recovery of CN^-
3.2	102
6.4	97
9.6	95
12.8	88
16.0	96
32.0	94

If the CdCO_3 is added 30 minutes after the cyanide and sulfide, recovery of duplicate 1- μg samples was only 1 and 10 percent. These results confirm the need to remove sulfide immediately from a cyanide solution. Two other interfering species were tested. It was found that on a mole for mole basis, thiocyanate ion, CNS^- , gives the same color development as cyanide, and sulfite ion, $\text{SO}_3^{=}$, interferes by preventing color formation.

The modified ASTM D2036-72 spectrophotometric procedure appears to be adequate for the determination of 1- μg HCN in the presence of large excesses of sulfide ion, and this technique was used to obtain the HCN results reported. The technique is described in more detail in Appendix C. Preliminary checks on $(\text{CN})_2$ interference indicated that about one-half of any $(\text{CN})_2$ present in the sample would be measured as HCN by this procedure.

Before going on to the next analytical procedure, we must report on the difficult availability of the barbituric acid reagent. Under the comprehensive Drug Abuse Prevention and Control Act of 1970, every person who manufactures, sells, or uses

any substance controlled under this act must register with the United States Department of Justice, Bureau of Narcotic and Dangerous Drugs. Barbituric acid is controlled as a Schedule IV substance. Without the BNDD certificate, purchase of barbituric acid is unlawful, and vendors will not supply the item without a BNDD registration number. Although a license costs only \$5.00, at least 10 weeks are required for processing an application, including a visit to the laboratories by U.S. Justice Department compliance investigators. In addition, because of the additional controls, the number of vendors has become limited. Our first purchase of 25 gm was a purified sample from Matheson, Coleman, and Bell. The order was for 100 gm, but only 25 gm was available through the local supply house. Subsequently, we were informed that MCB no longer provided barbituric acid. A second order of 100 gm required over 2 months to be filled by Eastman Organic Chemicals and the material was practical grade. The latter material gives a significantly higher blank (0.07 versus 0.01A) than the purified MCB material. As a result of limited availability of the reagent, we could not test the method out as extensively as desired. Since that time, the Rocketdyne purchasing department has purchased Eastman reagent grade barbituric acid, Cat. No. 1090, from the Frese Division of Scientific Chemical Co. in Los Angeles. One-hundred grams were received within 7 weeks of ordering.

Ammonia

Ammonia determinations in the pyrolysis gases were evaluated by three different chemical analysis methods: (1) distillation of a collected sample from alkaline solution, followed by titration with standard acid solution, (2) direct Nesslerization of collected samples, and (3) a phenate method. The first two of these methods suffered from some limitation and, therefore, the phenate method was used. In addition, an indirect method was developed based on the catalytic conversion of ammonia to elemental nitrogen:



Both the phenate and conversion methods were used for the fuel oil, coal, and model compound studies.

Sample Collection. For the indirect method (conversion of NH_3 to N_2 and H_2), there is no sample collection. The carrier stream is flowed continuously through the converter and into the gas chromatograph. For the distillation method, the sample was cold-trapped (-196°C) in a U-tube. At the end of the pyrolysis, the tube was disconnected while cold; the NH_3 was frozen (freezing point = -33.4°C); and several ml of 0.1N HCl added. The tube was then capped and allowed to warm to room temperature. The NH_3 , now dissolved in the HCl solution was transferred quantitatively to the Kjeldahl distillation apparatus for subsequent determination. In later experiments, when the Nessler and phenate colorimetric methods were used, the system was modified so that the effluent helium stream was bubbled directly into 25 cc of HCl solution.

Kjeldahl Distillation and Titration. A Kjeldahl ammonia distillation apparatus was assembled and checked out early in the program. At that time, pyrolysis of model compounds was anticipated to be as large as 25 μl . The sensitivity of the method, 34 μg (see Table A-4), is sufficient to detect less than 1-percent conversion of nitrogen for a 25 μl -sample of pyridine. Ammonia was determined in the pyrolysis products of 5- μl samples of pyridine and 2-picoline at temperatures where complete decomposition of model compound occurred. The trap downstream of the reactor was cooled to collect condensible products and ammonia in this trap was determined by distillation from alkaline solution, collection in boric acid solution, and titration with standard acid solution. Since unreacted starting material (pyridine and picoline) interfere slightly, as well as other organic amines, the end-point of the titration was not sharp and precision was not good. As the program progressed, and sample sizes down to 0.2 μl were used at temperatures where only partial decomposition occurred, it became apparent that this method could not be used because of its insensitivity.

Nessler Method. The Nesslerization method is the standard colorimetric procedure recommended in the Standard Methods and by ASTM (Ref. 139 and 140). A carefully prepared Nessler reagent may respond, under optimum conditions, to as little as 1- μg ammonia nitrogen; however, reproducibility below 5 μg may be erratic. This did, however, afford a tenfold increase in sensitivity over the Kjeldahl method. In several pyrolysis experiments, determination of ammonia was performed by the

Nessler method. Several of the samples developed a greenish turbidity, preventing the use of a photometer. Results were therefore obtained by visual comparison with prepared standards. It is reported (Ref. 139) that a number of aliphatic and aromatic amines, acetone, aldehydes, alcohols, and other undefined organic compounds can cause trouble. Compounds of this type have been found to yield a yellowish or greenish off-color or a turbidity. Sulfide has also been reported to cause turbidity following Nesslerization. Since methods of removal are time consuming and the interferences we encountered were not identified, the method was not used for subsequent experiments.

Phenate Method. The phenate colorimetric method for NH_3 was found to be quite sensitive and satisfactory for this program. The method (from page 232 of Ref. 139) is outlined in Appendix D.

Very small quantities of NH_3 , on the order of 1 to 2 μg , were formed during the pyrolysis experiments. To determine the reliability of the phenate NH_3 values reported, calibrations were conducted utilizing a dilute NH_3 (1.68 mole percent) in helium mixture. In duplicate experiments, 1.0 cc of this gas (9.26 μg NH_3) was introduced into a volumetric flask containing 0.1 N HCl and the NH_3 determined by the phenate method. The NH_3 recoveries were 9.6 and 9.4 μg , indicating that the phenate method is satisfactory for measuring small quantities of NH_3 .

Conversion to Nitrogen (An Indirect Method). After investigating the above analytical techniques for determining the small amount of ammonia formed during pyrolysis of fossil fuel samples, a catalytic decomposition technique was developed which, in combination with gas chromatography, was finally used to determine indirectly the amount of ammonia formed. At temperatures of 900 C or higher, ammonia decomposes completely to elemental nitrogen and hydrogen when passed through a nickel tube or a tube packed with granular nickel metal (Table A-5):



When ammonia was run through the quartz tube, used for the pyrolysis studies of model compounds, it was not decomposed up to temperatures of 1100 C (Table A-5).

By placing a heated (1050 C) 1/8-inch nickel tube after the quartz pyrolysis tube, ammonia can be determined by running duplicate experiments: one with the nickel tube unheated (or bypassing it) and the second with the tube at 1050 C. Ammonia is calculated from the increase in elemental nitrogen from the first experiment to the second. The sensitivity of this method is better than 1 μg NH_3 (Table A-4) and interference may be less than by other methods.

TABLE A-5. DECOMPOSITION OF AMMONIA

Nickel Tube		Quartz Tube	
Temperature, C	% Conversion to N_2	Temperature, C	% Conversion to N_2
520	1.1	530	0.0
630	15	650	0.0
750	64	800	0.0
890	100	900	0.0
1000	100	1000	0.054
		1080	0.14

This method was used for all of the subsequent model compound and fossil fuel pyrolysis experiments. Most experiments were run with the heated nickel tube in the line, so that results were calculated as the sum of NH_3 and N_2 . In most cases, this value was low (<5 percent conversion of organic N); therefore, there was no need to determine only the ammonia.

To prevent any catalytic conversion of HCN to N_2 , a tube containing Ascarite (NaOH on asbestos) was placed between the exit end of the pyrolysis reactor and the catalytic converter. The Ascarite trapped the HCN, but not the NH_3 which was then catalytically converted to N_2 and H_2 . After the effluent gases were passed through a liquid nitrogen-cooled trap, the remaining gases were gas chromatographed.

After a number of experiments were performed with fuel oil and coal samples, it was found that the quartz tube was no longer "inert" toward ammonia. Ammonia, when

passed through the tube at 1100 C was decomposed to N_2 . It was assumed that metallic deposits (from the coal or fuel oils) on the quartz wall were now catalytically decomposing the ammonia. When this phenomenon occurs, the method is limited to the determination of the sum of NH_3 and N_2 .

Oxides of Nitrogen, NO_x

The Saltzman method was used to determine nitrogen dioxide, NO_2 , plus nitric oxide, NO , from oxidative pyrolysis and residue experiments. In order to determine NO_x at levels which account for as little as 1-percent conversion of organic nitrogen, a method was needed that was sensitive to less than 1 μg of nitrogen as NO_x . The colorimetric method of Saltzman (Ref. 141 and 142) has this sensitivity. The TECO Model 10A chemiluminescent analyzer, which was used in Phase II of this program, was considered. However, with these small batch samples, considerable modification of the apparatus would be required. The Saltzman method is one of the most widely used for the determination of NO_2 . The determination of both NO and NO_2 (NO_x) necessitates oxidation of the NO . The Saltzman technique for batch NO_x analysis from flames (about 95 percent of which is NO) was recently critically evaluated using oxygen as the oxidizer (Ref. 145) and optimum operating conditions were established. Halstead and co-workers (Ref. 146) also reported on the use of oxygen to convert NO to NO_2 . Using information from both papers, a system for collecting samples from the oxidative pyrolysis experiments for determination of NO_x was designed and assembled.

In the oxidative pyrolysis experiments with model compounds, the oxides of nitrogen were analyzed spectrophotometrically using the Saltzman reagent. Samples were taken in evacuated 1-liter pyrex flasks that contained 30 ml of Saltzman reagent. The key step in the analysis was the slow oxidation of NO to NO_2 , since the reagent is for the determination of NO_2 . After the sample (about 0.2 atm) was introduced, pressure in the flask was brought up to 1 atm with oxygen. In calibration experiments, a known standard of 130 ppm NO in N_2 was used. In a typical experiment, 55 torr of the standard was introduced into an evaluated 1-liter flask, then pressurized to 650 torr with O_2 (to bring the NO concentration to 11 ppm), and allowed to stand 24 hours. In experiments of this type recoveries

of 89, 99, and 92 percent were obtained by this method for samples containing 8, 13, and 14 micrograms of NO, respectively. These recoveries were measured against a calibration curve using nitrite ion, NO_2^- . Because these calibration samples contained 6 to 11 ppm of NO after being pressurized to 1 atm with oxygen, Fig. 2 of D. H. Fine's review of the Saltzman method (Ref. 145) suggests that much less than 100-percent recovery would be expected. This figure is misleading, however, because with 4:1 oxygen dilution, the curve labeled 5-ppm NO applies to the case where the initial NO concentration is only 1 ppm, etc. Thus, a 10-ppm sample under our conditions would correspond to the curve labeled 50 ppm in Fine's paper, and a recovery of about 95 percent would be predicted. This is in good agreement with the results obtained.

The following equation, which is equivalent to Fine's Eq. No. 3, but is more useful in predicting the expected extent of NO oxidation under given conditions, is derived in Appendix E.

$$\% \text{ NO Unreacted} = \frac{100}{(0.089 P_{\text{O}_2} t w_{\text{NO}}/V) + 1} \quad (\text{A-8})$$

where

P_{O_2} = partial O_2 pressure in torr (a constant)
 t = time in hours
 w_{NO} = initial NO in micrograms
 V = flask volume in cc

Under our standard conditions of $t = 24$, $P_{\text{O}_2} = 600$ torr and $V = 1000$ cc, this equation becomes:

$$\% \text{ Unreacted} = 100/(1.30 w_{\text{NO}} + 1) \quad (\text{A-9})$$

Thus, for the calibration runs with 8, 13, and 14 μg of NO, the predicted yields are 91, 94 and 95 percent, respectively.

APPENDIX B

COAL AND RESIDUE ANALYSIS

Three coal samples were analyzed for nitrogen in January 1973 by the Dumas method. The results obtained are shown in the first column of Table B-1. These analyses were repeated 4 months later, giving the much lower results shown. The reason for these lower results is not known, but sample inhomogeneity must be suspected. After the second series of analyses, the percent volatiles* were determined (ASTM Method D-271) for these coals as well as the percent nitrogen in the residues. It can be seen from the table that only about one-fourth of the nitrogen remained in the residue (or less if the higher nitrogen values are correct). These are smaller amounts of nonvolatile nitrogen than have been estimated previously (Ref. 2 and 71).

TABLE B-1. COAL ANALYSES AND VOLATILE NITROGEN RESULTS

Coal	N, weight percent		Percent Volatiles	N, weight percent in Residue	Percent N in Residue
	January 1973	May 1973			
IFRF-A	1.16	0.54, 0.64	27.3	0.16	21.5
IFRF-N	1.47	0.91, 1.16	41.5	0.18	11.5
EPA	1.17	0.60	38.0	0.27	27.8
EPA (Duplicate)		0.58	38.9	0.25	26.5

*7 Minutes of heating at 950 C.

APPENDIX C

MODIFIED ASTM METHOD D2036-72, HYDROGEN CYANIDE IN A HELIUM STREAM CONTAINING HYDROGEN SULFIDE

SCOPE

This method covers the determination of hydrogen cyanide at the microgram level in a helium carrier gas stream containing up to 30 times as much hydrogen sulfide as hydrogen cyanide.

REAGENTS

Prepare the reagents exactly as described in the indicated paragraphs of ASTM D2036-72:

Chloramine-T, para. 6.8

Hydrochloric Acid (1 + 9), para. 6.11

Phenolphthalein Indicator, para. 6.14

Potassium Cyanide, Stock Solution, para. 6.15

Potassium Cyanide, Standard Solution, para. 6.16

Pyridine - Barbituric Acid Reagent, para. 6.19*

Sodium Carbonate, Anhydrous, Baker No. 3602

Cadmium Carbonate, Powder, B & A No. 1483

EQUIPMENT

Test Tubes, 25 by 175 mm

Centrifuge Tubes, Graduated, Pear Shape, VW&R No. 21119-001

*When preparing pyridine-barbituric acid reagent, as described in para 6.19 of ASTM D2036-72, the barbituric acid does not completely dissolve and it varies from one bottle of material to another. Filter the solution several days after preparation through Whatman No. 4 paper.

Centrifuge, International, Model AE (with appropriate head, trunnion rings, and centrifuge holder)

5.0-cm Matched Cells (visible region)

Cary 14 Recording Spectrophotometer (or equivalent)

Micro-stirring Bars (1/2-inch length by 1/8-inch diameter)

SAMPLING

Place 125 milligrams of anhydrous sodium carbonate, 40 mg of cadmium carbonate, and a micro-stirring bar in a 25- by 175-mm test tube. Add 25 ml of distilled water and stir to dissolve the sodium carbonate. Collect the sample by bubbling the helium effluent from the pyrolysis tube through the stirred solution, for 5 minutes, using a 20-gage stainless-steel needle. Analyze the collected sample immediately.

SUMMARY OF METHOD

The sample is centrifuged to remove suspended cadmium carbonate-cadmium sulfide. Aliquots of the supernatant liquid are then analyzed as described in ASTM D2036-72, page 557, para. 12.3.1 and 12.3.2. To save barbituric acid reagent, one-half the called-for recipes were used and, to increase sensitivity, 5.0-cm cells were used instead of 1.0 cm.

PROCEDURE

Transfer the collected sample to a 100-ml, pear-shaped centrifuge tube. Stopper lightly with a cork stopper and place in a centrifuge holder. Place 25 ml of distilled water in another tube, place it in a holder, stopper, and bring its weight to within 0.1 gram of the sample tube and holder on a double-beam trip balance. Place the centrifuge holders in opposite trunnion rings in the centrifuge and centrifuge for 5 minutes at 1500 rpm.

Immediately transfer an appropriate aliquot of the sample into a 25-ml volumetric flask. (An aliquot up to 20 ml can be used.) Bring the volume to 10 ml with sodium carbonate solution (125 mg/10 ml). Place a micro-stirring bar in the flask. Add one drop of phenolphthalein indicator solution. Add HCl (1 + 9) dropwise with constant stirring until the solution becomes colorless. Add 1 ml of chloramine-T solution and mix; then immediately add 2.5 ml of pyridine-barbituric acid solution and again mix. Dilute to the mark with water; mix well by inversion and allow 8 minutes for color development. Measure the absorbance of the developed color with the spectrophotometer at 578 nm in a 5.0-cm cell within 15 minutes.*

Prepare a calibration curve from 0.25 to 1.5 µg "HCN" using the standard potassium cyanide solution. The calibration curve is fairly reproducible. Therefore, only one standard (1 µg) is needed every time samples are run, if the same pyridine-barbituric acid solution is being used. Run a blank every time a sample is run, but read the sample(s) against distilled water. Using the calibration curve and the following equation, determine the total micrograms of HCN collected in the original sample:

$$\mu\text{g HCN} = A \times \frac{B}{C}$$

where

A = micrograms of cyanide read from calibration curve

B = total milliliters of absorbing solution used

*The solution, during and after color development, liberates gas and when it is in the cell, bubble formation on the cell windows can cause false readings. If this occurs, it can be minimized by tapping firmly on the wall of the cell with your finger (Caution: cells are fragile.)

APPENDIX D

PHENATE METHOD (TENTATIVE) FOR NH_3 MEASUREMENT-STANDARD METHODS FOR THE EXAMINATION OF WATER AND WASTEWATER*

1. General Discussion

- a. Principle: An intensely blue compound, indophenol, is formed by the reaction of ammonia, hypochlorite and phenol catalyzed by a manganous salt.
- b. Interference: Over 500 mg/l alkalinity, over 100 mg/l acidity; color and turbidity interfere. These interferences may be removed by preliminary distillation.

2. Apparatus

- a. Colorimetric Equipment--One of the following is required:
 1. Spectrophotometer, for use at 630 m μ with a light path of approximately 1 cm.
 2. Filter photometer, equipped with a red-orange filter having a maximum transmittance near 630 m μ and providing a light path of approximately 1 cm.
- b. Magnetic Stirrer.

3. Reagents

- a. Ammonia-free water: Prepare as directed in Preliminary Distillation Step, Section 132A.3a.
- b. Hypochlorous acid reagent: To 40 ml distilled water add 10 ml of a 5% commercial bleach. Adjust pH to 6.5-7.0 with HCl. Prepare this unstable reagent weekly.

*13th Edition, 1971, pp 232 and 233

- c. Manganous sulfate solution, 0.003 M: Dissolve 50 mg $\text{MnSO}_4 \cdot \text{H}_2\text{O}$ in 100 ml distilled water.
- d. Phenate reagent: Dissolve 2.5 g sodium hydroxide, NaOH , and 10 g phenol, $\text{C}_6\text{H}_5\text{OH}$, in 100 ml ammonia-free water. Since this reagent darkens on standing, prepare weekly.
- e. Stock ammonium solution: Dissolve 381.9 mg anhydrous ammonium chloride, NH_4Cl , dried at 100 C, in ammonia-free water, and dilute to 1,000 ml;
 $1.00 \text{ ml} = 100 \text{ } \mu\text{g N} = 122 \text{ } \mu\text{g NH}_3$.
- f. Standard ammonium solution: Dilute 5.00 ml stock ammonium solution to 1,000 ml with ammonia-free water; $1.00 \text{ ml} = 0.500 \text{ } \mu\text{g N} = 0.610 \text{ } \mu\text{g NH}_3$.

4. Procedure

To a 10.00-ml sample in a 50-ml beaker, add 1 drop (0.05 ml) manganous sulfate solution. Place on a magnetic stirrer and add 0.5 ml hypochlorous acid solution, followed immediately the the addition, a drop at a time, of 0.6 ml phenate reagent. Avoid erratically low results by adding the phenate reagent without appreciable delay and yet not too rapidly. Use bulb pipets for convenient delivery of the reagents. Mark the pipet for hypochlorous acid at the 0.5-ml level and deliver the phenate reagent from a pipet which has been calibrated by counting the number of drops previously found to be equivalent to 0.6 ml. Stir vigorously during addition of the reagents. Since the color intensity is affected somewhat by the age of the reagents, carry a blank and a standard through the procedure along with each batch of unknowns. Measure the color after zeroing the photometer on the blank. (Color formation is complete in 10 min and is stable for at least 24 hr. Although the blue color has a maximum absorbance at 630 m μ , satisfactory measurements can be made in the 600-660 m μ region.) Prepare a calibration curve in the ammonia nitrogen range of 0.1-5 μg , treating the standards exactly as the sample throughout the procedure.

5. Calculation

Beer's law governs. Calculate the ammonia concentration as follows:

$$\text{mg/l Ammonia N} = \frac{A \times B}{C \times S} \times \frac{D}{E}$$

C = absorbance of standard, and S = ml unknown water sample used, D = total distillate collected, including the acid absorbent, and E = ml distillate used for color development. The ratio D/E applies only to the distilled samples, and should be ignored when the color is developed on undistilled samples.

6. Precision and Accuracy

See Section 132B.6 and Table 132. (2).

BIBLIOGRAPHY

Rossum, J. R. & P. A. Villarruz. 1963. Determination of ammonia by the indophenol method. JAWWA 55:657.

Weatherburn, M. W. 1967. Phenolhypochlorite reaction for determination of ammonia. Anal. Chem. 39:971.

APPENDIX E

DERIVATION OF NO OXIDATION EQUATION

$$-d(\text{NO})/dt = k(\text{NO})^2(\text{O}_2) \quad (\text{E-1})$$

Integration of this equation gives::

$$k(\text{O}_2)t = \frac{1}{(\text{NO})} - \frac{1}{(\text{NO})^0} \quad (\text{E-2})$$

$$k(\text{O}_2)t(\text{NO})^0 = \frac{(\text{NO})^0}{(\text{NO})} - 1 \quad (\text{E-3})$$

$$\frac{(\text{NO})}{(\text{NO})^0} = \frac{1}{k(\text{O}_2)t(\text{NO})^0 + 1} \quad (\text{E-4})$$

Substituting the following into Eq. E-4:

$$\begin{aligned} k &= 2.4 \times 10^9 \exp(+1046/RT) \\ &= 1.41 \times 10^{10} (\text{m/cc})^{-2} \text{ sec}^{-1} \text{ at } 298 \text{ K} \end{aligned}$$

$$\begin{aligned} (\text{O}_2)_{\text{m/cc}} &= P_{\text{O}_2}^{\text{torr}} \div 760RT \\ &= P_{\text{O}_2} \div (760 \times 82.1 \times 298) \\ &= 5.35 \times 10^{-8} P_{\text{O}_2} \end{aligned}$$

$$(\text{NO})_{\text{m/cc}}^0 = 3.3 \times 10^{-8} (W_{\text{NO}})_{\mu\text{g}} \div V_{\text{cc}}$$

$$t_{\text{sec}} = 3600 t_{\text{hrs}}$$

gives Eq. E-5:

$$\text{Percent NO Unreacted} = \frac{100}{(0.089 P_{\text{O}_2} t W_{\text{NO}}/V) + 1} \quad (\text{E-5})$$

APPENDIX F

THERMOCOUPLE RADIATION CORRECTION

The determination of the flame temperature profiles with a thermocouple necessitates that a correction be made for radiation cooling of the thermocouple wire. The formulation used to correct the measurements made in this study is attributed to Kaskan (Ref. 132), and considers heat transfer from the gas to the wire to occur by convective heat transfer due to flow at right angles to single cylinders. The correlation for the heat transfer coefficient, h , under these flow conditions is given as (Ref. 147):

$$h = 0.8 \frac{k}{d_w} (Re)^{1/4} \quad (F-1)$$

Equating the rate of heat gain via convection to the radiation heat loss, one obtains the following equation for the temperature correction:

$$\Delta T = 1.25\sigma \epsilon (Re)^{-1/4} \frac{d_w}{k} (T_w^4 - T_e^4) \quad (F-2)$$

The emissivity of the platinum, ϵ , was taken to be 0.2. This was judged to be about the average total emittance for platinum given in Ref. 148 between 1400 and 1800 K. The thermal conductivity of the gas, k , was computed at the adiabatic flame temperature by Rocketdyne's Thermochemical Computer Code and corrected to the measured gas temperature by multiplying it by the ratio of the corresponding thermal conductivities of pure argon. The gaseous viscosity term which appears in the Reynolds number, Re , was determined from a plot of viscosity versus flame temperature made up from data generated by Rocketdyne's Thermochemical Computer Code.

APPENDIX G

FLAME-PROBING DATA

The data obtained in the flame-probing experiments are listed in Tables G-1 through G-19. Mass spectroscopy data are presented in Tables G-12 through G-19. Most of these results are plotted in Fig. 56 through 86 presented in the main body of the report.

TABLE G-1. FLAME 1, $\phi = 0.8$, 2500 PPM NH_3

Distance, mm	Time*, msec	T, K	v, cm/sec	NO, ppm	NO ₂ **, ppm
1.39	0.0314	1592	258	471	0
1.64	0.124	1700	281.6	539	0
1.89	0.211	1778	294.6	619	4.6
2.14	0.294	1841	306	758	2.7-4.6
2.39	0.374	1892	314	870	6.4-7.3
2.64	0.453	1935	321.5	1003	3.6
2.89	0.530	1967	326.8	1172	0
3.14	0.606	1994	331.3	1350	0-2.7
3.39	0.681	2016	334.9	1523	0
3.64	0.756	2032	337.6	1664	0
3.89	0.830	2045	339.8	1702	0
4.14	0.903	2053	341.2	1755	0
4.39	0.976	2061	342.5	1788	0
4.64	1.049	2065	343.2	1808	0
4.89	1.122	2070	344	1811	0
5.4	1.27	2074	344.7	1828	0
5.89	1.412	2076	345	1829	0
6.4	1.56	2078	345A	1798	0

*Time = zero at T = 1550 K

**NO₂ mole fraction measured with molybdenum catalyst at T = 400 C

TABLE G-2. FLAME 1, COMPLETE RERUN, $\phi = 0.8$, 2500 PPM NH_3

Distance, mm	Time*, msec	T, K	v, cm/sec	NO, ppm	NH_3^{**} , ppm
1.45	-0.059	1465	243.4	394	814
1.77	0.064	1628	270.5	464	733
2.10	0.182	1737	288.6	558	497
2.42	0.290	1816	301.7	684	141
2.75	0.398	1871	310.8	863	109
3.07	0.500	1907	316.8	1157	87
3.40	0.603	1931	320.8	1514	0
3.72	0.703	1945	323.1	1660	0
4.05	0.803	1954	324.6	1699	0
4.55	0.957	1965	326.5	1806	0
5.55	1.262	1977	328.4	1856	0
6.55	1.566	1977	328.4	1879	0
7.55	1.871	1975	328.2	1855	0
9.05	2.329	1969	327.1	1881	0
10.05	2.635	1964	326.3	1850	0

*Time = zero at $T = 1550$ K

** NH_3 mole fraction measured with molybdenum catalyst at 800 C

TABLE G-3. FLAME 2, $\phi = 0.8$, 2500 PPM HCN

Distance, mm	Time*, msec	T, K	v, cm/sec	NO, ppm	HCN, ppm
7.04	1.707	2050	341	1594	
6.54	1.561	2050	341	1583	
6.04	1.414	2048	340	1567	
5.54	1.267	2047	340	1542	60
5.04	1.12	2043	339	1470	122
4.54	0.972	2035	338	1401	175
4.04	0.824	2020	335	1238	260
3.54	0.674	1996	331	1017	498
3.04	0.521	1951	324	736	900
2.80	0.447	1919	319	639	1037
2.54	0.364	1875	307	539	1270
2.05	0.201	1748	289	390	1478
1.59	0.0347	1589	263	310	1670
1.31	-0.0766	1470	241	247	1878

*Time = zero at T = 1550 K

TABLE G-4. FLAME 3, $\phi = 1.5$, 2500 PPM HCN

Distance, mm	Time*, msec	T, K	v, cm/sec	NO, ppm	HCN**, ppm
2.85	0.176	1360	193.2	24.5	
3.35	0.420	1510	216	38	
3.85	0.641	1635	235	52	
4.35	0.846	1735	251.6	72	
4.85	1.039	1820	265.6	87	
5.35	1.223	1882	276.5	114	
5.85	1.401	1928	285	151	
6.35	1.574	1962	291.4	174	-
6.85	1.744	1985	296.5	202	1200
7.35	1.913	2003	299.2	216	1463
8.11	2.166	2012	300.2	254	1700
8.85	2.410	2012	300.2	266	1912
9.35	2.574	2011	300.1	271	2008

*Time = zero at $T = 1250$ K

**HCN measured using molybdenum catalyst at $T = 800$ C with no air addition.

TABLE G-5. FLAME 3 RERUN $\phi = 1.5$, 2500 PPM HCN

Distance, mm	Time*, msec	T**, K	v, cm/sec	NO, ppm	HCN*** ppm
3.0	0.25	1407	200	44.6	2039
3.5	0.485	1550	219	63.3	1780
4.0	0.700	1670	236	78.8	1703
4.5	0.901	1761	249	95.8	1622
5.25	1.183	1870	275	112.9	1333
5.75	1.361	1920	284	162.5	1267
6.25	1.536	1957	290	177.6	1157
5.0		1840	267	103	1314
6.75	1.706	1982	294	202	1058
7.25	1.875	2000	298	239	987
7.75	2.042	2009	299	282	858
8.25	2.208	2012	301	308	802
8.75	2.373	2011	301	348	715
9.25	2.537	2008	300	378	650
10.0	2.787	2004	300	442	538
10.75	3.038	2000	299	476	473
11.5	3.288	1996	298	498	439
12.25	3.54	1990	297.5	522	391
13.25	3.88	1984	296.6	552	340

*Time = zero at T = 1250 K

**Temperature profile is from original flame 4 experiment

***HCN measured using molybdenum catalyst at T = 800 C with air addition to aid efficiency of conversion of HCN to NO

TABLE G-6. FLAME 4, $\phi = 1.5$, 2500 PPM NH_3

Distance, mm	Time*, msec	T,** K	v, cm/sec	NO, ppm	NO ₂ *** ppm
1.85	-0.406	990	137.1	37	0.6
2.35	-0.076	1190	166	35.6	3.0
2.85	0.199	1386	195.2	50.4	3.3
3.35	0.441	1524	218	77.7	4.8-5.5
3.85	0.661	1635	237.9	113	5.6-6.3
4.35	0.863	1732	257.5	152	7.9
4.85	1.051	1825	274	207	5.8
5.35	1.228	1904	289	249	0
5.85	1.398	1968	298.7	284	0
6.35	1.564	2017	305.8	317	0
7.10	1.806	2066	313.6	395	0
7.85	2.047	2080	309.8	416	0

*Time = zero at $T = 1250$ K

**Temperature measurements were made at different distances than those at which product samples were drawn. The temperature measurements are plotted in Fig. 68. Temperatures listed here were read off that plot.

***NO₂ mole fraction measured with molybdenum catalyst at $T = 400$ C

TABLE G-7. FLAME 4 RERUN, $\phi = 1.5$, 2500 PPM NH_3

Distance, mm	Time*, msec	T*** K	v, cm/sec	NO, ppm	NH ₃ , ppm	HCN**, ppm
2.52	0.0227	1265	177	58	1818	986
3.02	0.285	1433	204	78	1636	916
3.51	0.513	1560	226	93	1850	1000
4.02	0.729	1668	246	127	1719	966
4.52	0.925	1763	264.5	155	1754	984
5.02	1.108	1856	280	183	1805	1012
5.52	1.283	1930	293	220	1818	1018
6.02	1.451	1985	302	281	1701	971
6.52	1.615	2030	308	273	1612	920
7.02	1.776	2060	312	320	1431	833
6.77	1.686	2047	310	311	-	-
6.52	1.615	2030	308	298	-	-
7.52	1.937	2078	309.5	353	1261	746
8.02	2.098	2080	309.8	402	1111	646
8.77	2.341	2078	309.5	447	940	544
9.50	2.583	2075	309	518	774	447
10.27	2.826	2064	307.3	560	670	378
11.27	3.152	2056	306.2	609	532	306

*Time = zero at T = 1250 K

**Data on NH_3 additive reduced as if it were HCN

***Temperature profile is from original flame 1 experiment (Fig. 68)

TABLE G-8. FLAME 5, $\phi = 0.8$, 1793 PPM HCN + ADDITIONAL ARGON (DR = 1.4)

Distance, mm	Time*, msec	T, K	v, cm/sec	NO, ppm	HCN, ppm
9.265	2.755	1870	237.9	1523	66.7
7.765	2.127	1888	240.2	1496	87
6.776	1.715	1890	240.4	1436	137
6.765	1.715	1890	240.4	1410	-
6.265	1.503	1883	239.5	1334	187
5.765	1.294	1882	239.5	1245	242
5.445	1.160	1877	238.8	1172	304
5.035	0.998	1861	236.7	975	444
5.28	1.091	1871	238	1078	356
4.805	0.890	1848	235.1	871	574
4.63	0.816	1836	233.6	783	717.6
4.385	0.753	1814	230.8	642	903
4.245	0.692	1799	228.9	586	1017
4.065	0.614	1780	226.4	496	1059
3.845	0.516	1752	222.9	428	1167
3.645	0.425	1720	218.8	386	1280
3.435	0.328	1688	214.7	344	1370
3.015	0.1278	1605	204.2	254	1456

*Time = zero at T = 1550 K

TABLE G-9. FLAME 6, $\phi = 0.8$, 675 PPM NO + 1525 PPM HCN

Distance, mm	Time*, msec	T, K	v, cm/sec	NO, ppm	HCN, ppm
6.00	1.373	1991	330.5	1942	
5.50	1.222	1989	330.3	1909	35.7
5.00	1.071	1985	329.6	1866	29.8
4.50	0.919	1979	328.6	1789	71.2
4.00	0.766	1966	326.4	1637	148
3.75	0.690	1957	324.9	1528	207
3.50	0.612	1947	323.2	1407	241
3.25	0.535	1930	320.4	1241	276
3.00	0.456	1904	316.1	1108	448
2.75	0.376	1860	308.8	1013	679
2.50	0.294	1808	300.2	901	851
2.25	0.210	1740	288	838	942
2.00	0.121	1661	274.9	791	1045
1.75	0.0272	1575	259.8	751	1168
1.46	-0.0886	1466	240.8	726	1227

*Time = zero at T = 1550 K

TABLE G-10. FLAME 7, $\phi = 1.5$, 675 PPM NO + 2500 PPM HCN

Distance mm	Time,* msec	T, K	v, cm/sec	NO, ppm	HCN, ppm
1.46	-0.657	890	121.4	476	1586
2.00	-0.257	1092	148.9	488	1549
2.50	0.006	1277	166.1	478	1470
3.00	0.276	1415	202.1	451	1440
3.50	0.511	1558	224.5	428	1335
4.00	0.724	1677	243.9	393	1282
4.50	0.921	1787	262.5	262	1171
5.00	1.107	1864	277.1	309	1149
5.50	1.284	1924	286	316	1088
6.00	1.457	1971	292	349	1035
6.50	1.626	2000	297.3	279	984
7.00	1.794	2018	299.9	339	852
7.50	1.960	2025	301	376	824
8.00	2.126	2028	301.3	457	683
8.50	2.292	2029	301.5	496	632
9.00	2.457	2027	303.3	564	561
9.75	2.705	2025	303	657	527

*Time = zero at T = 1250 K

TABLE G-11. FLAME 8, $\phi = 1.5$, 675 PPM NO

Distance, mm	Time*, msec	T, K	v, cm/sec	NO, ppm	HCN, ppm
1.50	-0.483	965	131.5	502	8.2
2.00	-0.138	1157	157.7	510	35.8
2.50	0.149	1339	189.3	485	31
3.00	0.398	1492	212.3	457	37.4
3.50	0.622	1623	232.4	416	50.7
4.00	0.825	1735	261.7	352	66.3
4.50	1.011	1821	274.6	296	96
5.00	1.190	1872	282.3	239	115
5.50	1.365	1927	290.6	217	118
6.00	1.536	1955	294.8	204	121
6.50	1.705	1970	297	173	126
7.00	1.873	1977	298	184	110
7.75	2.124	1976.6	298.4	190	86
8.75	2.460	1972	297.4	225	50
9.75	2.797	1965	296.4	244	33.2
10.75	3.135	1959	295.5	266	13.9
11.75	3.474	1953	294.5	283	2.8

*Time = zero at T = 1250 K

TABLE G-12. FLAME 1 RERUN, $\phi = 0.8$, 2500 PPM NH_3

Compound	Sample No.							
	1*	2*	3	4	5	6	7*	8
H_2			1.37**	1.38	1.77	1.86		1.6
CH_4			0.022	0.157	0.55	1.21		4.0
NH_3			0.09	0.069	0.03			0.014
H_2O			12.97	12.56	11.44	10.22		5.85
C_2H_2			0.023	-	-	0.009		0.04
CO			4.49	4.98	4.85	3.82		-
N_2			0.916	1.2	1.02	1.58		-
O_2			6.14	6.64	8.11	8.94		14.94
Ar			68.7	69.18	69.0	69.8		72.94
CO_2			4.58	3.87	2.89	1.96		0.32
NO_x			0.24	0.22	0.16	0.102		0.07
H_2CO			-	-	0.037	0.07		0.028
C_2H_6			0.014	0.077	0.013	-		0.2
C_2H_4			-	0.061	0.091	0.14		-
HCN			0.024	-	-	0.012		0.02
Distance, mm	4.55	4.05	3.72	3.40	3.07	2.75	2.42	1.77
Time, msec	0.956	0.803	0.703	0.603	0.500	0.398	0.2902	0.0642

*Samples 1, 2, and 7 were destroyed when the break seal was opened inadvertently by mass spectroscopists.

**Mole percent

TABLE G-13. FLAME 2, $\phi = 0.8$ 2500 PPM HCN

Compound	Sample No.						
	4	5	6	7	8	9	10
H ₂	0.75*	0.76	0.89	1.11	1.21	1.03	0.86
CH ₄	0.037	0.034	0.086	0.534	1.58	2.80	3.85
NH ₃	0.034	0.003	-	-	-	-	-
H ₂ O	14.0	13.9	14.94	12.66	10.23	7.88	5.09
C ₂ H ₂	0.077	0.063	-	0.05	0.023	-	-
CO	1.50	2.28	3.49	3.93	3.51	2.62	0.98
N ₂	1.78	1.53	1.27	0.59	0.35	0.224	0.25
O ₂	5.40	5.73	6.23	7.17	9.96	12.59	13.75
Ar	70.4	70.4	68.8	70.9	70.6	70.9	73.1
CO ₂	5.66	4.91	3.70	2.78	2.13	1.62	1.29
NO _x	0.13	0.126	0.118	0.11	0.064	0.026	0.0403
H ₂ CO	0.13	0.054	-	0.04	0.08	0.066	-
C ₂ H ₆	-	0.044	0.047	-	-	0.05	0.25
C ₂ H ₄	0.003	-	-	0.08	0.16	0.16	0.58
HCN	0.13	0.07	-	0.075	0.088	0.053	-
Distance, mm	4.54	4.04	3.54	3.04	2.54	2.05	1.59
Time, msec	0.972	0.824	0.674	0.521	0.364	0.201	0.0347

Samples 1 and 3 had large air leaks; this condition could not be corrected.

Sample 2 had an extremely poor carbon balance.

* Mole percent

TABLE G-14. FLAME 3, $\phi = 1.5$, 2500 PPM HCN

Compound	Sample No.									
	1	2	3	4	5	6	7	8	9	10
H ₂	0.17*	8.62	8.86	9.01	7.35	7.36	7.125	6.76	5.83	4.78
CH ₄	12	0.061	0.051	0.069	0.108	0.227	0.84	1.76	3.33	5.34
NH ₃	0.036	0.012	0.032	0.042	0.048	0.036	0.029	0.007	0.009	-
H ₂ O	-	14.96	14.44	14.50	16.1	14.95	14.22	12.48	10.37	8.27
C ₂ H ₂	0.10	0.058	0.079	0.054	0.134	0.058	0.146	0.111	0.063	0.057
CO	-	9.984	9.95	9.91	9.86	10.0	9.135	8.057	5.65	4.50
N ₂	4.8	1.089	1.27	1.08	0.986	0.80	0.713	0.676	1.204	2.44
O ₂	18	0.22	0.0615	0.34	0.565	1.18	2.83	4.816	7.50	10.31
A _r	65	60.81	59.69	61.27	60.95	61.79	62.12	62.97	62.97	62.78
CO ₂	-	3.99	4.52	3.78	3.32	2.82	2.10	1.574	0.87	0.581
NO _x	0.026	0.024	0.081	0.077	0.067	0.044	0.040	0.011	-	0.008
H ₂ CO	0.12	0.0499	0.050	-	0.0036	-	-	-	0.020	0.052
C ₂ H ₆	-	-	-	0.066	-	0.309	0.192	0.042	0.398	0.178
C ₂ H ₄	0.025	0.2	0.071	0.234	0.206	0.418	0.484	0.491	0.472	0.319
HCN	0.27	0.044	0.127	-	0.035	-	-	-	-	0.032
Distance, mm		8.85	7.35	6.85	6.35	5.85	5.35	4.85	4.35	3.85
Time, msec		2.41	1.913	1.744	1.574	1.401	1.223	1.039	0.846	0.651

Sample 1 was a sample of unburned mixed combustible fed to the burner

*Mole percent

TABLE G-15. FLAME 4, $\phi = 1.5$, 2500 PPM NH_3

Compound	Sample No.												
	1**	2	3	4	5	6	7*	8	9	10	11	12	13
H_2	-	2.4***	3.2	7.88	10.39	10.43		8.20	8.62	8.49	6.96	5.90	4.9
CH_4	13.0	12.0	12.0	0.0042	0.029	0.122		0.837	2.54	4.96	7.16	8.85	10.5
NH_3	-	0.006	0.002	0.005	0.0008	0.0008		0.005	0.0027	0.0037	0.001	0.0039	0.005
H_2O	0.23	0.046	0.092	16.28	13.50	13.2		13.8	9.42	8.72	3.45	1.72	0.11
C_2H_2	-	-	-	0.073	0.029	0.174		0.319	0.327	0.164	0.097	0.0984	0.074
CO	0.26	1.1	1.2	8.38	8.66	9.56		7.34	6.17	5.11	3.48	2.656	1.7
N_2	0.60	-	0.032	1.84	1.56	1.48		1.12	1.81	0.666	0.599	0.384	0.39
O_2	18.0	16.0	16.0	0.302	0.364	0.756		2.68	5.81	8.67	11.60	13.77	15.0
A_r	68.0	68.0	68.0	61.21	62.35	61.74		63.01	62.60	62.07	65.75	65.9	67.0
CO_2	0.006	0.15	0.18	3.44	3.20	2.78		1.73	1.36	0.904	0.58	0.413	0.23
NO_x	-	0.004	-	0.054	0.048	0.056		0.0259	0.013	0.009	0.003	0.0069	0.006
H_2CO	0.002	-	-	-	-	0.063		0.015	0.033	0.091	0.023	0.038	0.026
C_2H_6	0.016	0.11	0.19	0.101	0.156	-		0.121	0.029	0.10	0.242	0.0619	-
C_2H_4	0.004	0.003	-	-	0.182	0.235		0.155	0.154	0.301	0.184	0.061	-
HCN	-	-	-	-	-	-		-	0.009	-	-	0.045	0.063
Distance, mm		1.85	2.35	7.85	7.10	6.35	5.85	5.35	4.85	4.35	3.85	3.35	2.85
Time, msec				2.047	1.806	1.564	1.40	1.228	1.051	0.862	0.661	0.441	0.199

*Sample 7 developed an air leak when MS analysis was performed

**Sample 1 was a sample of unburned mixed combustible fed to the burner

***Mole percent

TABLE G-16. FLAME 5, $\phi=0.8$, 1793 PPM HCN + ADDITIONAL ARGON (DR = 1.4)

Compound	Sample No.									
	1	2	3	4	5	6	7	8	9	10
H ₂	0.56*	0.51	0.58	0.815		0.808	0.73	0.66	0.438	0.078
CH ₄	0.01	0.02	0.02	0.111		0.74	1.39	2.09	0.022	5.3
NH ₃	0.043	0.032	0.069	0.035		0.034	0.021	0.007	0.043	-
H ₂ O	10.7	10.9	10.79	10.26		8.54	7.18	6.40	11.64	-
C ₂ H ₂	-	-	0.043	0.088		-	-	0.024	0.006	0.022
CO	2.49	2.78	2.78	3.52		3.10	2.41	1.80	2.33	-
N ₂	0.58	0.575	0.77	0.898		0.855	0.854	1.23	0.596	2.61
O ₂	3.97	3.90	4.085	4.91		7.24	8.45	10.44	3.63	16
A _r	76.57	77.03	77.05	75.94		77.08	76.11	76.89	76.35	76
CO ₂	4.34	3.90	3.81	3.06		1.50	0.928	0.494	5.40	-
NO _x	0.157	0.139	0.121	0.111		0.048	0.033	0.036	0.149	0.02
H ₂ CO	-	0.186	-	0.033		-	0.0195	0.104	0.037	0.09
C ₂ H ₆	0.64	-	0.043	-		0.263	0.213	-	-	-
C ₂ H ₄	0.09	0.087	-	-		0.018	0.088	0.123	0.149	0.12
HCN	-	0.002	0.05	0.13		0.006	0.004	0.123	-	0.16
Distance, mm	6.265	5.765	5.445	5.035	4.63	4.245	3.845	3.435	6.765	-
Time, msec	1.503	1.294	1.16	0.988	0.816	0.692	0.516	0.328	1.715	-

Sample 10 was a sample of unburned premixed combustible fed to the burner

*Mole percent

TABLE G-17. FLAME 6, $\phi = 0.8$, 675 PPM NO + 1525 PPM HCN

Compound	Sample No.							
	1	2	3	4	5	6	7	8
H ₂	1.022*	1.11	1.11	1.503	1.71	2.14	1.504	1.11
CH ₄	0.0158	0.0167	0.025	0.103	0.627	1.85	3.309	4.66
NH ₃	0.0827	0.056	0.0926	0.131	0.0427	0.0526	0.059	-
H ₂ O	13.63	13.52	13.31	12.45	11.43	8.34	5.631	4.877
C ₂ H ₂	0.011	0.0037	-	-	0.053	-	-	0.071
CO	2.97	3.426	4.258	4.70	4.844	3.216	0.582	-
N ₂	-	-	-	-	-	-	-	-
O ₂	4.785	5.004	5.37	6.182	8.025	11.168	14.84	16.21
Ar	70.62	70.37	70.35	70.47	70.28	71.14	73.19	72.93
CO ₂	6.60	5.93	5.09	4.134	2.75	1.56	0.531	-
NO _x	0.297	0.194	0.222	0.225	0.152	-	0.0762	0.142
H ₂ CO	0.0158	0.086	0.036	-	0.0066	0.29	-	0.0304
C ₂ H ₆	-	-	-	0.15	0.1235	-	0.572	-
C ₂ H ₄	0.0901	0.0565	0.157	0.0921	-	0.244	-	-
HCN	0.0344	0.047	-	-	0.105	0.166	0.0191	0.192
Distance, mm	5.00	4.50	4.00	3.50	3.00	2.50	2.00	1.46
Time, msec	1.071	0.919	0.766	0.612	0.456	0.295	0.121	-0.0886

*Mole percent

TABLE G-18. FLAME 7, $\phi = 1.5$, 675 PPM NO + 2500 PPM HCN

Compound	Sample No.							
	1	2	3	4	5	6	7	8
H ₂	6.20*	7.21	8.24	12.59	8.13	8.107	8.39	7.72
CH ₄	7.99	4.504	0.947	0.126	0.032	0.022	0.0308	0.0327
NH ₃	-	0.07	0.069	0.126	0.12	0.079	0.0811	0.069
H ₂ O	4.27	8.798	13.10	10.86	15.32	15.707	15.35	16.229
C ₂ H ₂	0.069	0.16	0.104	0.0639	0.029	0.0286	0.045	0.0472
CO	-	3.60	9.278	10.65	10.158	10.13	10.254	9.994
N ₂	-	-	-	-	-	-	-	-
O ₂	13.13	7.524	2.82	0.255	0.12	0.043	0.028	0.0136
Ar	68.31	66.06	62.49	61.96	61.00	60.80	60.60	60.87
CO ₂		0.731	2.18	3.58	4.34	4.70	4.848	4.815
NO _x	0.0189	0.023	0.036	0.0513	0.0545	0.057	0.149	0.118
H ₂ CO	0.147	0.118	0.069	0.019	-	0.035	-	0.0254
C ₂ H ₆	-	0.094	-	-	0.102	-	-	-
C ₂ H ₄	0.252	0.35	0.70	0.368	0.139	0.0857	0.077	0.0436
HCN	0.147	0.13	-	-	0.027	0.068	0.078	0.10
Distance, mm	3.00	4.00	5.00	6.00	7.00	8.00	9.00	10.50
Time, msec	0.276	0.724	1.107	1.457	1.794	2.126	2.457	2.952

*Mole percent

TABLE G-19. FLAME 8, $\phi = 1.5$, 675 PPM NO

Compound	Sample No.							
	1	2	3	4	5	6	7	8
H ₂	5.21*	6.38	13.04	10.576	11.48	11.445	13.73	8.68
CH ₄	9.03	6.28	2.207	0.26	0.058	0.034	0.077	0.027
NH ₃	0.0021	0.0142	0.0692	0.026	0.096	0.077	0.0176	0.018
H ₂ O	3.295	6.58	6.09	12.004	12.07	12.45	9.38	15.41
C ₂ H ₂	0.017	0.094	0.291	0.0423	0.0076	0.015	0.147	0.0397
CO	-	1.113	7.424	10.576	10.52	10.49	10.79	10.16
N ₂	-	-	-	-	-	-	-	-
O ₂	13.916	11.216	4.465	1.096	0.316	0.105	0.055	0.031
Ar	68.02	67.82	63.21	61.54	61.23	61.04	59.82	60.95
CO ₂	-	0.182	1.706	3.173	4.018	4.58	4.806	4.80
NO _x	0.0106	0.0081	0.0361	0.0298	0.041	0.035	0.074	0.066
H ₂ CO	0.106	0.098	0.2307	-	0.032	0.0315	0.186	0.019
C ₂ H ₆	-	0.263	-	0.125	-	-	-	-
C ₂ H ₄	0.213	0.263	0.492	0.49	0.277	0.105	0.05	0.023
HCN	-	-	0.0873	-	-	0.0019	0.255	0.048
Distance, mm	2.5	3.5	4.5	5.5	6.5	7.75	8.75	9.75
Time, msec	0.149	0.622	1.011	1.365	1.705	2.124	2.46	2.797

*Mole percent

APPENDIX H

DERIVATION OF ONE-DIMENSIONAL FLOW EQUATION INCLUDING DIFFUSION AND CHEMICAL REACTION

Considering two plane sectors, 1 cm^2 in area and perpendicular to the direction of flow, located a small distance apart at axial positions x_1 and x_2 , $dx = x_2 - x_1$. The molar flowrates of species i through the first and second sectors, respectively, is given by the expressions:

$$vC_{i,1} - D_{ij} \left(\frac{dC_i}{dx} \right)_1 \quad (\text{H-1})$$

and

$$vC_{i,2} - D_{ij} \left(\frac{dC_i}{dx} \right)_2 \quad (\text{H-2})$$

where

v = gas velocity, cm/sec

C_i = concentration of i , moles/cc

D_{ij} = diffusion coefficient for i in excess j , cm^2/sec

Since the volume between the plane sectors is $dx \text{ cm}^3$, the moles of i lost by chemical reaction per second in this volume is $R_i dx$, where R_i is the reaction rate of i in $\text{moles}/\text{cm}^3\text{-sec}$. Therefore,

$$vC_{i,2} - D_{ij} \left(\frac{dC_i}{dx} \right)_2 = vC_{i,1} - D_{ij} \left(\frac{dC_i}{dx} \right)_1 - R_i dx \quad (\text{H-3})$$

$$R_i = D_{i,j} \frac{1}{dx} \left[\left(\frac{dC_i}{dx} \right)_2 - \left(\frac{dC_i}{dx} \right)_1 \right] - \frac{v}{dx} (C_{i,2} - C_{i,1}) \quad (\text{H-4})$$

$$R_i = D_{i,j} \frac{d^2C_i}{dx^2} - v \frac{dC_i}{dx} \quad (\text{H-5})$$

APPENDIX I

APPLICATION OF MODELS TO PREDICT COMBUSTION BEHAVIOR

SINGLE DROPLET APPLICATION

Although the droplet/particle, KDM, and GKAP* models described in the body of this report are presently uncoupled, they may be combined to analyze the overall behavior of the droplet, vapor reactions, and fate of all species as they diffuse to the bulk gas stream. This sequence is schematically illustrated in Fig. I-1 where the areas of interest are the droplet surface, diffusion zone (which could include a flame front if the appropriate model were used, and the bulk gas flow-field. Several input parameters must be specified in order to select the appropriate droplet model (i.e., vaporization or flame-front) and to initialize the input parameters required to start the solution procedure. The first step is to specify the convective conditions around the droplet. Based on the relative velocity between the gas and droplet (for an oil droplet) either the vaporization or flame-front model is selected. If the relative velocity is greater than about 10 to 20 ft/sec, the vaporization model should be selected. For relative velocities of less than 10 ft/sec, the flame-front model is used. This velocity criterion is based on the fact that as the relative velocity increases, the flame surrounding a droplet will be swept into the wake of the droplet and, therefore, at high relative velocities, the droplet vaporizes without a flame front surrounding the droplet. The exact extinction velocity can only be determined by a detailed kinetic/diffusion analysis around the droplet, and is dependent upon the fuel, environmental oxygen concentration, and temperature. (Note: This detailed study is performed later in the analysis so that the analyzer will know if he selected the correct model.)

*Ultrasystems program developed for the EPA describing the bulk gas species and flow characteristics.

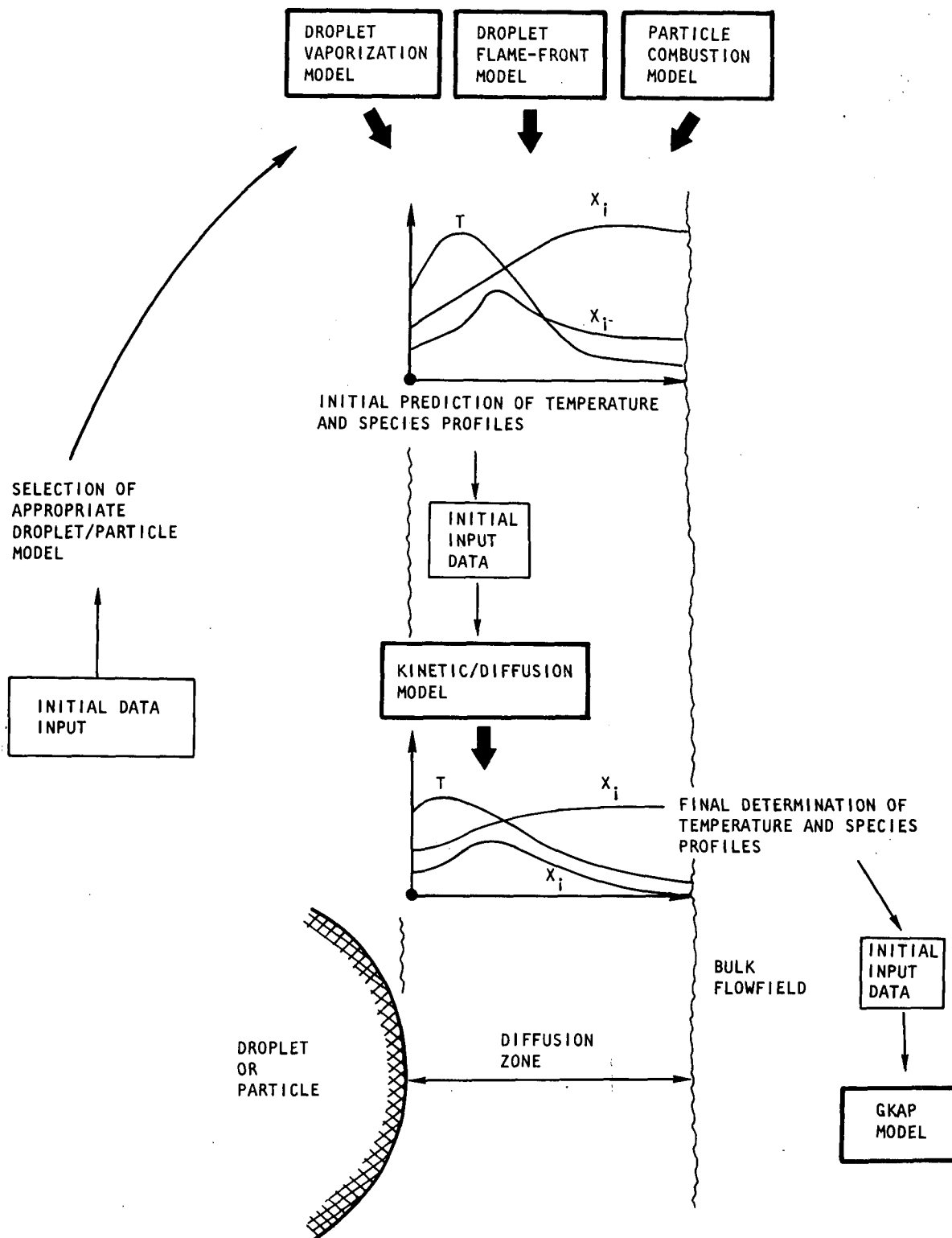


Figure I-1. Simplified Schematic Showing the Required Sequence of the Models

The droplet/particle ensemble models calculate: (1) the droplet/particle composition, temperature, and diameter "life-histories;" (2) combustion rate of each droplet particle species; (3) droplet/particle heating rate; and (4) estimated film phenomena, including film thickness and composition/temperature profiles through the film. It should be noted that depending on which droplet/particle model is used, the assumption of infinite or zero kinetic rates for reactions between the droplet surface and the bulk stream is assumed. This assumption, however, does not in the end affect the results, since the various profiles as output from the particle ensemble model are used only as initial input to the average kinetic/diffusion model (KDM) where the actual kinetics are considered. The KDM model is only executed for the droplets/particles at selected times during the droplet lifetime in order to reduce overall computing time. The droplet temperature calculated by the particle ensemble model (previously) and composition are now used as initial droplet surface boundary conditions in the KDM model. In addition, the film thickness calculated by the ensemble model is used to define the outer boundary radius of the film. Lastly, gas phase composition is used to define the composition at the outer boundary. It should again be emphasized that the estimated film composition and temperature profiles calculated by the ensemble model are used only as initial input profiles in the KDM model.

Based on the boundary conditions and detailed kinetic reactions, the KDM program solves the continuity, diffusion, and energy equations for each droplet/particle in order to calculate the exact specie mole fraction, specie molar flowrate, and temperature profiles in the film surrounding the droplet/particle. These calculations include the production rate of pollutant species, such as NO, CO, and unburned hydrocarbons in the film. This model provides corrected values for the temperature and species concentration profiles in the diffusion zone as depicted in Fig. I-1.

Since the KDM program includes the effects of convection (through the film thickness) and fuel kinetics, the model is capable of determining if a flame surrounds the droplet/particle. If the KDM calculations are not in agreement with the model used as the particle ensemble model in relationship to flame structure, then

the correct particle ensemble model must be executed in order to determine the correct input data for the KDM model.

Lastly, as shown in Fig. I-1, the KDM output, specifically the molar flowrates at the outer boundary of the film, are then used as mass addition input terms for the General Kinetic Addition Program (GKAP). The GKAP program calculates the gas flow-rate, composition, temperature, velocity, and/or pressure along the streamtube. These calculations include emission levels generated by gas phase kinetics and pollutants produced in the film surrounding the droplets/particles (through the mass addition terms).

COMBUSTOR APPLICATION

Although the droplet and kinetic/diffusion submodels described in this report are written for a single droplet, it is possible to extend them from the analysis of a single droplet to a complete fuel spray by assuming that the initial distribution of drops within any streamtube is identical to the overall distribution of drop sizes initially injected into the combustor, and then summing the individual droplet contributions. While this type of model assumes uniform mixing in the radial direction along any given streamtube, it does not restrict streamtubes from having differing equivalence ratios. Lastly, the model in its present form will not consider mass addition from other streamtubes, nor does it allow for droplet-droplet interactions within the same streamtube. However, even with these restrictions, the models used in this manner can be useful to the research scientist or design engineer.

The general method for analyzing the streamtube flow is somewhat different than that described for a single droplet because of the variation of flow parameters as a function of axial length. First, gas flow conditions (such as temperature, velocity, and oxygen concentration) along the streamtube are estimated, based on experimental data and/or past experience. These estimated gas flow conditions are then used as input data to the particle ensemble combustion model (Fig.I-2). The particular particle ensemble model to be used is selected as previously discussed.

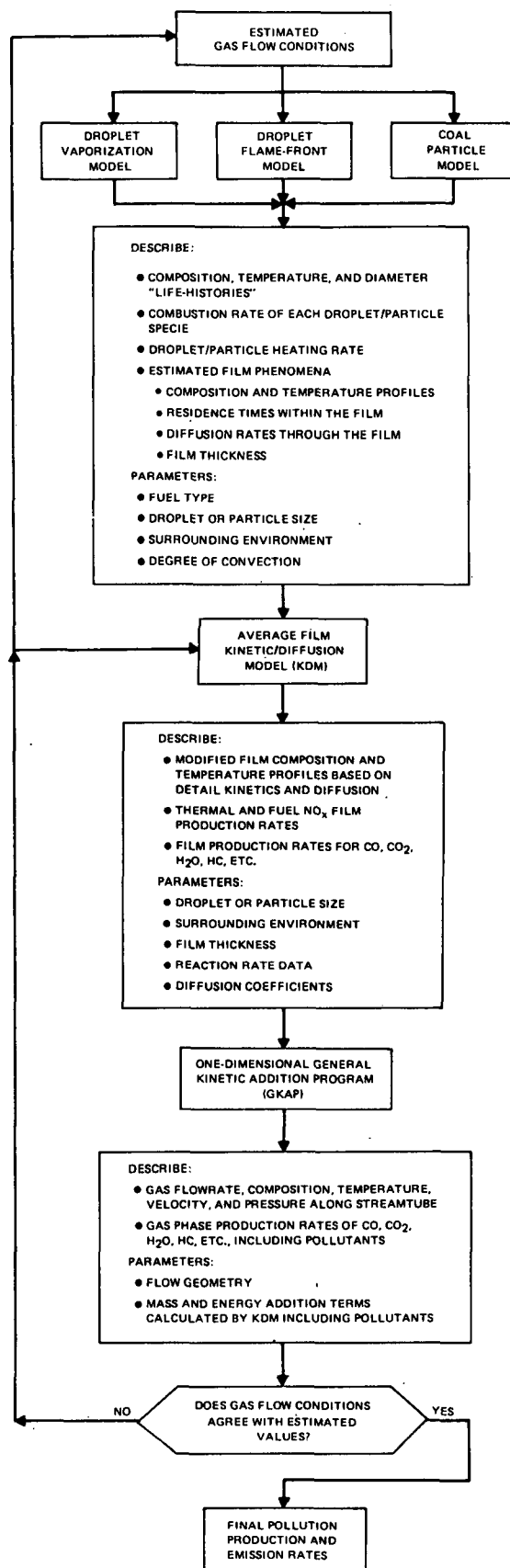


Figure I-2. Flow Diagram for Determination of Combustor Emission Levels

As before, the output of the droplet/particle model is input to the KDM model. For the streamtube case, the KDM model is only executed at selected locations along the streamtube to reduce overall computing time. The calculated results are the input into the GKAP model. If the gas temperature and composition along the streamtube that are calculated by GKAP are different than the temperatures and compositions used as boundary conditions in the KDM calculations, the KDM and GKAP calculations must be rerun with the new gas temperatures and compositions. If the GKAP gas temperatures, velocities, and oxygen concentrations are different than the conditions used in the particle ensemble model calculations, the particle ensemble, KDM, and GKAP programs must be re-executed with the new estimated gas flow conditions. The gas temperature, velocities, and oxygen concentrations are only checked for the possibility of re-executing the particle ensemble model because the ensemble models are most sensitive to these gas variables.

After agreement has been obtained between gas flow variables calculated by GKAP and the estimated values used in the particle ensemble and KDM models, GKAP yields the final emission levels, including both gas-phase- and two-phase-generated pollutants.

Since the particle ensemble models are insensitive to gas variables, except temperature, velocity, and oxygen concentration, overall computation time would be reduced if these variables could be determined without executing the KDM program. The main reason for this time reduction is that the KDM program requires at least an order of magnitude more computation time than does the particle ensemble models or the GKAP program. If experimental temperature, velocity, and oxygen composition data are available, then the particle ensemble model can be executed only once to obtain the input data required by KDM. If no experimental data are available, then the user must estimate the gas flow variables before executing the particle ensemble model. The initial guess of the variables will probably not be correct. Therefore, the following procedure should be used to converge on the gas flow variables.

First, the flow variables are estimated, based on past experience (Fig. I-3). Then the particle ensemble model is executed to determine both the fuel combustion and oxygen consumption rates. These mass addition terms are then used as input to the GKAP program, which calculates the gas temperature, velocity, and oxygen concentration. These variables are then compared with the estimated values and the procedure repeated until convergence has been obtained. After convergence has been obtained, the KDM program is executed, and the procedure is the same as discussed in the previous paragraphs. It is recommended that this procedure be applied to a selected set of data where little or no recirculation occurred to determine the validity of the model approach.

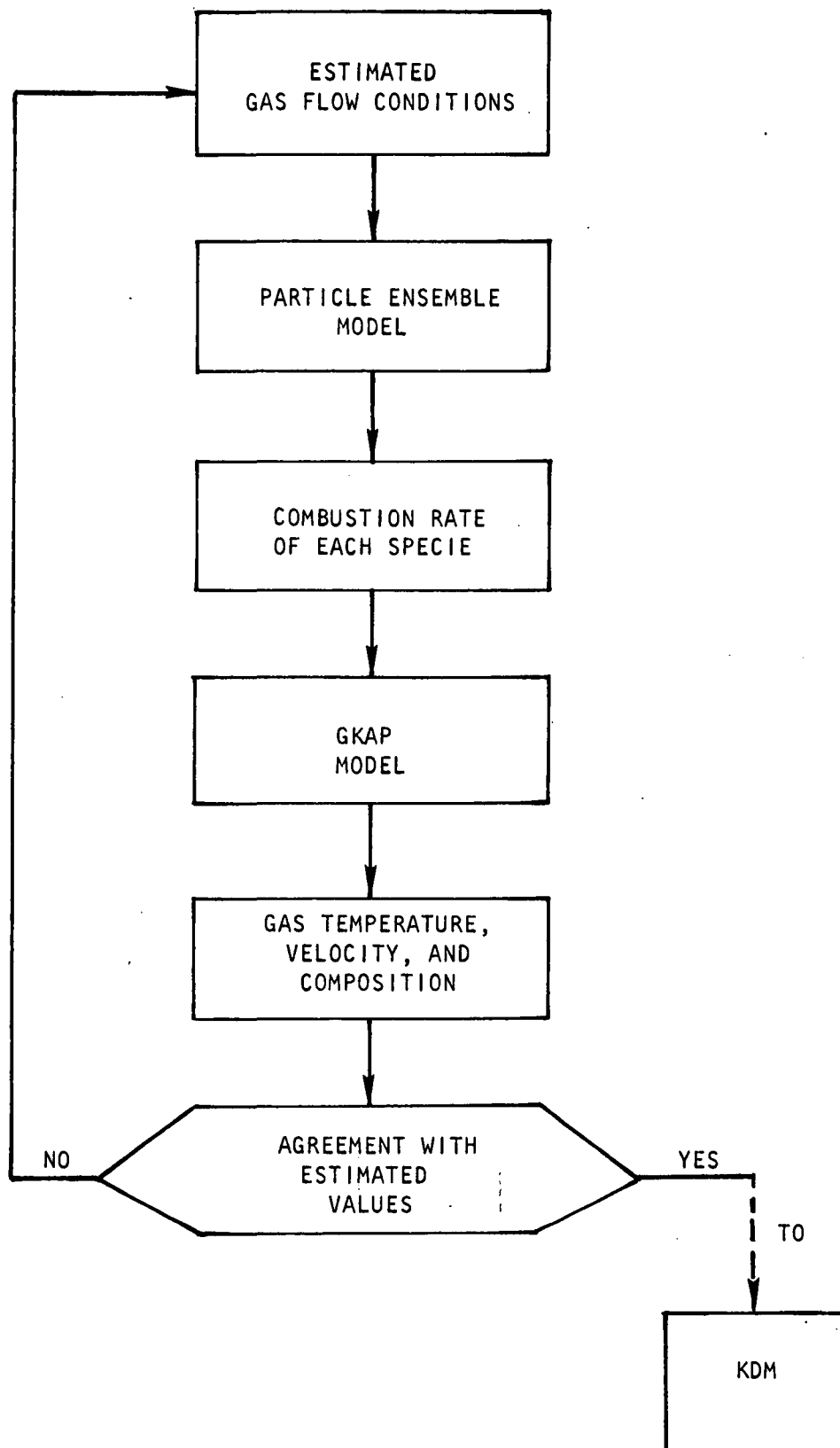


Figure I-3. Estimation Procedure for Gas Flow Conditions

NOMENCLATURE

A	Pre-exponential factor in rate constant or burner exit port area
A_o	Area of orifice
B	Pre-exponential coefficient in forward Arrhenius reaction rate equation
c	Molar density
C	Orifice constant or centigrade
CA	Chemiluminescent analyzer
C_i	Concentration of species i
C_p	Specific heat at constant pressure
d_w	Diameter of thermocouple wire
D	Diffusivity
D_{ij}	Diffusion coefficient of species i into species j
DR	Dilution ratio: $(Ar/O_2)/3.76$
E	Activation energy or electrical potential
ΔE	Forward activation energy in Arrhenius reaction rate equation
f_i	Mole fraction of species i
F	Mass flowrate
g	Acceleration of gravity
h	Heat transfer coefficient
H	Enthalpy
ΔH_{298}°	Heat of formation
ΔH_{VAP}	Latent heat of vaporization
i	Summation indices or species number
IFRF	International Flame Research Foundation
j	Summation indices or species number
k	Thermal conductivity
	or
	Summation indices or species number
	or
	Reaction rate constant

k'	Thermal conductivity
K	Kelvin
K_c	Equilibrium constant
ℓ	Summation indices or species number
m	Summation indices or species number
M	Molecular weight
MC	Model Compound
MW	Molecular weight
n	Summation indices or species number
N	Reaction order
\dot{N}	Molar flowrate
Nu_H, Nu_M	Nusselt numbers for heat and mass transfer
P	Pressure
ppm	Parts per million (volumetric basis)
q_c	Heat of combustion
Q	Heat transfer rate
Q_c	Heat of Combustion
r	Radius or radial coordinate
R	Gas constant or reaction rate
\dot{R}	Reaction rate
Re	Reynold's Number
S	Entropy
SS	Stainless Steel
t	time
T	Temperature
\bar{T}	Time integrated average temperature of combustion gas from the burner face to a distance y
T_e	Temperature of surroundings
T_G	Gas temperature (model compound reactor)
T_s	Temperature of the NO calibration standard gas at the critical flow sampling orifice
T_u	Temperature of the unknown gas at the critical flow sampling orifice

T_w	Temperature of thermocouple wire or wall temperature
v	Velocity
V	Volume
\dot{V}	Flowrate of gas to the CA from the sonic sampling orifice
V_i	Diffusion velocity of species i
\dot{V}_s	Flowrate of NO calibration standard gas to the CA from the sonic sampling orifice
\dot{V}_u	Flowrate of unknown gas through a sonic sampling orifice to the CA
W	Weight
\dot{W}	Total volumetric feedrate to the burner
x	Distance
X	Mole fraction
y	Distance from the burner
Y	Volume fraction
Z	Heat blockage parameter
α	Heat transfer parameter, stoichiometric coefficient, or temperature exponent
β	Flame radius parameter
γ	Ratio of specific heats
δ	Density based on total volume
ϵ	Emissivity
ν	Stoichiometric coefficient
ξ	Dimensionless coordinate
ρ	Density
σ	Stefan-Boltzmann constant
ϕ	Equivalence ratio (fuel-air)

Subscripts

d - droplet
f - flame
g - gas
H - heterogenous
I - inside
l - liquid
NBP - normal boiling point
Ø - outside
ox - oxidizer
p - particle
R - radiation
S - surface
t, T - total
v, VAP - vapor, vaporization, or volatile
 δ_M, δ_H - outer boundary of the mass and heat transfer film

REFERENCES

1. Flagan, R. C., "NO Formation from Fuel Bound Nitrogen in an Oil Fired Burner," MIT Thesis, May 1973.
2. Sternling, C. V. and J.O.L. Wendt, "Kinetic Mechanisms Governing the Fate of Chemically Bound Sulfur and Nitrogen in Combustion," Final Report S-14129, Shell Development Co., Emeryville, Calif., EPA Contract EHS-D-71-45, Task 14, August 1972.
3. Martin, G. B. and E. E. Berkau, "An Investigation of the Conversion of Various Fuel Nitrogen Compounds to Nitrogen Oxides in Oil Combustion," AICHE Symposium Series, Vol. 68, No. 126, 45(1972).
4. Turner, D. W., R. L. Andrews, and C. W. Siegmund, "Influence of Combustion Modification and Fuel Nitrogen Content on Nitrogen Oxides Emissions from Fuel Oil Combustion," Ibid, p. 55 (1972).
5. Bartok, W., V. S. Engleman, R. Goldstein, and E. G. del Valle, "Basic Kinetic Studies and Modeling of Nitric Oxide Formation in Combustion Processes," Ibid, p. 30 (1972).
6. American Flame Days Meeting, Chicago, Illinois, July 1972.
7. EPA-65012-73-021, "Proceedings, EPA Coal Combustion Seminar," Research Triangle Park, N. C., June 1973.
8. Symposium on "Control of NO_x Emissions from Stationary Sources," AIChE 66th Annual Meeting, Philadelphia, Nov. 1973.
9. EPA Contractor's Meeting on NO_x Kinetics, University of Arizona, Tucson, Arizona, March 1974.
10. Ball, J. S. et al., "Nitrogen Content of Crude Petroleums," Ind. & Eng. Chem., 43, 2577 (1951).
11. Albert, D. K., "Determination of Nitrogen Compound Types and Distribution in Petroleum by Gas Chromatography with a Coulometric Detector," Anal. Chem., 39, 1113 (1967).

12. Ball, J. S., et al., "Composition of Colorado Shale-Oil Naptha," Ind & Eng. Chem., 41, 581 (1949).
13. Ball, J. S. and W. J. Wenger, "How Much Nitrogen in Crudes from your Area?" Petroleum Refiner, April 1958.
14. Ball, J. S. and H. T. Rall, "Nonhydrocarbon Components of a California Petroleum," Amer. Petr. Inst., 42, Sect. III, 128 (1962).
15. Bradenburg, C. F. and D. R. Latham, "Spectroscopic Identification of Basic Nitrogen Compounds in Wilmington Petroleum," J. Chem. and Eng. Data, 13, 391 (1968).
16. Brown, D., et al., "Gas-Liquid Chromatographic Separation and Spectrometric Identification of Nitrogen Bases in Hydrocracked Shale Oil Naptha," Anal. Chem., 42, 146 (1970).
17. Cady, W. E. and H. S. Seelig, "Composition of Shale Oil," Ind. and Eng. Chem., 44, 2636 (1952).
18. Cook, G. L. and F. M. Church, "Determination of Pyridines by Infrared Spectroscopy," Anal. Chem., 38, 993 (1956).
19. Dinneen, G. U., et al., "Composition of Crude Shale Oils," Ind. and Eng. Chem., 44, 2632 (1952).
20. Dinneen, G. U., et al., "Application of Separation Techniques to a High-Boiling Shale-Oil Distillate," Anal. Chem., 27, 185 (1955).
21. Dinneen, G. U., et al., "Estimation of Types of Nitrogen Compounds in Shale-Oil Gas Oil," Anal. Chem., 30, 2026 (1958).
22. Drushel, H. V., and A. L. Sommers, "Isolation and Identification of Nitrogen Compounds in Petroleum," Anal. Chem., 38, 19 (1966).
23. Fabbro, L. A., et al., "Extension of the Microcoulometric Determination of Total Bound Nitrogen in Hydrocarbons and Water," Anal. Chem., 43, 1671 (1971).
24. Haines, W. E., "Some Chemical and Physical Techniques for Separation and Identification of Nitrogen Compounds in Petroleum," Div. of Sci. and Tech. (Summer Symp), Vol. 42 (VIII), 1962.

25. Haines, W. E., et al., "Techniques for Separating and Identifying Nitrogen Compounds in Petroleum and Shale Oil," Seventh World Petroleum Congress.
26. Haines, W. E., et al., "Development of Analytical Techniques for Heavy Hydrocarbons and Related Compounds," 26th Mid-Year Meeting American Petroleum Institute, Division of Refining, San Francisco, May 1971.
27. Heistand, R. N., "Automated Kjeldahl Determination of Nitrogen in Petroleum," Anal. Chem., 42, 903 (1970).
28. Helm, R. V. et al., "Distribution of Nitrogen Compounds in Wilmington, Calif., Petroleum," Ind. and Eng. Chem. and Eng. Data Series, Vol. 2, No. 1, 95 (1957).
29. Helm, R. U., et al., "Identification of Carbazole in Wilmington Petroleum through Use of Gas-Liquid Chromatography and Spectroscopy," Anal. Chem., 32, 1975 (1960).
30. Hunt, R. H., and M. J. O'Neal, Jr., "The Composition of Petroleum," Advances in Petroleum Chemistry and Refining, Vol. 10, J. J. McKetta, Editor, John Wiley & Sons, Inc., New York, 1965.
31. Janssen, A. G., et al., "Isolation and Identification of Pyrrole and 2-Methylpyrrole from Shale Oil," J. Amer. Chem. Soc., 73, 4040 (1951).
32. Jewell, D. M. and R. E. Snyder, "Selective Separations of Nonbasic Nitrogen Compounds from Petroleum by Anion Exchange of Ferric Chloride Complexes," J. Chromatog., 38, 351 (1968).
33. Jewell, D. M., et al., "Ion-Exchange, Coordination, and Adsorption Chromatographic Separation of Heavy-End Petroleum Distillates," Anal. Chem., 44, 1391 (1972).
34. Jewell, D. M., et al., "Combination of Techniques for the Characterization of Residuals," Division Petroleum Chemistry, American Chemical Society Annual Meeting, New York, August 1972.
35. Kirk, R. E., and D. E. Othmer (Editor), Encyclopedia of Chemical Technology Interscience Encyclopedia, Inc., New York (1953).
36. Latham, D. R., et al., "Nonbasic Nitrogen Compounds in Petroleum," Hydrocarbon Analysis, ASTM STP 389, Am. Soc. Testing Materials, p. 385 (1965).

37. Lochte, H. L., "Petroleum Acids and Bases," Ind. and Eng. Chem., 44, 2597 (1952).
38. McDonald, F. R., et al., "Qualitative Applications of the NMR Spectra of Alkylpyridines: Part 1. Chemical Shifts of the Ring Protons," Appl. Spectroscopy, 22, 325 (1968).
39. Ibid: "Part 2. Chemical Shifts of the Protons of the Alkyl Substituents," 22, 329 (1968).
40. McKay, J. F., et al., "The Separation of Acidic Compound Types Isolated from High-Boiling Petroleum Distillates," Separation Science, 7, 361 (1972).
41. Morandi, J. R. and H. B. Jensen, "Comparison of Porphyrins from Shale Oil, Oil Shale, and Petroleum by Absorption and Mass Spectroscopy," J. Chem. and Eng. Data, 11, 81 (1966).
42. Morris, J. C., et al., "Review Article on Nonmetal Elements and Compounds in Oils," Anal. Chem., 43, No. 5, 187R (1971).
43. Ode, W. H., "Coal Analysis and Mineral Matter," Chemistry of Coal Utilization, Supplementary Volume, H. H. Lowry, Editor, NAS-NRC Committee on Chemistry of Coal, John Wiley & Sons, Inc., New York, 1963.
44. Okuno, I., et al., "Type Analysis of Nitrogen in Petroleum Using Nonaqueous Potentiometric Titration and Lithium Aluminum Hydride Reaction," Anal. Chem., 37, 54 (1965).
45. Petersen, J. C., et al., "Molecular Interactions of Asphalt, Tentative Identification of 2-Quinolones in Asphalt and their Interaction with Carboxylic Acids Present," Anal. Chem., 43, 1491 (1971).
46. Poulson, R. E., "Stationary Phases for Separation of Basic and Nonbasic Nitrogen Compounds or Hydrocarbons by Gas-Liquid Chromatography," J. Chromatographic Science, 7, 152 (1969).
47. Richter, F. P., et al., "Distribution of Nitrogen in Petroleum According to Basicity," Ind. and Eng. Chem., 44, 2601 (1952).
48. Sauer, R. W., et al., "Nitrogen Compounds in Domestic Heating Oil Distillates," Ind. and Eng. Chem., 44, 2606 (1952).

49. Smith, J. R., et al., "Separation of Nitrogen Compounds by Adsorption from Shale Oil," Anal. Chem., 22, 867 (1950).
50. Snyder, L. R. and B. E. Buell, "Characterization and Routine Determination of Certain Non-Basic Nitrogen Types in High Boiling Petroleum Distillates by Means of Linear Elution Adsorption Chromatography," Anal. Chim. Acta, 33, 285 (1965).
51. Snyder, L. R., B. E. Buell, and H. E. Howard, "Nitrogen and Oxygen Compound Types in Petroleum - Total Analysis of a 700-850 F Distillate from a California Crude," Anal. Chem., 40, p. 1303 (1968).
52. Snyder, L. R., "Nitrogen and Oxygen Compound Types in Petroleum-Total Analysis of a 400-700 F Distillate from a California Crude Oil," Anal. Chem., 41, 314 (1969).
53. Van Meter, R. A., et al., "Oxygen and Nitrogen Compounds in Shale-Oil Naptha," Anal. Chem., 24, 1758 (1952).
54. Ward, L. F., et al., "Nitrogen Compounds in Distillate Fuels," Anal. Chem., 25, 1070 (1953).
55. Wenger, W. J. and J. S. Ball, "Characteristics of Crude Oils from Utah," Paper No. 42, Bulletin 54 - Oil and Gas Possibilities of Utah, Re-evaluated, Utah Geological and Mineralogical Survey, 1963.
56. Nenner, I and G. S. Schule, "Temporary Negative Ions and Election Affinities of Benzene and N-Heterocyclic Molecules: Pyridine, Pyredazine, Pyrimidine, Pyrazine, and S-Triazine," J. Chem. Phys., 62, 1747 (1975).
57. Karr, E. Jr., "Chemistry of Coal Utilization: Supplementary Volume," W. H. Ode, editor, Wiley, New York, pp. 545-554.
58. Martin, G. B. and E. E. Berkau, "Evaluation of Various Combustion Modification Techniques for Control of Thermal and Fuel-Related Nitrogen Oxide Emissions," 14th Combustion Symposium International, 1972.
59. Heap, M. P., T. M. Lowes and R. Walmsley, "Emission of NO from Large Turbulent Diffusion Flames" 14th Combustion Symposium (International), 1972, p. 883.

60. Heap, M. P., T. M. Lowes and R. Walmsley, "NO Formation in Pulverized Coal Flames," European Combustion Symposium, 1973, p. 493.
61. Shaw, J. T. and A. C. Thomas, "Oxides of Nitrogen in Relation to Combustion in Coal" 7th Inter Conf on Coal Science, Prague, 1968.
62. Bowman, C. T., "Kinetics of NO Formation in Combustion Processes" 14th Combustion Symposium (International), 1972, p. 729.
63. DeSoete, G., "The Mechanism of Formation of NO from HN_3 and Amines in Hydrocarbon Flames," Rev. Inst. Fr. du Petr. Ann. Combustion Liquide, 28(1), 96(1973).
64. DeSoete, G., "III-Formation of NO in Flames, Formation of NO from Fuel Nitrogen, B-Cyanogen," Preprint-B., I.F.P.-21.309.
65. DeSoete, G. and A. Querand, "Formation of NO from Fuel Nitrogen C-Added NO," Preprint, Inst. Fr. du Petrole, 1973.
66. Fenimore, C. P., "Formation of NO from Fuel Nitrogen in Ethylene Flames," Comb. and Flame, 19, 289 (1972).
67. Sawyer, R. F., W. J. McLean, and C. M. Maes, "The Production of NO in NHS Oxidation Flames Ammonia Oxidation Flames," Comb. Sci. and Tech, 6, 47 (1972).
68. Fine, D. H., S. M. Slater, A. F. Sarofim, and G. C. Williams, "Nitrogen in Coal as a Source of NO Emission from Furnaces, Fuel, 53, 120 (1974).
69. Kaskan, W. E. and D. E. Hughes, "Mechanism of Decay of Ammonia in Flame Gases From an $\text{NH}_3/20$ Flame," Comb. and Flame, 20, 381 (1973).
70. Merryman, E. L. and A. Levy, "NO₂ Formation," Proc Third Inter Clean Air Congress, Dusseldorf, West Germany, Oct. 1973.
71. Johnson, C. T., Jr., "The Conversion of Fuel Bound Nitrogen to NO in Low Volatile Pulverized Coal Flames," MIT Thesis, 1973.
72. Slater, S. M., "NO Formation in the Combustion of Nitrogen-Containing Hydrocarbons," MIT Thesis, 1973.
73. Sarofim, A. F., G. C. Williams, M. Modell, and S. M. Slater, "Conversion of Fuel Nitrogen to NO in Premixed and Diffusion Flames," AICHE 66th Annual Meeting, Philadelphia November 1973.

74. Hazard, H. R., "Conversion of Fuel Nitrogen to NO_x in a Compact Combustor," J. Eng. Power, 185, July 1974.
75. Martin, G. B. and E. E. Berkau, "Preliminary Evaluation of Flue Gas Recirculation as a Control Method for Thermal and Fuel Related Nitric Oxide Emissions," Western States Sect Mtg, The Combustion Institute, Oct. 1971.
76. Bartok, A. R. Crawford, E. H. Manny, and G. J. Piegari, "Reduction of Nitrogen Oxide Emissions from Electric Utility Boilers by Modified Combustion Operation," American Flame Days Mtg., 1972.
77. Turner, E. W. and C. W. Siegmund, "Staged Combustion and Flue Gas Recycle: Potential for Minimizing NO_x from Fuel Oil Combustion," American Flame Days Mtg., 1972.
78. Flagan, R. C., F. Pompel and J. P. Appleton, "Atmospheric Pressure Burner Studies II: NO Formation by Combustion of Nitrogen Containing Fuels," Central States Sect Mtg., The Combustion Institute, March 1972.
79. Pershing, D. W., G. B. Martin and E. E. Berkau, "Influence of Design Variables on the Production of Thermal and Fuel NO from Residual Oil and Coal Combustion," AICHE 66th Annual Meeting, Philadelphia, November 1973.
80. Armento, W. J. and W. L. Sage, "The Effect of Design and Operation Variables NO_x Formation in Coal Fired Furnaces: Status Report," AICHE 66th Annual Meeting, Philadelphia, November 1973.
81. Pai, R. H., R. E. Sommerlad and R. P. Welden, " NO Emission, and Evaluation of Test Data and Design," AICHE 66th Annual Meeting, Philadelphia, November 1973.
82. Flagan, R. C. and J. P. Appleton, " NO Formation from Fuel Bound Nitrogen in an Oil Fired Burner," AICHE 66th Annual Meeting, Philadelphia, November 1973.
83. Henry, J. M., C. R. McCann, J. J. Demeter and D. Bienstock, " NO_x Control by Flue Gas Recirculation in Pulverized Coal Combustion," AICHE 66th Annual Meeting, Philadelphia, November 1973.

84. Pershing, D. W., J. W. Brown and E. E. Berkau, "Relationship of Burner Design to the Control of NO_x Emissions through Combustion Modification," EPA Coal Combustion Seminar, June 1973.
85. Heap, M. P., T. M. Lowes, R. Walmsley and H. Bartelds, "Burner Design Principles for Minimum NO_x Emissions," EPA Coal Combustion Seminar, June 1973.
86. England, C. and J. Houseman, "NO_x Reduction Techniques in Pulverized Coal Combustion," EPA Coal Combustion Seminar, June 1973.
87. McCann, C. R., J. J. Demeter and D. Bienstock, "Preliminary Evaluation of Combustion Modifications for Control of Pollutant Emissions from Multi-Burner Coal-Fired Combustion Systems," EPA Coal Combustion Seminar, June 1973.
88. Crawford, A. R., E. H. Manny, and W. Bartok, "NO_x Emission Control for Coal-Fired Utility Boilers," EPA Coal Combustion Seminar, June 1973.
89. Flagan, R. C., S. Galant and J. P. Appleton, "Rate Constrained Partial Equilibrium Models for the Formation of Nitric Oxide from Organic Fuel Nitrogen," Comb. and Flame 22, 299-311 (1974).
90. Armento, J. W., "Effects of Design and Operating Variables on NO_x from Coal-Fired Furnaces--Phase II," EPA Report EPA-650/2-74-002b, February 1975.
91. Hurd, C. D., et al., "Pyrolytic Formation of Arenes. I. Survey of General Principles and Findings," J. Amer. Chem. Soc., 84, 4509 (1962)
92. Hurd, C. D. and J. I. Simon, "Pyrolytic Formation of Arenes. III. Pyrolysis of Pyridine, Picolines and Methylpyrazine," Ibid, 4519 (1962).
93. Johns, I. B., et al., "Thermal Stability of Some Organic Compounds," J. Chem and Eng. Data, 7, 277 (1962).
94. Hirsch, S. S. and M. R. Lilyquist, "Thermal Stability of Model Compounds Related to Thermostable Polymers by Pyrolysis-Gas Chromatography," J. Appl. Polymer, Sci., 11, 305 (1967).

95. Jennings- E. C. and K. P. Dimick, "Gas Chromatography of Pyrolytic Products of Purines and Pyrimidines," Anal. Chem., 34, 1543 (1962).
96. Jacobson, I. A., Jr. et al., "Thermal Reactions of Organic Nitrogen Compounds I. 1-Methylpyrrole," J. Phys. Chem., 62, 1563 (1958).
97. Jacobson, I. A. Jr. and H. B. Jensen, "Thermal Reactions of Organic Nitrogen Compounds. II. 1-N-Butylpyrrole," J. Phys. Chem., 66, (1962).
98. Ibid, "III. 1-Isopropylpyrrole," J. Phys. Chem., 68, 3068 (1964).
99. Smith, E. B. and H. B. Jensen, "Autoxidation of Three 1-Alkylpyrroles," J. Org. Chem. 32, 3330 (1967)
100. Lovas, F. J. and F. O. Clark, "Pyrolysis of Ethylamine I. Microwave Spectrum and Molecular Constants of Vinylamine," J. Chem. Phys., 62, 1925 (1975).
101. Merryman, E. L. and A. Levy, "Nitrogen Oxide Formation in Flames: The Roles of NO₂ and Fuel Nitrogen," 15th Combustion Symposium (International), 1974.
102. Zeldovich, Я. B., "The Oxidation of Nitrogen in Combustion and Explosion," ACTA Physicochimica, USSR, XXI, No. 4 577 (1946).
103. Zeldovich, Я. B., P. Я. Sadovnikov, and D. A. Frank-Kamenetskii, "Oxidation of Nitrogen in Combustion," 209 pages, Publishing House of the Academy of Sciences of USSR, Moscow-Leninsrad, 1947 (Translated by M. Shelef of the Ford Motor Company).
104. Singer, J. M., et al., "Flame Characteristics Causing Air Pollution: Production of Oxides of Nitrogen and CO," Bureau of Mines, Report of Investigation 6958, 1966.
105. Leonard, P. A. and A. M. Mellor, "Partial Equilibrium Approximations for Computing NO Formation Rates," 1974 Spring Meeting, Western States Section, The Combustion Institute, Pullman, Washington.
106. Takagi, T., et al., "Evaluation of Various Factors Affecting NO Formation and Effectiveness of Some Emission Control Systems," Fuel, 53, 114 (1974).
107. Bartok, W. and V. S. Engleman, "Definition of the Mechanisms and Kinetics of the Formation of NO_x and Other Pollutants Under Normal and Combustion Modification Conditions," Progress Report No. 1, EPA Contract NO. 68-02-0224, 1973.

108. Fendell, F. E., P. C. Coates and E. B. Smith, AIAA Journal, Vol. 6, 1968, p. 1953.
109. Bracco, F. V., Fourteenth Symposium (International) on Combustion, The Combustion Institute, Pittsburgh, 1973, pp. 831-42.
110. Ranz, W. E. and W. R. Marshall, Jr., Chemical Engineering Progress, Vol. 48, 1952, pp. 141-46 and 173-180.
111. Rossini, F. D., K. S. Pitzer, R. L. Arnett, R. M. Braun, and G. C. Pimental, Selected Values of Physical and Thermodynamic Properties of Hydrocarbons and Related Compounds, Carnegie Press (1953).
112. Field Study of Emissions from Oil Burners, 1971.
113. Othmer, D. F., P. W. Maurer, C. J. Molinary, and R. C. Kowalski, "Correlating Vapor Pressures and Other Physical Properties," Industrial and Engineering Chemistry, Vol. 49, No. 1, January 1957, pp 125-137.
114. Othmer, D. F., and D. Zudkevitch, "Correlating Latent Heats and Entropies of Vaporization with Temperature," Industrial and Engineering Chemistry, Vol. 51, No. 6, June 1959, pp. 791-796.
115. von Fredersdorff, C. G. and M. A. Elliot, "Coal Gasification," Chapter 20 of Chemistry of Coal Utilization, Supplementary Volume, (H. H. Lowry, Editor), Wiley, New York, 1963.
116. Howard, J. B. and R. H. Essenhigh, "Pyrolysis of Coal Particles in Pulverized Fuel Flames," I&EC Process Design and Development, Vol. 6, No. 1, January 1967, pp 74-84.
117. Dainton, A. D., and Elliot, D. E.: "Researches into Combustion of Coal," Seventh World Power Conference, Transactions, 1968, pp 525-546.
118. Essenhigh, R. H., R. Froberg and J. B. Howard, "Combustion Behavior of Small Particles," Industrial and Engineering Chemistry, Vol. 57, No. 9, September 1965, pp 33-43 and 65.
119. Smith, I. W., "Kinetics of Combustion of Size-Graded Pulverized Fuels in the Temperature Range 1200-2270 K," Combustion and Flame, Vol. 17, (1971), pp. 303-314.

120. Axworthy, A. E., Jr, "Chemistry and Kinetics of Fuel Nitrogen Conversion to Nitric Oxide," 66th Annual AIChE Mts, Philadelphia, Pennsylvania, November 1973.
121. Axworthy, A. E. and M. Schuman, "Investigation of the Mechanism and Chemistry of Fuel Nitrogen Conversion to Nitrogen Oxides in Combustion," EPA Coal Combustion Seminar, Triangle Park, North Carolina, June 1973.
122. Levy, A., EPA Contractors Mtg on NO_x Kinetics, University of Arizona, Tucson, March 1974.
123. Benson, S. W., "Thermochemical Kinetics," John Wiley and Sons, New York, 1968.
124. Janz, G. J., "The direct Cyanogenation of Benzene," J. Am. Chem. Soc. 74, 4529 (1952).
125. Ruhemann, S., Braunkohle, 28, 749 (1929).
126. Johnson, G. E., et al., "Hydrogen Cyanide Produced from Coal and Ammonia," I&EC, Process Design and Development, 7, 137 (1968).
127. Robertus, R. J., et al., "Suppression of Thermal and Fuel Nitric Oxide Production in Pulverized Coal-Fired Furnaces," 1974 Spring Meeting of the Western States Section, The Combustion Institute, Pullman, Washington.
128. Snyder, R. E. Gulf Research and Development Co., Pittsburgh, Pennsylvania (Personal Communication).
129. Ramachandran, L. V., et al., "Formation of HCN by the Pyrolysis of Nitrogen-Enriched Coal," Proc. Symp. Chem. Oil Coal, 1969 (Publ. 1972) 499-505 (C.A. 81:66022n).
130. Andersen, J. W. and R. Friedman, "An Accurate Gas Metering System for Laminar Flow Studies," Rev. Sci. Instr. 20, 61 (1949).
131. Fristrom, R. M. and A. A. Westenberg, Flame Structure, McGraw-Hill, New York, 1965.
132. Kaskan, W. E. "The Dependence of Flame Temperature on Mass Burning Velocity," Sixth Symposium (International) on Combustion, pp. 134-143, New York, Reinhold Publication Corporation, 1957.

133. Diehl, R. C. and R. J. Haren, 1st Quarter 1972 Progress Report, Bureau of Mines.
134. Merryman, E. L. and A. Levy, "NO_x Formation in Combustion: Anomalous Early NO₂ Formation," Proceeding of the Third International Clean Air Congress, p. C117, Dusseldorf, Germany (1973).
135. Allen, J. D., "Probe Samplings of Oxides of Nitrogen from Flames," Comb. and Flame, 24, 133 (1975).
136. Davies, P. B. and B. A. Thrush, Trans. Far. Soc. 64, 1836 (1968).
137. Mulvihill, J. N. and L. F. Phillips, 15th Combustion Symposium (International), Tokyo, 1974.
138. Brocklehurst, B. and K. R. Jennings, "Reactions of Nitrogen Atoms in the Gas Phase," Progress In Reaction Kinetics, Vol. 4, G. Porter, Editor, pp 3-36, Pergamon Press, London, 1967.
139. Standard Methods for the Examination of Water and Wastewater, 13th Edition, 1971.
140. Annual Book of ASTM Standards, "Water; Atmospheric Analysis," Part 23, 1973.
141. Saltzman, B. E., Anal. Chem. 32, 135-137 (1960).
142. Saltzman, B. E., Anal. Chem. 26, 1949 (1954).
143. Orion Research Instruction Manual, Cyanide Ion Activity Electrode, Form IM94-06/271, 1972.
144. Hihiro, K. and Y. Yamamoto, "A New Spectrophotometric Determination of Cyanide by Solvent Extraction," Anal. Letters, 6, 761 (1973).
145. Fine, D., Environmental Science and Technology, 6, 348-350 (1972).
146. Halstead, C. J. et. al., Analyst 97, 55-63 (1972).
147. McAdams, W. H., Heat Transmission, p. 259, McGraw-Hill, New York 1954.
148. Touloukian, Y. S. and D. P. DeWitt, Thermo Physical Properties of Matter, Vol. 7, "Thermal Radiative Properties-Metallic Elements and Alloys," pp. 525-4, IFI/Plenum, New York, New York, 1970.

TECHNICAL REPORT DATA (Please read Instructions on the reverse before completing)			
1. REPORT NO. EPA-600/2-76-039		3. RECIPIENT'S ACCESSION NO.	
4. TITLE AND SUBTITLE Chemistry of Fuel Nitrogen Conversion to Nitrogen Oxides in Combustion		5. REPORT DATE February 1976	
		6. PERFORMING ORGANIZATION CODE	
7. AUTHOR(S) A. E. Axworthy, G. R. Schneider, M. D. Shuman, and V. H. Dayan		8. PERFORMING ORGANIZATION REPORT NO. R-9698	
9. PERFORMING ORGANIZATION NAME AND ADDRESS Rocketdyne Division Rockwell International 6633 Canoga Avenue Canoga Park, CA 91304		10. PROGRAM ELEMENT NO. 1AB014; ROAPs 21ADG08/21BCC12	
		11. CONTRACT/GRANT NO. 68-02-0635	
12. SPONSORING AGENCY NAME AND ADDRESS EPA, Office of Research and Development Industrial Environmental Research Laboratory Research Triangle Park, NC 27711		13. TYPE OF REPORT AND PERIOD COVERED Final; 6/72-5/75	
		14. SPONSORING AGENCY CODE EPA-ORD	
15. SUPPLEMENTARY NOTES EPA project officer for this report is B. Martin, 919/549-8411, Ext 2235.			
16. ABSTRACT The report gives results of an experimental and analytical investigation of chemical mechanisms involved in the conversion of fuel nitrogen to NOx in combustion. The pyrolysis of fossil fuels and model fuel nitrogen compounds was investigated, droplet and particle combustion models were developed, and premixed flat-flame burner experiments were conducted to study the conversion of HCN and NH3 to NOx in low-pressure CH4-O2-Ar flames. Decomposition rates and products were measured in helium from 850 to 1100C for pyridine, benzonitrile, quinoline, and pyrrole; products were measured for six No. 6 fuel oils, one crude oil, and two coals. HCN was the major nitrogen-containing pyrolysis product; the amount formed increased with temperature. NH3 was a minor product and little if any N2 was formed. The burner experiments demonstrated that fuel NO forms relatively slowly above the luminous zone in the same region where CO is oxidized to CO2 or later. Although HCN and NH3 gave similar yields of NO, the NH3 reacted very early in the flame front; most of the HCN survived the luminous zone and then reacted slowly. A mechanism was proposed in which fuel NO forms via the reaction: O + NCO = NO + CO.			
17. KEY WORDS AND DOCUMENT ANALYSIS			
a. DESCRIPTORS		b. IDENTIFIERS/OPEN ENDED TERMS	c. COSATI Field/Group
Air Pollution Pyrolysis Chemical Reactions Fossil Fuels Combustion Hydrogen Cyanide Nitrogen Ammonia Conversion Nitrogen Oxides		Air Pollution Control Fuel Nitrogen	13B 07D 21B 21D 07B
18. DISTRIBUTION STATEMENT Unlimited		19. SECURITY CLASS (This Report) Unclassified	21. NO. OF PAGES 373
		20. SECURITY CLASS (This page) Unclassified	22. PRICE